

UC Merced

UC Merced Electronic Theses and Dissertations

Title

Estimating plant-accessible water storage through evaluating evapotranspiration in the semi-arid western United States using eddy-covariance, remote sensing, and spatially distributed data

Permalink

<https://escholarship.org/uc/item/16h200ht>

Author

Rungee, Joseph

Publication Date

2019

Peer reviewed|Thesis/dissertation

**Estimating plant-accessible water storage through evaluating
evapotranspiration in the semi-arid western United States using
eddy-covariance, remote sensing, and spatially distributed data**

A dissertation submitted in partial satisfaction of the requirements
for the degree of Doctor of Philosophy

by

Joseph Rungee

Committee in charge:

Professor Roger Bales, Chair
Professor Michael Goulden
Professor Mohammad Safeeq
Professor Marc Beutel
Professor LeRoy Westerling

Spring 2019

Portion of Chapter 2 © 2018 Hydrological Processes

Joseph Rungee, 2019

All rights reserved

The dissertation of Joseph Rungee, titled Estimating plant-accessible water storage through evaluating evapotranspiration in the semi-arid western United States using eddy-covariance, remote sensing, and spatially distributed data, is acceptable in quality and form for publication on microfilm and electronically:

Chair _____ Date _____

Roger Bales, Ph.D.

_____ Date _____

Michael Goulden, Ph.D.

_____ Date _____

Mohammad Safeeq, Ph.D.

_____ Date _____

Marc Beutel, Ph.D.

_____ Date _____

LeRoy Westerling, Ph.D.

Contents

Contents	iv
List of Figures	vi
List of Tables	xvi
1 Introduction	3
1.1 Methods for measuring evapotranspiration	4
1.2 Methods for estimating evapotranspiration across the landscape	6
1.3 Objectives of this study	7
1.4 Bibliography	10
2 Evapotranspiration response to multi-year dry periods in the semi-arid western United States¹	17
2.1 Introduction	19
2.2 Methods	21
2.3 Results	25
2.4 Discussion	29
2.5 Conclusions	32
2.6 Bibliography	43
3 Closing the mountain water balance: evapotranspiration patterns and uncertainties in tributaries to California's Central Valley, USA	49
3.1 Introduction	51
3.2 Methods	53
3.3 Results	58
3.4 Discussion	63
3.5 Conclusions	68
3.6 Bibliography	79
4 Response of subsurface water storage in California's headwaters to a changing climate	85
4.1 Introduction	87
4.2 Methods	89

4.3	Results	94
4.4	Discussion	98
4.5	Conclusions	102
4.6	Bibliography	112
5	Conclusion	118
A	Appendices for Chapter 2	121
A.1	150
A.2	150
A.3	150
A.4	150
B	Appendices for Chapter 3	150
B.1	156
B.2	156
B.3	156
B.4	156
C	Appendices for Chapter 4	156

List of Figures

2.1	Flux-tower locations. Color codes and different markers represent land-cover types. The background is the IGBP layer for the region.	37
2.2	Monthly means of measured evapotranspiration (ET), potential evapotranspiration (PET), rain plus snowmelt (rain + snowmelt), and total precipitation (precipitation). The solid shaded area represents the average monthly ET supported by seasonal storage and the hatched area represents evapotranspiration as sublimation and does not contribute PAWS drawdown. See Table 2.1 for site characteristics. Note: the values here are averaged monthly values, and shaded area may not exactly match Figure 2.3 mean ET from storage values which are calculated on an annual basis. Bold denotes Mediterranean climate sites.	38
2.3	Amount of evapotranspiration (ET) supported by plant-accessible water storage for each water year on record by site. Site abbreviation is followed by state abbreviation. Other site characteristics are given in Table I. Vertical black lines separate land-cover types. Bold denotes Mediterranean climate sites.	39
2.4	a.1-5. Annual precipitation versus evapotranspiration (ET) by land-cover type for all sites (b.1-5 legend included here), b.1-5. annual precipitation vs. evapotranspiration after removing all energy and precipitation-limited sites, and site years with annual precipitation below the mean, and c.1-5 show ranges of maximum ET for the five land-cover types.	40
2.5	Measured annual evapotranspiration (ET), estimated potential evapotranspiration (PET), and precipitation (P) for all years of record shown in the Budyko framework by land-cover type. Refer to Table 2.1 for site characteristics.	41
2.6	Plant-accessible-water-storage drawdown, starting water year and land-cover type for all sites experiencing a multi-year dry period. Red circles indicate the plant-accessible-water-storage deficit ($\sum P - ET$) and month in which evapotranspiration declined significantly, relative to wet-year values. Bold denotes Mediterranean climate sites.	42

3.1	Study area showing locations of flux towers and land-cover classification, unimpaired streamflow gauges, and delineated river basins. The background shows the IGBP land-cover.	71
3.2	Plots of individual regressions of evapotranspiration (ET) with considered climatic variables, Normalized Difference Vegetation Index (NDVI), annual precipitation (P), the mean of the current and previous years annual precipitation (PP), and temperature (T). Marker size increases with deviation from the mean, were larger markers represent wetter (circle) or drier (triangle) years.	72
3.3	Modeled evapotranspiration versus measured evapotranspiration considering different data sources and variable combinations. Data sources include Landsat (LS) and MODIS (MOD) for NDVI, and PRISM 800 m (800m) and 4 km (4km) climate data products. Variables considered were all (NDVI, PP, T, vegetation bias correction), NoT (NDVI, PP, vegetation bias correction), NoV (NDVI, PP, T), NoVT (NDVI and PP), and only NDVI.	73
3.4	Modeled evapotranspiration validation by data source and input variables. Leave-one-WY-out was performed by leaving out all measured evapotranspiration values for a given water year for calibration and validated using the removed years and Leave-one-site-out was performed by using all but one site for calibration and validated using the removed site.	74
3.5	Evapotranspiration estimated as PRISM precipitation minus full natural flow (P-Q) versus modeled evapotranspiration (ET) from the MOD800m data. Legend displays basins from north to south, averaged over 2001-2012. Annual values of P and ET for each basin can be seen in Figure B.1.	75
3.6	Variability of 800m PRISM temperature and precipitation, MODIS NDVI, modeled evapotranspiration (MOD800m_All), and runoff calculated as the difference of precipitation and evapotranspiration ($P - ET$) by latitude and elevation. Different color contour lines are to improve visibility only.	76
3.7	Flux tower representativeness of precipitation, temperature, and modeled evapotranspiration. Stars are flux towers within the boundary of the study area, and the circles are the remaining flux towers in California. See Figure B.2 for general trends with modeled ET and precipitation binned by temperature and temperature binned by precipitation.	77
3.8	a) mean-annual precipitation (P), modeled evapotranspiration (ET, MOD800m_All) and evapotranspiration from storage (ETs) by basin and per 100 m in elevation measured in km; b) is a normalized histogram of area by elevation; c) is a normalized histogram of volumetric runoff by elevation. SL indicates the historical rain-snow transition.	78

4.1	Site map of California, USA, with the boundaries of the 14 basins used and the locations of stream gauges where unimpaired runoff is calculated.	106
4.2	Time-series plots of $P - Q$ for the entire record and ET (1985-2018). Red line is the 15-year moving average, solid black line is the long-term (LT, entire time-series) Theil-Sens slope, and the dashed black line is the near-term (NT, 34-year) Theil-Sens slope values in mm-yr^{-1}	107
4.3	Basin-scale water balance by elevation for each basin. Numbers correspond to the basins from north to south as presented in Figure 4.1. These were calculated following Bales et al. (2018), where height above the bar is runoff and height below the bar is evapotranspiration.	108
4.4	Time-series of annual change in storage (ΔS , solid line), ΔS plus the offset, e (dashed line), and the area-weighted sum of negative precipitation (P) minus evapotranspiration (ET) pixels from the annual basin maps (circles). ΔS was calculated as $P - Q - ET$, and e was calculated as the offset of the ET vs. $P - Q$ scatter plots from the 1:1 line (first column).	109
4.5	Basin-scale trends between change in storage with precipitation (P), temperature (T), evapotranspiration (ET), unimpaired runoff (Q), snow-water equivalent (SWE), and the timing of 90 percent melt from peak SWE (90%M). Filled-inner circles represent p-values ≤ 0.1 and lines are p-values > 0.1 . Colors represent a positive (blue) or negative (red) trend. Marker size is the absolute value of Kendalls tau (τ), where the perimeter circle represents a τ of 1.	110
4.6	Time-series analysis of ΔS and water-cycle-related features. Columns LT $P - Q$, NT $P - Q$, P , T , ET , Q , SWE, 90%M, and ΔS are time series trend analyses for Long-term $P - Q$, Near-term (34-year) $P - Q$, precipitation, temperature, evapotranspiration, runoff, snow-water equivalent and the timing of 90 percent melt from peak SWE, respectively. Circles represent p-value ≤ 0.1 and lines are p-values > 0.1 . r^2 values were calculated via linear regression and slopes, m , are Theil-Sens slopes with units of $^{\circ}\text{C/yr}$ for T, otherwise mm yr^{-1}	111
A.1.1	US-Blo monthly evapotranspiration (ET) and precipitation for each water year	122
A.1.2	MB monthly evapotranspiration (ET) and precipitation for each water year	123
A.1.3	US-Vcp monthly evapotranspiration (ET) and precipitation for each water year	124
A.1.4	US-CZ3 monthly evapotranspiration (ET) and precipitation for each water year	125

A.1.5	US-NR1 monthly evapotranspiration (ET) and precipitation for each water year	126
A.1.6	US-Vcm monthly evapotranspiration (ET) and precipitation for each water year	127
A.1.7	US-GLE monthly evapotranspiration (ET) and precipitation for each water year	128
A.1.8	US-CZ2 monthly evapotranspiration (ET) and precipitation for each water year	129
A.1.9	US-SCf monthly evapotranspiration (ET) and precipitation for each water year	130
A.1.10	RMEA monthly evapotranspiration (ET) and precipitation for each water year	131
A.1.11	US-Ton monthly evapotranspiration (ET) and precipitation for each water year	132
A.1.12	US-CZ1 monthly evapotranspiration (ET) and precipitation for each water year	133
A.1.13	US-SRM monthly evapotranspiration (ET) and precipitation for each water year	134
A.1.14	US-Var monthly evapotranspiration (ET) and precipitation for each water year	135
A.1.15	US-SCg monthly evapotranspiration (ET) and precipitation for each water year	136
A.1.16	US-Wkg monthly evapotranspiration (ET) and precipitation for each water year	137
A.1.17	USA monthly evapotranspiration (ET) and precipitation for each water year	138
A.1.18	USS monthly evapotranspiration (ET) and precipitation for each water year	139
A.1.19	RMES monthly evapotranspiration (ET) and precipitation for each water year	140
A.1.20	US-SCs monthly evapotranspiration (ET) and precipitation for each water year	141
A.1.21	US-Whs monthly evapotranspiration (ET) and precipitation for each water year	142
A.1.22	US-SRC monthly evapotranspiration (ET) and precipitation for each water year	143
A.1.23	US-SCw monthly evapotranspiration (ET) and precipitation for each water year	144
A.1.24	US-SCc monthly evapotranspiration (ET) and precipitation for each water year	145
A.1.25	US-SCd monthly evapotranspiration (ET) and precipitation for each water year	146

A.2.1	Boxplots of annual evapotranspiration supported by storage when accounting for snow (black) and when considering all snow as rain (red) for all snow-influenced sites.	147
A.3.1	Regressions of site-year evapotranspiration (ET) with precipitation (P) and temperature (T).	148
A.4.1	Regressions of site-year evapotranspiration (ET) from subsurface plant-accessible water storage (PAWS) with precipitation (P) and temperature (T).	149
B.1.1	Individual site year, by basin, of precipitation (P) and evapotranspiration (ET).	152
B.2.1	Best fit first order power functions between evapotranspiration and precipitation binned by temperature (a.) and temperature binned by precipitation (b.).	153
B.3.1	Plot of all site years of $P - Q$ and ET . The data is binned by wet and dry years with best fit line, where wet years are years above a given basins 34-year mean and dry year are below.	154
B.4.1	Plots of all site years of $P - Q$ and ET by basin. The data is binned by wet and dry years with best fit line, where wet years are years above a given basins 34-year mean and dry year are below.	155
C.1.1	Covariance matrix for Shasta, where dS is change in storage, P is precipitation, T is temperature, ET is evapotranspiration, FNF is unimpaired runoff, SWE is snow-water equivalent, and 90% Mday is the timing of 90% snowmelt from peak SWE.	157
C.1.2	Covariance matrix for Feather, where dS is change in storage, P is precipitation, T is temperature, ET is evapotranspiration, FNF is unimpaired runoff, SWE is snow-water equivalent, and 90% Mday is the timing of 90% snowmelt from peak SWE.	158
C.1.3	Covariance matrix for Yuba, where dS is change in storage, P is precipitation, T is temperature, ET is evapotranspiration, FNF is unimpaired runoff, SWE is snow-water equivalent, and 90% Mday is the timing of 90% snowmelt from peak SWE.	159
C.1.4	Covariance matrix for American, where dS is change in storage, P is precipitation, T is temperature, ET is evapotranspiration, FNF is unimpaired runoff, SWE is snow-water equivalent, and 90% Mday is the timing of 90% snowmelt from peak SWE.	160
C.1.5	Covariance matrix for Cosumnes, where dS is change in storage, P is precipitation, T is temperature, ET is evapotranspiration, FNF is unimpaired runoff, SWE is snow-water equivalent, and 90% Mday is the timing of 90% snowmelt from peak SWE.	161
C.1.6	Covariance matrix for Mokelumne, where dS is change in storage, P is precipitation, T is temperature, ET is evapotranspiration, FNF is unimpaired runoff, SWE is snow-water equivalent, and 90% Mday is the timing of 90% snowmelt from peak SWE.	162

C.1.7	Covariance matrix for Stanislaus, where dS is change in storage, P is precipitation, T is temperature, ET is evapotranspiration, FNF is unimpaired runoff, SWE is snow-water equivalent, and 90% Mday is the timing of 90% snowmelt from peak SWE.	163
C.1.8	Covariance matrix for Tuolumne, where dS is change in storage, P is precipitation, T is temperature, ET is evapotranspiration, FNF is unimpaired runoff, SWE is snow-water equivalent, and 90% Mday is the timing of 90% snowmelt from peak SWE.	164
C.1.9	Covariance matrix for Merced, where dS is change in storage, P is precipitation, T is temperature, ET is evapotranspiration, FNF is unimpaired runoff, SWE is snow-water equivalent, and 90% Mday is the timing of 90% snowmelt from peak SWE.	165
C.1.10	Covariance matrix for San Joaquin, where dS is change in storage, P is precipitation, T is temperature, ET is evapotranspiration, FNF is unimpaired runoff, SWE is snow-water equivalent, and 90% Mday is the timing of 90% snowmelt from peak SWE.	166
C.1.11	Covariance matrix for Kings, where dS is change in storage, P is precipitation, T is temperature, ET is evapotranspiration, FNF is unimpaired runoff, SWE is snow-water equivalent, and 90% Mday is the timing of 90% snowmelt from peak SWE.	167
C.1.12	Covariance matrix for Kaweah, where dS is change in storage, P is precipitation, T is temperature, ET is evapotranspiration, FNF is unimpaired runoff, SWE is snow-water equivalent, and 90% Mday is the timing of 90% snowmelt from peak SWE.	168
C.1.13	Covariance matrix for Tule, where dS is change in storage, P is precipitation, T is temperature, ET is evapotranspiration, FNF is unimpaired runoff, SWE is snow-water equivalent, and 90% Mday is the timing of 90% snowmelt from peak SWE.	169
C.1.14	Covariance matrix for Kern, where dS is change in storage, P is precipitation, T is temperature, ET is evapotranspiration, FNF is unimpaired runoff, SWE is snow-water equivalent, and 90% Mday is the timing of 90% snowmelt from peak SWE.	170
C.2.1	Time series of major variables for Shasta. The red and blue vertical shading represents multiyear dry and wet periods, respectively. . .	171
C.2.2	Time series of major variables for Feather. The red and blue vertical shading represents multiyear dry and wet periods, respectively. . .	172
C.2.3	Time series of major variables for Yuba. The red and blue vertical shading represents multiyear dry and wet periods, respectively. . .	173
C.2.4	Time series of major variables for American. The red and blue vertical shading represents multiyear dry and wet periods, respectively. . .	174
C.2.5	Time series of major variables for Cosumnes. The red and blue vertical shading represents multiyear dry and wet periods, respectively. . .	175
C.2.6	Time series of major variables for Mokelumne. The red and blue vertical shading represents multiyear dry and wet periods, respectively. . .	176

C.2.7	Time series of major variables for Stanislaus. The red and blue vertical shading represents multiyear dry and wet periods, respectively.	177
C.2.8	Time series of major variables for Tuolumne. The red and blue vertical shading represents multiyear dry and wet periods, respectively.	178
C.2.9	Time series of major variables for Merced. The red and blue vertical shading represents multiyear dry and wet periods, respectively. . .	179
C.2.10	Time series of major variables for San Joaquin. The red and blue vertical shading represents multiyear dry and wet periods, respectively.	180
C.2.11	Time series of major variables for Kings. The red and blue vertical shading represents multiyear dry and wet periods, respectively. . .	181
C.2.12	Time series of major variables for Kaweah. The red and blue vertical shading represents multiyear dry and wet periods, respectively. . .	182
C.2.13	Time series of major variables for Tule. The red and blue vertical shading represents multiyear dry and wet periods, respectively. . .	183
C.2.14	Time series of major variables for Kern. The red and blue vertical shading represents multiyear dry and wet periods, respectively. . .	184
C.3.1	Time series of normalized major variables for Shasta. The red and blue vertical shading represents multiyear dry and wet periods, respectively.	185
C.3.2	Time series of normalized major variables for Yuba. The red and blue vertical shading represents multiyear dry and wet periods, respectively.	186
C.3.3	Time series of normalized major variables for Feather. The red and blue vertical shading represents multiyear dry and wet periods, respectively.	187
C.3.4	Time series of normalized major variables for American. The red and blue vertical shading represents multiyear dry and wet periods, respectively.	188
C.3.5	Time series of normalized major variables for Cosumnes. The red and blue vertical shading represents multiyear dry and wet periods, respectively.	189
C.3.6	Time series of normalized major variables for Mokelumne. The red and blue vertical shading represents multiyear dry and wet periods, respectively.	190
C.3.7	Time series of normalized major variables for Stanislaus. The red and blue vertical shading represents multiyear dry and wet periods, respectively.	191
C.3.8	Time series of normalized major variables for Tuolumne. The red and blue vertical shading represents multiyear dry and wet periods, respectively.	192
C.3.9	Time series of normalized major variables for Merced. The red and blue vertical shading represents multiyear dry and wet periods, respectively.	193

C.3.10	Time series of normalized major variables for San Joaquin. The red and blue vertical shading represents multiyear dry and wet periods, respectively.	194
C.3.11	Time series of normalized major variables for Kings. The red and blue vertical shading represents multiyear dry and wet periods, respectively.	195
C.3.12	Time series of normalized major variables for Kaweah. The red and blue vertical shading represents multiyear dry and wet periods, respectively.	196
C.3.13	Time series of normalized major variables for Tule. The red and blue vertical shading represents multiyear dry and wet periods, respectively.	197
C.3.14	Time series of normalized major variables for Kern. The red and blue vertical shading represents multiyear dry and wet periods, respectively.	198
C.4.1	Runoff (blue), evapotranspiration (green), precipitation (dotted hatch), and change in storage (red) binned by basins and elevation for water year 1985. Number corresponds with Basin numbers in Figure 1. .	199
C.4.2	Runoff (blue), evapotranspiration (green), precipitation (dotted hatch), and change in storage (red) binned by basins and elevation for water year 1986. Number corresponds with Basin numbers in Figure 1. .	200
C.4.3	Runoff (blue), evapotranspiration (green), precipitation (dotted hatch), and change in storage (red) binned by basins and elevation for water year 1987. Number corresponds with Basin numbers in Figure 1. .	201
C.4.4	Runoff (blue), evapotranspiration (green), precipitation (dotted hatch), and change in storage (red) binned by basins and elevation for water year 1988. Number corresponds with Basin numbers in Figure 1. .	202
C.4.5	Runoff (blue), evapotranspiration (green), precipitation (dotted hatch), and change in storage (red) binned by basins and elevation for water year 1989. Number corresponds with Basin numbers in Figure 1. .	203
C.4.6	Runoff (blue), evapotranspiration (green), precipitation (dotted hatch), and change in storage (red) binned by basins and elevation for water year 1990. Number corresponds with Basin numbers in Figure 1. .	204
C.4.7	Runoff (blue), evapotranspiration (green), precipitation (dotted hatch), and change in storage (red) binned by basins and elevation for water year 1991. Number corresponds with Basin numbers in Figure 1. .	205
C.4.8	Runoff (blue), evapotranspiration (green), precipitation (dotted hatch), and change in storage (red) binned by basins and elevation for water year 1992. Number corresponds with Basin numbers in Figure 1. .	206
C.4.9	Runoff (blue), evapotranspiration (green), precipitation (dotted hatch), and change in storage (red) binned by basins and elevation for water year 1993. Number corresponds with Basin numbers in Figure 1. .	207

C.4.10	Runoff (blue), evapotranspiration (green), precipitation (dotted hatch), and change in storage (red) binned by basins and elevation for water year 1994. Number corresponds with Basin numbers in Figure 1. .	208
C.4.11	Runoff (blue), evapotranspiration (green), precipitation (dotted hatch), and change in storage (red) binned by basins and elevation for water year 1995. Number corresponds with Basin numbers in Figure 1. .	209
C.4.12	Runoff (blue), evapotranspiration (green), precipitation (dotted hatch), and change in storage (red) binned by basins and elevation for water year 1996. Number corresponds with Basin numbers in Figure 1. .	210
C.4.13	Runoff (blue), evapotranspiration (green), precipitation (dotted hatch), and change in storage (red) binned by basins and elevation for water year 1997. Number corresponds with Basin numbers in Figure 1. .	211
C.4.14	Runoff (blue), evapotranspiration (green), precipitation (dotted hatch), and change in storage (red) binned by basins and elevation for water year 1998. Number corresponds with Basin numbers in Figure 1. .	212
C.4.15	Runoff (blue), evapotranspiration (green), precipitation (dotted hatch), and change in storage (red) binned by basins and elevation for water year 1999. Number corresponds with Basin numbers in Figure 1. .	213
C.4.16	Runoff (blue), evapotranspiration (green), precipitation (dotted hatch), and change in storage (red) binned by basins and elevation for water year 2000. Number corresponds with Basin numbers in Figure 1. .	214
C.4.17	Runoff (blue), evapotranspiration (green), precipitation (dotted hatch), and change in storage (red) binned by basins and elevation for water year 2001. Number corresponds with Basin numbers in Figure 1. .	215
C.4.18	Runoff (blue), evapotranspiration (green), precipitation (dotted hatch), and change in storage (red) binned by basins and elevation for water year 2002. Number corresponds with Basin numbers in Figure 1. .	216
C.4.19	Runoff (blue), evapotranspiration (green), precipitation (dotted hatch), and change in storage (red) binned by basins and elevation for water year 2003. Number corresponds with Basin numbers in Figure 1. .	217
C.4.20	Runoff (blue), evapotranspiration (green), precipitation (dotted hatch), and change in storage (red) binned by basins and elevation for water year 2004. Number corresponds with Basin numbers in Figure 1. .	218
C.4.21	Runoff (blue), evapotranspiration (green), precipitation (dotted hatch), and change in storage (red) binned by basins and elevation for water year 2005. Number corresponds with Basin numbers in Figure 1. .	219
C.4.22	Runoff (blue), evapotranspiration (green), precipitation (dotted hatch), and change in storage (red) binned by basins and elevation for water year 2006. Number corresponds with Basin numbers in Figure 1. .	220
C.4.23	Runoff (blue), evapotranspiration (green), precipitation (dotted hatch), and change in storage (red) binned by basins and elevation for water year 2007. Number corresponds with Basin numbers in Figure 1. .	221

C.4.24	Runoff (blue), evapotranspiration (green), precipitation (dotted hatch), and change in storage (red) binned by basins and elevation for water year 2008. Number corresponds with Basin numbers in Figure 1. .	222
C.4.25	Runoff (blue), evapotranspiration (green), precipitation (dotted hatch), and change in storage (red) binned by basins and elevation for water year 2009. Number corresponds with Basin numbers in Figure 1. .	223
C.4.26	Runoff (blue), evapotranspiration (green), precipitation (dotted hatch), and change in storage (red) binned by basins and elevation for water year 2010. Number corresponds with Basin numbers in Figure 1. .	224
C.4.27	Runoff (blue), evapotranspiration (green), precipitation (dotted hatch), and change in storage (red) binned by basins and elevation for water year 2011. Number corresponds with Basin numbers in Figure 1. .	225
C.4.28	Runoff (blue), evapotranspiration (green), precipitation (dotted hatch), and change in storage (red) binned by basins and elevation for water year 2012. Number corresponds with Basin numbers in Figure 1. .	226
C.4.29	Runoff (blue), evapotranspiration (green), precipitation (dotted hatch), and change in storage (red) binned by basins and elevation for water year 2013. Number corresponds with Basin numbers in Figure 1. .	227
C.4.30	Runoff (blue), evapotranspiration (green), precipitation (dotted hatch), and change in storage (red) binned by basins and elevation for water year 2014. Number corresponds with Basin numbers in Figure 1. .	228
C.4.31	Runoff (blue), evapotranspiration (green), precipitation (dotted hatch), and change in storage (red) binned by basins and elevation for water year 2015. Number corresponds with Basin numbers in Figure 1. .	229
C.4.32	Runoff (blue), evapotranspiration (green), precipitation (dotted hatch), and change in storage (red) binned by basins and elevation for water year 2016. Number corresponds with Basin numbers in Figure 1. .	230
C.4.33	Runoff (blue), evapotranspiration (green), precipitation (dotted hatch), and change in storage (red) binned by basins and elevation for water year 2017. Number corresponds with Basin numbers in Figure 1. .	231
C.4.34	Runoff (blue), evapotranspiration (green), precipitation (dotted hatch), and change in storage (red) binned by basins and elevation for water year 2018. Number corresponds with Basin numbers in Figure 1. .	232

List of Tables

2.1	Sites characteristics. The IGBP land-cover types are evergreen needle-leaf forests (ENF), mixed forests (MF), woody savannas (WSA), grasslands (GRA), and shrublands (OSH).	34
2.2	Precipitation and snow data sources.	35
2.3	Resistance and plant-accessible-water-storage drawn during multi-year dry periods resulting in evapotranspiration (ET) attenuation.. . . .	36
3.1	Sites characteristics.	70
4.1	Basin characteristics and 34-year mean-annual values.	104
4.2	Tree mortality following the 2012-2016 drought.	105
B.1	Model parameters for all models for Equation 1.	151

Acknowledgments

First and foremost, I would like to thank my advisor, Dr. Roger C. Bales, for his mentoring, encouragement, and support. His dedication to the progression of my education, research and professional development will never be forgotten. He was always quick to respond to questions and available whenever I needed guidance. I would also like to thank Dr. Susan Hubbard for her guidance and support as my advisor at the Lawrence Berkeley National Lab during my DOE fellowship. I would like to thank my committee members, Dr. Michael Goulden, Dr. Mohammad Safeeq, Dr. Marc Beutel, and Dr. LeRoy Westerling for their comments and feedback regarding the development of my PhD research. I am grateful to Dr. Martha Conklin from UC Merced, and Dr. Steven Glaser and Dr. Steven Maurer from UC Berkeley, who provided enlightening conversations and constructive comments on my work. I would like to extend special thanks to Dr. Qin Ma, who as a labmate, coauthor, and friend invited me to many potlucks at her home and would always take the time to help analyze my results. Another special thanks to Patrick Womble and his family (Atalie and Alexander) who always offered their home when I stayed in Merced, and for all the adventures shared in the Sierra Nevada. Another special thanks to Melissa Thaw, who introduced me to climbing, and great discussions of our research. I would like to thank all my colleagues in Merced, Henry Pai, Michelle Gilmore, Erin Stacy, Mari-beth Kniffin, Xiende Meng, and Jim Roche; in Berkely, Zeshi Zheng, Ziran Zhang, Francesco Avanzi, Sami Makel, and Tessa Maurer; and many others for all the moments we shared. You all made my time in California exciting and enjoyable! I would like to thank all my friends and family in Tennessee who visited and provided an escape from academia, Teejay Eaton, Thomas Demonbreun, James Hayes, Harrison Florida, John Michael Rungee, Seth Elliott, Connor Thompson, Jimmy Jones, and many others. As well as my good friends in the Bay area, Greg Sako, Liam Weaver, Siddhartha Chattopadhyay, Jillian Mrsny, and many others. I am forever indebted to my parents, Dr. James and Catherine Rungee, for their seffless love, care, understanding, and guidance throughout the entirety of my life. Finally, I would like to give my deepest gratitude to my fiance, Lisa Gellerman, who has providing unconditional love and emotional support throughout the entirety of this journey. Thank you for putting up with me! My research is supported by the National Science Foundation, Southern California Edison Fellowship, UC Merced Bobcat Fellowship, and the Department of Energy's Graduate Student Research Program Fellowship. Portion of Chapter 2 is a reprint of the paper in (Evapotranspiration response to multiyear dry periods in the semiarid western United States). Permission to use this paper in the dissertation has been granted by John Wiley & Sons Ltd.

Abstract

Estimating plant-accessible water storage through evaluating evapotranspiration in the semi-arid western United States using eddy-covariance, remote sensing, and spatially distributed data

by

Joseph Rungee

Doctor of Philosophy in Environmental Systems

University of California, Merced

Professor Roger Bales, Chair

The studies within this dissertation use a suite of long-term flux-tower, remotely sensed, and spatially distributed data to more accurately assess the withdrawal of subsurface plant-accessible water storage during multi-year dry periods, more accurately represent measurements of evapotranspiration across the landscape, and examine how vegetation use of plant-accessible water storage varies along latitudinal and elevation gradients, and with time. First, a suite of flux towers from across the arid and semi-arid western United States were used to assess the response of evapotranspiration under varying climates and vegetation types to drought. Here we found that regions experiencing a Mediterranean climate are substantially more dependent on subsurface storage than those receiving a summer monsoon, but available plant-accessible subsurface water storage in the Mediterranean climates can support evapotranspiration for the entirety of a multi-year dry period at some locations. It was also discovered that a transition from snow to rain could increase dependency vegetation on plant-accessible subsurface water storage by as much as 20% at energy-limited, snow-dominated sites. Next, measurements of evapotranspiration were distributed across the 14 river basins draining into California's Central Valley. This was performed by expanding on cur-

rent remotely sensed-based methods to include climatic data and consider vegetation type. This novel approach decreased the root-mean-square error by 31-50% when compared to methods only using NDVI and was insensitive to the spatial resolution of data used. This product showed that evapotranspiration was greatest in the northern basins, peaking at lower elevations, and decreased in magnitude while peaking at higher elevations as latitude decreased. It was also revealed that runoff was derived in primarily one of two ways in this region, the rain-dominated north where annual rainfall grossly exceeds annual evapotranspiration; and the snowmelt-driven south where most precipitation contributes to high-elevation snowpack in energy-limited areas. Finally, the 14 basins draining into California's Central Valley could be binned into four groups based upon what water-balance components and climatic variables were most highly correlated with changes in subsurface water storage, the northernmost, northern, mid-range and southern basins. The results showed that the southern basins may have already reached a critical threshold in storage drawdown, explaining why tree mortality is so widespread in the region, and that the northern and northernmost basins will likely follow a similar path if measures are not taken to reduce evapotranspiration. The studies in this dissertation provided comprehensive analyses of how evapotranspiration spatially varies and how its response to climate extremes alters the hydrologic cycle. Spatial products are in high demand for water resources and forest management applications, and although quantifying uncertainties remain a challenge, these products provide substantial value to improving our understanding of the water cycle.

Chapter 1

Introduction

Arid and semi-arid regions experiencing a Mediterranean climate are characterized as having cool-wet winters followed by hot-dry summers (Lock and Dallman, 2000). In these regions, plant-accessible subsurface water storage plays a vital role in sustaining these ecosystems during the peak growing season when little to no precipitation occurs (Arkley, 1981; Klos et al., 2018). However, the water balance in these regions appear particularly vulnerable to projected increases in the frequency, duration, and severity of droughts and heat waves over the coming century (Giorgi and Lionello, 2008; Stocker et al., 2013). Quantifying the water balance and ecosystem response to perturbations in plant-accessible water storage is poorly understood, but imperative to adequately manage water and forests in these regions.

Assessing and quantifying these vulnerabilities require accurate partitioning of the annual water balance, given as $S = P - Q - ET$, into its individual components, change in subsurface water storage within the basin (S), precipitation (P), basin runoff (Q), and evapotranspiration (ET). Measures of precipitation are widely available from point measurements to spatially distributed products (Daly et al., 2008; Rodell et al., 2004), and streamflow measurements are available at several latitudes in the United States (Hirsch and Costa, 2004). However, physical measurements of evapotranspiration, which accounts for more than half of precipitation in arid and semi-arid regions, are limited (Bales et al., 2006; Goulden et al., 2012), and studies on

plant-accessible subsurface water storage have mostly focused on near-surface storage (Klos et al., 2018). This makes partitioning the water available for ET and ΔS challenging, limiting our ability to fully understand how these water-balance components vary in space and time.

1.1 Methods for measuring evapotranspiration

Methods for local measurements of evapotranspiration, or its components, can be binned into two categories, direct and indirect. Common direct methods include weighing lysimeters (Hargreaves and Samani, 1985; Liu et al., 2002), and eddy covariance (Baldocchi et al., 1988; Nagler et al., 2005). Weighing lysimeters are containers installed in the field and measure the change in mass within the container, where decreases in weight are assumed to be evapotranspiration (Howell et al., 1991). These instruments are typically used in areas with homogenous, low-growing and shallow-rooted vegetation provided they need to capture the root zone and only provide point measurements (Pruitt and Angus, 1960). Eddy covariance is a rapid sampling method that calculates evapotranspiration as:

$$ET = L\overline{(\rho w)'q'}, \quad (1.1)$$

where ET is evapotranspiration, L is the latent heat of vaporization of water, $(\rho w)'$ is the departure of air density (ρ) and the vertical wind component (w) from their mean values, and q' is the departure of specific humidity (q) from its mean value (Dyer, 1961; Swinbank, 1951). These departures are averaged over a short time period (generally 30 minutes) of high-frequency sampling (10-20 Hz) to provide a flux rate. Eddy covariance has been considered the most accurate measure of evapotranspiration in Mediterranean climates (Rana and Katerji, 2000; Wilson and Baldocchi, 2000). Some drawbacks of eddy-covariance include cost of installation and maintenance, determining the contributing area, and increased likelihood of data gaps due to power outages and low frictional velocity (Goulden et al., 2012; Rana and Katerji, 2000).

Common examples of indirect methods include catchment water balance (Bosch and Hewlett, 1982) and the Bowen ratio (Malek and Bingham, 1993). Catchment water balance is the process of resolving the simplified water balance:

$$ET = P - Q, \quad (1.2)$$

where ET is annual evapotranspiration, P is annual precipitation, and Q is annual runoff. The primary fallbacks of this approach include an inability to produce sub-annual estimates, provides only a catchment-scale estimate, and neglects changes in storage (Wilson et al., 2001). The Bowen ratio calculates evapotranspiration by solving the energy balance, expressed as:

$$LE = \frac{R_n - G}{1 + \beta}, \quad (1.3)$$

where LE is the latent heat flux, R_n is net radiation, G is the ground heat flux, and β is the Bowen ratio. When assuming no horizontal gradients between temperature and humidity, can be simplified to:

$$\beta = \gamma \frac{\Delta T}{\Delta e}, \quad (1.4)$$

where γ is the psychrometric constant ($0.0677 \text{ kPa } ^\circ\text{C}^{-1}$) and ΔT and Δe are the vertical gradients in temperature and vapor pressure, respectively (Xing et al., 2008). The primary drawbacks of this method are that it requires very accurate measurements temperature, vapor pressure, net radiation and the ground heat flux, and are particularly important in very dry conditions where ΔT can be high driving up the Bowen ratio and leading to an underestimation of evapotranspiration (Angus and Watts, 1984).

Measured evapotranspiration has been applied in studies across many disciplines. It has been used to develop and/or validate crop reference evapotranspiration values (Amayreh and Al-Abed, 2005; Hargreaves and Samani, 1985; Li et al., 2008; Walter et al., 2001; Yoder et al., 2005), assess vegetation responses to drought (Aronson et al., 1987; Carrow, 1995; Jacobs et al., 2002; Zha et al., 2010), and effects of disturbance (Lu et al., 2011; South et al., 1998). Although, these studies generally have a limited scope due to limited data which results in using a point measurement to represent a

vegetation type or single extreme event. This leads to large gaps in knowledge for how a given vegetation type responds to extreme events under varying climate regimes, and how a given sites responds to varying degrees of extreme events.

1.2 Methods for estimating evapotranspiration across the landscape

Methods for estimating evapotranspiration across the landscape can also be generalized into two groups, Physically based and statistical models (Long et al., 2014). Physically based models attempt to close the water and energy balances at the catchment to global scale, where actual evapotranspiration is generally calculated as a function of available energy and limited by available water (Fisher et al., 2005; Vörösmarty et al., 1998). The primary advantages of these methods are that they simulate the physical processes of the environment and can provide information across any point in space and time (Kite and Droogers, 2000). Ultimately, physically based models can be the most appropriate method for estimating evapotranspiration, although they are currently bottlenecked by data availability and are often too computationally intensive to consistently outperform other methods (Goulden and Bales, 2014; Kite and Droogers, 2000; Long et al., 2014), especially in complex landscapes where high spatial-resolution data is important (Bales et al., 2006).

Satellite-based methods provide a variety of ways to estimate evapotranspiration. One approach includes resolving surface-energy-budget equations such as the Penman-Monteith (Mu et al., 2007, 2011) and Priestley-Taylor (Jin et al., 2011). Like other physically based models, these approaches provide a robust representation of evapotranspiration (Zheng et al., 2017), while requiring accurate climatic, energy and biophysical data (Goulden et al., 2012; Lettenmaier, 2017). Another approach is statistically based, using either predictive relationships between observations and satellite imagery (Glenn et al., 2010), or machine-learning algorithms (Chen et al., 2014). Annual evapotranspiration has exhibited a predictive relation-

ship with satellite-based vegetation indices (Goulden et al., 2012; Groeneveld et al., 2007), but appears to poorly represent evapotranspiration during climate extremes, such as droughts, especially in regions dominated by evergreen forests (Nagler et al., 2005). Machine-learning algorithms provide an advanced data-driven approach for representing complex, non-linear systems (Goldberg and Holland, 1988), but have a higher risk of overfitting observations, increasing error outside the calibration range (Domingos, 2012; Solomatine and Shrestha, 2009).

The ability to spatially estimate evapotranspiration with reasonable confidence has significantly advanced our understanding of hydrologic and ecosystem processes. It has been used to assess hydrologic and ecological responses to drought (Bales et al., 2018), estimate subsurface-water storage available to plants during dry seasons (Fellows and Goulden, 2017), assess responses to disturbance or treatment (Bond-Lamberty et al., 2009; Roche et al., 2018), and infer evapotranspiration responses to climate change (Goulden and Bales, 2014). Despite these advancements, many large-scale monitoring efforts and research still use potential evapotranspiration or a precipitation- or temperature-based index in place of these products. This is largely due to the aforementioned drawbacks of the individual methods, where physically based models lack the spatial resolution and are computationally intensive, and statistical models lack the temporal resolution and have shown to poorly represent climate extremes. This provides a need for further investigation to improve the efficiency of physically based models and resolve the issues of statistical models either over-fitting observations or missing climate extremes.

1.3 Objectives of this study

In this dissertation, we used a suite of eddy-covariance flux-tower measurements of evapotranspiration to assess how much storage was depleted before a response to multi-year dry periods was observed at the point scale, and then used a data-driven approach to distribute evapotranspiration across the landscape and assess how the drawdown of water and evapotranspiration response to drought vary by changes in

climate, elevation and latitude. The main questions addressed were 1) how does climate affect the response of evapotranspiration to multi-year dry periods within and between vegetation types?, 2) where is uncertainty greatest in closing the water balance?, 3) what governs the drawdown of plant-accessible water storage and how resilient are the river basins draining into California's Central Valley to climate extremes? These questions were addressed through:

1. Compared how measured evapotranspiration responds to multi-year dry periods across the semi-arid southwest United States considering different vegetation types and climate regimes. The results provided insight for which characteristics improve dry-period resistance, and how much subsurface water storage can be withdrawn before a response in evapotranspiration is observed.
2. Used a suite of flux-tower measurements across California to develop an improved data-driven approach for spatially distributing evapotranspiration using satellite-based imagery and statistically distributed climatic data. This product was assessed by performing a basin-scale mass balance to examine where uncertainties exist. The results suggested that the majority of uncertainty is likely attributed to the precipitation data as a result of well-documented snow undercatch, but uncertainties are likely notable from the current network of flux towers poorly representing the precipitation-temperature space. The product also revealed that runoff is mostly from below the rain-snow transition where precipitation grossly exceeding evapotranspiration in the northern basins and above where evapotranspiration is energy limited in the southern basins.
3. Used the distributed evapotranspiration product to examine how evapotranspiration and storage responded to a hot 4-year drought (2012-2015) as compared to a cool 6-year drought (1987-1992), and what drives changes in storage. Our findings revealed that the hot drought experienced large withdrawals from storage, whereas the cool drought had a net surplus for every year except for the first, despite the mean precipitation over the drought periods being nearly equal.

Further investigation revealed runoff, annual precipitation, and annual-mean temperature have much greater inter-annual variability than evapotranspiration but are poorly indicative of whether change in storage will be positive or negative. This phenomenon appears to be mostly driven by the timing of the growing season, when water becomes available to the vegetation and how rapidly the water leaves the system, resulting in higher runoff.

1.4 Bibliography

- Amayreh, J. and Al-Abed, N. (2005). Developing crop coefficients for field-grown tomato (*Lycopersicon esculentum* Mill.) under drip irrigation with black plastic mulch. *Agricultural Water Management*, 73(3):247–254.
- Angus, D. and Watts, P. (1984). Evapotranspiration - How Good is the Bowen Ratio Method? pages 133–150.
- Arkley, R. J. (1981). Soil Moisture Use by Mixed Conifer Forest in a Summer-Dry Climate¹. *Soil Science Society of America Journal*, 45(2):423.
- Aronson, L. J., Gold, A. J., and Hull, R. J. (1987). Cool-Season Turfgrass Responses to Drought Stress¹. *Crop Science*, 27(6):1261.
- Baldocchi, D. D., Hincks, B. B., and Meyers, T. P. (1988). Measuring Biosphere-Atmosphere Exchanges of Biologically Related Gases with Micrometeorological Methods. *Ecology*, 69(5):1331–1340.
- Bales, R. C., Goulden, M. L., Hunsaker, C. T., Conklin, M. H., Hartsough, P. C., OGeen, A. T., Hopmans, J. W., and Safeeq, M. (2018). Mechanisms controlling the impact of multi-year drought on mountain hydrology. *Scientific reports*, 8(1):690.
- Bales, R. C., Molotch, N. P., Painter, T. H., Dettinger, M. D., Rice, R., and Dozier, J. (2006). Mountain hydrology of the western United States. *Water Resources Research*, 42(8).
- Bond-Lamberty, B., Peckham, S. D., Gower, S. T., and Ewers, B. E. (2009). Effects of fire on regional evapotranspiration in the central Canadian boreal forest. *Global Change Biology*, 15(5):1242–1254.
- Bosch, J. and Hewlett, J. (1982). A review of catchment experiments to determine the effect of vegetation changes on water yield and evapotranspiration. *Journal of Hydrology*, 55(1-4):3–23.

- Carrow, R. N. (1995). Drought Resistance Aspects of Turfgrasses in the Southeast: Evapotranspiration and Crop Coefficients. *Crop Science*, 35(6):1685.
- Chen, Y., Xia, J., Liang, S., Feng, J., Fisher, J. B., Li, X., Li, X., Liu, S., Ma, Z., Miyata, A., et al. (2014). Comparison of satellite-based evapotranspiration models over terrestrial ecosystems in china. *Remote Sensing of Environment*, 140:279–293.
- Daly, C., Halbleib, M., Smith, J. I., Gibson, W. P., Doggett, M. K., Taylor, G. H., Curtis, J., and Pasteris, P. P. (2008). Physiographical sensitive mapping of climatological temperature and precipitation across the conterminous United States. *International Journal of Climatology*, 28:2031–2064.
- Domingos, P. (2012). A few useful things to know about machine learning. *Communications of the ACM*, 55(10):78.
- Dyer, A. J. (1961). Measurements of evaporation and heat transfer in the lower atmosphere by an automatic eddy-correlation technique. *Quarterly Journal of the Royal Meteorological Society*, 87(373):401–412.
- Fellows, A. W. and Goulden, M. L. (2017). Mapping and understanding dry season soil water drawdown by California montane vegetation. *Ecohydrology*, 10(1):1–12.
- Fisher, J. B., DeBiase, T. A., Qi, Y., Xu, M., and Goldstein, A. H. (2005). Evapotranspiration models compared on a Sierra Nevada forest ecosystem. *Environmental Modelling & Software*, 20(6):783–796.
- Giorgi, F. and Lionello, P. (2008). Climate change projections for the Mediterranean region. *Global and Planetary Change*, 63(2-3):90–104.
- Glenn, E. P., Nagler, P. L., and Huete, A. R. (2010). Vegetation Index Methods for Estimating Evapotranspiration by Remote Sensing. *Surveys in Geophysics*, 31(6):531–555.
- Goldberg, D. E. and Holland, J. H. (1988). Genetic Algorithms and Machine Learning. *Machine Learning*, (3):95–99.

- Goulden, M. L., Anderson, R. G., Bales, R. C., Kelly, A. E., Meadows, M., and Winston, G. C. (2012). Evapotranspiration along an elevation gradient in California's Sierra Nevada. *Journal of Geophysical Research*, 117(G3):G03028.
- Goulden, M. L. and Bales, R. C. (2014). Mountain runoff vulnerability to increased evapotranspiration with vegetation expansion. *Proceedings of the National Academy of Sciences*, 111(39):14071–14075.
- Groeneveld, D. P., Baugh, W. M., Sanderson, J. S., and Cooper, D. J. (2007). Annual groundwater evapotranspiration mapped from single satellite scenes. *Journal of Hydrology*, 344(1-2):146–156.
- Hargreaves, G. H. and Samani, Z. A. (1985). Reference Crop Evapotranspiration from Temperature. *Applied Engineering in Agriculture*, 1(2):96–99.
- Hirsch, R. M. and Costa, J. E. (2004). U.S. stream flow measurement and data dissemination improve. *Eos, Transactions American Geophysical Union*, 85(20):197–203.
- Howell, T. A., Schneider, A. D., and Jensen, M. E. (1991). History of lysimeter design and use for evapotranspiration measurements. In *Lysimeters for evapotranspiration and environmental measurements*, pages 1 – 9. ASCE.
- Jacobs, J. M., Mergelsberg, S. L., Lopera, A. F., and Myers, D. A. (2002). Evapotranspiration from a wet prairie wetland under drought conditions: Paynes Prairie Preserve, Florida, USA. *Wetlands*, 22(2):374–385.
- Jin, Y., Randerson, J. T., and Goulden, M. L. (2011). Continental-scale net radiation and evapotranspiration estimated using MODIS satellite observations. *Remote Sensing of Environment*, 115(9):2302–2319.
- Kite, G. and Droogers, P. (2000). Comparing evapotranspiration estimates from satellites, hydrological models and field data. *Journal of Hydrology*, 229(1-2):3–18.
- Klos, P. Z., Goulden, M. L., Riebe, C. S., Tague, C. L., OGeen, A. T., Flinchum, B. A., Safeeq, M., Conklin, M. H., Hart, S. C., Berhe, A. A., et al. (2018). Subsurface

- plant-accessible water in mountain ecosystems with a mediterranean climate. *Wiley Interdisciplinary Reviews: Water*, 5(3):e1277.
- Lettenmaier, D. P. (2017). Observational breakthroughs lead the way to improved hydrological predictions. *Water Resources Research*, 53(4):2591–2597.
- Li, S., Kang, S., Li, F., and Zhang, L. (2008). Evapotranspiration and crop coefficient of spring maize with plastic mulch using eddy covariance in northwest China. *Agricultural Water Management*, 95(11):1214–1222.
- Liu, C., Zhang, X., and Zhang, Y. (2002). Determination of daily evaporation and evapotranspiration of winter wheat and maize by large-scale weighing lysimeter and micro-lysimeter. *Agricultural and Forest Meteorology*, 111(2):109–120.
- Lock, M. and Dallman, P. R. (2000). Plant Life in the World’s Mediterranean Climates. The Mediterranean Basin, South Africa, Australia, Chile and California. *Kew Bulletin*, 55(1):250.
- Long, D., Longuevergne, L., and Scanlon, B. R. (2014). Uncertainty in evapotranspiration from land surface modeling, remote sensing, and GRACE satellites. *Water Resources Research*, 50(2):1131–1151.
- Lu, N., Chen, S., Wilske, B., Sun, G., and Chen, J. (2011). Evapotranspiration and soil water relationships in a range of disturbed and undisturbed ecosystems in the semi-arid Inner Mongolia, China. *Journal of Plant Ecology*, 4(1-2):49–60.
- Malek, E. and Bingham, G. E. (1993). Comparison of the Bowen ratio-energy balance and the water balance methods for the measurement of evapotranspiration. *Journal of Hydrology*, 146:209–220.
- Mu, Q., Heinsch, F. A., Zhao, M., and Running, S. W. (2007). Development of a global evapotranspiration algorithm based on MODIS and global meteorology data. *Remote Sensing of Environment*, 111(4):519–536.

- Mu, Q., Zhao, M., and Running, S. W. (2011). Improvements to a MODIS global terrestrial evapotranspiration algorithm. *Remote Sensing of Environment*, 115(8):1781–1800.
- Nagler, P., Scott, R., Westenburg, C., Clevery, J., Glenn, E., and Huete, A. (2005). Evapotranspiration on western U.S. rivers estimated using the Enhanced Vegetation Index from MODIS and data from eddy covariance and Bowen ratio flux towers. *Remote Sensing of Environment*, 97(3):337–351.
- Pruitt, W. O. and Angus, D. E. (1960). Large weighing lysimeter for measuring evapotranspiration. *American Society of Agricultural and Biological Engineers*.
- Rana, G. and Katerji, N. (2000). Measurement and estimation of actual evapotranspiration in the field under Mediterranean climate: a review. *European Journal of Agronomy*, 13(2-3):125–153.
- Roche, J. W., Goulden, M. L., and Bales, R. C. (2018). Estimating evapotranspiration change due to forest treatment and fire at the basin scale in the Sierra Nevada, California. *Ecohydrology*, 11(7):e1978.
- Rodell, M., Houser, P. R., Jambor, U., Gottschalck, J., Mitchell, K., Meng, C.-J., Arsenault, K., Cosgrove, B., Radakovich, J., Bosilovich, M., Entin, J. K., Walker, J. P., Lohmann, D., and Toll, D. (2004). The Global Land Data Assimilation System. *Bulletin of the American Meteorological Society*, 85(3):381–394.
- Solomatine, D. P. and Shrestha, D. L. (2009). A novel method to estimate model uncertainty using machine learning techniques. *Water Resources Research*, 45(12).
- South, C., Susan, C., Grimmond, B., and Wolfe, C. P. (1998). Evapotranspiration rates from wetlands with different disturbance histories: Indiana Dunes National Lakeshore. *Wetlands*, 18(2):216–229.
- Stocker, T., Qin, D., Plattner, G.-K., Tignor, M., Allen, S., Boschung, J., Nauels, A., Xia, Y., and Bex, V. (2013). *IPCC, 2013: Climate Change 2013: The Physical*

- Science Basis. Contribution of Working Group I to the Fifth Assessment Report of the Intergovernmental Panel on Climate Change.* Cambridge University Press, Cambridge, United Kingdom and New York, NY, USA.
- Swinbank, W. (1951). The measurement of vertical transfer of heat and water vapor by eddies in the lower atmosphere. *Journal of Meteorology*, 8(3):135–145.
- Vörösmarty, C., Federer, C., and Schloss, A. (1998). Potential evaporation functions compared on US watersheds: Possible implications for global-scale water balance and terrestrial ecosystem modeling. *Journal of Hydrology*, 207(3-4):147–169.
- Walter, I. A., Allen, R. G., Elliott, R., Jensen, M. E., Itenfisu, D., Mecham, B., Howell, T. A., Snyder, R., Brown, P., Echings, S., Spofford, T., Hattendorf, M., Cuenca, R. H., Wright, J. L., and Martin, D. (2001). ASCE’s Standardized Reference Evapotranspiration Equation. In *Watershed Management and Operations Management 2000*, pages 1–11, Reston, VA. American Society of Civil Engineers.
- Wilson, K. B. and Baldocchi, D. D. (2000). Seasonal and interannual variability of energy fluxes over a broadleaved temperate deciduous forest in North America. *Agricultural and Forest Meteorology*, 100(1):1–18.
- Wilson, K. B., Hanson, P. J., Mulholland, P. J., Baldocchi, D. D., and Wullschlegel, S. D. (2001). A comparison of methods for determining forest evapotranspiration and its components: sap-flow, soil water budget, eddy covariance and catchment water balance. *Agricultural and Forest Meteorology*, 106(2):153–168.
- Xing, Z., Chow, L., Meng, F.-R., Rees, H., Steve, L., and Monteith, J. (2008). Validating Evapotranspiration Equations Using Bowen Ratio in New Brunswick, Maritime, Canada. *Sensors*, 8(1):412–428.
- Yoder, R., Odhiambo, L. O., and Wright, W. C. (2005). Evaluation of methods for estimating daily reference crop evapotranspiration at a site in the humid southeast united states. *Applied engineering in agriculture*, 21(2):197–202.

Zha, T., Barr, A. G., van der Kamp, G., Black, T. A., McCaughey, J. H., and Flanagan, L. B. (2010). Interannual variation of evapotranspiration from forest and grassland ecosystems in western Canada in relation to drought. *Agricultural and Forest Meteorology*, 150(11):1476–1484.

Zheng, H., Yu, G., Wang, Q., Zhu, X., Yan, J., Wang, H., Shi, P., Zhao, F., Li, Y., Zhao, L., Zhang, J., and Wang, Y. (2017). Assessing the ability of potential evapotranspiration models in capturing dynamics of evaporative demand across various biomes and climatic regimes with ChinaFLUX measurements. *Journal of Hydrology*, 551:70–80.

Chapter 2

Evapotranspiration response to multi-year dry periods in the semi-arid western United States¹

Abstract

Analysis of measured evapotranspiration shows that subsurface plant-accessible water storage (PAWS) can sustain evapotranspiration through multi-year dry periods. Measurements at 25 flux-tower sites in the semi-arid western United States, distributed across five land-cover types, show both resistance and vulnerability to multi-year dry periods. Average (\pm standard deviation) evapotranspiration ranged from 660 ± 230 mm yr⁻¹ (October-September) in evergreen needleleaf forests to 310 ± 200 mm yr⁻¹ in grasslands and shrublands. More than 52% of the annual evapotranspiration in Mediterranean climates is supported on average by seasonal drawdown of subsurface PAWS, versus 29% in monsoon-influenced climates. Snowmelt replenishes dry-season PAWS by as much as 20% at sites with significant seasonal snow accumulation but was insignificant at most sites. Evapotranspiration exceeded precipitation in more than half of the observation years at sites below 35 °N. Annual evapotranspiration at non-energy-limited sites increased with precipitation, reaching a mean wet-year evapotranspiration of 833 mm for evergreen needleleaf forests, 861 mm for mixed forests,

558 mm for woody savannas, 367 mm for grasslands and 254 mm for shrublands. Thirteen sites experienced at least one multi-year dry period, when mean precipitation was more than one standard deviation below the historical mean. All vegetation types except evergreen needleleaf forests responded to multi-year dry periods by lowering evapotranspiration and/or significantly year-over-year depletion of subsurface PAWS. Sites maintained wet-year evapotranspiration rates for 8 to 33 months before attenuation, with a corresponding net PAWS drawdown of as much as 334 mm. Net drawdown at many sites continued until the dry period ended, resulting in an overall cumulative withdrawal of as much as 558 mm. Evergreen needleleaf forests maintained high evapotranspiration during multi-year dry periods with no apparent PAWS drawdown; these forests are currently resilient drought, but may prove vulnerable to longer and warmer dry periods that reduce snowpack storage and accelerate evapotranspiration. ¹

¹This chapter is a revision of (Rungee et al., 2018). Evapotranspiration response to multi-year dry periods in the semi-arid western United States. *Hydrological Processes*

2.1 Introduction

Mountain watersheds supply approximately two thirds of freshwater in arid regions, serving as an essential or supportive water source for approximately 44% of the global population (Viviroli et al., 2007). The complex topography, steep temperature and precipitation gradients with elevation, high inter-annual climate variability, and heterogeneous vegetation distribution in these watersheds limit our ability to accurately estimate and represent major components of the hydrologic cycle (Bales et al., 2006). Multi-year dry periods are arguably the most complex yet least understood natural hazard, with slow progression and long-term socio-economic effects. Gaps in knowledge of drought resistance exacerbate the impacts of multi-year dry periods by impeding anticipatory planning and operational water-resources management decisions (Cancelliere et al., 2007; Mishra and Desai, 2005; Modarres, 2007). The frequency, intensity and duration of drought are anticipated to increase in the coming century (Stocker et al., 2013), and history is an incomplete guide to future stresses.

Evapotranspiration accounts for the majority of water leaving a semi-arid region watershed (Bales et al., 2006), and the timing and magnitude of precipitation and evapotranspiration govern basin runoff. Evapotranspiration is challenging to measure directly at individual sites, and shows high spatial heterogeneity with water availability, temperature, vegetation type and vapor pressure variability (Viessman and Lewis, 2003). Many drought assessments either supplement actual evapotranspiration with potential evapotranspiration (PET) or develop an index that is based largely on precipitation. Poor correlation in the inter-annual variability of precipitation and evapotranspiration (Oishi et al., 2010), and the often weak relationship between evapotranspiration and temperature in water-limited regions can lead to misrepresentation of evapotranspiration (McAfee, 2013). The evapotranspiration response to drought varies significantly with vegetation type (Vicente-Serrano et al., 2013); this variation is generally unaccounted for in PET-based indices and underscores the need to consider actual evapotranspiration when assessing drought stress

across landscapes (Bales et al., 2018).

Subsurface plant-accessible water storage (PAWS) capacity has been defined as the amount of subsurface water that is accessible for extraction by roots (Klos et al., 2018). This reservoir of water sustains evapotranspiration during periods when evapotranspiration exceeds precipitation, and is important both seasonally and during multi-year dry periods (Bales et al., 2018, 2011). A second water store, seasonal snowpack, extends the period that subsurface PAWS is replenished after precipitation ends. This can be especially important for locations with long summer dry periods such as Californias Sierra Nevada, where the snow-cover period averages 2-3 weeks longer for each 300-m increase in elevation, reflecting both more precipitation and later melt (Bales et al., 2015; Rice et al., 2011). The spatial response of evapotranspiration to the cumulative depletion of subsurface PAWS during multi-year dry periods, and of the effect of reduced snowpack storage on PAWS depletion as climate warms, are not well known. Advances in technology have improved our ability to quantify components of the hydrologic cycle, as well as examine and monitor the impacts of multi-year dry periods. The growing network of eddy-covariance flux towers provides direct measurements of the land-atmosphere fluxes of water, carbon and energy. Eddy-covariance data have been used to examine drought in Canadian boreal forests (Zha et al., 2010); and scaled to assess drought impacts across river basins in the western United States (Bales et al., 2018). Precipitation and evapotranspiration time series can be combined to infer the seasonal and multi-year net drawdown of PAWS (Fellows and Goulden, 2017).

We combined multi-year records of precipitation with evapotranspiration records measured by eddy covariance to estimate the PAWS drawdown at tower sites across the semi-arid western United States. These measurements were compared across and within vegetation types and climatic regimes to address three questions. First, how do annual values and seasonal trends of evapotranspiration vary by climate and land-cover type? Second, what amount of annual dry-season evapotranspiration is supported by the seasonal drawdown of PAWS, and how does this vary by climate and land-cover type? Third, how much PAWS is available to support evapotranspiration

during multi-year dry periods?

2.2 Methods

We used existing eddy-covariance datasets to assess the effects of multi-year dry periods on measured evapotranspiration. We defined multi-year dry periods as three or more consecutive years having a mean dry-period annual precipitation at least one standard deviation below the sites historical mean. Evapotranspiration and temperature data from eddy-covariance flux towers were compiled and processed, along with site characteristics. Precipitation data for the sites were obtained from a variety of sources. We used daily and monthly evapotranspiration and precipitation data during the dry season to quantify the fraction of annual evapotranspiration that is supported by subsurface plant-accessible water storage (PAWS). We also calculated the net long-term drawdown of subsurface PAWS before any attenuation of evapotranspiration was observed during multi-year dry periods. Finally, we looked at how snowpack storage affects the seasonal evapotranspiration dependency on PAWS and how this may change with a shift from snow to rain.

Study area

This study focused on sites in the western United States, in and near the Sierra Nevada, Rocky, San Jacinto, Jemez, and Santa Catalina mountains. The study area is bounded by latitudes 31.75-43.15 °N and longitudes 121.00-105.60 °W (Figure 2.1). These areas are categorized as semi-arid to arid, with mean-annual (October through September) precipitation ranging from 139 to 1341 mm per year, and average annual temperatures ranging from -0.9 to 23.3 °C (Table 2.1). The study sites have an elevation range of 129 to 3190 m above mean sea level, and include evergreen needleleaf forests, mixed forests, woody savannas, grasslands, and shrublands.

Data

Sites having at least five years of continuous data were compiled through direct correspondence with principal investigators and/or the Ameriflux website (<http://ameriflux.lbl.gov/>), providing 25 flux-tower sites and 223 site years of data. Data gaps, due to power outages, sensor malfunctions or low-turbulence periods were filled using multiple steps (Aubinet et al., 2012). First, night-time friction-velocity thresholds were calculated, and night-time values below the threshold removed (Gu et al., 2005). Second, linear regression with the carbon-dioxide flux, photosynthetically active radiation and temperature, and multiple linear regression with any combination of the three variables were compared to determine the best fit for gap filling. The best-fit model was then used to gap fill 30-min evapotranspiration data, iterating over three filling increments (30, 90, and 365 days). Data gaps were not filled with the best-fit model if over 90% of the data available for regression were missing in an iteration, or the r^2 for the best-fit model was less than the r^2 threshold, determined by gap filling the 30-min data using incoming photosynthetically active or solar radiation (Goulden et al., 2012). Third, small gaps in the 30-min data (≤ 3 hrs) were filled using linear interpolation. Fourth, the remaining gaps in the 30-min data were filled using the relationship developed to determine the r^2 threshold if above 0.4, otherwise by linear interpolation. Fifth, the gap-filled 30-min data were summed to daily values, and the energy balance closed by linear regression of turbulent fluxes (latent and sensible heat) and available energy ($R_{net}-G$) forced through the origin (Goulden et al., 2012; Twine et al., 2000). Energy-balance closure was not performed on sites either being cited as unnecessary (Scott et al., 2010), or in warm deserts, as this has shown to overestimate evapotranspiration by up to 20% resulting in mean evapotranspiration greater than precipitation (Biederman et al., 2018). If the ground heat flux was missing from the dataset, it was estimated as:

$$G = 0.35 \times (R_{net} e^{0.9 \times \ln(1-fc)}), \quad (2.1)$$

where G is the soil heat flux, R_{net} is the net radiation measured from the flux tower, fc is the fractional canopy cover (Norman et al., 1996). This step was only needed

for three sites, and fractional canopy cover values were obtained from literature and discussion with flux-tower principal investigators. Here, 0.36 was used for US-Vcm (Broxton et al., 2015; Harpold et al., 2015), 0.67 was used for US-Vcp, and 0.05 was used for US-SCd. Daily evapotranspiration values were limited to be a maximum of vegetation-corrected Hamon PET (Rao et al., 2011).

Locally measured precipitation data were used where available. Precipitation data were obtained through literature review and direct discussion with flux-tower principal investigators (Table 2.2). Site-corrected monthly PRISM precipitation data were used to extend all precipitation datasets back to 1981. This provided a minimum 35-year distribution for multi-year dry-period detection. 800-m PRISM data were corrected to the site observations on a monthly timestep by linear regression through the origin. All site data agreed well with PRISM ($r^2=0.77$).

30-min flux-tower measurements of temperature were aggregated to daily average values, and data gaps filled with 800-m PRISM data. Monthly aggregated temperature data were used to estimate vegetation-corrected Hamon PET (Rao et al., 2011). These data were used to identify energy-limited sites in a Budyko framework.

We used three steps to determine the contribution of snowpack storage to PAWS. Ten sites were identified as receiving snow based on monthly mean daily temperature $\leq 1^\circ\text{C}$ (Marks et al., 2013). At one site it was determined that snow was intermittent, and that melt was fast relative to our monthly time step. Snow accumulation and melt for the other nine sites with a possible seasonal snow influence were estimated from co-located SNOTEL stations or other on-site measurements (Table 2.2). For three sites with snow-depth but not snow-water-equivalent data, precipitation was assumed to be all snow during the periods when depth was increasing, and snowmelt was assumed to be proportional to decreases in snow depth, neglecting snow compaction. Snow-water-equivalent (SWE) data were blended with rain-gauge precipitation data to calculate winter snow accumulation and melt. All snowmelt was assumed to contribute to subsurface PAWS, and precipitation during snowmelt periods was assumed to be rain.

Analysis

Sites with a Hamon-corrected potential evapotranspiration to precipitation ratio of <0.8 were considered extremely energy limited. Sites with a ratio approximately equal to one (0.8-1.2) were classified into energy vs. moisture limitation based on the slope of the regression between growing-season temperature (April-September) and annual evapotranspiration, with a positive slope indicating energy-limitation (Garcia et al., 2014; Karnieli et al., 2010). This step was taken to minimize uncertainty in the Hamon PET. A sites mean wet-year evapotranspiration was calculated from the evapotranspiration observed during years with above average precipitation. These values were used to detect the response of evapotranspiration to multi-year dry periods.

Critical PAWS drawdown is defined as the net drawdown from the onset of a multi-year dry period until a significant evapotranspiration decline is observed. The critical year was identified as the point during a multi-year dry period when cumulative annual evapotranspiration dropped below 80% of a sites mean wet-year evapotranspiration. As many sites lacked sufficient data to generate a non-skewed distribution, the 80% threshold provided a consistent value across all sites. This threshold was selected by assessing plots of annual evapotranspiration, accumulated at a daily timestep for all years on record and observing how the daily accumulated trends responded to multi-year dry periods. The critical month during that year was then identified as the inflection point of the cumulative-annual evapotranspiration curve. The inflection was detected using a three-month sliding window to minimize false detection from an anomaly or inter-annual monthly variability. Critical drawdown was calculated as the net drawdown of PAWS from the onset of the multi-year dry period to the critical month. Dry-period drawdown was estimated as the net drawdown of PAWS over the entire multi-year period.

The effect of the delayed contribution of snowmelt to the amount of dry-season PAWS needed to supplement evapotranspiration was assessed considering all precipitation falling as rain.

Limitations and sources of Uncertainty

We identified four potential sources of uncertainty. First, evapotranspiration measurements are made at only a limited number of sites, and do not represent all of the climate, geology and vegetation variability of this region. Further, the mean available flux-tower record for the 25 sites was less than 9 years; and of the 223 site years of data, 58 involved multi-year dry periods.

Second, data processing to fill gaps involved assumptions, such as the decision to force close the energy balance. Literature on this topic is controversial, with some circumstantial evidence that the imbalance in the energy budget ($R_{net}G = LE + H$), where R_{net} is net radiation, G is the soil heat flux, LE is latent heat and H is sensible heat, is related to an underestimation of LE and H (Wilson et al., 2002), and other analyses showing that correcting for this imbalance leads to an over estimation of evapotranspiration (Biederman et al., 2018). We determined whether or not to close the energy balance based on literature reports that forced closure is especially problematic at warm desert sites (Biederman et al., 2018; Scott et al., 2010).

Third, our assumption that all precipitation infiltrates and contributes to PAWS could lead to an underestimation of evapotranspiration withdrawal from storage and thus PAWS at sites where high-intensity rainfall results in overland flow.

Fourth, our assumption of negligible lateral flow could lead to an overestimation of critical PAWS drawdown for sites with water convergence, and an underestimation for sites with divergence (Fellows and Goulden, 2017).

2.3 Results

Seasonal variability and dependence on plat-accessible water storage

Mean monthly evapotranspiration and precipitation show seasonal patterns for each site, with winter periods when precipitation exceeds evapotranspiration, and

summer when evapotranspiration is supported by subsurface PAWS drawdown (Figure 2.2). Nine of the 25 sites had appreciable snowfall and snowmelt, and the remaining sites received little or no snow. The snowpack at five sites was sufficiently long-lasting to introduce a one-month lag before evapotranspiration relied on subsurface PAWS (US-CZ3, US-NR1, US-Vcm, US-GLE, RMEA). The hatched areas represent evapotranspiration from sublimation (Molotch et al., 2009; Schlaepfer et al., 2014).

Evapotranspiration peaks during the winter and spring at the warmer sites, and later at the colder sites. Sites with a Mediterranean climate (indicated by bold lettering in Figure 2.2) receive precipitation mainly during the cool season. The seven sites in the interior Southwest receive a summer monsoon (indicated by non-bold lettering in Figure 2.2) and have year-round precipitation. Evapotranspiration peaks during the summer at the monsoon-influenced sites, with smaller peaks in the winter at warmer sites and spring at colder sites. Evapotranspiration peaks in the summer at the Colorado and Wyoming sites. PET values are shown on Figure 2 for reference.

Annual evapotranspiration averaged from 514 to 892 mm yr⁻¹ at the evergreen needleleaf and mixed forest sites, and from 131 to 502 mm yr⁻¹ at the savanna, grassland and shrubland sites in Arizona and southern California. Annual evapotranspiration from subsurface storage were calculated by integrating the shaded areas in Figure 2.2 for each site year (Figures A.1.1-25). The four forested sites in California had the greatest values, averaging about 258 to 512 mm yr⁻¹, with savanna, grassland and shrubland sites in Arizona and southern California have the least, 67 to 198 mm yr⁻¹ (Figure 2.3). Over half of the annual evapotranspiration at most of the Mediterranean climate sites was supported by subsurface storage ($52 \pm 8\%$, mean \pm standard deviation), versus less than one third at the monsoon-dominated sites ($31 \pm 9\%$).

Shrublands showed the largest inter-site range of mean evapotranspiration, 131 to 538 mm yr⁻¹, and large within-site inter-annual ranges, e.g. 0.45 to 1.73 times the mean at US-SCd in southern California (Table 2.1, Figure 2.4). However, the three Idaho shrublands, which are energy limited, had ranges averaging 0.95 to 1.04 times

the mean. Evergreen needleleaf forests also exhibited a large range between sites, with mean evapotranspiration values ranging from 514 to 892 mm yr⁻¹. Within-site interannual ranges were relatively low for US-NR1 (0.93 to 1.07) and US-CZ3 (0.92 to 1.12), with the first energy limited and the second non-energy limited. The range for the mixed-forest US-CZ2 was much wider (0.70 to 1.40). The two relatively warm forested sites in New Mexico had asymmetric ranges (0.49 to 1.21). Savanna and grassland sites averaged 342 to 599 and 293 to 340 mm yr⁻¹, respectively; and had interannual ranges from 0.67 to 1.54 at US-Wkg and 0.74 to 1.50 at US-CZ1, to 0.94 to 1.05 at energy-limited RMEA.

Maximum evapotranspiration by land-cover type

Annual evapotranspiration increased with precipitation up to a maximum threshold that varied by land-cover type (Figure 2.4a). Two evergreen needleleaf forest (US-GLE and US-NR1), one woody savanna (RMEA) and three shrubland (RMES, USA, USS) sites were energy limited. Removing these energy limited sites and years with below average precipitation gives mean values of maximum water year evapotranspiration of 833, 861, 558, 367 and 254 mm yr⁻¹ for the evergreen needleleaf forest, mixed forest, woody savanna, grassland and shrubland land-cover types, respectively (Figure 2.4b-c). This is equivalent to 84, 110, 113, 87 and 95 percent of mean non-energy-limited site precipitation, respectively.

Site response to multi-year dry periods

High evaporative index values across many sites and years suggest that PAWS helps to support evapotranspiration during multi-year dry periods (Figure 2.5). Thirteen of the sites had at least one multi-year dry period in the record, and two of the sites had two dry periods (Table 2.3). All but two of these (US-CZ3 and US-Blo) showed an attenuation of evapotranspiration (Figure 2.6). The two evergreen needleleaf forest sites failed to show a cumulative decrease in storage, and neither experienced an attenuation of evapotranspiration. The two mixed-forest sites had critical

PAWS drawdowns of 334 and 272 mm, and resistances of 21 months. All woody-savanna sites exhibited an attenuation of evapotranspiration, with one, US-SRM, showing no cumulative depletion of storage. US-CZ1 and US-SRM had low resistances, 8 and 12 months, respectively, compared to US-Ton which had two multi-year dry periods, both of which showed resistances of 20 months before an attenuation of evapotranspiration was observed. All grassland multi-year dry periods exhibited an attenuation of evapotranspiration, with one site having two dry periods but no PAWS drawdown (US-Var), and the other (US-SCg) having a critical PAWS drawdown of 40 mm. Dry-period resistance for grasslands ranged from 8 to 32 months. All shrubland sites experiencing a multi-year dry period showed an attenuation of evapotranspiration, with only US-SCc showing no cumulative depletion of PAWS. Shrubland critical PAWS drawdown ranged from 38 to 288 mm, with resistances ranging from 11 to 23 months. All land-cover types showed continued drawdown of PAWS through the remainder of their multi-year dry periods.

Effect of snowpack on PAWS dependency

Precipitation that falls as snow rather than rain delays infiltration, which shortens the duration of dry season drawdown and reduces the amount of mean-annual evapotranspiration supported by PAWS. The occurrence of snow rather than rain, and the timing of subsequent melt, augmented subsurface PAWS by an average of about 4% at US-Vcp, 4% at US-CZ3, 17% at US-NR1, 20% at US-GLE, 9% at RMEA, and near zero or negative at US-Vcm, USA, USS and RMES (Figure A.2.1). The contribution of snowmelt during peak evapotranspiration years was as high as 8% at US-Vcp, 10% at US-CZ3, 7% at US-NR1 and 23% at US-GLE, 4% at RMEA.

2.4 Discussion

Annual and seasonal evapotranspiration by land-cover type and climate

Annual evapotranspiration measured across the 25 sites ranged from 66 to 1066 mm yr⁻¹, with higher rates in evergreen-needleleaf and mixed forests, and lower rates in grasslands and shrublands in Arizona and southern California. Evapotranspiration was positively correlated with precipitation ($r^2=0.58$) and negatively with temperature ($r^2=0.35$), and cooler, wetter sites typically had a higher annual evapotranspiration (Figure A.3).

We further investigated the relationship between evapotranspiration, temperature and precipitation seasonality by classifying the sites into four groups: energy-limited Mediterranean (Idaho), non-energy-limited Mediterranean (California), energy-limited monsoon (Wyoming and Colorado), and non-energy-limited monsoon (New Mexico and Arizona). Shrublands showed the greatest variation between energy-limited and non-energy-limited sites, with energy-limited Mediterranean locations exhibiting the highest average annual evapotranspiration (509 mm) and non-energy-limited Mediterranean sites exhibiting the lowest (194 mm). Shrublands displayed the greatest relative ranges in annual evapotranspiration and precipitation, and have been shown to have high variability in leaf area index and spacing as a function of water availability, shrub size, species, and competition (Phillips and Macmahon, 1981). A relatively high vegetation density at the energy-limited Mediterranean sites, which also have higher annual precipitation, may have offset a shorter growing season. No significant correlations in annual evapotranspiration with climate were apparent at the remaining sites. One site, US-Vcp, showed a mean-annual evapotranspiration that was greater than mean-annual precipitation. Calculations of the Topographic Wetness Index (not shown) indicated that US-Vcp is in an area of water convergence, suggesting that evapotranspiration may be supported by lateral inputs.

Mediterranean sites showed distinct peaks in evapotranspiration during summer,

when precipitation was generally low. Evapotranspiration at sites experiencing a monsoon generally peaked with summer precipitation. Most sites having significant snow accumulation showed evapotranspiration peaking 35 months following the last significant winter storm. The consistent lag of peak evapotranspiration after the transition from snow accumulation to melt suggests that an earlier timing of peak snow-water equivalent may lead to earlier peaks in evapotranspiration, consistent with the findings of Hamlet et al. (2007).

Dry-season water drawdown

Figures 2.2-3, 2.5 show that evapotranspiration in all land-cover types and climates is sustained in part by the seasonal withdrawal of subsurface storage. The fraction of mean-annual evapotranspiration supported by seasonal subsurface PAWS drawdown ranged from 16 to 64%. PAWS drawdown had a weak positive correlation with precipitation ($r^2=0.10$, $p=0.005$) and a strong positive correlation with annual temperature ($r^2=0.70$, $p<0.001$) at sites with seasonal snowpack (Figure A.4). Drawdown at rain-dominated sites was positively correlated with precipitation ($r^2=0.51$, $p<0.001$) and negatively with temperature ($r^2=0.49$, $p<0.001$). This indicates the lagged contribution of snowmelt to PAWS currently reduces the dependence on dry-season PAWS and suggests these areas may be vulnerable to an increased reliance on seasonal PAWS with climate warming. Evapotranspiration at sites with a Mediterranean climate showed the most dependency on subsurface PAWS, with average values of 53% for non-energy-limited and 48% for energy-limited sites. Monsoon-influenced sites depended on PAWS for 33% of annual evapotranspiration at non-energy-limited and 18% at energy-limited sites. This is consistent with the seasonal trends of evapotranspiration in Figure 2.2, which show the peak growing season for Mediterranean sites occurring during a period with little to no rain, whereas evapotranspiration at monsoon sites peaks with monsoonal precipitation.

Evapotranspiration supported by PAWS during multi-year dry periods

Evergreen needleleaf forests maintained high rates of evapotranspiration despite the occurrence of multi-year dry periods, whereas evapotranspiration in the other land-cover types was attenuated (Table 2.3). Figure 2.2 shows that measured evapotranspiration closely tracked evaporative demand, with a narrow gap for sites where annual precipitation grossly exceeded evapotranspiration (US-Blo and US-CZ3). A smaller gap between measured and potential evapotranspiration was observed at energy-limited sites (US-NR1 and US-GLE). This suggests evergreen needleleaf forests occur at locations with sufficient access to water to meet the evaporative demand. Mixed-forest sites used substantial amounts of subsurface PAWS, and the remaining land-cover types varied significantly, ranging from no dry-period drawdown to several hundred millimeters. High values of net drawdown at mixed forested sites suggests that current levels of evapotranspiration may be unsustainable, with drought-induced tree mortality observed at US-CZ2 during California's 2012-2015 drought (Bales et al., 2018).

Effect of snowpack on PAWS dependency

The presence of snowpack storage delayed the recharge of PAWS and decreased the mean-annual amount of evapotranspiration supported by subsurface PAWS for all snow-influenced sites but two (US-Vcm and RMES). Snowpack provided the greatest benefits for the two energy-limited evergreen needleleaf forest sites (US-NR1 and US-GLE), augmenting subsurface PAWS by 17-20%. These sites may become more vulnerable to multi-year dry periods if warming reduces the fraction of precipitation falling as snow. For example, as warmer temperatures shift from precipitation from snow to rain and melt snow earlier, the rain + snow lines on Figure 2.3 will more closely resemble the precipitation lines, increasing the shaded areas that represent evapotranspiration from PAWS drawdown. At warmer snow sites such as US-Vcp, US-Vcm and US-CZ3 this effect will be relatively small in most years but important

in years when late-spring (April-June) precipitation is small (Figure A.1). At colder sites that currently have lower dependence on PAWS such as US-NR1 and US-GLE, this shift from snow to rain large relative increases in demand on PAWS will occur in most years (Figure A.1).

Loss of snowpack storage had little or no effect on reliance on PAWS at the energy-limited woody savanna and shrubland sites (RMEA, USA, USS and RMES) in most years, but appear sensitive to precipitation type in years with little spring rain or snowfall. The US-CZ2 and US-SCf sites relied heavily on year-over-year PAWS drawdown during multi-year dry-periods, and are also particularly vulnerable to episodic tree mortality (Bales et al., 2018). A loss of snowpack storage with warming at some sites may increase the reliance on PAWS drawdown with implications for forest die-off. As warming extends the growing season, higher spring evapotranspiration at most sites will increase withdrawal from PAWS (Figures 2.3 and A.1). In general, the effect will be more pronounced at sites that currently have significant snow accumulation, limited dependence on PAWS and relatively uniform monthly precipitation (e.g. US-NR1, US-GLE). At all sites that currently have snow snowpack storage, the combination of higher evapotranspiration in a warmer spring and limited late-spring and early summer precipitation will increase dependence on PAWS. That is, as snow shifts to rain, the timing of precipitation will become more important in determining PAWS drawdown and thus moisture stress. While large winter snow accumulation can somewhat offset a drier spring, interannual variability in spring temperature and energy balance, and thus snowmelt timing, will also become more important.

2.5 Conclusions

We used a suite of eddy-covariance flux towers across the semi-arid western United States to assess the response of evapotranspiration to multi-year dry periods. Mediterranean climate sites showed greater dependency on seasonal plant-accessible water storage (PAWS), suggesting that vegetation distribution in these areas is particularly sensitive to subsurface PAWS capacity. Time-series during multi-year dry peri-

ods showed that all land-cover types except evergreen needleleaf forests exhibited a year-over-year depletion of subsurface PAWS, which allowed a normal range of evapotranspiration to be maintained. Evergreen needleleaf forests maintained wet-year evapotranspiration rates with no net PAWS drawdown despite multi-year dry periods, indicating sufficient available water to meet the evapotranspiration demand. Mixed-forests withdrew the most from PAWS with one site drawing more than 530 mm over a multi-year dry period. The delayed recharge of PAWS by snowmelt most benefits the energy-limited evergreen needleleaf forests, where it decreases seasonal drawdown by 17-20%. A shift from snow to rain may increase the vulnerability of forests to multi-year dry periods.

Table 2.1: Sites characteristics. The IGBP land-cover types are evergreen needleleaf forests (ENF), mixed forests (MF), woody savannas (WSA), grasslands (GRA), and shrublands (OSH).

Site ¹	Site Abbr.	Lat	Lon	Elev., m	Mean precip, mm	Mean ET, mm	Mean temp, °C	IGBP ²	Period of record
Blodgett Forest	BF	38.90	-120.63	1315	1341	892	11.4	ENF	1998-2007
Mount Bigelow	MB	32.42	-110.73	2583	720	718	9.6	ENF	2010-2015
Valles Caldera Ponderosa Pine	US-Vcp	35.86	-106.60	2495	457	704	6.5	ENF	2008-2014
Providence	US-CZ3	37.07	-119.20	2015	1379	644	8.6	ENF	2009-2015
Niwot Ridge	US-NR1	40.03	-105.55	3050	873	629	1.5	ENF	2000-2014
Valles Caldera Mixed Conifer	US-Vcm	35.89	-106.53	3035	795	531	4.5	ENF	2008-2014
GLEES	US-GLE	41.36	-106.24	3190	1282	514	-0.9	ENF	2001-2015
Soaproot Saddle	US-CZ2	37.03	-119.26	1160	934	658	13.5	MF	2011-2015
James Reserve	US-SCf	33.81	-116.77	1770	637	626	12.6	MF	2007-2014
Reynolds Mountain East Aspen	RMEA	43.07	-116.76	2055	987	599	5.7	WSA	2008-2012
Tonzi Ranch	US-Ton	38.43	-121.00	169	578	539	16.3	WSA	2002-2015
San Joaquin Experimental Range	US-CZ1	37.11	-119.73	405	502	378	17.7	WSA	2011-2015
Santa Rita Mesquite	US-SRM	31.82	-110.87	1116	406	342	18.6	WSA	2005-2015
Vaira Ranch Grassland	US-Var	38.41	-120.95	129	579	340	15.8	GRA	2002-2015
Walnut Gulch Kendall Grassland	US-SCg	33.74	-117.70	470	363	305	16.7	GRA	2007-2015
Walnut Gulch	US-Wkg	31.74	-109.94	1531	329	293	17.0	GRA	2005-2015
Upper Sheep Aspen	USA	43.12	-116.72	1984	576	538	5.9	OSH	2005-2012
Upper Sheep Sagebrush	USS	43.12	-116.72	1878	575	500	6.3	OSH	2006-2012
Reynolds Mountain East Sagebrush	RMES	43.07	-116.76	2098	814	472	5.3	OSH	2003-2007
Coastal Sage	US-SCs	33.73	-117.70	475	357	340	16.9	OSH	2007-2015
Walnut Gulch Lucky Hills	US-Whs	31.74	-110.05	1372	300	275	17.1	OSH	2008-2015
Santa Rita Creosote	US-SRC	31.91	-110.84	991	341	224	19.3	OSH	2009-2012
Pinyon	US-SCw	33.61	-116.46	1280	234	190	15.9	OSH	2007-2015
Pinyon Burn	US-SCc	33.61	-116.45	1300	234	152	15.8	OSH	2007-2015
Low Desert	US-SCd	33.65	-116.37	275	139	131	23.3	OSH	2007-2012

¹ Related publications: US-Blo, (Goldstein et al., 2000); US-Vcp, (Litvak, 2016), US-Vcm, (Litvak, 2016); US-NR1, (Monson et al., 2002); US-GLE, (Frank et al., 2014); US-Ton and US-Var, (Ma et al., 2007); US-SRM, US-Wkg and US-Whs, (Scott et al., 2006); US-SRC, (Wolf et al., 2016). **Bold denotes Mediterranean climate sites.**

² IGBP refers to the International Geosphere-Biosphere Programme land-cover classification system.

Table 2.2: Precipitation and snow data sources.

Site ¹	Precipitation data source	Snow data source
US-Blo	Flux-tower measurements	
MB	Mt. Lemon gauge	
US-Vcp	Remote Automated Weather Station (RAWS) Redondo Station	Cooperative Observer Network (COOP) Wolf Canyon station
US-CZ3	United States Forests Service Upper Met Providence station	On-site snow-pillow data
US-NR1	United Station Climate Reference Network Boulder 14W station 7 SNOTEL 663: Niwot	
US-Vcm	RAWS Jemez station	SNOTEL 708: Quemazon
US-GLE	National Atmospheric Deposition Program WY95 until (<2008), then a NOAA IV ETI Instrument Systems, Fort Collins, CO, USA (2008-present)	SNOTEL 367: Brooklyn Lake
US-CZ2	RAWS Mountain Rest station	
US-SCF	COOP Idyllwild Fire station	
RMEA	US Department of Agriculture Agricultural Research Service Northwest Watershed Research Center (NWRC) rmsp3 station	On-site snow-pillow data
US-Ton	Western Regional Climate Center (WRCC) Camp Pardee station	
US-CZ1	RAWS Hurley station	
US-SRM	Flux-tower measurements	
US-Var	WRCC Camp Pardee station	
US-SCg	PRISM	
US-WKG	Flux-tower measurements	
USA	NWRC 138j10 station	On-site snow-depth data
USS	NWRC 138j10 station	On-site snow-depth data
RMES	NWRC 176 station	On-site snow-depth data
US-SCs	PRISM	
US-Whs	Flux-tower measurements	
US-SRC	Santa Rita Experimental range Northeast station	
US-SCw	Boyd Deep Canyon Research Center Pinyon Crest station	
US-SCc	Boyd Deep Canyon Research Center Pinyon Crest station	
US-SCd	Boyd Deep Canyon Research Center Pinyon Crest station	

¹ Note: data accessed between 2/2/2018-2/10/2018. Bold denotes Mediterranean climate sites.

Table 2.3: Resistance and plant-accessible-water-storage drawn during multi-year dry periods resulting in evapotranspiration (ET) attenuation..

Site ¹	Dry period WY start	Dry period WY end	Critical annual ET, mm	Critical calendar year	Critical calendar month	Dry-period resistance, months	Critical PAWS draw-down, mm	Dry-period draw-down, mm
US-CZ3	2012	2015	581	-	-	-	-	-
US-Blo	2001	2004	790	-	-	-	-	-
US-CZ2	2012	2015	782	2013	7	21	334	558
US-SCf	2012	2014	682	2013	7	21	272	382
US-Ton	2012	2015	537	2013	6	20	154	450
US-Ton	2007	2009	537	2008	6	20	173	255
US-CZ1	2012	2015	415	2012	6	8	0	184
US-SRM	2009	2014	344	2009	10	12	38	0
US-SCg	2012	2015	30	2013	10	19	40	223
US-Var	2012	2015	324	2014	6	32	0	0
US-Var	2007	2009	324	2007	6	8	0	0
US-SCs	2012	2015	362	2013	9	23	288	416
US-SCw	2012	2015	222	2012	10	12	51	113
US-Whs	2011	2013	261	2011	12	14	38	39

¹ Bold denotes Mediterranean climate sites.

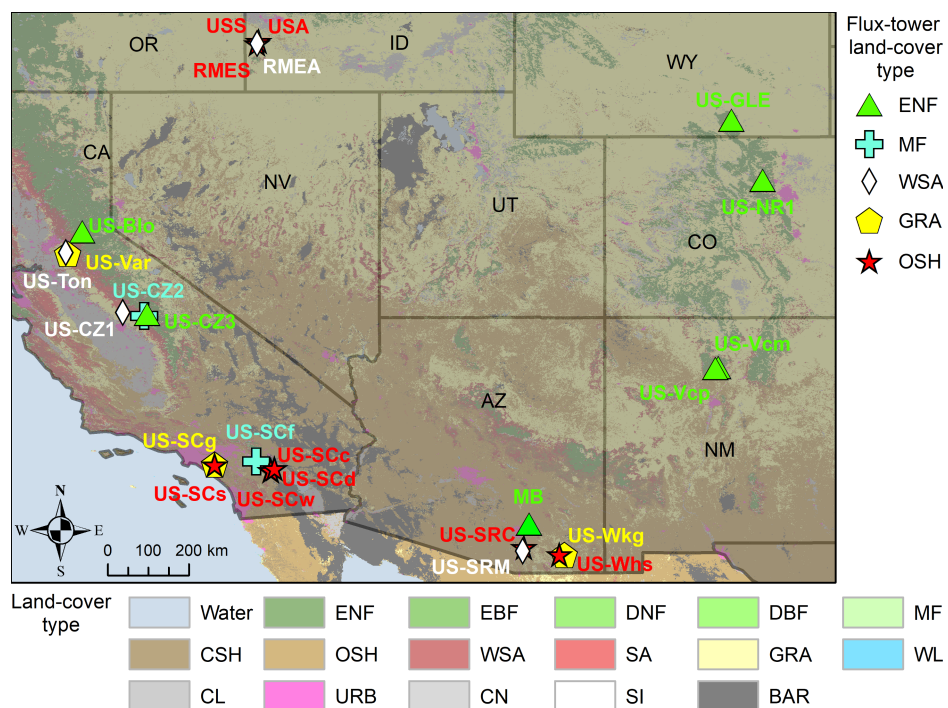


Figure 2.1: Flux-tower locations. Color codes and different markers represent land-cover types. The background is the IGBP layer for the region.

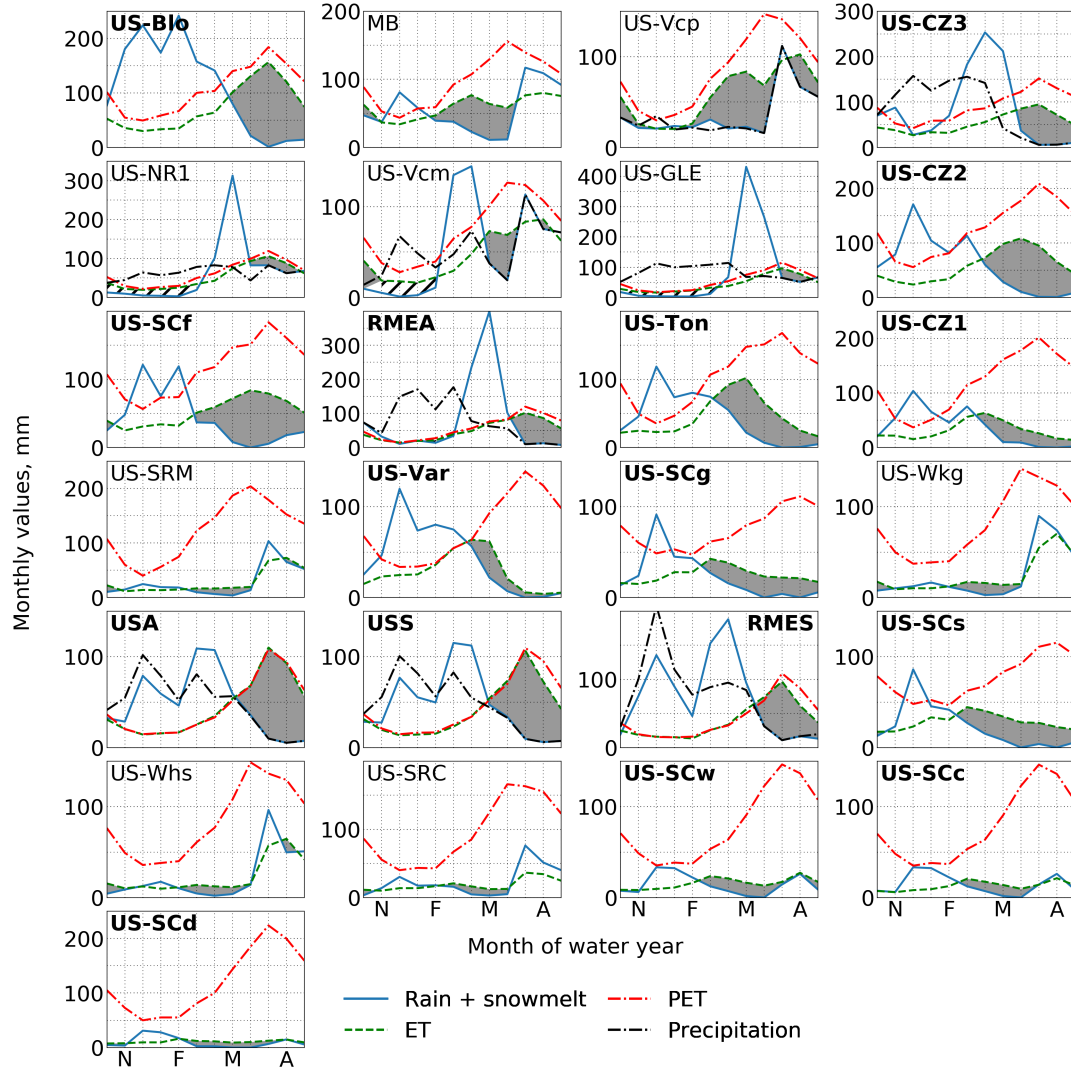


Figure 2.2: Monthly means of measured evapotranspiration (ET), potential evapotranspiration (PET), rain plus snowmelt (rain + snowmelt), and total precipitation (precipitation). The solid shaded area represents the average monthly ET supported by seasonal storage and the hatched area represents evapotranspiration as sublimation and does not contribute PAWS drawdown. See Table 2.1 for site characteristics. Note: the values here are averaged monthly values, and shaded area may not exactly match Figure 2.3 mean ET from storage values which are calculated on an annual basis. Bold denotes Mediterranean climate sites.

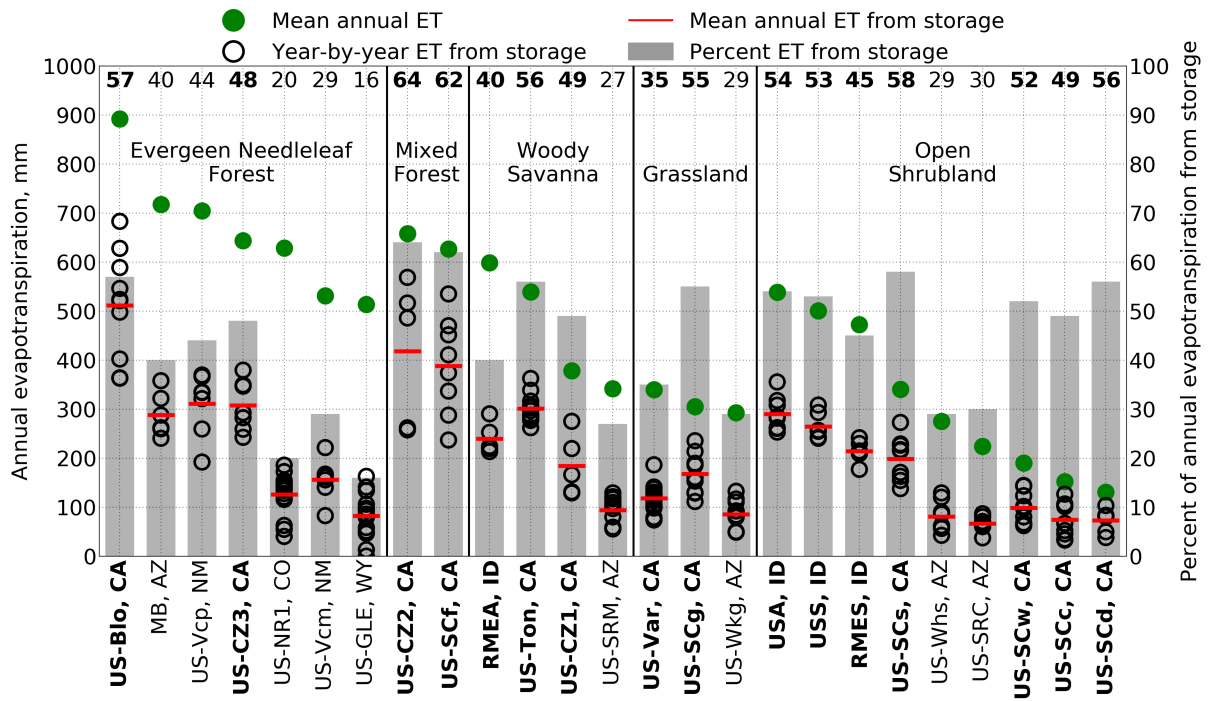


Figure 2.3: Amount of evapotranspiration (ET) supported by plant-accessible water storage for each water year on record by site. Site abbreviation is followed by state abbreviation. Other site characteristics are given in Table I. Vertical black lines separate land-cover types. Bold denotes Mediterranean climate sites.

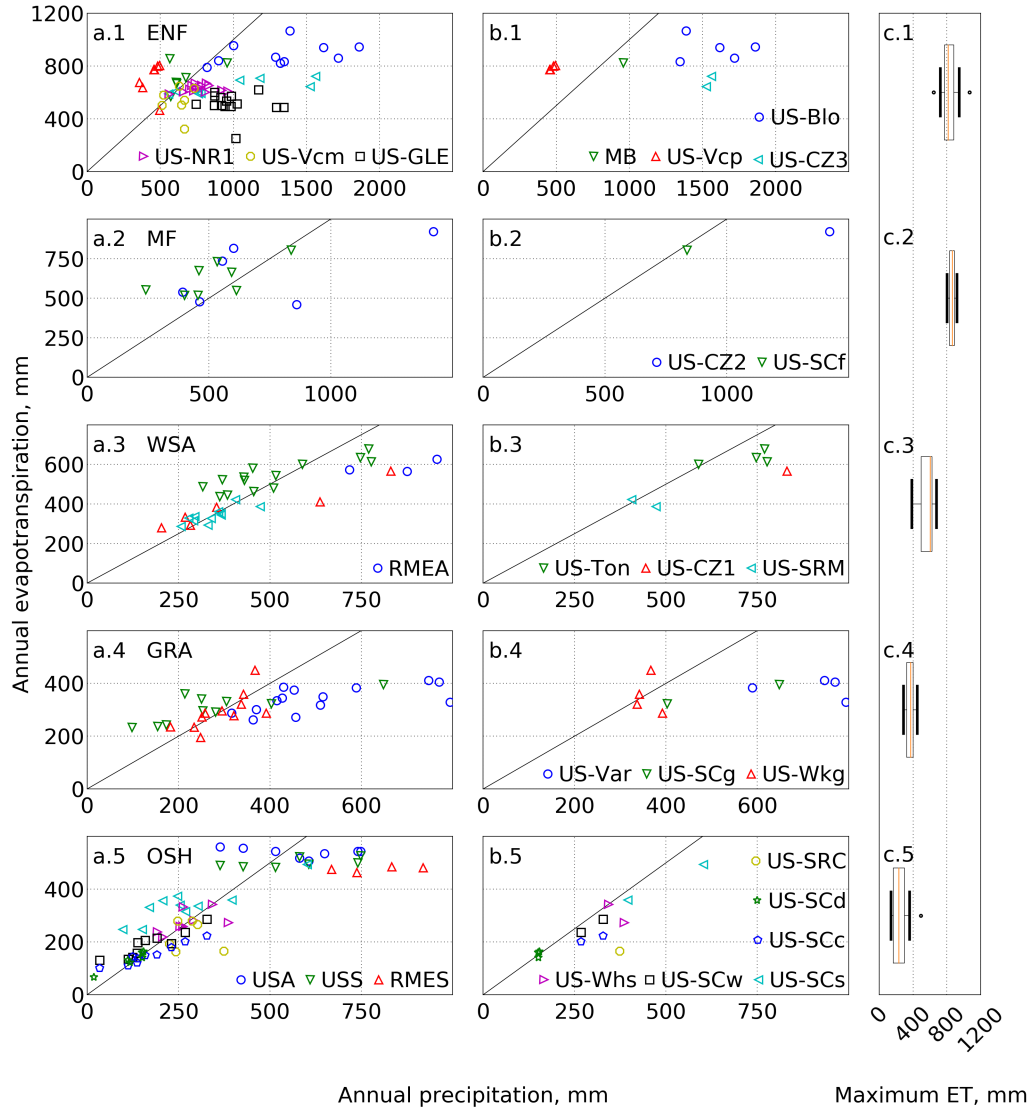


Figure 2.4: a.1-5. Annual precipitation versus evapotranspiration (ET) by land-cover type for all sites (b.1-5 legend included here), b.1-5. annual precipitation vs. evapotranspiration after removing all energy and precipitation-limited sites, and site years with annual precipitation below the mean, and c.1-5 show ranges of maximum ET for the five land-cover types.

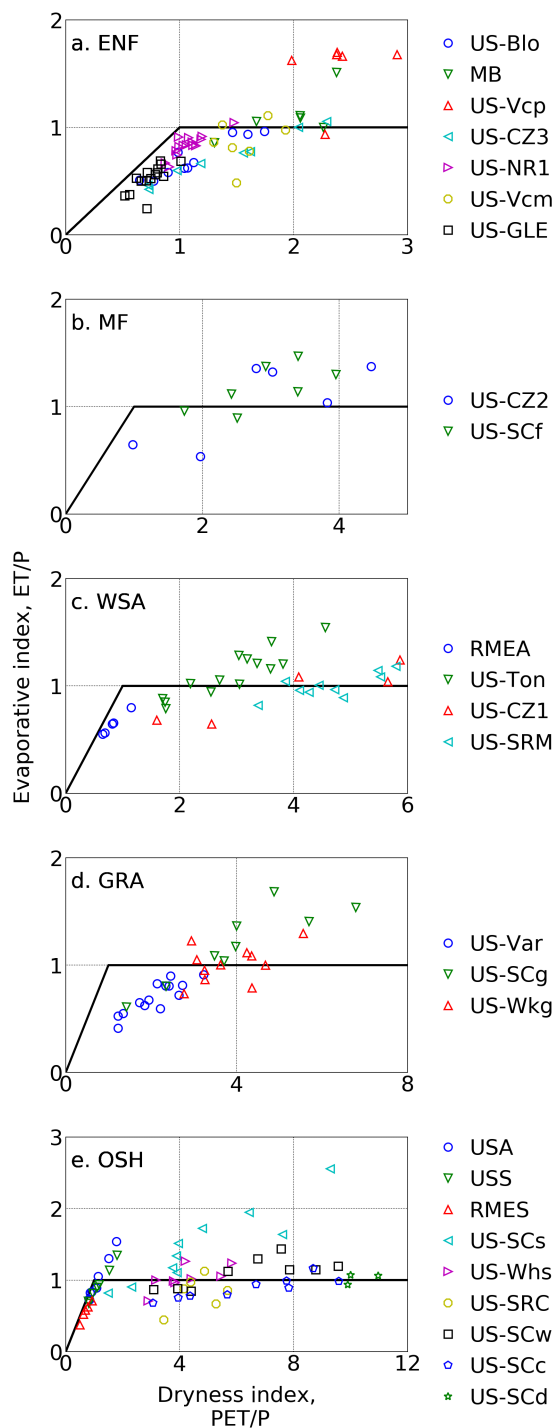


Figure 2.5: Measured annual evapotranspiration (ET), estimated potential evapotranspiration (PET), and precipitation (P) for all years of record shown in the Budyko framework by land-cover type. Refer to Table 2.1 for site characteristics.

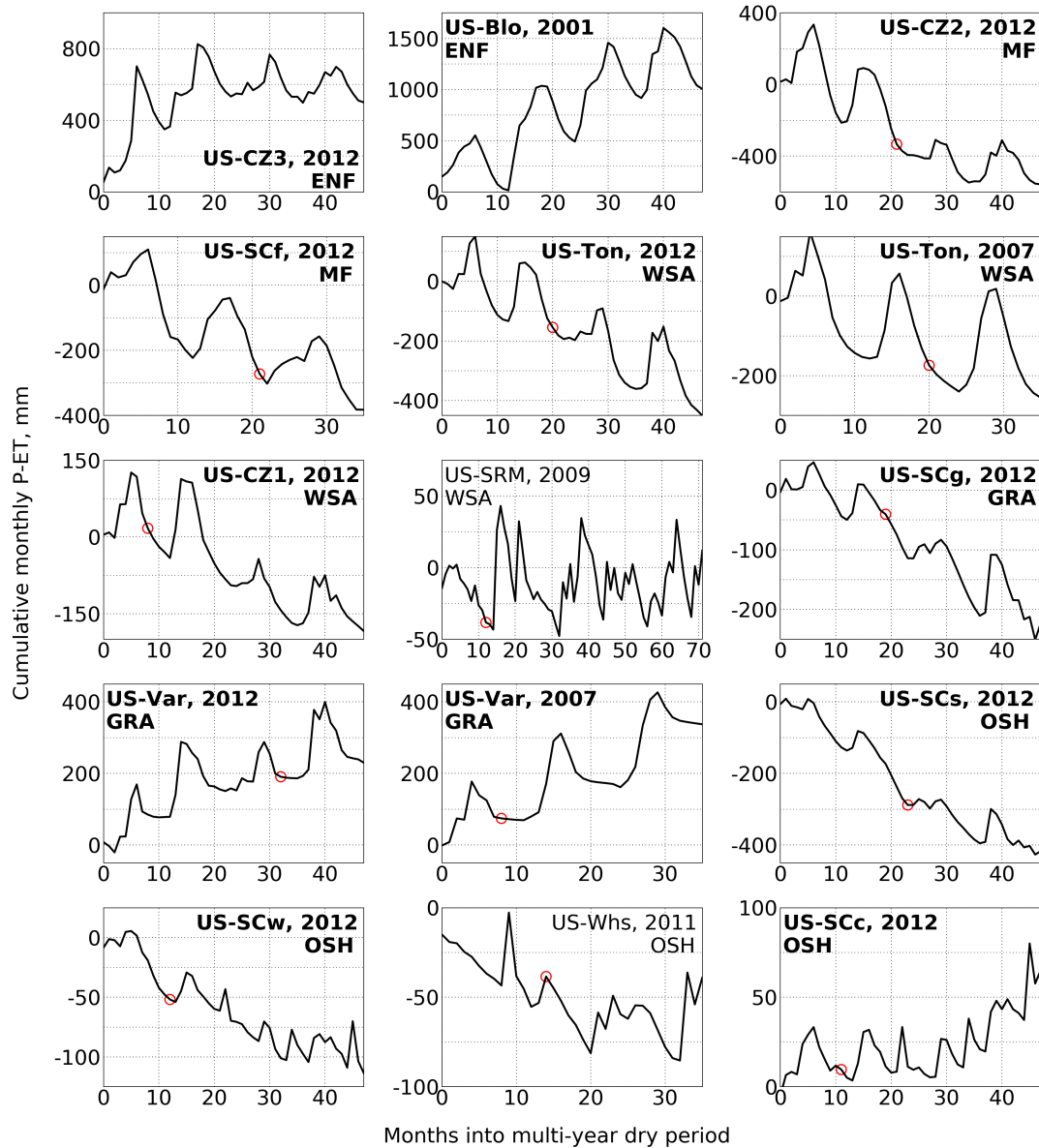


Figure 2.6: Plant-accessible-water-storage drawdown, starting water year and land-cover type for all sites experiencing a multi-year dry period. Red circles indicate the plant-accessible-water-storage deficit ($\sum P - ET$) and month in which evapotranspiration declined significantly, relative to wet-year values. **Bold denotes Mediterranean climate sites.**

2.6 Bibliography

- Aubinet, M., Vesala, T., Papale, D., and Eds (2012). *Eddy covariance: a practical guide to measurement and data analysis*. Springer Science & Business Media.
- Bales, R. C., Goulden, M. L., Hunsaker, C. T., Conklin, M. H., Hartsough, P. C., O'Geen, A. T., Hopmans, J. W., and Safeeq, M. (2018). Mechanisms controlling the impact of multi-year drought on mountain hydrology. *Scientific reports*, 8(1):690.
- Bales, R. C., Hopmans, J. W., O'Geen, A. T., Meadows, M., Hartsough, P. C., Kirchner, P., Hunsaker, C. T., and Beaudette, D. (2011). Soil Moisture Response to Snowmelt and Rainfall in a Sierra Nevada Mixed-Conifer Forest. *Vadose Zone Journal*, 10(3):786.
- Bales, R. C., Molotch, N. P., Painter, T. H., Dettinger, M. D., Rice, R., and Dozier, J. (2006). Mountain hydrology of the western United States. *Water Resources Research*, 42(8).
- Bales, R. C., Rice, R., and Roy, S. B. (2015). Estimated Loss of Snowpack Storage in the Eastern Sierra Nevada with Climate Warming. *Journal of Water Resources Planning and Management*, 141(2):04014055.
- Biederman, J. A., Scott, R. L., Arnone III, J. A., Jasoni, R. L., Litvak, M. E., Moreo, M. T., Papuga, S. A., Ponce-Campos, G. E., Schreiner-McGraw, A. P., and Vivoni, E. R. (2018). Shrubland carbon sink depends upon winter water availability in the warm deserts of North America. *Agricultural and Forest Meteorology*, 249:407–419.
- Broxton, P. D., Harpold, A. A., Biederman, J. A., Troch, P. A., Molotch, N. P., and Brooks, P. D. (2015). Quantifying the effects of vegetation structure on snow accumulation and ablation in mixed-conifer forests. *Ecohydrology*, 8(6):1073–1094.
- Cancelliere, A., Mauro, G. D., Bonaccorso, B., and Rossi, G. (2007). Drought forecasting using the standardized precipitation index. *Water Resources Management*, 21(5):801–819.

- Fellows, A. W. and Goulden, M. L. (2017). Mapping and understanding dry season soil water drawdown by California montane vegetation. *Ecohydrology*, 10(1):1–12.
- Frank, J. M., Massman, W. J., Ewers, B. E., Huckaby, L. S., and Negrón, J. F. (2014). Ecosystem CO₂/H₂O fluxes are explained by hydraulically limited gas exchange during tree mortality from spruce bark beetles. *Journal of Geophysical Research: Biogeosciences*, 119(6):1195–1215.
- Garcia, M., Fernández, N., Villagarcía, L., Domingo, F., Puigdefábregas, J., and Sandholt, I. (2014). Accuracy of the TemperatureVegetation Dryness Index using MODIS under water-limited vs. energy-limited evapotranspiration conditions. *Remote Sensing of Environment*, 149:100–117.
- Goldstein, A. H., Hultman, N. E., Fracheboud, J. M., Bauer, M. R., and Panek, J. A. (2000). Effects of climate variability on the carbon dioxide, water, and sensible heat fluxes above a ponderosa pine plantation in the Sierra Nevada (CA). 101:113–129.
- Goulden, M. L., Anderson, R. G., Bales, R. C., Kelly, A. E., Meadows, M., and Winston, G. C. (2012). Evapotranspiration along an elevation gradient in California’s Sierra Nevada. *Journal of Geophysical Research*, 117(G3):G03028.
- Gu, L., Falge, E. M., Boden, T., Baldocchi, D. D., Black, T. A., Saleska, S. R., Suni, T., Verma, S. B., Vesala, T., Wofsy, S. C., and Xu, L. (2005). Objective threshold determination for nighttime eddy flux filtering. *Agricultural and Forest Meteorology*, 128(3-4):179–197.
- Hamlet, A. F., Mote, P. W., Clark, M. P., and Lettenmaier, D. P. (2007). Twentieth-Century Trends in Runoff, Evapotranspiration, and Soil Moisture in the Western United States*. *Journal of Climate*, 20(8):1468–1486.
- Harpold, A. A., Molotch, N. P., Musselman, K. N., Bales, R. C., Kirchner, P. B., Litvak, M., and Brooks, P. D. (2015). Soil moisture response to snowmelt timing in mixed-conifer subalpine forests. *Hydrological Processes*, 29(12):2782–2798.

- Karnieli, A., Agam, N., Pinker, R. T., Anderson, M., Imhoff, M. L., Gutman, G. G., Panov, N., and Goldberg, A. (2010). Use of NDVI and Land Surface Temperature for Drought Assessment: Merits and Limitations. *Journal of Climate*, 23(3):618–633.
- Klos, P. Z., Goulden, M. L., Riebe, C. S., Tague, C. L., OGeen, A. T., Flinchum, B. A., Safeeq, M., Conklin, M. H., Hart, S. C., Berhe, A. A., et al. (2018). Subsurface plant-accessible water in mountain ecosystems with a mediterranean climate. *Wiley Interdisciplinary Reviews: Water*, 5(3):e1277.
- Litvak, M. (2016). Ameriflux us-vcn valles caldera mixed conifer.
- Ma, S., Baldocchi, D. D., Xu, L., and Hehn, T. (2007). Inter-annual variability in carbon dioxide exchange of an oak / grass savanna and open grassland in California. 147:157–171.
- Marks, D., Winstral, A., Reba, M., Pomeroy, J., and Kumar, M. (2013). An evaluation of methods for determining during-storm precipitation phase and the rain/snow transition elevation at the surface in a mountain basin. *Advances in Water Resources*, 55:98–110.
- McAfee, S. A. (2013). Methodological differences in projected potential evapotranspiration. *Climatic Change*, 120(4):915–930.
- Mishra, A. K. and Desai, V. R. (2005). Drought forecasting using stochastic models. *Stochastic Environmental Research and Risk Assessment*, 19(5):326–339.
- Modarres, R. (2007). Streamflow drought time series forecasting. *Stochastic Environmental Research and Risk Assessment*, 21(3):223–233.
- Molotch, N. P., Brooks, P. D., Burns, S. P., Litvak, M., Monson, R. K., McConnell, J. R., and Musselman, K. (2009). Ecohydrological controls on snowmelt partitioning in mixed-conifer sub-alpine forests. *Ecohydrology*, 2(2):129–142.

- Monson, R. K., Turnipseed, A. A., Sparks, J. P., Harley, P. C., Scott-Denton, L. E., Sparks, K., and Huxman, T. E. (2002). Carbon sequestration in a high-elevation, subalpine forest. *Global Change Biology*, 8(5):459–478.
- Norman, J. M., Kustas, W. P., and Humes, K. S. (1996). Source approach for estimating soil and vegetation energy fluxes in observations of directional radiometric surface temperature. 1923(94):2344.
- Oishi, A. C., Oren, R., Novick, K. A., Palmroth, S., and Katul, G. G. (2010). Inter-annual invariability of forest evapotranspiration and its consequence to water flow downstream. *Ecosystems*, 13(3):421–436.
- Phillips, D. L. and Macmahon, J. A. (1981). Competition and spacing patterns in desert shrubs. 69(1):97–115.
- Rao, L. Y., Sun, G., Ford, C. R., and Vose, J. M. (2011). Modeling Potential Evapotranspiration of Two Forested Watersheds in the Southern Appalalations. 54(1):2067–2078.
- Rice, R., Bales, R. C., Painter, T. H., and Dozier, J. (2011). Snow water equivalent along elevation gradients in the Merced and Tuolumne River basins of the Sierra Nevada. *Water Resources Research*, 47(8).
- Rungee, J. P., Bales, R. C., and Goulden, M. L. (2018). Evapotranspiration response to multi-year dry periods in the semi-arid western United States. *Hydrological Processes*.
- Schlaepfer, D. R., Ewers, B. E., Shuman, B. N., Williams, D. G., Frank, J. M., Massman, W. J., and Lauenroth, W. K. (2014). Terrestrial water fluxes dominated by transpiration: Comment. *Ecosphere*, 5(5):art61.
- Scott, R. L., Hamerlynck, E. P., Jenerette, G. D., Moran, M. S., and Barron-Gafford, G. A. (2010). Carbon dioxide exchange in a semidesert grassland through drought-induced vegetation change. *Journal of Geophysical Research*, 115(G3):G03026.

- Scott, R. L., Huxman, T. E., Cable, W. L., and Emmerich, W. E. (2006). Partitioning of evapotranspiration and its relation to carbon dioxide exchange in a Chihuahuan Desert shrubland. *Hydrological Processes*, 20(15):3227–3243.
- Stocker, T., Qin, D., Plattner, G.-K., Tignor, M., Allen, S., Boschung, J., Nauels, A., Xia, Y., and Bex, V. (2013). *IPCC, 2013: Climate Change 2013: The Physical Science Basis. Contribution of Working Group I to the Fifth Assessment Report of the Intergovernmental Panel on Climate Change*. Cambridge University Press, Cambridge, United Kingdom and New York, NY, USA.
- Twine, T., Kustas, W., Norman, J., Cook, D., Houser, P., Meyers, T., Prueger, J., Starks, P., and Wesely, M. (2000). Correcting eddy-covariance flux underestimates over a grassland. *Agricultural and Forest Meteorology*, 103(3):279–300.
- Vicente-Serrano, S. M., Gouveia, C., Camarero, J. J., Beguería, S., Trigo, R., López-Moreno, J. I., Azorín-Molina, C., Pasho, E., Lorenzo-Lacruz, J., Revuelto, J., Morán-Tejeda, E., and Sanchez-Lorenzo, A. (2013). Response of vegetation to drought time-scales across global land biomes. *Proceedings of the National Academy of Sciences of the United States of America*, 110(1):52–7.
- Viessman, W. and Lewis, G. L. (2003). *Introduction to Hydrology*. Pearson Education Inc., Upper Saddle River, fifth edition.
- Viviroli, D., Du, H. H., Messerli, B., Meybeck, M., and Weingartner, R. (2007). Mountains of the world , water towers for humanity : Typology , mapping , and global significance. *Water Resources Research*, 43(7):1–13.
- Wilson, K., Goldstein, A., Falge, E., Aubinet, M., Baldocchi, D., Berbigier, P., Bernhofer, C., Ceulemans, R., Dolman, H., Field, C., Grelle, A., Ibrom, A., Law, B., Kowalski, A., Meyers, T., Moncrieff, J., Monson, R., Oechel, W., Tenhunen, J., Valentini, R., and Verma, S. (2002). Energy balance closure at FLUXNET sites. *Agricultural and Forest Meteorology*, 113(1-4):223–243.

- Wolf, S., Keenan, T. F., Fisher, J. B., Baldocchi, D. D., Desai, A. R., Richardson, A. D., Scott, R. L., Law, B. E., Litvak, M. E., Brunsell, N. A., et al. (2016). Warm spring reduced carbon cycle impact of the 2012 us summer drought. *Proceedings of the National Academy of Sciences*, 113(21):5880–5885.
- Zha, T., Barr, A. G., van der Kamp, G., Black, T. A., McCaughey, J. H., and Flanagan, L. B. (2010). Interannual variation of evapotranspiration from forest and grassland ecosystems in western canada in relation to drought. *Agricultural and Forest Meteorology*, 150(11):1476–1484.

Chapter 3

Closing the mountain water balance: evapotranspiration patterns and uncertainties in tributaries to Californias Central Valley, USA

Abstract

Spatially resolved annual evapotranspiration (ET) was calculated across the 14 head-water river basins draining into Californias Central Valley, USA, based on flux-tower measurements and data-driven models using satellite greenness, gridded precipitation and temperature, and land-cover data. Stepwise regression resulted in a root-mean square error (RMSE) of 57 mm, a mean absolute error (MAE) of 42 mm, and an r^2 of 0.93. ET across the 14 basins averaged 558 mm. Leave-one-out cross validation revealed that model generation was sensitive to site removal, increasing the RMSE and MAE by 66 and 74%, respectively, implying that additional strategically located towers would improve ET predictions. Leave-one-out with individual years was less sensitive, implying that longer records are less important. Average basin-scale ET

agreed well with annual precipitation minus runoff, with deviations in the wet and dry years suggesting withdrawal or recharge of subsurface regolith storage. ET peaked at lower elevations in the north (>39.2 °N) and higher elevations in the south, closely tracking the 11 °C mean temperature isocline. ET appeared to be water limited above 12 °C and below 1000 mm, and energy limited at lower temperatures or higher precipitation. The majority of runoff in northern basins was generated below the rain-snow transition, and at snow-dominated elevations in the southern basins. Precipitation and evapotranspiration in this region are closely balanced, and small shifts in either may cause disproportionate changes in water storage and runoff.

3.1 Introduction

On average, 61% of California's annual precipitation is allocated to evapotranspiration in source-water river basins (DWR, 2014). In some areas annual evapotranspiration exceeds annual precipitation during dry years, drawing from multi-year storage (Rungee et al., 2018). The recent 2012-2015 warm-dry period triggered feedbacks that either increased or reduced precipitation minus evapotranspiration, an index of runoff (Bales et al., 2018). There is an acute need to restore mountain watersheds in California and across the western United States by thinning overstocked forests; this effort may prioritize areas with important co-benefits for reducing the risk of high-intensity wildfire, enhancing stream runoff, sequestering carbon, and other services (Krofcheck et al., 2018; Liang et al., 2018; Saksa et al., 2017). This creates a need for more-accurate information about how hydrologic fluxes and stores respond to climate variability and change, and to predict responses of evapotranspiration and runoff to watershed management (Roche et al., 2018).

Despite the importance of evapotranspiration management for runoff in this region, physical measurements and methods to accurately distribute evapotranspiration across the landscape are limited (Bales et al., 2006; Goulden et al., 2012), and current methods have shown to produce considerable differences in evapotranspiration magnitude between one another (Chen et al., 2014). This is due in part to the spatial and temporal variability of evapotranspiration, especially in Mediterranean-climate mountainous regions with distinct wet and dry seasons, high heterogeneity in topography and land cover, and sharp gradients in precipitation and temperature (Bales et al., 2006). Evapotranspiration is often estimated through model simulations, as the residual of extrapolated precipitation and runoff, or as its potential using an empirical relationship with temperature and validated with pan evaporation (Farahani, H. J. et al., 2007; Ryu et al., 2008).

Eddy-covariance flux towers provide temporally resolved measurements of evapotranspiration at the local scale (0.1-1.0 km²), and have been cited as the most accurate approach for measuring evapotranspiration in Mediterranean climates (Rana and

Katerji, 2000; Wilson and Baldocchi, 2000). Flux towers have been installed around the globe over the last 20 years to measure water, carbon and energy exchanges across various climates and land-cover types (Ryu et al., 2008). Long-term time series of data are increasingly available, providing information on the evapotranspiration response to multi-year climate variability Bales et al. (2018); Rungee et al. (2018).

Satellite-based observations are greatly improving hydrologic predictions and forecasting (Lettenmaier, 2017), and have created and improved methods for extrapolating evapotranspiration to regional and global scales (Allen et al., 2007; Chen et al., 2014; Gouliden et al., 2012; Jung et al., 2010). These methods can be categorized into two groups. The first, physically based methods, are derived from surface-energy-budget equations such as the Penman-Monteith (Mu et al., 2007, 2011) and Priestley-Taylor (Jin et al., 2011). While these methods provide a robust representation of evapotranspiration (Zheng et al., 2017), they require accurate climatic, energy and biophysical data that have high spatial variability in mountain regions (Gouliden et al., 2012; Lettenmaier, 2017). Physically based models may ultimately provide the best solution, but are currently bottlenecked by limited data and are too computationally intensive to be practical at large scales for fine-resolution estimates across heterogeneous terrain (Gouliden and Bales, 2014).

The second, statistically based methods, use data-driven relationships between observed evapotranspiration and remotely sensed vegetation indices with or without meteorological data (Glenn et al., 2010). Many studies have revealed a strong correlation between annual evapotranspiration and vegetation indices such as NDVI (normalized difference vegetation index) and EVI (enhanced vegetation index) in mountainous terrain for semi-arid regions (Gouliden et al., 2012; Groeneveld et al., 2007). However, vegetation indices appear to miss the variability of evapotranspiration during climate extremes and droughts, and in regions dominated by evergreen forests (Nagler et al., 2005). Machine-learning algorithms provide an advanced statistical method for generating relationships with evapotranspiration (Chen et al., 2014), but the limited availability of flux-tower data increases the risks of overfitting and extrapolation outside the calibration range.

We combined eddy covariance measured evapotranspiration with remotely sensed and spatially distributed climatic data to model annual evapotranspiration across the 14 mountainous river basins draining into Californias Central Valley, USA. Our primary objectives were to assess: 1) how input variables and resolution affect the ability to represent measured evapotranspiration, 2) how well modeled evapotranspiration compares with basin-scale evapotranspiration estimated as the residual of basin-scale precipitation and unimpaired runoff, 3) how uncertainty in the components of the water balance may be reduced, and 4) where runoff originates in each basin, and its relationship to precipitation and temperature patterns.

3.2 Methods

We used physical measurements of evapotranspiration coupled with remotely sensed vegetation greenness and land-cover data, and spatially distributed climatological data, to expand the method for scaling evapotranspiration across the landscape developed by (Goulden et al., 2012). First, 12 non-linear relationships were developed between evapotranspiration using variables of different spatial resolutions. All relationships were spatially and temporally compared to determine which combination of variables best describes the evapotranspiration patterns. The best-performing relationship was used to generate maps of evapotranspiration over river basins draining into Californias Central Valley and compared with estimates of evapotranspiration calculated as the residual of precipitation and unimpaired runoff. Finally, modeled evapotranspiration was binned by elevation and basin to assess the relationships with latitude, elevation, temperature and precipitation.

Study area

This study focused on the main 14 headwater river basins draining into Californias Central Valley (Figure 3.1). California is characterized by a Mediterranean climate, experiencing mild to cold wet winters and mild to hot dry summers. The majority

of annual precipitation in this region occurs as snowfall from a small number of large storms (Bales et al., 2006; Dettinger et al., 2011). Study area elevation ranged from 37 to 4412 m, and basin mean-annual precipitation and temperature ranged from 561 to 1631 mm yr⁻¹ and 6.7 to 13.4 °C, respectively.

Statistical model

Annual NDVI, annual precipitation, mean-annual temperature, and the mean of the current and previous years annual precipitation were considered for building a statistical model for evapotranspiration. The mean of the current and previous years precipitation were included to account for the hysteretic relationship between precipitation and evapotranspiration observed in Mediterranean climates due to plant-accessible water storage supporting evapotranspiration during multi-year dry periods (Klos et al., 2018; Rungee et al., 2018).

The model was developed by first creating best-fit relationships between evapotranspiration and potential variables considering linear regression and a single-term power function. The individual best-fit relationships were combined using step-wise regression. Variable inclusion was based on p-value thresholds and all variables were tested for collinearity using the Belsley method (Belsley et al., 1980). Relationships were created for all combinations of MODIS and Landsat, and the 800-m and 4-km PRISM products, producing four general equations. IGBP land-cover classes were included by introducing the five main land-cover types as dummy variables in the step-wise regression.

Data

Evapotranspiration data were taken at 13 eddy-covariance flux towers in California, providing 111 site years of data (Table 3.1). These sites are distributed across the central and southern part of the state, with at least two sites for each of five primary vegetation types that account for more than 95% of the study area. Data gaps from equipment malfunction, power outages and poor atmospheric conditions (Gu et al.,

2005) were filled using multiple linear regression considering an energy (photosynthetically active radiation), flux (carbon flux) and climatic (temperature) component iterating over a series of r^2 , data-availability, and gap-size thresholds (Rungee et al., 2018). Remaining gaps were filled as a function of incoming solar radiation (Goulden et al., 2012). The gap-filled data were then summed annually (October-September).

The footprints for all flux towers were viewed as a 0.5×1.0 -km rectangle, where the x direction is perpendicular to the mean-annual wind direction. Flux tower coordinates were centered in the x direction (0.25-km on either side), with a headwind distance of 0.9-km and a tailwind distance of 0.1-km.

MODIS (Moderate Resolution Imaging Spectrometer) and Landsat 5, 7 and 8 were used to map the normalized difference vegetation index (NDVI) at 250 or 30-m resolution, respectively. Landsat NDVI values were calculated from the top-of-atmosphere surface reflectance product downloaded from Google Earth Engine. NDVI values among different Landsat sensors were homogenized by cross-calibrating Landsat 7 (NDVI in 2012) and Landsat 8 (NDVI in 2013-2015) into Landsat 5 (Su et al., 2017; Sulla-Menashe et al., 2016). Annual Landsat NDVI maps were generated by averaging all pixels in a water year (October-September). Pixels with shadow, snow, or cloud were excluded from the calculation (Zhu and Woodcock, 2012). MODIS NDVI was obtained from the MYD13Q1.006 Terra Vegetation Indices 16-Day NDVI 250-m product, providing a continuous time series of maps from 2000 to 2015 (Didan, 2015). Annual MODIS NDVI maps were generated by averaging all pixels in a year (October-September). The 250-m 16-day pixel-reliability band was used to detect and remove poor pixels.

The International Geosphere-Biosphere Programme (IGBP) global vegetation-classification scheme data was obtained from MODIS MCD12Q1.051 Land Cover Type Yearly Global 500-m product (Friedl et al., 2010). These data were used to consider vegetation type and had a continuous time-series of annual values for 2001-2012.

Daily precipitation and temperature data were obtained from the Parameter-elevation Regression on Independent Slopes Model (PRISM) (Daly et al., 2008). Both

the 800-m and 4-km products were included. Both precipitation and temperature were used to generate regressions with flux-tower evapotranspiration, and precipitation was also used to calculate evapotranspiration as the difference between precipitation and reported values of unimpaired runoff.

Calculations of unimpaired runoff, the natural runoff from a basin considering no upstream damming, diversions or human alterations, were obtained from the California Department of Water Resources (California Data Exchange Center (CDEC), accessed Oct 19, 2017). Values were taken from streamflow gauges that best represented the 14 basins (Figure 3.1). All basins had water-year data for 1995-2015, except Shasta (1999-2015).

30-m Shuttle Radar Topography Mission (SRTM, accessed Jan 16, 2018) digital elevation data was downloaded from Google Earth Engine, and used to bin all data in 100-m elevation increments (Farr et al., 2007). The elevation labels refer to the lower limits of each bin (e.g., the 100 m label corresponds to 100-199 m).

Snow-covered area was obtained from the snow reanalysis dataset developed from Landsat 5-8 data (Margulis et al., 2016). This dataset was used to determine the historical basin-mean rain-snow-transition elevation. Jan 1 to March 15 daily snow-covered-area maps were averaged by basin for each year and then over the 1985-2016 period. The averaged maps were then binned into 100-m elevation bands and linear interpolation was used between the two elevation bands above and below 50% fractional-snow-covered area to estimate the altitudinal transition from rain to snow.

Analysis

Leave-one-out cross validation was used to assess the individual models temporal and spatial sensitivities. Temporal sensitivities were assessed by removing an individual water year for model building and then evaluated on the water year removed. This was iterated over all water years on record, leading to the removal of 1 (1998-2001) up to 11 (2011) site years in an iteration. Spatial sensitivities were assessed by removing an individual site for model building and then evaluated on the site removed. This

was iterated over all sites, leading to the number of site years removed in a single iteration ranging from 2 (US-CZ4) to 14 (US-Ton and US-Var). Performance was assessed by comparing the root-mean-square and mean-absolute errors for all models, and the best performing model was used for the remaining analyses.

The best-performing model was used to model evapotranspiration across the 14 river basins and compared to evapotranspiration estimated as the difference of PRISM precipitation and CDEC unimpaired runoff ($P - Q$). The PRISM product resolution for the $P - Q$ estimates of evapotranspiration was the same as the resolution for the best performing model.

Trends by elevation and latitude were assessed by binning the evapotranspiration, NDVI, precipitation and temperature into 100-m increments by basin. Finally, the difference of binned precipitation and evapotranspiration was multiplied by basin areas to observe the elevational distribution of runoff generation.

Sources of uncertainty

We identified three primary sources of uncertainty. First, eddy-covariance flux towers are mainly in water-limited vs. energy-limited locations, thus covering only part of the climatic range of the region. The Sierra Nevada have been cited as especially under represented (Yang et al., 2008), although more flux towers have been added to the Ameriflux dataset since 2008. Data availability is also limited temporally, with a mean of 8 years available for the 13 flux towers used. Power outage and instrument failure can lead to month-long gaps; and different methods of gap filling can lead to variability in results. Moreover, estimates of the flux-tower footprint are uncertain, and require information on canopy structure, the distribution of sources and sinks, and atmospheric conditions to resolve complex and heterogeneous flows (Kljun et al., 2015). This may lead to a misrepresentation of flux-tower NDVI, precipitation and temperature.

Second, PRISM data have a monthly mean absolute error of 4.7 to 12.6 mm, leading to a potential annual error of ± 98.2 mm (Daly et al., 2008). A comparison

of PRISM precipitation with snow-water equivalent calculated from snow-pillow data has shown that PRISM precipitation can undermeasure individual storms by 50% in the Sierra Nevada, with potential annual underestimates of up to 20% (Lundquist et al., 2015). These errors may lead to an underestimation of basin-scale evapotranspiration when estimated as the difference of PRISM precipitation and unimpaired runoff.

Third, CDEC unimpaired runoff is calculated by adding reservoir-storage change, reservoir evaporation, exports to other basins and diversions to irrigation, while subtracting imports from other basins and return flow from irrigation diversions to streamflow measurements downstream of the basins major reservoirs (Qualley et al., 2000). Additionally, sources of uncertainty result from uncharacterized diversions, using historical monthly patterns for changes in storage, imports and exports where measured data are unavailable, estimates of open-water evaporation where measurements are unavailable, and correction adjustments made with constant values if measurements are unavailable. These sources of uncertainty may overestimate unimpaired runoff where corrections exceed actual values and underestimate unimpaired runoff where the cumulative amount of neglected diversions are significant.

3.3 Results

Relationship between climatic variables and measured evapotranspiration

NDVI had the best overall regression with measured evapotranspiration, explaining 73% of the variance, but poorly accounted for differences between wet and dry years, especially for evergreen needleleaf forest, mixed forest and woody savanna sites, as shown by the low variance in NDVI and the high variance in evapotranspiration (Figure 3.2a). Annual PRISM precipitation explained 63% of the variance in measured evapotranspiration, with more outliers observed during dry years, most notably in forest sites (Figure 3.2b). The mean of the current and previous years precipitation

increased the explained variance of annual PRISM precipitation from 63 to 71% (Figure 3.2c). PRISM temperature had a negative correlation with evapotranspiration, explaining 30% of the variance (Figure 3.2d).

Influence of variable inclusion and resolution on estimated evapotranspiration

Stepwise regression of the individual relationships resulted in the general expression:

$$ET = w_{NDVI}(a_{NDVI}NDVI^{b_{NDVI}}) + w_P(a_PP^{b_P}) + w_T(a_TT + b_T) + w_{lc}(LC) + int, \quad (3.1)$$

where ET is predicted evapotranspiration, $NDVI$ is the normalized difference vegetation index, P is PRISM precipitation, T is PRISM temperature, LC is landcover, int is the intercept, w are the variable weights determined by stepwise regression, and a and b are constants for the individual input variables (Table B.1). Different combinations of input variables and data sources were considered to assess their potential contributions, and all models were an improvement over using just NDVI (Figure 3.3). Without vegetation type, temperature did not significantly improve the regression strength and was removed by the stepwise regression, making the models without vegetation type (NoV) and without both vegetation type and temperature (NoVT) equivalent (NoV not shown). ET was least sensitive to PRISM resolution with the mean-absolute difference <0.15 mm in root-mean-squared (RMSE) and mean-absolute (MAE) error. It was most sensitive to variable inclusion, with an increase in RMSE by 7% and MAE 12% from the model with all variables (AllVars) to that with temperature removed (NoT); and relative increases 33% and 45%, respectively, when temperature and vegetation type were removed. On average, using MODIS instead of Landsat NDVI gave 8% lower RMSE and 6% lower MAE. Landsat NDVI with vegetation type showed that ET for grasslands was overestimated by 160 ± 14 (mean \pm standard deviation) and for shrublands by 124 ± 10 mm yr⁻¹. Using MODIS NDVI resulted in underestimating evergreen needleleaf forests by 67 ± 1 mm

for AllVars, overestimated mixed forests by 66 ± 1 mm for NoT, and overestimated Grasslands and Shrublands by 158 ± 3 and 93 ± 9 mm, respectively, for both (Table B.1).

Model spatial and temporal validation

The AllVars models had an RMSE of 60 ± 4 and MAE of 45 ± 3 mm-yr⁻¹ (Figure 3.4), and all statistics hereafter are with respect to the AllVars model. Leave-one-WY-out slightly increased mean RMSE by 9% and MAE by 8%, while leave-one-site-out increased these errors by 66 and 74%, respectively. The difference in error between evaluation methods decreased as more variables were removed. Leave-one-WY-out RMSE increased by 7 and 3% and MAE by 6 and 2% for NoT and NoVT, respectively. Leave-one-site-out RMSE increased by 62 and 16% and MAE by 72 and 16% for NoT and NoVT, respectively. MOD800m had the lowest errors in 22 of 24 tests. MOD4km outperformed MOD800m for leave-one-site-out-All with a slight reduction in RMSE (3%) and MAE (4%). MOD4km also showed that temperature was reintroduced in the NoV variable selection when US-Var was the site removed, resulting in slightly higher RMSE and MAE errors when compared to NoVT, and the only instance when the two models differ.

Modeled evapotranspiration versus $P - Q$

The MODIS with 800-m PRISM data model (MOD800m, Figure 3.3-3.4) provided the lowest error in 22 of 24 tests and was used to model measured evapotranspiration across the 14 basins for the 12 years (2001 to 2012) of available land-cover data, providing 168 basin years of data. Values of ET were compared with basin-scale estimates of $P - Q$ for all models (Figure 3.5). ET and $P - Q$ showed a general increase from south to north, with notable exceptions being the Shasta, Feather and Tule river basins. ET values were less than $P - Q$ for the San Joaquin, Kings, and Kern river basin. RMSE and MAE were least for the AllVars model and greatest for the NoT model.

Trends by elevation and latitude

Temperature decreases with both latitude and elevation (Figure 3.6). The apparent temperature gradient is greatest between latitudes 36.1 to 37.8 °N, corresponding with the greatest range in elevation.

PRISM precipitation shows distinct trends with latitude and elevation. In the central and southern Sierra, precipitation increases with elevation. In the northern basins the pattern is mixed, with no consistent elevation gradient. The greatest ranges of precipitation were observed in higher latitudes, ranging over 1000 mm along their elevational transects, although there was no significant relationship between elevation range and precipitation range.

Visually, NDVI appeared the most similar to modeled evapotranspiration, but with more extreme peaks. The lowest values of NDVI occurred at the higher and lower latitudinal ranges. NDVI values greater than 0.80 were generally observed between 37.7 and 39.2 latitude °N, and between 500-1300 m elevation. The greatest NDVI value was observed at 41.4 latitude °N and 1000 m elevation.

ET was greatest in the higher latitudes °N, peaking at mid to lower elevations, and generally decreasing at lower latitudes. Latitude 39.6 °N had the greatest *ET* (1088 mm) at an elevation of 1000 m. Only latitudes above 39.2 °N observed *ET* values greater than 1000 mm, with these values ranging from 400 to 1200 m in elevation. The lowest values of *ET* were observed at latitudes between 36.1 to 37.1 °N and 40.9 to 41.6 °N with minimum values generally occurring near the highest elevations, except latitudes 41.4 and 41.6 °N where the minimum values occurred near the lowest elevations.

Runoff (*Q*) calculated as $P - ET$ showed that runoff is more efficiently generated at higher elevations. Runoff over 2200 mm was observed at latitude 43.1 at 3100 m. Runoff approached zero at some lower elevation sites at lower latitude.

Evapotranspiration trends by precipitation and temperature

Evapotranspiration generally increased with temperature and precipitation (Figure 3.7), linearly increasing 57 mm per °C when temperatures above 7.5 °C were removed ($r^2=0.43$, not shown). Evapotranspiration increased 0.75 mm per mm of precipitation below 990 mm of precipitation ($r^2=0.50$, not shown). Evapotranspiration increased 58 mm per °C, explaining 71% of the variance when annual precipitation was greater than 1040 mm, whereas the overall relationship explained 28% of the variance. The correlation between evapotranspiration and precipitation peaked at both low (≤ -1.6 °C) and high (≥ 12.2 °C) temperatures, explaining 87% and 80% of the variance, respectively, using a power function.

Basin runoff generation

The ratio of annual precipitation to modeled evapotranspiration is greatest at higher elevations for all basins (Figure 3.8a). The high-elevation zones represent a small fraction of area in the northern-most basins (Figure 3.8b) leading to negligible runoff (Figure 3.8c). The ratio of precipitation to evapotranspiration ranged from 1-48 across all basins and elevation bins, with 75% of runoff generated below 2000 m in elevation in northern basins (Shasta, Feather, Yuba, American and Cosumnes) and 70% generated above 2000 m in southern basins (Tuolumne, Merced, San Joaquin, Kings, Kaweah, Tule and Kern) (Figure 3.8c). Evapotranspiration exceeded precipitation during several of the study years at 600 to 1700 m in the Tule, 200-300, 900, 1000-1300 m in the Kaweah, and at the lowest elevations in the Stanislaus, Tuolumne, Cosumnes, and San Joaquin river basins (Figure 3.8a). The rain-snow-transition line generally rose as latitude decreased and occurred near an annual temperature of 10.8 ± 0.84 °C (mean \pm standard deviation).

3.4 Discussion

Effects of variable inclusion and resolution on estimating evapotranspiration

MODIS NDVI outperformed Landsat NDVI in predictions of evapotranspiration, while PRISM resolution differences had a negligible effect. MODIS provides daily scenes that are aggregated to 8- and 16-day cloud-free, atmospherically corrected composite images, whereas Landsat scenes are collected less frequently, leading to fewer cloud-free images. Snow and increased cloud cover during winter could lead to growing-season biased annual Landsat NDVI values. Future research is needed to assess the importance of seasonal biases in processing Landsat imagery in areas with snow cover. Landsat NDVI has been found to be more sensitive to mountainous terrain, especially during months with low solar elevation, whereas MODIS NDVI was found to be notably insensitive (Sesnie et al., 2012). A 0.5-km² footprint results in the inclusion of about 556 Landsat pixels versus around 8 for MODIS, making Landsat more sensitive to errors in footprint direction, shape and size.

Using all variables produced the lowest RMSE and MAE relative to the other models. The difference between RMSE and MAE was also the lowest, suggesting that including all variables reduced the magnitude of outliers compared to the other models. Removing temperature increased the RMSE by 17% and MAE by 29% from the AllVars model. Considering individual land-cover types, evergreen-needleleaf-forest evapotranspiration revealed a positive relationship with temperature, explaining 83% of the variance. Despite that the percent area coverage of evergreen needleleaf forests has increased from 39 to 54% from 2001-2012, reanalysis developing an independent regression between temperature and evergreen-needleleaf-forest evapotranspiration was not performed because only 17 site-years of data were available. Future research should consider developing individual land-cover type relationships between flux-tower measurements and temperature once sufficient data become available.

Comparing ET with $P - Q$

ET compared to $P - Q$ had an RMSE of 104 mm, MAE of 84 mm, and mean bias error of 52 mm across all 168 basin years of data. ET was about 17% greater than $P - Q$ for the six northern basins. The findings of Lundquist et al. (2015) suggest that this may be due to undermeasurement of precipitation due to snow undercatch. The Kings River basin had the densest network of flux towers within the study area and appeared to represent the 5 mid-latitude basins (Stanislaus, Tuolumne, Merced, San Joaquin, Kings) well, with all five having at least the sixth smallest difference from $P - Q$ for all models. The consistent agreement we found between ET and $P - Q$ supports our approach for modeling evapotranspiration and its value for understanding the mechanisms governing the hydrologic cycle and ecosystem health.

How can uncertainty be reduced?

The leave-one-out evaluations showed that modeling evapotranspiration is more sensitive to a lack of spatial versus temporal sampling. This corroborates Papale et al. (2015), who used an artificial neural network to upscale eddy-covariance flux-tower observations of latent heat and gross primary production, concluding that uncertainty in temporal extrapolation is relatively small compared to spatial extrapolation. Papale et al. (2015) also found that sample size affected uncertainty by $\pm 25\%$ in latent heat and $\pm 50\%$ in gross primary production, with uncertainty being greatest where spatial variability was high. Flux towers in the Sierra Nevada are somewhat limited in extent, especially when considering the ranges of precipitation and temperature (Figure 3.7). The current network of flux towers mostly captures evapotranspiration in hot and dry areas, mostly representing only one quadrant of the precipitation-temperature space. Moreover, the evapotranspiration in colder areas (annual-mean temperature ≤ 2.5 °C) is currently being estimated in part from observations at hot and dry locations, which have a similar low NDVI. A few additional flux towers that sampled the unrepresented extremes (below 2.5°C; above 1500 mm precipitation) could significantly improve the estimates of regional evapotranspiration.

When considering all basins, the slope of the regression line between ET and $P - Q$ during wet and dry years were close to 1.0, but offset about 53 mm higher, suggesting an underestimate of P , overestimate of Q , or both (Figure B.3). PRISM precipitation poorly represents measured values in the high Sierra, in part due to snow undercatch, which is exacerbated in large storms (Lundquist et al., 2015) and a lack of representative data (Zhang et al., 2017). This may explain why ET generally exceeds $P - Q$ in the northern basins (Figure 3.5, B.4). Under catch of large storms can lead to a 20% undermeasurement of annual precipitation (Lundquist et al., 2015); a snow undercatch correction would be sufficient to bring all northern basins to the 1:1 line in Figure 3.5. Future research should consider strategies for more-accurate precipitation data, including new measurements.

The slopes of $P - Q$ vs modeled ET across years within individual basins ranged from 0.21 to 0.72 (Figure B.4). These slopes reflect that $P - Q$ underestimates plant-accessible water for evapotranspiration during dry years when it is supplemented by multi-year subsurface storage; and $P - Q$ overestimates ET in wet years, when storage is replenished. The broader range of $P - Q$ values compared to ET , after accounting for possible bias by adjusting the mean $P - Q$ to match mean ET for each basin, may be interpreted as change in storage (ΔS), where negative represents drawdown and positive represents recharge. However, doing this calculation on the annual data did not always provide a consistent pattern for positive ΔS in wet years and negative ΔS in dry years. Although the dry year pattern was consistent with the pattern in Bales et al. (2018) for the Kings River basin using just spatial P and ET patterns, where dry years (2004, 2007, 2012-15) showed ΔS values of -22 to -52 mm, averaged across the basin, and the current analysis showed ΔS values of -32 to -66 (2004, 2007, 2012). Although this pattern was not consistent across all basins which showed ΔS values from 24 to -121 mm. Three wet years (2005, 2006, 2011) failed to give consistently positive ΔS values in the current analysis (averages of $+65$, -86 , $+17$, respectively). The mean ET and $P - Q$ values for the Kings River basin suggest a much smaller bias than in other basins, where uncertainties are apparently higher.

It should be noted that the $P - Q$ vs. ET best-fit slopes are likely exaggerated

due to the disproportionate number of dry years in the record. This is similar to the findings of Zhang et al. (2008) who used the Budyko framework to partition precipitation into evapotranspiration and runoff, and concluded that the omission of interannual storage variability may be a primary source of deviation between partitioned and observed runoff. The skewness to the left of the 1:1 line further supports the underestimation of precipitation in the Sierra Nevada suggested by Lundquist et al. (2015). Alternatively, ET may be somewhat inflated by high precipitation due to limited wet years available for calibration or no physical measurements above a mean precipitation of 1400 mm (Figure 3.7, Table 3.1). Future work should consider a catchment-scale analysis with dense networks of flux towers and precipitation gauges, and accurate runoff measurements to determine where biases exist.

Uncertainty in the unimpaired-flow calculations are challenging to quantify. Updating instrumentation, data-processing and gap-filling techniques and efforts to account for all diversions could improve this calculation. Further research is needed to quantify this uncertainty and to perform a cost-benefit analysis of the practical value of better understanding the water balance of river basins.

Climate controls on evapotranspiration

The mean-annual precipitation for the time period of the best model (2001-2012) is 964 mm, suggesting that evapotranspiration in this area is often water limited. The relationships observed between evapotranspiration with precipitation and temperature coincides with the findings of Rungee et al. (2018) that evapotranspiration at two evergreen needleleaf forests in the Sierra Nevada showed no response to their respective droughts having mean-annual precipitation exceeding 1000 mm, whereas two mixed forests with mean-annual precipitation less than 990 mm and temperatures greater than 12.2 °C exhibited significant withdrawals from subsurface water storage and widespread forest die-off. The relationships between evapotranspiration and precipitation for temperature values below 2.5 °C (Figure B.2a) and temperature for precipitation exceeding 1500 mm (Figure B.2b) should be taken with caution pro-

vided these values are extrapolated beyond the sampling extent. It is recommended that flux towers be installed to more accurately represent these areas.

Where does basin runoff originate?

The values from Figure 3.8 showed peak basin runoff occurs 1680 ± 249 m above peak evapotranspiration in the northern (Shasta, Feather, Yuba, American and Cosumnes) compared to 2800 ± 342 m in the southern basins (Tuolumne, Merced, San Joaquin, Kings, Kaweah, Tule and Kern). The ratio of precipitation to evapotranspiration was generally about 10% higher in the southern (49% mean) basins relative to the northern (39% mean) except for the Kaweah (35%) and Tule (7%), suggesting runoff is generated more efficiently above the rain-snow transition. This points to two types of basins in this region that produce runoff differently. The northern basins produce runoff primarily below 2000 to 2500 m, where high levels of evapotranspiration (500 to 1000 mm) are exceeded by higher levels of precipitation (around 1500 mm). The southern basins, on the other hand, produce runoff primarily from high elevations (above 2000 m), where low levels of evapotranspiration (less than 500 mm) are exceeded by moderate levels of precipitation (around 1000 mm).

These two modes of runoff generation suggest that a warming climate will affect the water balance of southern vs. northern basins through different mechanisms. Increasing temperature is expected to increase evapotranspiration in energy-limited forests, even if vegetation density remains constant, leading to decreased runoff. The northern basins are predominantly energy limited and have abundant water, making them susceptible to this effect. The north includes five basins (Shasta, Feather, Yuba, American and Cosumnes) that have historically been critical for California's water supply. The southern basins are mostly water limited at lower elevation and energy limited at higher elevation. Warming in lower elevation, southern forest is unlikely to decrease runoff, given that ET already approaches P in much of this area (Figure 3.8). Warming in this zone is more likely to increase stress and episodic dieback. Most of the runoff in the south is generated by sparsely vegetated higher elevation

zones that are currently energy limited. Warming that reduces this energy limitation and allows upslope vegetation expansion has the potential to reduce runoff (Goulden and Bales, 2014). The rate vegetation can redistribute up slope is poorly understood, and is expected to lag, as even rapid vegetation expansion is measured on a decadal timescale (Kelly and Goulden, 2008; Salzer et al., 2009).

The critical questions for the impact of warming on the water balance in this region include: 1) To what extent has and will warming accelerate evapotranspiration in lower elevation, northern forest? 2) To what extent has and will warming increase episodic stress in lower elevation, southern forest? 3) How rapidly and to what extent will warming drive vegetation expansion at higher, southern locations?

3.5 Conclusions

Our data-driven approach used readily available and accessible data to estimate the local and regional evapotranspiration in complex topography. It showed no significant sensitivity to resolution of gridded (PRISM) precipitation data, and a slight sensitivity to the use of MODIS versus Landsat NDVI. MODIS NDVI with 800-m PRISM data had the lowest RMSE and MAE for 22 of 24 evaluation tests and agreed well with evapotranspiration estimated as the difference of precipitation and unimpaired runoff considering each variable inclusion model, with an average 52 mm bias. Precipitation remains a large uncertainty in closing the water balance across mountain basins and limits our ability to quantitatively assess the impact of forest die-off, disturbance and annual meteorology on runoff.

Peak evapotranspiration was greatest in northern basins, and lower in magnitude but peaking at higher elevations further south, suggesting a warmer climate may shift peak evapotranspiration to higher elevation. The current placement of eddy-covariance flux towers showed that much of the precipitation-temperature space is not sampled, leading to uncertainty in modeled evapotranspiration. Additionally, strategically placed instrumentation could improve the understanding and representation of this system. Runoff in northern basins was generated primarily below the

rain-snow-transition, where precipitation grossly exceeded evapotranspiration, and at higher elevations in the southern basins where evapotranspiration is energy limited. The runoff volume in northern basins under a warmer climate appear particularly vulnerable to increased evaporative demand, whereas the steep temperature gradient with elevation in the southern basins may somewhat limit this effect.

Table 3.1: Sites characteristics.

Site ¹	Site Abbr.	Lat	Lon	Elev., m	Mean precip, mm	Mean ET, mm	Mean temp, °C	IGBP ^{2, 3}	Period of record
Blodgett Forest	US-Blo	38.90	-120.63	1315	1385	892	13.5	ENF	1998-2007
Shorthair	US-CZ4	37.07	-118.99	2710	1017	389	4.8	ENF	2011, 2016
Providence	US-CZ3	37.07	-119.20	2015	967	644	8.8	ENF	2009-2016
Soaproot Saddle	US-CZ2	37.03	-119.26	1160	841	658	13.4	MF	2011-2016
James Reserve	US-SCf	33.81	-116.77	1770	652	626	12.0	MF	2007-2014
Tonzi Ranch	US-Ton	38.43	-121.00	169	554	539	16.6	WSA	2002-2015
San Joaquin Experimental Range	US-CZ1	37.11	-119.73	405	510	378	16.4	WSA	2011-2016
Vaira Ranch	US-Var	38.41	-120.95	129	591	340	16.6	GRA	2002-2015
Grassland	US-SCg	33.74	-117.70	470	363	305	18.5	GRA	2007-2016
Coastal Sage	US-SCs	33.73	-117.70	475	356	340	18.5	OSH	2007-2016
Pinyon	US-SCw	33.61	-116.46	1280	261	190	15.2	OSH	2007-2016
Pinyon Burn	US-SCc	33.61	-116.45	1300	258	152	15.1	OSH	2007-2016
Low Desert	US-SCd	33.65	-116.37	275	142	131	22.0	OSH	2007-2012

¹ Related publications: US-Blo, (Goldstein et al., 2000); US-Ton and US-Var, (Ma et al., 2007).

² IGBP refers to the International Geosphere-Biosphere Programme land-cover classification system.

³ The IGBP land-cover types are evergreen needleleaf forests (ENF), mixed forests (MF), woody savannas (WSA), grasslands (GRA), and shrublands (OSH).

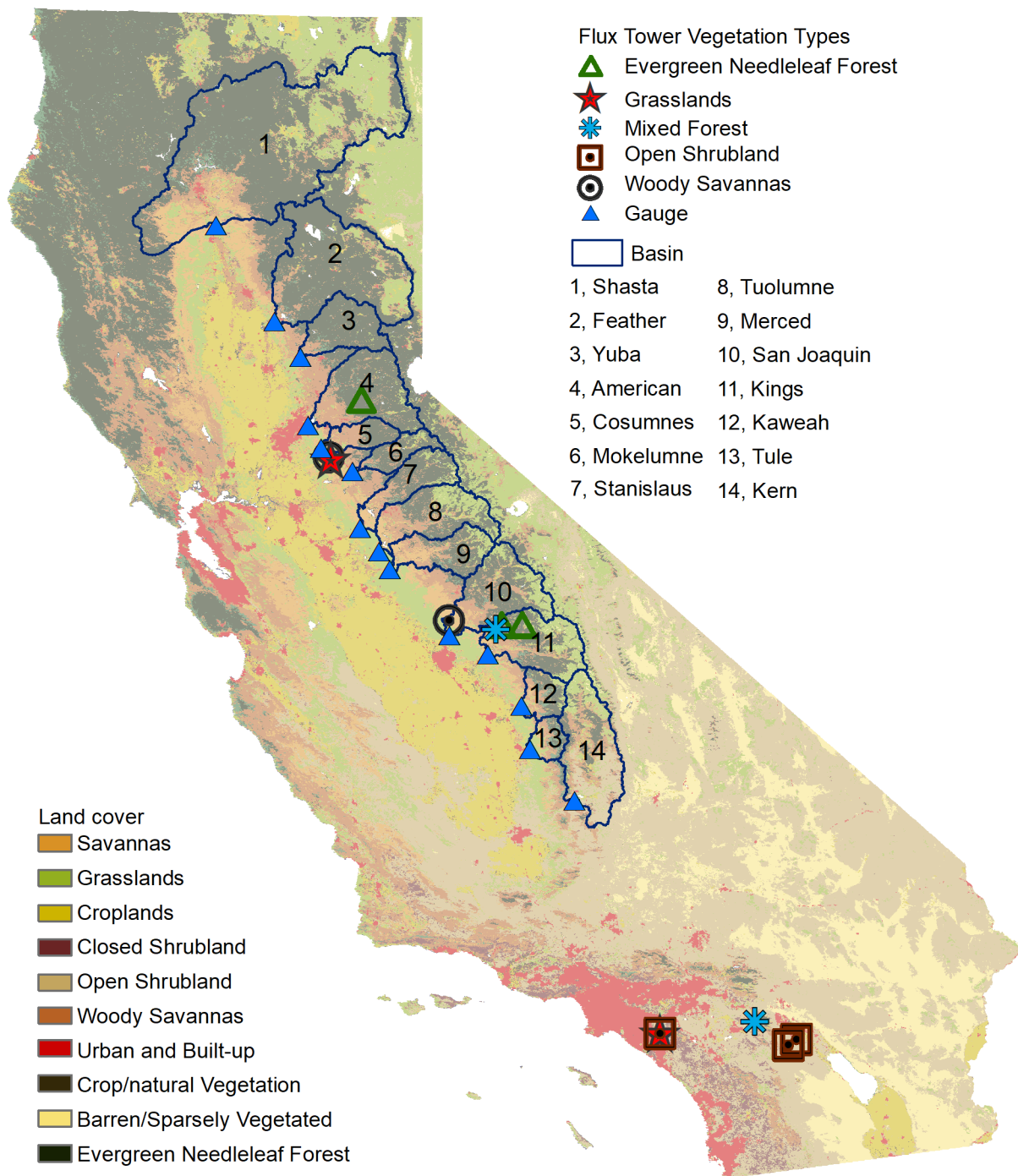


Figure 3.1: Study area showing locations of flux towers and land-cover classification, unimpaired streamflow gauges, and delineated river basins. The background shows the IGBP land-cover.

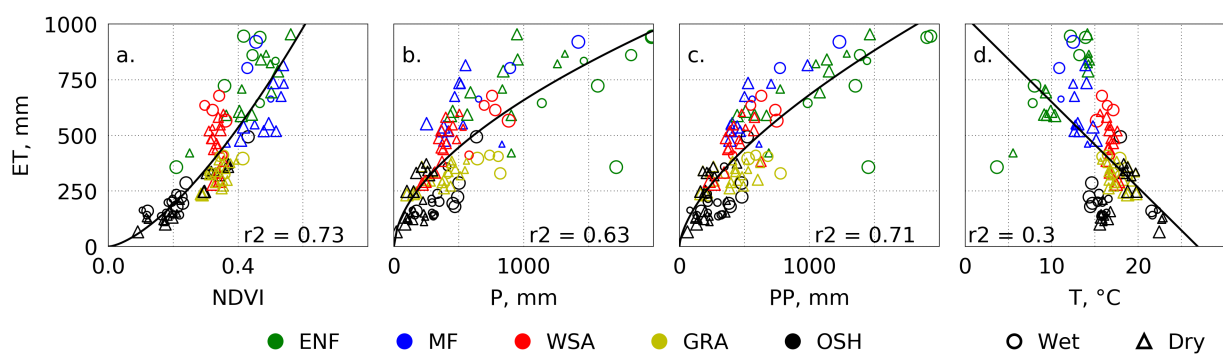


Figure 3.2: Plots of individual regressions of evapotranspiration (ET) with considered climatic variables, Normalized Difference Vegetation Index (NDVI), annual precipitation (P), the mean of the current and previous years annual precipitation (PP), and temperature (T). Marker size increases with deviation from the mean, were larger markers represent wetter (circle) or drier (triangle) years.

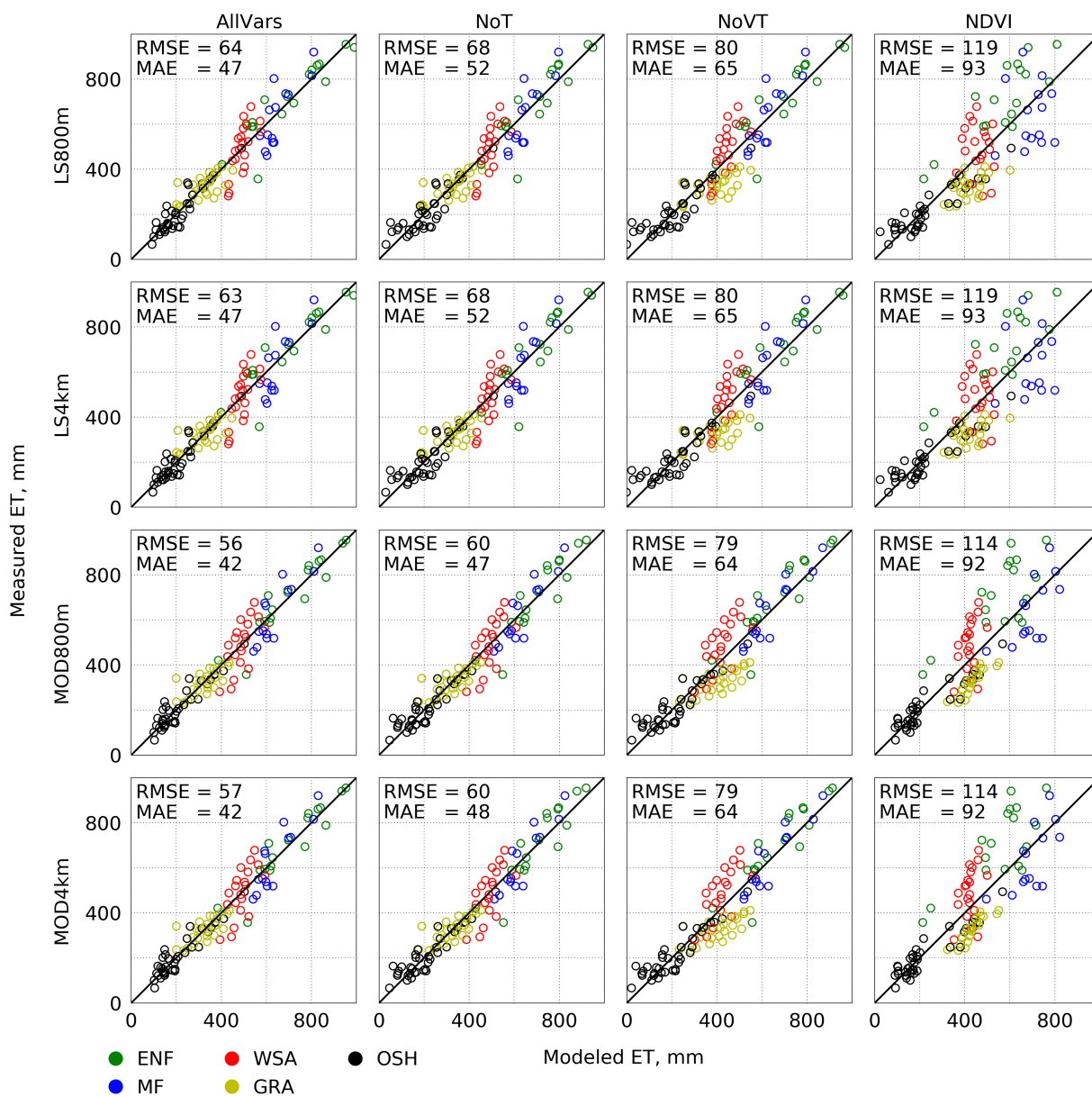


Figure 3.3: Modeled evapotranspiration versus measured evapotranspiration considering different data sources and variable combinations. Data sources include Landsat (LS) and MODIS (MOD) for NDVI, and PRISM 800 m (800m) and 4 km (4km) climate data products. Variables considered were all (NDVI, PP, T, vegetation bias correction), NoT (NDVI, PP, vegetation bias correction), NoV (NDVI, PP, T), NoVT (NDVI and PP), and only NDVI.

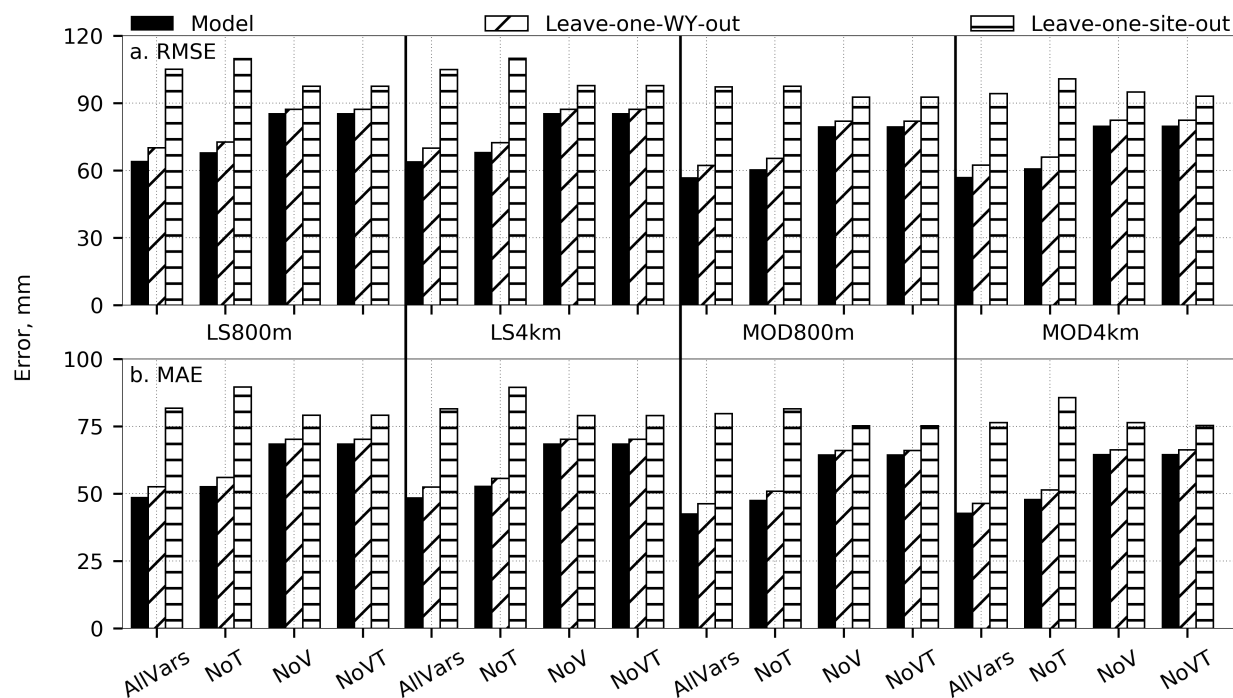


Figure 3.4: Modeled evapotranspiration validation by data source and input variables. Leave-one-WY-out was performed by leaving out all measured evapotranspiration values for a given water year for calibration and validated using the removed years and Leave-one-site-out was performed by using all but one site for calibration and validated using the removed site.

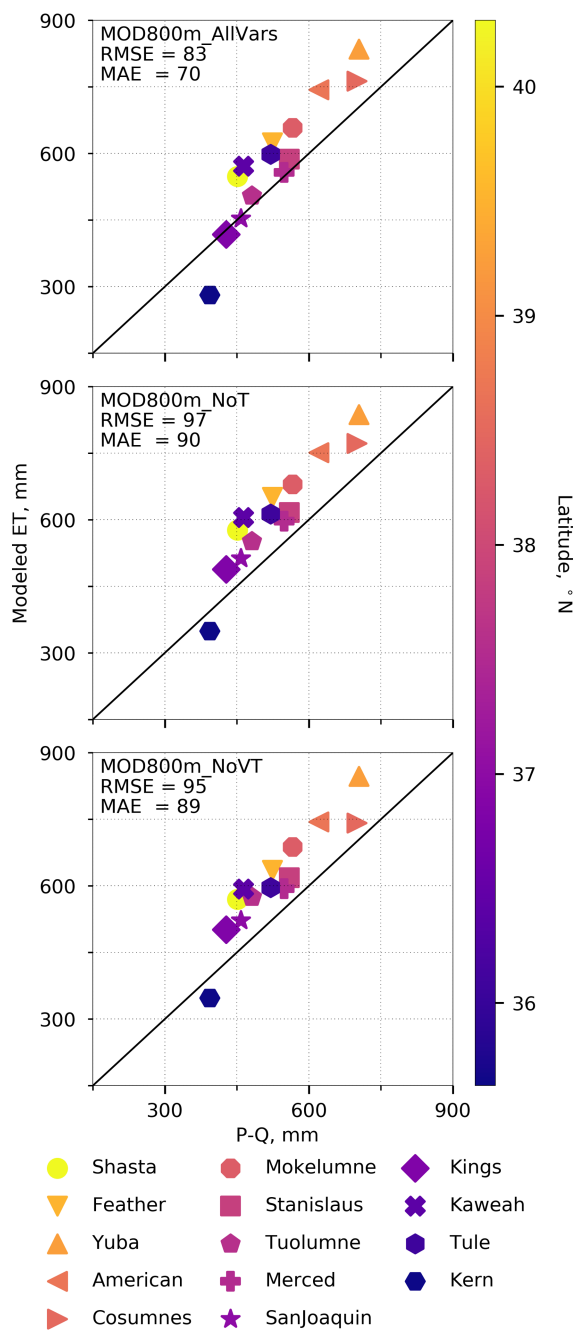


Figure 3.5: Evapotranspiration estimated as PRISM precipitation minus full natural flow (P-Q) versus modeled evapotranspiration (ET) from the MOD800m data. Legend displays basins from north to south, averaged over 2001-2012. Annual values of P and ET for each basin can be seen in Figure B.1.

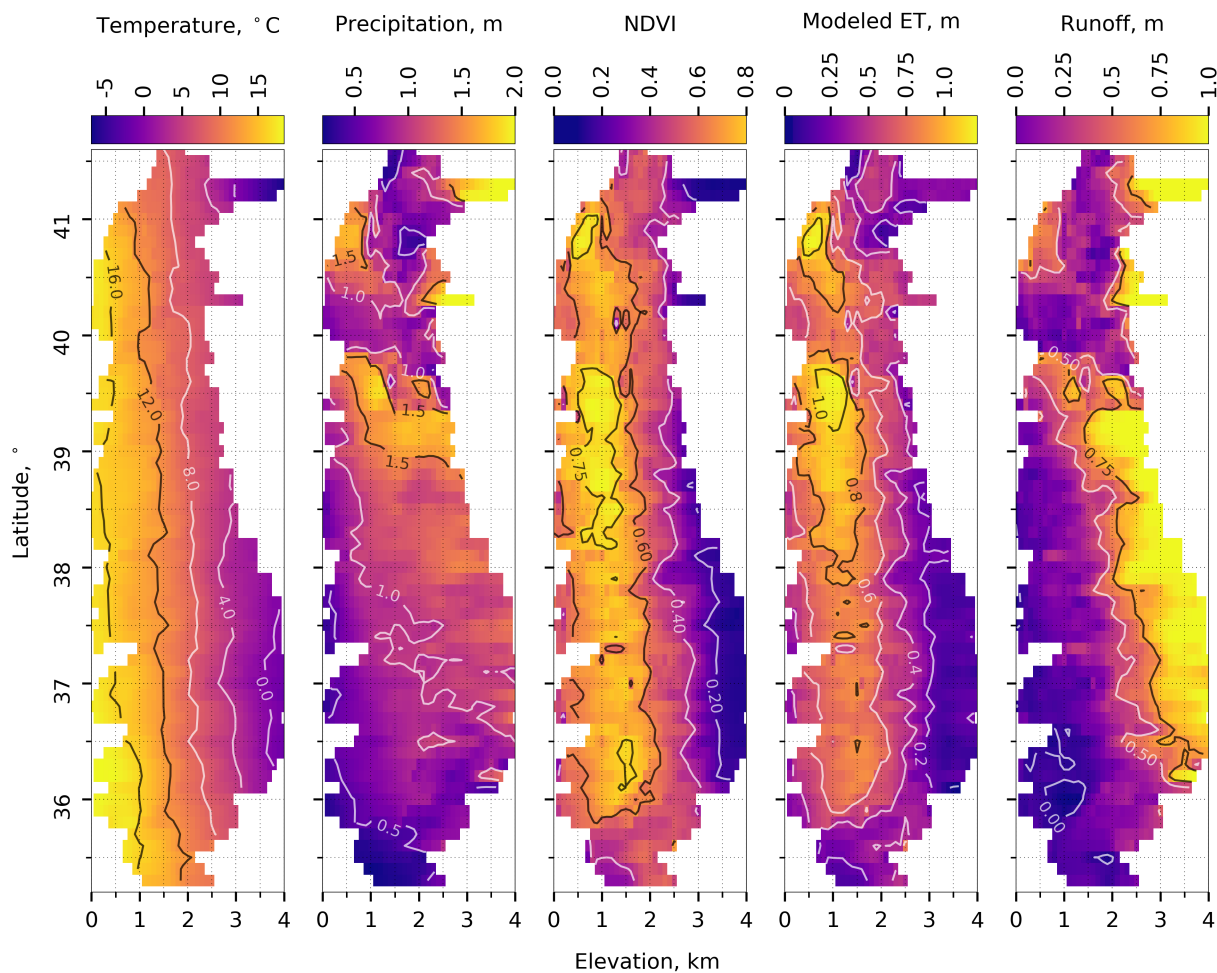


Figure 3.6: Variability of 800m PRISM temperature and precipitation, MODIS NDVI, modeled evapotranspiration (MOD800m_All), and runoff calculated as the difference of precipitation and evapotranspiration ($P - ET$) by latitude and elevation. Different color contour lines are to improve visibility only.

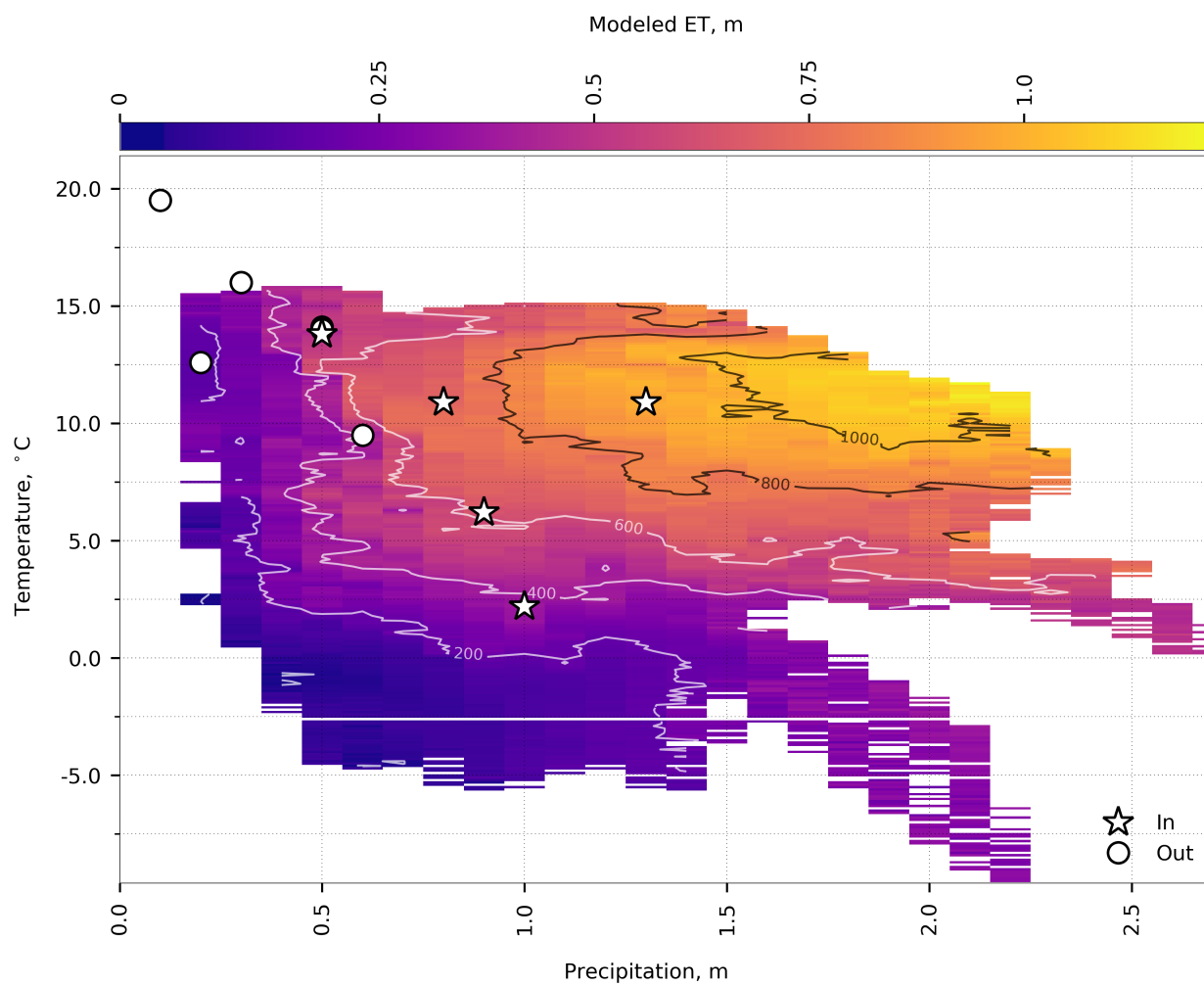


Figure 3.7: Flux tower representativeness of precipitation, temperature, and modeled evapotranspiration. Stars are flux towers within the boundary of the study area, and the circles are the remaining flux towers in California. See Figure B.2 for general trends with modeled ET and precipitation binned by temperature and temperature binned by precipitation.

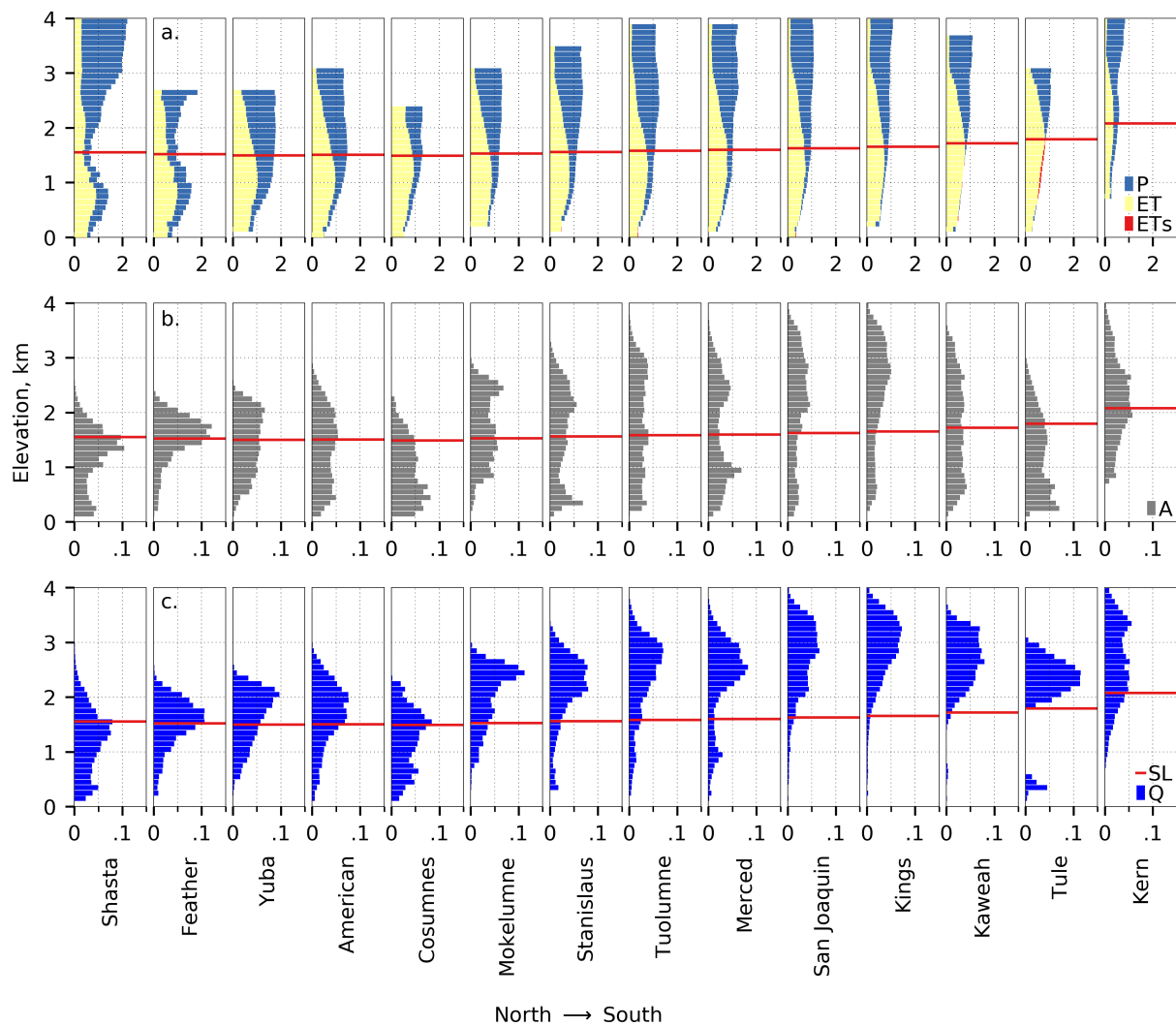


Figure 3.8: a) mean-annual precipitation (P), modeled evapotranspiration (ET, MOD800m.All) and evapotranspiration from storage (ETs) by basin and per 100 m in elevation measured in km; b) is a normalized histogram of area by elevation; c) is a normalized histogram of volumetric runoff by elevation. SL indicates the historical rain-snow transition.

3.6 Bibliography

- Allen, R. G., Tasumi, M., and Trezza, R. (2007). Satellite-Based Energy Balance for Mapping Evapotranspiration with Internalized Calibration (METRIC) Model. *Journal of Irrigation and Drainage Engineering*, 133(4):380–394.
- Bales, R. C., Goulden, M. L., Hunsaker, C. T., Conklin, M. H., Hartsough, P. C., OGeen, A. T., Hopmans, J. W., and Safeeq, M. (2018). Mechanisms controlling the impact of multi-year drought on mountain hydrology. *Scientific reports*, 8(1):690.
- Bales, R. C., Molotch, N. P., Painter, T. H., Dettinger, M. D., Rice, R., and Dozier, J. (2006). Mountain hydrology of the western United States. *Water Resources Research*, 42(8).
- Belsley, D. A., Kuh, E., and Welsch, R. E. (1980). *Regression Diagnostics*. Wiley Series in Probability and Statistics. John Wiley & Sons, Inc., Hoboken, NJ, USA.
- Chen, Y., Xia, J., Liang, S., Feng, J., Fisher, J. B., Li, X., Li, X., Liu, S., Ma, Z., Miyata, A., et al. (2014). Comparison of satellite-based evapotranspiration models over terrestrial ecosystems in china. *Remote Sensing of Environment*, 140:279–293.
- Daly, C., Halbleib, M., Smith, J. I., Gibson, W. P., Doggett, M. K., Taylor, G. H., Curtis, J., and Pasteris, P. P. (2008). Physiographical sensitive mapping of climatological temperature and precipitation across the conterminous United States. *International Journal of Climatology*, 28:2031–2064.
- Dettinger, M. D., Ralph, F. M., Das, T., Neiman, P. J., and Cayan, D. R. (2011). Atmospheric Rivers, Floods and the Water Resources of California. *Water*, 3(2):445–478.
- Didan, K. (2015). MOD13Q1 - MODIS/Terra Vegetation Indices 16-Day L3 Global 250m SIN Grid. *Nasa Lp Daac*, page 1.
- DWR, C. D. o. W. R. (2014). California Water Plan 2013: Strategic Plan (Volume 1). Technical report.

- Farahani, H. J. , Howell, T. A. , Shuttleworth, W. J. , and Bausch, W. C. (2007). Evapotranspiration: Progress in Measurement and Modeling in Agriculture. *Transactions of the ASABE*, 50(5):1627–1638.
- Farr, T. G., Rosen, P. A., Caro, E., Crippen, R., Duren, R., Hensley, S., Kobrick, M., Paller, M., Rodriguez, E., Roth, L., et al. (2007). The shuttle radar topography mission. *Reviews of geophysics*, 45(2).
- Friedl, M. A., Sulla-Menashe, D., Tan, B., Schneider, A., Ramankutty, N., Sibley, A., and Huang, X. (2010). MODIS Collection 5 global land cover: Algorithm refinements and characterization of new datasets. *Remote Sensing of Environment*, 114(1):168–182.
- Glenn, E. P., Nagler, P. L., and Huete, A. R. (2010). Vegetation Index Methods for Estimating Evapotranspiration by Remote Sensing. *Surveys in Geophysics*, 31(6):531–555.
- Goldstein, A. H., Hultman, N. E., Fracheboud, J. M., Bauer, M. R., and Panek, J. A. (2000). Effects of climate variability on the carbon dioxide , water , and sensible heat fluxes above a ponderosa pine plantation in the Sierra Nevada (CA). 101:113–129.
- Goulden, M. L., Anderson, R. G., Bales, R. C., Kelly, A. E., Meadows, M., and Winston, G. C. (2012). Evapotranspiration along an elevation gradient in California’s Sierra Nevada. *Journal of Geophysical Research*, 117(G3):G03028.
- Goulden, M. L. and Bales, R. C. (2014). Mountain runoff vulnerability to increased evapotranspiration with vegetation expansion. *Proceedings of the National Academy of Sciences*, 111(39):14071–14075.
- Groeneveld, D. P., Baugh, W. M., Sanderson, J. S., and Cooper, D. J. (2007). Annual groundwater evapotranspiration mapped from single satellite scenes. *Journal of Hydrology*, 344(1-2):146–156.

- Gu, L., Falge, E. M., Boden, T., Baldocchi, D. D., Black, T., Saleska, S. R., Suni, T., Verma, S. B., Vesala, T., Wofsy, S. C., et al. (2005). Objective threshold determination for nighttime eddy flux filtering. *Agricultural and Forest Meteorology*, 128(3-4):179–197.
- Jin, Y., Randerson, J. T., and Goulden, M. L. (2011). Continental-scale net radiation and evapotranspiration estimated using MODIS satellite observations. *Remote Sensing of Environment*, 115(9):2302–2319.
- Jung, M., Reichstein, M., Ciais, P., Seneviratne, S. I., Sheffield, J., Goulden, M. L., Bonan, G., Cescatti, A., Chen, J., De Jeu, R., et al. (2010). Recent decline in the global land evapotranspiration trend due to limited moisture supply. *Nature*, 467(7318):951.
- Kelly, A. E. and Goulden, M. L. (2008). Rapid shifts in plant distribution with recent climate change. *Proceedings of the National Academy of Sciences*, 105(33):11823–11826.
- Kljun, N., Calanca, P., Rotach, M. W., and Schmid, H. P. (2015). A simple two-dimensional parameterisation for Flux Footprint Prediction (FFP). *Geoscientific Model Development*, 8(11):3695–3713.
- Klos, P. Z., Goulden, M. L., Riebe, C. S., Tague, C. L., OGeen, A. T., Flinchum, B. A., Safeeq, M., Conklin, M. H., Hart, S. C., Berhe, A. A., et al. (2018). Subsurface plant-accessible water in mountain ecosystems with a mediterranean climate. *Wiley Interdisciplinary Reviews: Water*, 5(3):e1277.
- Krofcheck, D. J., Hurteau, M. D., Scheller, R. M., and Loudermilk, E. L. (2018). Prioritizing forest fuels treatments based on the probability of high-severity fire restores adaptive capacity in Sierran forests. *Global Change Biology*, 24(2):729–737.
- Lettenmaier, D. P. (2017). Observational breakthroughs lead the way to improved hydrological predictions. *Water Resources Research*, 53(4):2591–2597.

- Liang, S., Hurteau, M. D., and Westerling, A. L. (2018). Large-scale restoration increases carbon stability under projected climate and wildfire regimes. *Frontiers in Ecology and the Environment*, 16(4):207–212.
- Lundquist, J. D., Hughes, M., Henn, B., Gutmann, E. D., Livneh, B., Dozier, J., and Neiman, P. (2015). High-Elevation Precipitation Patterns: Using Snow Measurements to Assess Daily Gridded Datasets across the Sierra Nevada, California*. *Journal of Hydrometeorology*, 16(4):1773–1792.
- Ma, S., Baldocchi, D. D., Xu, L., and Hehn, T. (2007). Inter-annual variability in carbon dioxide exchange of an oak / grass savanna and open grassland in California. 147:157–171.
- Margulis, S. A., Cortés, G., Giroto, M., and Durand, M. (2016). A Landsat-Era Sierra Nevada Snow Reanalysis (1985-2015). *Journal of Hydrometeorology*, 17(4):1203–1221.
- Mu, Q., Heinsch, F. A., Zhao, M., and Running, S. W. (2007). Development of a global evapotranspiration algorithm based on MODIS and global meteorology data. *Remote Sensing of Environment*, 111(4):519–536.
- Mu, Q., Zhao, M., and Running, S. W. (2011). Improvements to a MODIS global terrestrial evapotranspiration algorithm. *Remote Sensing of Environment*, 115(8):1781–1800.
- Nagler, P., Scott, R., Westenberg, C., Clevery, J., Glenn, E., and Huete, A. (2005). Evapotranspiration on western U.S. rivers estimated using the Enhanced Vegetation Index from MODIS and data from eddy covariance and Bowen ratio flux towers. *Remote Sensing of Environment*, 97(3):337–351.
- Papale, D., Black, T. A., Carvalhais, N., Cescatti, A., Chen, J., Jung, M., Kiely, G., Lasslop, G., Mahecha, M. D., Margolis, H., et al. (2015). Effect of spatial sampling from european flux towers for estimating carbon and water fluxes with artificial

- neural networks. *Journal of Geophysical Research: Biogeosciences*, 120(10):1941–1957.
- Qualley, G. T., Buer, S. M., and Nemeth, S. E. (2000). Derivation of unimpaired runoff in the cooperative snow surveys program. Technical report, California Department of Water Resources.
- Rana, G. and Katerji, N. (2000). Measurement and estimation of actual evapotranspiration in the field under Mediterranean climate: a review. *European Journal of Agronomy*, 13(2-3):125–153.
- Roche, J. W., Goulden, M. L., and Bales, R. C. (2018). Estimating evapotranspiration change due to forest treatment and fire at the basin scale in the Sierra Nevada, California. *Ecohydrology*, 11(7):e1978.
- Rungee, J. P., Bales, R. C., and Goulden, M. L. (2018). Evapotranspiration response to multi-year dry periods in the semi-arid western United States. *Hydrological Processes*.
- Ryu, Y., Baldocchi, D. D., Ma, S., and Hehn, T. (2008). Interannual variability of evapotranspiration and energy exchange over an annual grassland in California. *Journal of Geophysical Research*, 113(D9):D09104.
- Saksa, P. C., Conklin, M. H., Battles, J. J., Tague, C. L., and Bales, R. C. (2017). Forest thinning impacts on the water balance of Sierra Nevada mixed-conifer headwater basins. *Water Resources Research*, 53(7):5364–5381.
- Salzer, M. W., Hughes, M. K., Bunn, A. G., and Kipfmueller, K. F. (2009). Recent unprecedented tree-ring growth in bristlecone pine at the highest elevations and possible causes. *Proceedings of the National Academy of Sciences*, 106(48):20348–20353.
- Sesnie, S. E., Dickson, B. G., Rosenstock, S. S., and Rundall, J. M. (2012). A comparison of Landsat TM and MODIS vegetation indices for estimating forage

- phenology in desert bighorn sheep (*Ovis canadensis nelsoni*) habitat in the Sonoran Desert, USA. *International Journal of Remote Sensing*, 33(1):276–286.
- Su, Y., Bales, R. C., Ma, Q., Nydick, K., Ray, R. L., Li, W., and Guo, Q. (2017). Emerging Stress and Relative Resiliency of Giant Sequoia Groves Experiencing Multiyear Dry Periods in a Warming Climate. *Journal of Geophysical Research: Biogeosciences*, 122(11):3063–3075.
- Sulla-Menashe, D., Friedl, M. A., and Woodcock, C. E. (2016). Sources of bias and variability in long-term Landsat time series over Canadian boreal forests. *Remote Sensing of Environment*, 177:206–219.
- Wilson, K. B. and Baldocchi, D. D. (2000). Seasonal and interannual variability of energy fluxes over a broadleaved temperate deciduous forest in North America. *Agricultural and Forest Meteorology*, 100(1):1–18.
- Yang, F., Zhu, A.-X., Ichii, K., White, M. A., Hashimoto, H., and Nemani, R. R. (2008). Assessing the representativeness of the AmeriFlux network using MODIS and GOES data. *Journal of Geophysical Research: Biogeosciences*, 113(G4).
- Zhang, L., Potter, N., Hickel, K., Zhang, Y., and Shao, Q. (2008). Water balance modeling over variable time scales based on the Budyko framework Model development and testing. *Journal of Hydrology*, 360(1-4):117–131.
- Zhang, Z., Glaser, S., Bales, R., Conklin, M., Rice, R., and Marks, D. (2017). Insights into mountain precipitation and snowpack from a basin-scale wireless-sensor network. *Water Resources Research*, 53(8):6626–6641.
- Zheng, H., Yu, G., Wang, Q., Zhu, X., Yan, J., Wang, H., Shi, P., Zhao, F., Li, Y., Zhao, L., et al. (2017). Assessing the ability of potential evapotranspiration models in capturing dynamics of evaporative demand across various biomes and climatic regimes with chinaflux measurements. *Journal of Hydrology*, 551:70–80.
- Zhu, Z. and Woodcock, C. E. (2012). Object-based cloud and cloud shadow detection in Landsat imagery. *Remote Sensing of Environment*, 118:83–94.

Chapter 4

Response of subsurface water storage in California's headwaters to a changing climate

Abstract

The residual of basin-scale annual precipitation and unimpaired runoff was partitioned into evapotranspiration and changes in storage (ΔS) across the 14 head water river basins draining into California's Central Valley using a spatially distributed evapotranspiration product. Temporal trends in the residual of precipitation and unimpaired runoff showed that the water available for evapotranspiration and storage has been declining for the entire period of record for the southern 7 basins, and that the slope of the trend has changed from positive to negative in the past 34-years for 5 of the 7 northern basins. Binning the residual of precipitation and evapotranspiration by basin and elevation showed that the low to mid-elevations are the most vulnerable to significant withdrawals from storage during dry years. Correlating ΔS with water-balance components and climatic variables showed that the 14 basins could be binned into 4 groups, southern, mid-range, northern, and northernmost. Comparing the intra-bin correlations with the temporal trends in each variable suggests that the southern and some mid-range basins have likely surpassed a lower threshold, whereas

energy limitation and annual precipitation grossly exceeding evapotranspiration has prevented extreme storage deficits in the northern and northernmost basins. Nevertheless, the current observed mortality in the southern basins may provide insight into future conditions in the northern basins if measures are not taken to decrease evaporative demand.

4.1 Introduction

Subsurface water storage plays an important role in semi-arid and arid Mediterranean climates, sustaining evapotranspiration and providing stream baseflows during the hot-dry summer when evaporative demand peaks and precipitation is low (Arkley, 1981; SNC, 2017). The majority of previous studies have focused on water stored in the shallow soil layer, even though studies roots extend well into the weathered-bedrock, and deep zones provide a substantial amount of water storage (Graham et al., 2010; Holbrook et al., 2014; Lewis and Burgy, 1964).

The annual change in storage (ΔS) is the residual of the water balance, expressed as:

$$\Delta S = P - ET - Q \quad (4.1)$$

where P is annual precipitation, ET is annual evapotranspiration, and Q is annual runoff. It is generally assumed that ΔS is less than zero during dry years, signifying a net withdrawal, and equal or greater than zero during wet years, signifying a net replenishment (Rungee et al., 2018; Swenson and Milly, 2006). Regional and global-scale water balances have shown that subsurface water storage has been declining as the result of increased demand (Famiglietti, 2014; Gleeson et al., 2012; Thomas et al., 2014). This removes a long-term assumption of data stationarity, reducing the representativeness and accuracy of physically based models and management strategies dependent on the historical record (Milly et al., 2008). This underscores the importance of understanding the individual components of the water balance, and of providing water resources and forest managers products that more accurately close the water balance.

In mountainous regions closing the water balance has been difficult for mainly three reasons. First, the individual components of the water balance have high spatial variability, so that local measurements poorly represent larger areas. This is especially true in mountain basins, which have steep temperature and precipitation gradients and often sparse observations (Bales et al., 2006). Second, our ability to accurately redistribute local measurements across the landscape is limited (Goulden

et al., 2012; Kirchner et al., 2014; Lundquist et al., 2015). Third, measurements of runoff for all catchments in a basin are limited, often restricting the calculation of the water balance to the basin scale; and even those basins-scale measurements are based on reconstructed flow, accounting for upstream diversions and man-made reservoirs (Qualley et al., 2000).

Until recent decades, estimates of evapotranspiration have relied on empirical or physically based formulae based temperature and meteorology. A primary limitation of these approaches is that they estimate potential evapotranspiration based on available energy and then infer actual evapotranspiration as a function of other climatic variables (soil moisture, vapor pressure deficit, wind speed, etc.) (Fisher et al., 2005). This can lead to under- and over-estimates of actual evapotranspiration based on a variety of uncertainties (Fisher et al., 2005; Shi et al., 2008). Over the past 20 years, eddy-covariance towers have been installed providing physical measurements of carbon, water, and energy fluxes at a spatial resolution of 0.1 to 1.0 km². These measurements are widely considered the most accurate method for measuring evapotranspiration in semi-arid and arid Mediterranean climates (Rana and Katerji, 2000).

Remotely sensed vegetation indices have recently become a widely used strategy for estimating and distributing measurements of evapotranspiration. Algorithms that combine vegetation indices with spatially distributed meteorological data agree well with eddy-covariance measured evapotranspiration ($r^2 = 0.93$) (Rungee et al., in review), thus providing all of the water-balance components needed to estimate ΔS . This study estimates annual basin-scale ΔS of the rivers draining into California's. My goal was to quantify: 1) how ΔS responds to climate extremes in California, 2) where the withdrawals occur in each basin and which areas are most vulnerable to future stress, and 3) how correlations between ΔS , climatic variables and water-balance components vary by basin.

4.2 Methods

I estimated annual changes in storage (ΔS) as $P - Q - ET$ using spatially distributed precipitation (P), unimpaired runoff (Q), and evapotranspiration (ET) for the 34-year period 1985 to 2018. At the basin scale, spatial and temporal patterns in ΔS were interpreted using climate and water-balance to identify correlations and variability. A time-series trend analysis was used to establish patterns and trends for the climate and water-balance attributes and infer how these variables and components may shift in the future.

Study area

The study is bounded by latitudes 35.36 to 40.51 °N and longitudes 121.64 to 117.98 °W (Figure 4.1). The climate in this region is Mediterranean, receiving the majority of precipitation during a cool-wet period (October-March) (Fellows and Goulden, 2017; SNC, 2017). Basin mean-annual precipitation ranges from 561 to 1631 mm and temperature from 6.7 to 13.4 °C. The 14 basins studied account for about 60% of California's developed water supply (SNC, 2017).

These basins have a substantial amount of below-ground plant-accessible water storage, sustaining vegetation through multi-year dry-periods (Rungee et al., 2018) while maintaining a forest biomass similar to that of tropical rain forest (Kelly and Goulden, 2016). This is due largely to the porous, deep layer of weathered and fractured regolith providing large water-holding capacity (Arkley, 1981; Graham et al., 2010; Lewis and Burgy, 1964). Observations of plant accessibility to subsurface storage have revealed rooting depths of 24 m (Lewis and Burgy, 1964) and multi-year dry-period withdrawals exceeding 550 mm of water-depth equivalent (Rungee et al., 2018).

Data

Normalized difference vegetation index (NDVI) was calculated from Landsat 5, 7, and 8 surface reflectance 30-m product, downloaded from Google Earth Engine. Landsat 7 and 8 were homogenized into Landsat 5 providing continuous data for 1985 to 2018 (Su et al., 2017; Sulla-Menashe et al., 2016). Annual values were taken as the average pixel value over water years (October-September), where water, cloud shadow, snow, and clouds were masked using the pixel_qa band.

Precipitation data were from the 4-km Parameter-elevation on Independent Slopes Model (PRISM), providing annual data for 1981 to 2018. The data were downscaled to 30-m resolution using nearest neighbor and used to estimate evapotranspiration across the landscape. The 4-km product was used in place of the 800-m product, because at the time of this study the 800-m product was only available through water year 2016.

Unimpaired runoff data for the 14 basins were provided by the California Department of Water Resources personnel (acquired 10/22/2018). This dataset provides estimates of the unimpaired runoff after removing human impacts such as damming or diversion. These data were used for the basin-scale mass-balance calculations. The compiled dataset covered 1901-2015, and was supplemented with more recent data from the California Department of Water Resources' California Data Exchange Center (accessed 10/23/2018).

The 30-m Landsat NDVI and rescaled 4-km PRISM precipitation and temperature were used to scale measured evapotranspiration across the landscape following Rungee et al. (in review). This method first determines the best-fit regression (linear or single-term power function) between physical measurements of evapotranspiration and input variables, then combines the best-fit regressions using stepwise regression. Temperature effects were removed by the stepwise regression, making the model a function of NDVI and precipitation. Physical measurements of evapotranspiration were obtained from eddy-covariance flux towers. and processed following Rungee et al. (in review).

Snow-water equivalent (SWE) was retrieved from a snow reanalysis dataset developed from Landsat 5 to 8 (Margulis et al., 2016). This dataset was used to assess relationships between the timing and magnitude of snow accumulation and melt with ΔS . It was also used in the time-series analyses.

Tree mortality data were retrieved from the United States Department of Agriculture Forest Services Aerial Detection Survey maps (accessed 12/13/2018). Annual maps were created for 1973 to 1978 and 1993 to 2018, and generated using aerial photography to identify dead trees (yellow to reddish brown). Areas with a mortality density of less than 1 tree per acre are considered normal and not included in the maps. The maps provide probable causes of death, but this study assumes all forms of death during and immediately following the 2012 to 2015 drought as drought induced. These maps were compared to the withdrawal of storage with percent basin area observing mortality during the 2012 to 2015 drought (includes 2016).

International Geosphere Biosphere Programme vegetation classification data was retrieved from Moderate Resolution Imaging Spectrometer (MODIS) Land Cover Type (MCD12Q1) Version 6 using Google Earth Engine. This product was used in conjunction with the tree mortality to quantify the percent of mortality in forested areas by basin to the 2012 to 2015 drought. Data for year 2011 were used to represent the predrought conditions. Forested pixels were selected as those representing evergreen needleleaf, evergreen broadleaf, deciduous needleleaf, deciduous broadleaf and mixed forests.

Analysis

The first step was to calculate the period of record for water available for evapotranspiration and ΔS was calculated as the residual of basin-mean precipitation and basin-scale estimates of unimpaired runoff. Next, ΔS was estimated using eq. 4.1 for the 1985 to 2018 period when spatial estimates of evapotranspiration are available. The correlation between the 1985 to 2018 estimates of ΔS and individual climatic variables and water balance components was then determined using Kendall's tau-b

(τ). τ is a nonparametric rank-correlation test, and for an independent list x and dependent list y is calculated as:

$$\tau = \frac{N_c - N_d}{\sqrt{(N_t + T) \times (N_t + U)}} \quad (4.2)$$

where N_c is the number of concordant pairs, N_d is the number of discordant pairs, N_t is the total number of pairs, and T and U are the number of ties in only x and y , respectively, where jointly tied pairs between x and y are not counted (Knight, 1966). τ was used because its rank-correlation characteristic removes the assumption of linearity between variables and because it is less sensitive to outliers.

Finally, time-series analyses were performed over all variables using τ , the Mann-Kendall test, and Theil-Sen's slope. τ was calculated in the same manner as equation 4.2, except using time as the dependent variable. The Mann-Kendall test was used to determine the significance of the individual trends, and thus τ . The Mann-Kendall test is a widely used tool for assessing temporal trends in water-cycle components primarily merited to its nonparametric characteristic, which makes it ideal for climatic data, which tend to be skewed (Jones et al., 2015; Yue et al., 2002). The test developed by Mann (1945) and Kendall (1955) sets a null hypothesis that no trend exists. The Mann-Kendall statistic M is calculated as:

$$M = \sum_{k=1}^{n-1} \sum_{j=k+1}^n \text{sgn}(x_j - x_k) \quad (4.3)$$

where $\text{sgn}(x_j - x_k)$ is the sign of $x_j - x_k$ given as 1, 0 or -1 , and n is the number of points. The test statistic, Z , is then calculated as:

$$Z = \begin{cases} \frac{S - 1}{\sqrt{\text{VAR}(S)}}, & \text{if } S > 0 \\ 0, & \text{if } S = 0 \\ \frac{S + 1}{\sqrt{\text{VAR}(S)}}, & \text{if } S < 0 \end{cases} \quad (4.4)$$

where $\text{VAR}(S)$ is the variance of S . If the absolute value of Z is greater than $Z_{1-\frac{\alpha}{2}}$ then the null hypothesis is rejected and the trend is significant (Warren and Gilbert, 1988). Finally, the magnitude of the trend was determined as the Theil-Sen's slope,

calculated as the median gradient for all pairs of points in the dataset (Sen, 1968; Theil, 1950).

Sources of uncertainty

The primary sources of uncertainty in this study are the errors existing in the data used to estimate ΔS . The PRISM dataset is typically erroneous in mountainous regions, where high-elevation measurements of precipitation are limited, leading to data extrapolation in place of interpolation (Daly et al., 1994). Daly et al. (2008) quantified mean monthly absolute errors, showing they range from ± 4.7 to ± 12.6 mm resulting in a potential annual error of ± 98.2 mm in the western United States. Depending on how the errors are propagated across the basins, its potential is greatest in the southern basins where precipitation is lowest. This error may be as high 20% due to undermeasure of annual precipitation with snow undercatch in the Sierra Nevada (Lundquist et al., 2015). This error may also be more significant for the southern basins, where the majority of precipitation falls as snow. Therefore, it is likely the mean-absolute errors reported by Daly et al. (2008) are lower than the errors for the area considered.

The second major source of error is from the evapotranspiration product. Rungee et al. (in review) discussed the uncertainties of this product in detail, stating that a notable source of uncertainty reflects the current network of flux towers, which poorly capture the precipitation-temperature space of the study area. Other sources of uncertainty reflect the development of the product, which uses PRISM precipitation, maximizing error if the correlation between evapotranspiration and PRISM precipitation is unrepresentative of the correlation between evapotranspiration and true precipitation. An additional source of uncertainty in the evapotranspiration product is the processing and gap filling of the flux-tower data. This is mostly due to uncertainties in the gap filling process, which are most acute when dealing with large gaps, and also treatment of energy balance closure (Biederman et al., 2018; Rungee et al., in review).

A third major source of uncertainty is derived from the calculated basin-scale values of unimpaired runoff. These values are created by adding reservoir change in storage, evaporation from the reservoir surface, upstream diversions, and subtracting returned diversions from measured reservoir outflow (Qualley et al., 2000). Errors in these calculations can be derived from unmeasured diversions, reservoir stage-storage estimates, estimates of reservoir evaporation, and reporting errors from human-recorded data. This will lead to an overestimation if losses are underestimated and an underestimation if losses are overestimated.

4.3 Results

Long and near-term trends in $P - Q$

$P - Q$ was calculated as far back as 1900 for some basins and all basins displayed high interannual variability, with a mean CV greater than 20% (Figure 4.2). A 15-year moving average shows long-term trends (period of record) for the seven northernmost basins to be positive, with slopes ranging from 0.23 to 1.35 mm yr⁻¹. In contrast, the seven southernmost basins showed negative slopes, ranging from -0.05 to -1.74 mm yr⁻¹. Theil-Sens slopes for the most-recent 34 years, encompassing the time period of available evapotranspiration data, showed that all slopes were negative except for the American and Cosumnes. All slopes decreased (by 86 to 561%) except for the Cosumnes, which increased by 79%.

Trends in evapotranspiration and runoff by elevation and basin

Figure 4.3 shows average evapotranspiration by basin for 1985 to 2018 by 100-m elevation bins (annual values shown in the appendix C.4). Precipitation generally increases with elevation but decreases in magnitude from north to south (Figure 4.3). For example, the 3000-m elevation mean-annual precipitation is 1728 mm in

the Shasta and 587 mm in the Kern. Evapotranspiration typically increased with elevation to a peak, but then decreased. The elevation of peak evapotranspiration typically increased from north to south while decreasing in magnitude. For example, evapotranspiration peaked at an elevation of 800 m and an annual value of 664 mm for the Shasta, and peaked at an elevation of 2500 m with an annual value of 372 mm for the Kern. Runoff, estimated as $P - ET$, exceeds evapotranspiration at mid elevations in the Shasta and Feather basins, and the elevational trends mirrored each other at the low to mid elevations, where increases in evapotranspiration coincided with increases in runoff and vice versa. In the American River basin evapotranspiration exceeds runoff up to an elevation of 1200 m. The highest elevation at which evapotranspiration continued to exceed runoff generally increased from north to south, with evapotranspiration exceeding runoff for all elevations up to 2900 m in the Kern.

Interannual variability in change in storage

ET calculated on a pixel-by-pixel basis for each year was combined with the $P - Q$ values in Figure 4.2 to estimate ΔS for the 1985 to 2018 period. Figure 4.4 provides a time series of ΔS for each basin to compare how ΔS varies in time, between basins, and to climate extremes. Shasta had the least interannual variability among the basins (71 mm) while the rest varied in the 78-113 mm range, with no distinct trend from north to south. The standard deviation of mean-annual values between basins was low (67 mm), although large negative ΔS values were not always consistent between basins (c.f. water years 1989, 1993, 1997, 2006, 2007). Interestingly, ΔS did not always express net increases during wet years and decreases during dry years. Other than the first year of the 1987-1992 drought, all basins but Shasta showed net increases in ΔS ranging from 24 to 675 mm; and during the 2012 to 2015 drought all basins except the Yuba, American and Cosumnes showed decreases in ΔS of -16 to -420 mm.

Plotting ET vs. $P - Q$ showed that not all basins had points evenly distributed

about the 1:1 line, meaning the water balance in these basins is either not in equilibrium or ΔS is underestimated if the mean basin ΔS (e) is positive and overestimated if negative. Values of e were especially negative for the Cosumnes (-144 mm), Stanislaus (-71 mm), Merced (-63 mm), Tule (-62 mm) and Kern (-102 mm) basins, meaning that on average, $P - Q < ET$; and values were very positive for the Shasta basin (62 mm). Adding e to ΔS forced closure of the 1985-2018 water balance. The cumulative ΔS during the 1987 to 1992 drought averaged 145 mm across all basins and averaged -299 mm for the 2012 to 2015 drought.

Interannual variability in change in storage

The correlation strength of 16 water-cycle-related attributes (Table Appendix C.1) to ΔS were determined using Kendalls tau, and the best fitting of these (Table 4.1) are presented in Figure 4.5. The correlations showed no consistent trend from north to south, but can be binned into four groups: the southern basins (Merced, San Joaquin, Kings, Kaweah, Tule, and Kern), mid-range basins (Cosumnes, Mokelumne, Stanislaus, and Tuolumne), northern basins (Yuba and American), and northernmost basins (Shasta and Feather). Covariance matrices for the best-fitting features with best-fit lines are provided in the supplementary section for each basin (Appendix figures C.1).

The southern basins mostly showed strong positive correlations with precipitation, runoff, SWE and 90%M, and a significant negative relationship with temperature. The two southernmost basins also showed a weak but significant positive relationship with evapotranspiration. The mid-range basins were the least consistent, with no single feature significant among all basins. For the Cosumnes and Stanislaus ΔS showed significant positive correlation with P, Q, SWE and 90%M and a negative significant relationship with T. The Mokelumne and Tuolumne basins behaved like the northern basins, only showing a significant negative correlation with ET.

The northern basins had a significant inverse correlation between ΔS and evapotranspiration, on average explaining 54% of the variance. All other variables had a

tau approaching zero.

The northernmost basins show significant (p-value < 0.1) and positive correlation between ΔS and precipitation, runoff, annual snow-water equivalent (SWE) and timing of 90 % melt from peak SWE (90%M), with precipitation having the highest r^2 (mean of 0.32). The northernmost basins showed no significant relationship between ΔS and temperature or evapotranspiration.

Time series analysis of change in storage and water-cycle-related features

Precipitation and runoff had no significant trends, and temperature showed the only consistent trend across all basins (Figure 4.5). The trends in temperature were significant for all basins except the Cosumnes, and positive for all basins, with slopes increasing from north to south. The period of record (LT) trends in $P - Q$ have a positive slope in the northern basins, versus a negative slope in the southern basins. The trends were significant for the Shasta, Yuba, American, Kings, Kaweah and Tule basins (Mann-Kendall p-value < 0.1), and the Feather and Kern trends were nearing significance (p-value < 0.14). The 34-year trends (NT) in $P - Q$ were negative except the American and Cosumnes, but only statistically significant for the Kaweah. The 34-year trends in ET were positive for all basins except the Kern, with significant trends ranging from 1.2 to 3.0 mm yr⁻¹, suggesting a 37 to 91 mm increase in evapotranspiration since 1985. Consequently, all 34-year trends in ΔS were negative with 5 of the 14 basins trends being significant, resulting in a 73 to 182 mm decrease in ΔS over this period. The slopes showed increases in annual-mean temperature of 1.0 to 2.3 °C over the 34-year period. The slopes of temporal trends in SWE were negative for all basins except the Stanislaus, but the Kern was the only basin to exhibit a statistically significant trend. Trends in the 90%M were negative for all basins except the Shasta and Stanislaus, but none were statistically significant.

4.4 Discussion

How does ΔS respond to extremes and how will it change in the future?

Comparing the 1987 to 1992 and 2012 to 2015 droughts show that ΔS can respond counter-intuitively to extremes in precipitation (Figure 4.3). Normalizing the time-series of ΔS and the water-balance-related features distinctly identified that although precipitation was similar, evapotranspiration and temperature were significantly lower in the 1987 vs. 2012 drought, and that SWE during the 1987 drought was higher and sustained longer into the summer (Appendix C.3). If a warmer climate reduces SWE and shifts its melt out earlier into the year or annual evapotranspiration increases, as seen in the 2012 drought, ΔS will likely become more responsive to anomalies in precipitation, with withdrawals similar to those observed during the 2012 drought becoming more frequent.

The 34-year Theil-Sens slopes show decreasing trends in ΔS for all 14 basins (Figure 4.5). Moreover, all slopes in $P - Q$ either shifted from positive to negative or became more negative for all basins except the American and Cosumnes. This means that a larger percentage of annual precipitation is being allocated to runoff, and therefore less water is available for ΔS and evapotranspiration. Moreover, evapotranspiration has an increasing trend for all basins over the past 34-years, except the Kern. This suggests that the water balance has not been balanced in the southern seven basins for a long time and has recently become imbalanced in the northern seven basins. Further, the difference in long-term mean slopes for the southern seven basins and the near-term mean slopes of the northern seven basins is about 0.12 mm, suggesting that $P - Q$ in the northern basins is on a similar trend trajectory as the southern basins have been over the past century. Therefore, responses to climate extremes in the southern seven basins may be an indication for how the northern seven basins will behave in the coming century, if their current $P - Q$ trends are sustained.

Comparing Figures 4.4 and 4.5 suggest that ΔS will likely continue to become

a larger negative number for all basins, provided nearly all correlations between ΔS and the water-balance-related features that would result in positive ΔS values have inverse temporal trend trajectories. However, this may not be the case for the southern seven basins where unprecedented levels of water stress (Bales et al., 2018) and widespread dieback (Tree Mortality Task Force, 2018) suggest that ΔS has reached a critical threshold. This is further supported by the temporal trends in evapotranspiration being insignificant in the southern basins despite the strong-increasing trends in temperature. This dieback has lowered evapotranspiration (Bales et al., 2018) in the Kings river basin, providing an opportunity for ΔS to somewhat recover, ideally returning the water balance to a homeostasis.

Where do negative values of ΔS occur?

2014 was the most severe year with regards to negative pixel values of ΔS for the 1985-2018 period and shows where ΔS is most vulnerable to a deficit in precipitation, especially when temperature is high (Appendix C.4.30). Although the northern basins had little to no elevation bands where withdrawals from storage were observed, the southern basins all showed withdrawals from at or near their lowest elevations up to elevations of 2800 m. Comparing the 2014 maps with the mean time-series maps shows that withdrawals from storage mirror evapotranspiration, where peak withdrawals from storage generally coincide with peak evapotranspiration. The same comparison for the northern basins show a more gradual decline in $P - ET$ from higher to lower elevations. Here, the ratio of drought $P - ET$ to mean $P - ET$ may provide some insight for where evapotranspiration may be over drafting, leading to withdrawals from storage in the future. Considering locations where storage was not withdrawn, values of this ratio ranged from near zero to 0.63. Here we are viewing ratio values below 0.2 as at risk of observing withdrawals. All northern basins except the Yuba and American basins showed ratios below 0.2 from their minimum elevations up to elevations of 1900 m, suggesting these ranges are likely the most vulnerable to experiencing significant withdrawals from storage in the future.

How do the correlations between ΔS and water-balance-related features vary from south to north?

The correlations between ΔS and the water-balance-related features vary by a combination of available energy, available water, precipitation type and physical characteristics, and the strength of correlations differ between the southern and northern basins, affecting how these basins respond to climate extremes. The southern basins had strong positive correlations with precipitation, runoff, SWE and 90%M, and a negative correlation with temperature. Considering these basins are largely water limited but snow dominated, the lack of a significant relationship with evapotranspiration in the southern basins (Merced, San Joaquin, Kings, Kaweah) suggests ΔS is likely the result of prolonged snow cover, which has been shown to reduce the dependency of evapotranspiration on seasonal subsurface-water storage drawdown (Rungee et al., in review). The Tule and Kern basins both showed a counter-intuitive positive relationship with evapotranspiration and had the two highest tau values with precipitation, suggesting they are extremely water limited. Further, the relationship between precipitation and evapotranspiration were two of the greatest and had regression slopes 30% greater than rest of the basins, on average, suggesting that the significant relationship with evapotranspiration is largely driven by the relationship between precipitation and evapotranspiration. This is in accordance with Wang and Alimohammadi (2012) who found that ΔS and evapotranspiration are especially sensitive to precipitation in water-limited systems.

The mid-range (Cosumnes, Mokelumne, Stanislaus and Tuolumne) basins had no consistent relationship between the features considered. The variability in relationships is likely driven by a combination of being within the latitudinal transition from energy to water-limited (Hawkins et al., 2003) and the transition from rain to snow-dominated runoff (Rungee et al., in review), and further complicated by topography which has been shown to alter the water balance between energy and water-limited in snow-dominated regions (Tague and Peng, 2013). The Cosumnes has the lowest elevation range of all basins and the second highest mean-annual temperature. A warmer

mean temperature is likely associated with an extended growing season and basins with a relatively high $\frac{ET}{P}$ ratio, despite its higher mean-annual precipitation magnitude relative to the southern basins. ΔS in the Mokelumne only had a correlation with evapotranspiration. Rungee et al. (in review) showed that more than 50% of the Mokelumnes area is above the rain-snow transition. Considering this along with its high mean-annual precipitation and SWE magnitudes suggests that the Mokelumne is currently energy limited, but can support increases in evapotranspiration expressed by its lower $\frac{ET}{P}$ ratio. The Stanislaus showed relationships similar to the southern basins; but based on its relatively high precipitation and SWE it would be assumed to have a lower $\frac{ET}{P}$ ratio, more like the northern basins. The Tuolumne was the only basin where ΔS had significant correlations with all evapotranspiration, SWE and 90%M. It is suspected that the combination of latitude and physical characteristics of the Stanislaus and Tuolumne make them closest to the energy-water-limited transition.

Evapotranspiration was the only consistent significant correlation with ΔS among the northern (Yuba and American) basins. The lack of relationship with precipitation is likely driven by these basins being energy limited, where the majority of precipitation variability is observed in runoff variability (Wang and Alimohammadi, 2012). This agrees with Rungee et al. (in review) who showed that the northern basins are generally energy limited, and that evapotranspiration could readily increase with an increase in available energy, in-turn increasing the dependency on subsurface water storage. This would likely result in large reductions in runoff despite increases in precipitation. Being a single-mode relationship suggests that storage in these basins are the most vulnerable since precipitation, SWE and 90%M have no effect, and the findings of Goulden and Bales (2014) suggest that a warmer climate may lead to vegetation expansion, increasing evaporative demand.

Relationships between ΔS and the independent features in the northernmost (Shasta and Feather) basins were similar to those in the southern basins. Precipitation, runoff, SWE, and 90%M were all positively correlated. Alternatively, the northmost basins were the only group that showed no relationship with either tem-

perature or evapotranspiration. The similarities with the southern basins may be explained in part by the northernmost basins having similar elevation ranges, $\frac{ET}{P}$ ratios, and mean-annual values of precipitation and evapotranspiration. However, SWE in the northern basins is a lower fraction of P , whereas SWE has been shown to supplement evapotranspiration during the summer in the southern basins (Rungee et al., 2018). Therefore, the similarities in correlations between the northernmost and southern basins may be somewhat coincidental and attributed to the differences in underlying geology. The northernmost basins geology consists largely of quaternary volcanic rock which is characterized by fast infiltration, high storage and retention, and slow draining, whereas the southern basins consists of a granitic bedrock with is less porous and fast draining (Dahlgren et al., 2004; Manga, 1999; Tague and Grant, 2009). Further, a $\frac{Q}{P}$ ratio near 0.5, with low temporal variance, suggests that ΔS in the northern most basins largely responds to precipitation magnitude (Appendix C.2.1-2, C.3.1-2), most obvious in 1987 (driest year in 34-year record) on Figure 4.3, which counters the precipitation-runoff relationship observed in the northern basins. This suggests the extra storage capacity at the northernmost basins may provide a similar benefit to summer evapotranspiration as SWE in the southern basins. This may also explain why the percent area of tree mortality was significantly less in the northernmost basins as compared to the southern (Table 4.2).

4.5 Conclusions

Time-series analysis of the significant water-balance-related features revealed that current trends mostly correspond with negative values of ΔS . However, a lack of correlation between ΔS and evapotranspiration in the southern seven basins despite significant positive slopes in temperature may suggest that storage has reached a critical low point. This may provide insight for why the observed widespread forest mortality to the recent drought was greatest in the southern seven basins. Further, the observed response in the southern seven basins may be indicative of the future response to the northern seven basins, provided the mean long-term slopes in $P - Q$

of the southern seven basins are within 0.11 mm of the mean near-term slopes in the northern basins.

2014 showed the greatest withdrawals with all southern seven basins observing significant withdrawals from storage ranging from their lowest elevations up to 2800 m. Alternatively the northern seven basins had very few, if any, elevation bins showing withdrawals from storage. Comparing the ratio of 2014 to the mean $P - ET$ for non-negative values showed that the low to mid elevations in the northern seven basins appear the most vulnerable to observing withdrawals in the future, although the American and Yuba basins had relatively high ratios for all elevation bins.

A 1985-2018 time-series analysis shows that ΔS and evapotranspiration is declining across the 14 major headwater basins draining into California's Central Valley. For the southern seven basins this has been occurring for the entire period of record but is recent (past 34 years) for the northern seven basins. Correlating a suite of water-balance-related features to ΔS allowed us to bin the basins into four categories, southern, midrange, northern and northernmost, showing that the factors influencing ΔS vary within this region.

Table 4.1: Basin characteristics and 34-year mean-annual values.

Basin	Area, km ²	Elev range, m	Mean elev, m	P*, mm	ET*, mm	Q*, mm	T*, °C	SWE*, mm	90%M*, WYD
Shasta	23,356	93-4303	1210	840	473	430	10.9	112	259
Feather	9,525	44-2834	1539	1098	562	544	9.8	285	247
Yuba	3483	74-2747	1444	1635	703	933	10.9	442	252
American	4823	37-3147	1348	1285	616	649	11.8	352	254
Cosumnes	1337	52-2375	945	1036	574	317	13.9	123	239
Mokelumne	1497	183-3140	1713	1222	582	629	10.2	502	258
Stanislaus	2582	85-3525	1616	1124	521	531	10.2	453	259
Tuolumne	4097	60-3964	1795	1048	469	570	9.3	468	265
Merced	2749	95-3944	1647	964	480	420	10.3	395	267
San Joaquin	4292	92-4228	2111	929	437	477	8.0	557	271
Kings	4790	171-4300	2332	914	416	490	7.1	575	267
Kaweah	2428	189-3818	1725	839	474	343	11.1	352	258
Tule	1044	165-3100	1219	669	455	151	13.9	131	236
Kern	6141	748-4412	2201	549	299	148	9.0	272	251

¹ Note. Elev is elevation, P is precipitation, ET is evapotranspiration, Q is unimpaired runoff, T is temperature, SWE is total-annual snow-water equivalent, 90%M is the water-year day (WYD) when 90% of peak SWE has melted.

* water-cycle-related features used in analyses.

Table 4.2: Tree mortality following the 2012-2016 drought.

Basin	Percent mortality of total area	Percent mortality of forested area	Percent forested area
Shasta	16%	24%	27%
Feather	19%	28%	42%
Yuba	22%	31%	58%
American	23%	33%	46%
Cosumnes	32%	47%	53%
Mokelumne	41%	63%	41%
Stanislaus	39%	72%	25%
Tuolumne	25%	57%	20%
Merced	38%	80%	24%
San Joaquin	46%	91%	16%
Kings	37%	83%	12%
Kaweah	64%	86%	29%
Tule	67%	93%	36%
Kern	33%	91%	4%

¹ Note. IGBP classifies a pixel as forested if covering more than 60% of the area. Therefore, discrepancies between the total percent tree mortality with percent forested is due to tree in pixels not classified as forested.

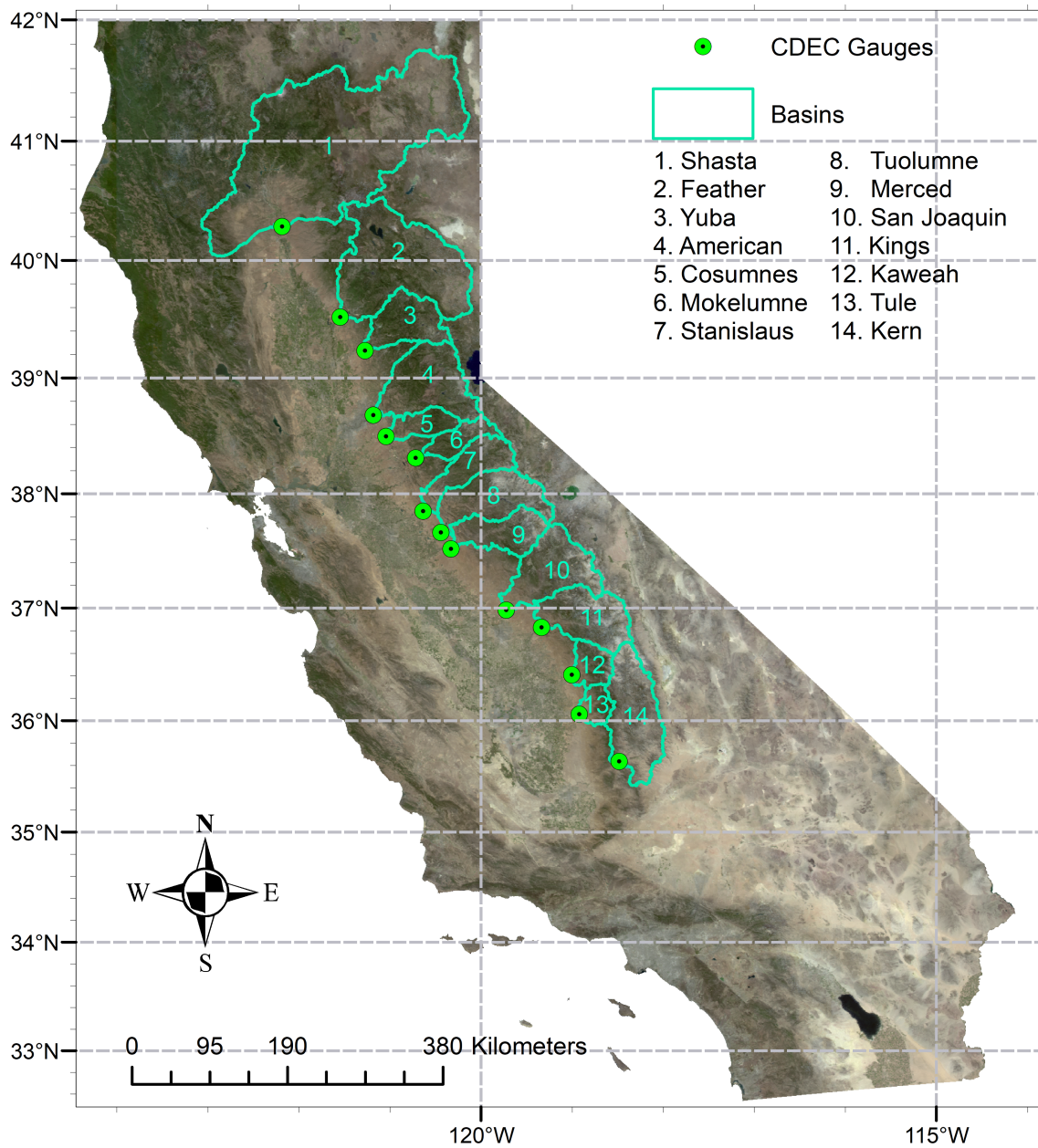


Figure 4.1: Site map of California, USA, with the boundaries of the 14 basins used and the locations of stream gauges where unimpaired runoff is calculated.

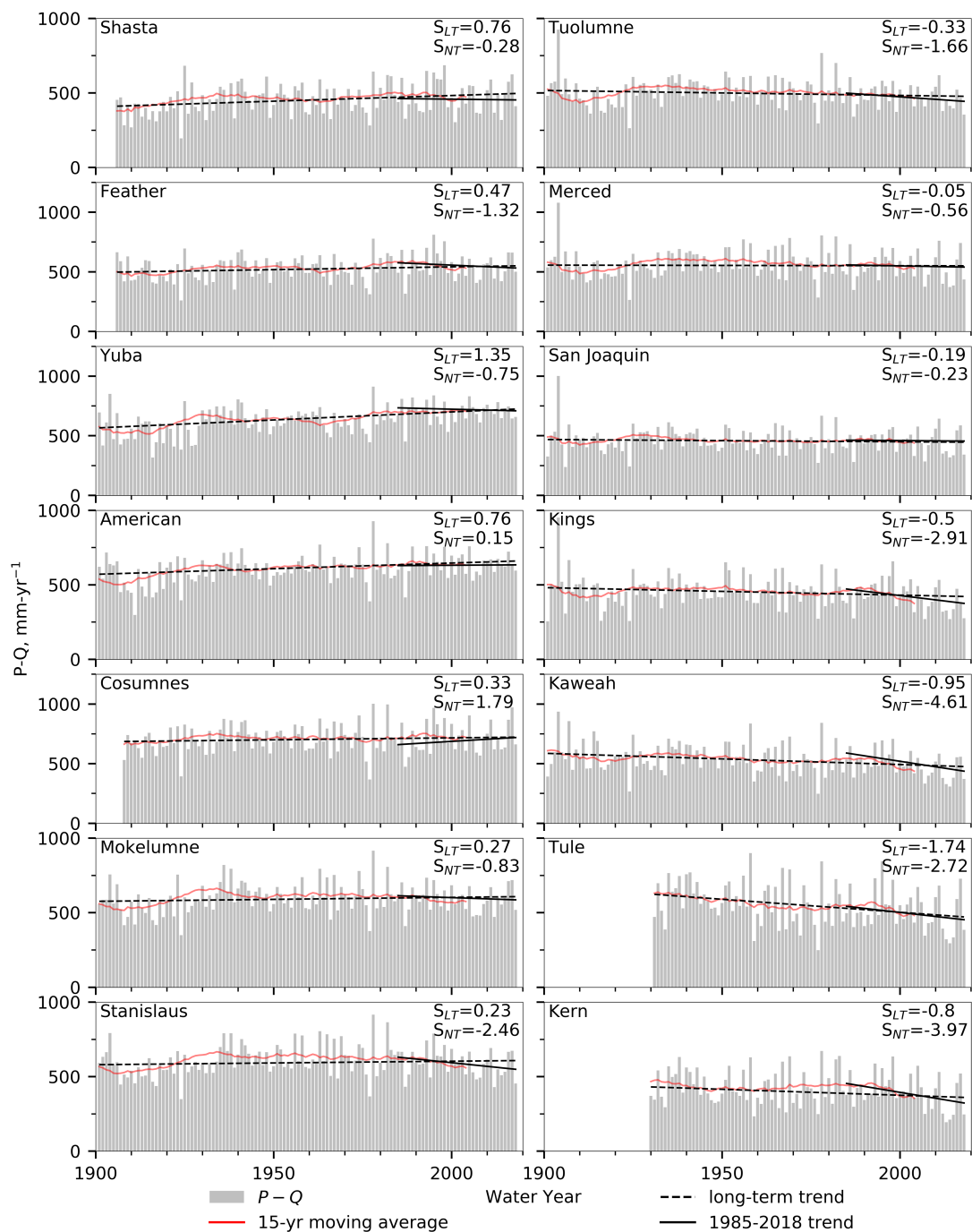


Figure 4.2: Time-series plots of $P - Q$ for the entire record and ET (1985-2018). Red line is the 15-year moving average, solid black line is the long-term (LT, entire time-series) Theil-Sens slope, and the dashed black line is the near-term (NT, 34-year) Theil-Sens slope values in mm-yr⁻¹.

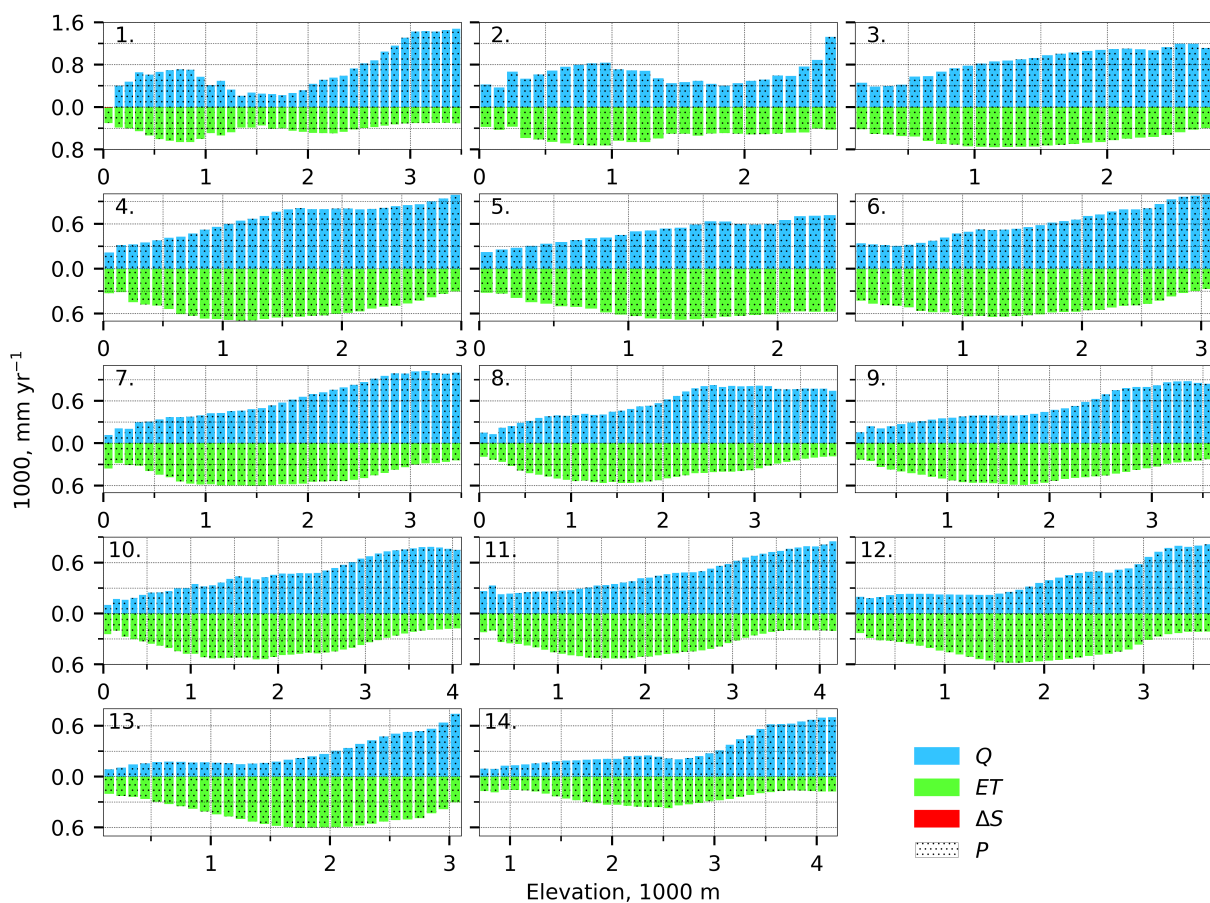


Figure 4.3: Basin-scale water balance by elevation for each basin. Numbers correspond to the basins from north to south as presented in Figure 4.1. These were calculated following Bales et al. (2018), where height above the bar is runoff and height below the bar is evapotranspiration.

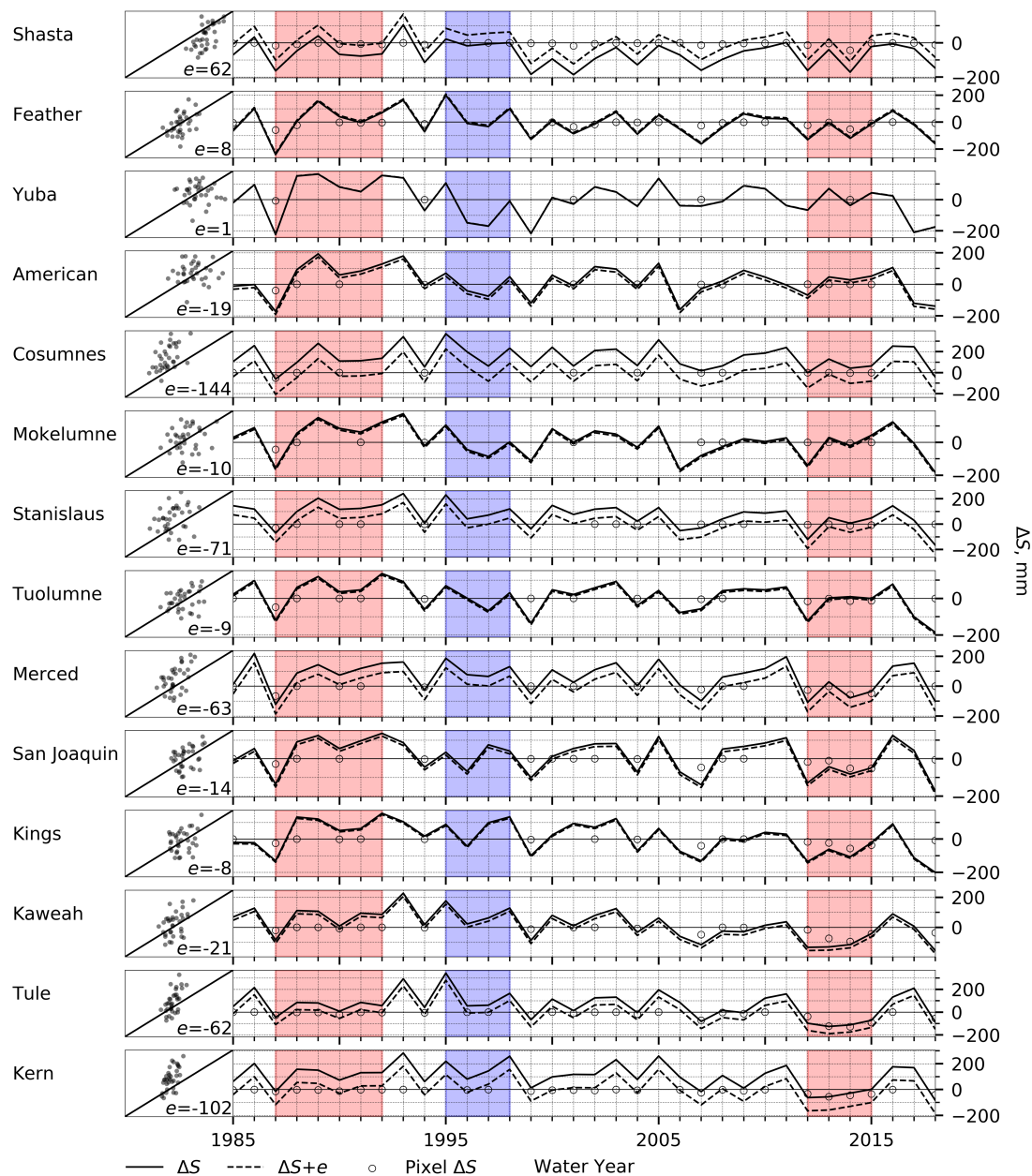


Figure 4.4: Time-series of annual change in storage (ΔS , solid line), ΔS plus the offset, e (dashed line), and the area-weighted sum of negative precipitation (P) minus evapotranspiration (ET) pixels from the annual basin maps (circles). ΔS was calculated as $P - Q - ET$, and e was calculated as the offset of the ET vs. $P - Q$ scatter plots from the 1:1 line (first column).

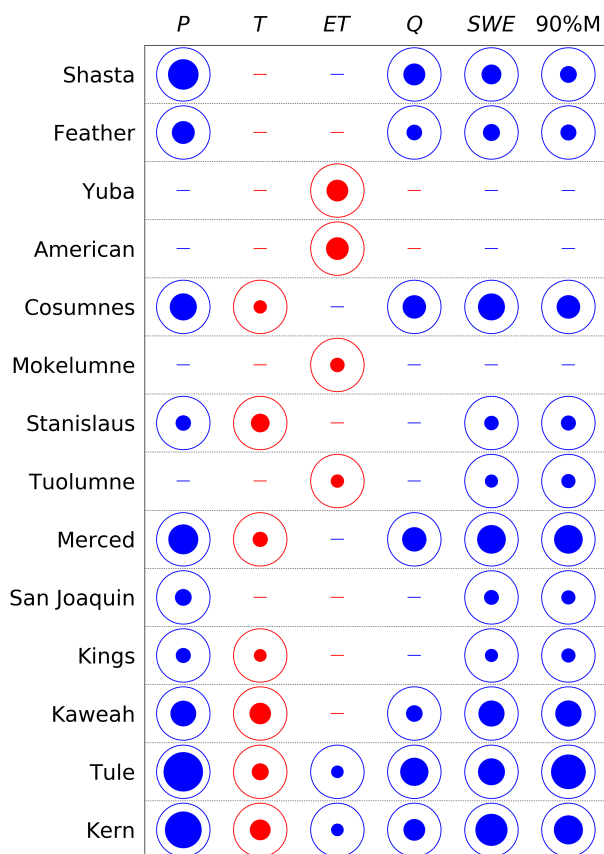


Figure 4.5: Basin-scale trends between change in storage with precipitation (P), temperature (T), evapotranspiration (ET), unimpaired runoff (Q), snow-water equivalent (SWE), and the timing of 90 percent melt from peak SWE ($90\%M$). Filled-inner circles represent p -values ≤ 0.1 and lines are p -values > 0.1 . Colors represent a positive (blue) or negative (red) trend. Marker size is the absolute value of Kendall's tau (τ), where the perimeter circle represents a τ of 1.





















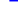




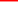

































































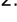
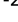








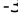








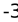

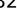

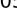
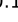
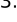




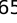


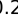
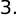
	LT $P - Q$	NT $P - Q$	P	T	ET	Q	SWE	90%M	ΔS
Shasta	0.76 	-0.32 	0.68 	0.04 	1.22 	-0.19 	-0.35 	0.15 	-1.32 
Feather	0.47 	-1.32 	0.77 	0.04 	1.23 	0.49 	-1.72 	-0.25 	-2.67 
Yuba	1.35 	-0.76 	3.63 	0.04 	2.32 	1.27 	-1.43 	-0.42 	-3.52 
American	0.76 	0.14 	3.08 	0.03 	2.18 	1.98 	-2.15 	-0.4 	-1.7 
Cosumnes	0.33 	1.79 	3.25 	0.02 	3.02 	2.6 	-0.82 	-0.44 	-1.71 
Mokelumne	0.27 	-0.83 	0.6 	0.05 	1.86 	3.03 	-1.24 	-0.48 	-2.88 
Stanislaus	0.23 	-2.46 	0.95 	0.05 	1.74 	3.53 	0.44 	0.13 	-3.57 
Tuolumne	-0.33 	-1.66 	1.08 	0.05 	1.12 	2.73 	-0.14 	-0.07 	-2.23 
Merced	-0.05 	-0.56 	0.61 	0.05 	1.51 	1.83 	-0.35 	-0.22 	-2.27 
San Joaquin	-0.19 	-0.23 	-0.49 	0.05 	1.52 	1.15 	-1.69 	-0.33 	-1.52 
Kings	-0.5 	-2.91 	-2.11 	0.06 	0.99 	0.13 	-4.7 	-0.36 	-4.17 
Kaweah	-0.95 	-4.61 	-3.62 	0.08 	0.86 	0.07 	-2.93 	-0.23 	-5.54 
Tule	-1.74 	-2.72 	-3.53 	0.07 	0.82 	-0.16 	-1.05 	-0.12 	-3.47 
Kern	-0.8 	-3.97 	-4.66 	0.07 	-0.65 	-0.47 	-4.21 	-0.26 	-3.28 

Figure 4.6: Time-series analysis of ΔS and water-cycle-related features. Columns LT $P - Q$, NT $P - Q$, P , T , ET , Q , SWE, 90%M, and ΔS are time series trend analyses for Long-term $P - Q$, Near-term (34-year) $P - Q$, precipitation, temperature, evapotranspiration, runoff, snow-water equivalent and the timing of 90 percent melt from peak SWE, respectively. Circles represent p-value ≤ 0.1 and lines are p-values > 0.1 . r^2 values were calculated via linear regression and slopes, m, are Theil-Sens slopes with units of $^{\circ}\text{C}/\text{yr}$ for T, otherwise mm yr^{-1} .

4.6 Bibliography

- Arkley, R. J. (1981). Soil Moisture Use by Mixed Conifer Forest in a Summer-Dry Climate. *Soil Science Society of America Journal*, 45(2):423.
- Bales, R. C., Goulden, M. L., Hunsaker, C. T., Conklin, M. H., Hartsough, P. C., O'Geen, A. T., Hopmans, J. W., Safeeq, M., O'Geen, A. T., Hopmans, J. W., and Safeeq, M. (2018). Mechanisms controlling the impact of multi-year drought on mountain hydrology. *Scientific Reports*, 8(1):690.
- Bales, R. C., Molotch, N. P., Painter, T. H., Dettinger, M. D., Rice, R., and Dozier, J. (2006). Mountain hydrology of the western United States. *Water Resources Research*, 42(8).
- Biederman, J. A., Scott, R. L., Arnone III, J. A., Jasoni, R. L., Litvak, M. E., Moreo, M. T., Papuga, S. A., Ponce-Campos, G. E., Schreiner-McGraw, A. P., and Vivoni, E. R. (2018). Shrubland carbon sink depends upon winter water availability in the warm deserts of North America. *Agricultural and Forest Meteorology*, 249:407–419.
- Dahlgren, R. A., Saigusa, M., and Ugolini, F. C. (2004). The nature, properties and management of volcanic soils. *Advances in agronomy*, 82(03):113–182.
- Daly, C., Halbleib, M., Smith, J. I., Gibson, W. P., Doggett, M. K., Taylor, G. H., Curtis, J., and Pasteris, P. P. (2008). Physiographical sensitive mapping of climatological temperature and precipitation across the conterminous United States. *International Journal of Climatology*, 28:2031–2064.
- Daly, C., Neilson, R. P., and Phillips, D. L. (1994). A statistical-topographic model for mapping climatological precipitation over mountainous terrain. *Journal of Applied Meteorology*, 33(2):140–158.
- Famiglietti, J. S. (2014). The global groundwater crisis. *Nature Climate Change*, 4:945.

- Fellows, A. W. and Goulden, M. L. (2017). Mapping and understanding dry season soil water drawdown by California montane vegetation. *Ecohydrology*, 10(1):1–12.
- Fisher, J. B., DeBiase, T. A., Qi, Y., Xu, M., and Goldstein, A. H. (2005). Evapotranspiration models compared on a Sierra Nevada forest ecosystem. *Environmental Modelling & Software*, 20(6):783–796.
- Gleeson, T., Wada, Y., Bierkens, M. F. P., and van Beek, L. P. H. (2012). Water balance of global aquifers revealed by groundwater footprint. *Nature*, 488(7410):197–200.
- Goulden, M. L., Anderson, R. G., Bales, R. C., Kelly, A. E., Meadows, M., and Winston, G. C. (2012). Evapotranspiration along an elevation gradient in California’s Sierra Nevada. *Journal of Geophysical Research*, 117(G3):G03028.
- Goulden, M. L. and Bales, R. C. (2014). Mountain runoff vulnerability to increased evapotranspiration with vegetation expansion. *Proceedings of the National Academy of Sciences*, 111(39):14071–14075.
- Graham, R., Rossi, A., and Hubbert, R. (2010). Rock to regolith conversion: Producing hospitable substrates for terrestrial ecosystems. *GSA Today*, pages 4–9.
- Hawkins, B. A., Field, R., Cornell, H. V., Currie, D. J., Guégan, J.-F., Kaufman, D. M., Kerr, J. T., Mittelbach, G. G., Oberdorff, T., O’Brien, E. M., Porter, E. E., and Turner, J. R. G. (2003). ENERGY, WATER, AND BROAD-SCALE GEOGRAPHIC PATTERNS OF SPECIES RICHNESS. *Ecology*, 84(12):3105–3117.
- Holbrook, W. S., Riebe, C. S., Elwaseif, M., L. Hayes, J., Basler-Reeder, K., L. Harry, D., Malazian, A., Dosseto, A., C. Hartsough, P., and W. Hopmans, J. (2014). Geophysical constraints on deep weathering and water storage potential in the southern sierra critical zone observatory. *Earth Surface Processes and Landforms*, 39(3):366–380.

- Jones, J. R., Schwartz, J. S., Ellis, K. N., Hathaway, J. M., and Jawdy, C. M. (2015). Temporal variability of precipitation in the Upper Tennessee Valley. *Journal of Hydrology: Regional Studies*, 3:125–138.
- Kelly, A. E. and Goulden, M. L. (2016). A montane Mediterranean climate supports year-round photosynthesis and high forest biomass. *Tree Physiology*, 36(4):459–468.
- Kendall, M. G. (1955). *Rank correlation methods*. Hafner Publishing Co.
- Kirchner, P. B., Bales, R. C., Molotch, N. P., Flanagan, J., and Guo, Q. (2014). LiDAR measurement of seasonal snow accumulation along an elevation gradient in the southern Sierra Nevada, California. *Hydrology and Earth System Sciences*, 18(10):4261–4275.
- Knight, W. R. (1966). A Computer Method for Calculating Kendall's Tau with Ungrouped Data. *Journal of the American Statistical Association*, 61(314):436–439.
- Lewis, D. C. and Burgy, R. H. (1964). The Relationship between oak tree roots and groundwater in fractured rock as determined by tritium tracing. *Journal of Geophysical Research*, 69(12):2579–2588.
- Lundquist, J. D., Hughes, M., Henn, B., Gutmann, E. D., Livneh, B., Dozier, J., and Neiman, P. (2015). High-Elevation Precipitation Patterns: Using Snow Measurements to Assess Daily Gridded Datasets across the Sierra Nevada, California*. *Journal of Hydrometeorology*, 16(4):1773–1792.
- Manga, M. (1999). On the timescales characterizing groundwater discharge at springs. *Journal of Hydrology*, 219(1-2):56–69.
- Mann, H. B. (1945). Nonparametric Tests Against Trend. *Econometrica*, 13(3):245.
- Margulis, S. A., Cortés, G., Giroto, M., and Durand, M. (2016). A Landsat-Era Sierra Nevada Snow Reanalysis (19852015). *Journal of Hydrometeorology*, 17(4):1203–1221.

- Milly, P. C. D., Betancourt, J., Falkenmark, M., Hirsch, R. M., Kundzewicz, Z. W., Lettenmaier, D. P., and Stouffer, R. J. (2008). Stationarity Is Dead: Whither Water Management? *Science*, 319(5863):573–574.
- Qualley, G. T., Buer, S. M., and Nemeth, S. E. (2000). Derivation of unimpaired runoff in the cooperative snow surveys program. Technical report, California Department of Water Resources.
- Rana, G. and Katerji, N. (2000). Measurement and estimation of actual evapotranspiration in the field under Mediterranean climate: a review. *European Journal of Agronomy*, 13(2-3):125–153.
- Rungee, J. P., Bales, R. C., and Goulden, M. L. (2018). Evapotranspiration response to multi-year dry periods in the semi-arid western United States. *Hydrological Processes*.
- Rungee, J. P., Ma, Q., Bales, R. C., and Goulden, M. L. (in review). Closing the mountain water balance: evapotranspiration patterns and uncertainties in tributaries to Californias Central Valley, USA. *Water Resources Research*.
- Sen, P. K. (1968). Robustness of Some Nonparametric Procedures in Linear Models. *The Annals of Mathematical Statistics*, 39(6):1913–1922.
- Shi, T.-T., Guan, D.-X., Wu, J.-B., Wang, A.-Z., Jin, C.-J., and Han, S.-J. (2008). Comparison of methods for estimating evapotranspiration rate of dry forest canopy: Eddy covariance, Bowen ratio energy balance, and Penman-Monteith equation. *Journal of Geophysical Research*, 113(D19):D19116.
- SNC (2017). Annual Report.
- Su, Y., Bales, R. C., Ma, Q., Nydick, K., Ray, R. L., Li, W., and Guo, Q. (2017). Emerging Stress and Relative Resiliency of Giant Sequoia Groves Experiencing Multiyear Dry Periods in a Warming Climate. *Journal of Geophysical Research: Biogeosciences*, 122(11):3063–3075.

- Sulla-Menashe, D., Friedl, M. A., and Woodcock, C. E. (2016). Sources of bias and variability in long-term Landsat time series over Canadian boreal forests. *Remote Sensing of Environment*, 177:206–219.
- Swenson, S. C. and Milly, P. C. D. (2006). Climate model biases in seasonality of continental water storage revealed by satellite gravimetry. *Water Resources Research*, 42(3).
- Tague, C. and Grant, G. E. (2009). Groundwater dynamics mediate low-flow response to global warming in snow-dominated alpine regions. *Water Resources Research*, 45(7):W07421.
- Tague, C. and Peng, H. (2013). The sensitivity of forest water use to the timing of precipitation and snowmelt recharge in the California Sierra: Implications for a warming climate. *Journal of Geophysical Research: Biogeosciences*, 118(2):875–887.
- Theil, H. (1950). A rank-invariant method of linear and polynomial regression analysis, Part 3. In *Proceedings of Koninklijke Nederlandse Akademie van Wetenschappen A*, pages 1397—1412.
- Thomas, A. C., Reager, J. T., Famiglietti, J. S., and Rodell, M. (2014). A GRACE-based water storage deficit approach for hydrological drought characterization. *Geophysical Research Letters*, 41:1537 – 1545.
- Tree Mortality Task Force (2018). Tree Mortality: Facts and Figures.
- Wang, D. and Alimohammadi, N. (2012). Responses of annual runoff, evaporation, and storage change to climate variability at the watershed scale. *Water Resources Research*, 48(5).
- Warren, J. and Gilbert, R. O. (1988). Statistical Methods for Environmental Pollution Monitoring. *Technometrics*, 30(3):348.

Yue, S., Pilon, P., and Cavadias, G. (2002). Power of the MannKendall and Spearman's rho tests for detecting monotonic trends in hydrological series. *Journal of Hydrology*, 259(1-4):254–271.

Chapter 5

Conclusion

This dissertation emphasized the importance and benefits of accurate measurements of evapotranspiration for both local analyses and as a tool for distributing evapotranspiration across the landscape. In Chapter 2 we provide the first eddy-covariance region-scale assessment of how evapotranspiration varies by climate and vegetation type in the semi-arid western United States. On average, over 50% of annual evapotranspiration in the Mediterranean climate sites, which receive most precipitation during the winter, is supported by subsurface water storage versus less than 30% in sites experiencing a summer monsoon. The Mediterranean climate sites are also more susceptible to multi-year dry periods but have access to a vast amount of subsurface plant-accessible water storage, where one mixed-forest site withdrew over 530 mm of storage over the course of a 4-year drought, and evergreen needleleaf forest sites showing no response. Critical drawdown thresholds were also examined for all sites observing multi-year dry periods that showed a significant decrease in annual evapotranspiration. Critical drawdown thresholds range from 38 to 334 mm with high variability both within and across vegetation types. Lastly, it was found that a transition from snow to rain could increase dependency on storage by as much as 20% at sites that are currently energy limited. These findings can be used to better estimate the response of evapotranspiration during multi-year dry periods, improving water resources management drought strategies.

Chapter 3 used the California flux towers from Chapter 2 to expand upon current methods for distributing evapotranspiration across the landscape, which generally only use a remotely sensed vegetation index, by incorporated climatic variables and vegetation type. Root-mean-squared error was reduced by 31-50% and was relatively insensitive to input variable resolution. The spatial evapotranspiration product showed that evapotranspiration was greatest in the northern basin, and while decreasing in magnitude with latitude peak evapotranspiration occurred at higher elevations. Further, the product showed that runoff was mostly derived below the rain-snow transition as rain grossly exceeding evapotranspiration in the northern seven basins, and above the rain-snow transition as snowmelt in areas where evapotranspiration is energy limited in the southern seven basins. It is likely that runoff in the northern basins will be more vulnerable and respond more quickly to climate warming due to evapotranspiration being energy limited, whereas the steep elevation gradient in the southern basins will provide some buffer to warming. Comparing the distribution of flux towers to the precipitation-temperature space revealed poor representation of all extremes except hot-dry areas, leading to unknown uncertainties where evapotranspiration is expected to be highest. This study provides an instance of how improved spatial products can contribute to the deciphering of water-balance-component variability within a region and expresses the need for improved infrastructure for better management tools.

Chapter 4 used the evapotranspiration product developed in Chapter 3 to perform a long-term water-balance calculation for the 14 river basins draining into California's Central Valley and assessed the interannual variability subsurface water storage. The time-series analysis showed that change in storage (ΔS) has been mostly decreasing over the past 34 years and will likely continue unless evapotranspiration demand is reduced. Comparing how storage varies by basin along their elevation gradients showed that the lower to mid elevations appear the most vulnerable to significant withdrawals from storage when there is a water deficit. The basins could be binned into four groups based on the correlations between basin ΔS to water-balance components and climate variables and showed that the correlations between bins varied.

Overall, this dissertation demonstrates some of the benefits physical measurements of evapotranspiration provide for improving our ability close the water balance and better understand the role of ΔS and the subsequent ecosystem response, especially during climate extremes where withdrawals from storage can be significant. Specifically, that ΔS significantly supplements evapotranspiration during dry periods, making its interannual variability much greater. And moreover, that the decrease in the residual of precipitation and runoff with time shows that subsurface water storage is being over withdrawn leading to ecosystem water stress if no immediate efforts are taken to reduce evaporative demand. The studies herein were limited in spatial and temporal extent due mostly to the limited data availability from the current networks of eddy-covariance flux-towers. But as more data becomes available the scope of studies such as these can be expanded. It will be important in the future that new flux-tower installations strongly consider current flux-tower locations to improve temperature, precipitation, and vegetation representativeness. Quantifying uncertainty in spatially distributed water-balance-component products is a study question that needs to be investigated, as the error in any individual component can have widespread and long-lasting implications for water resources and forest management.

Appendix A

Appendices for Chapter 2

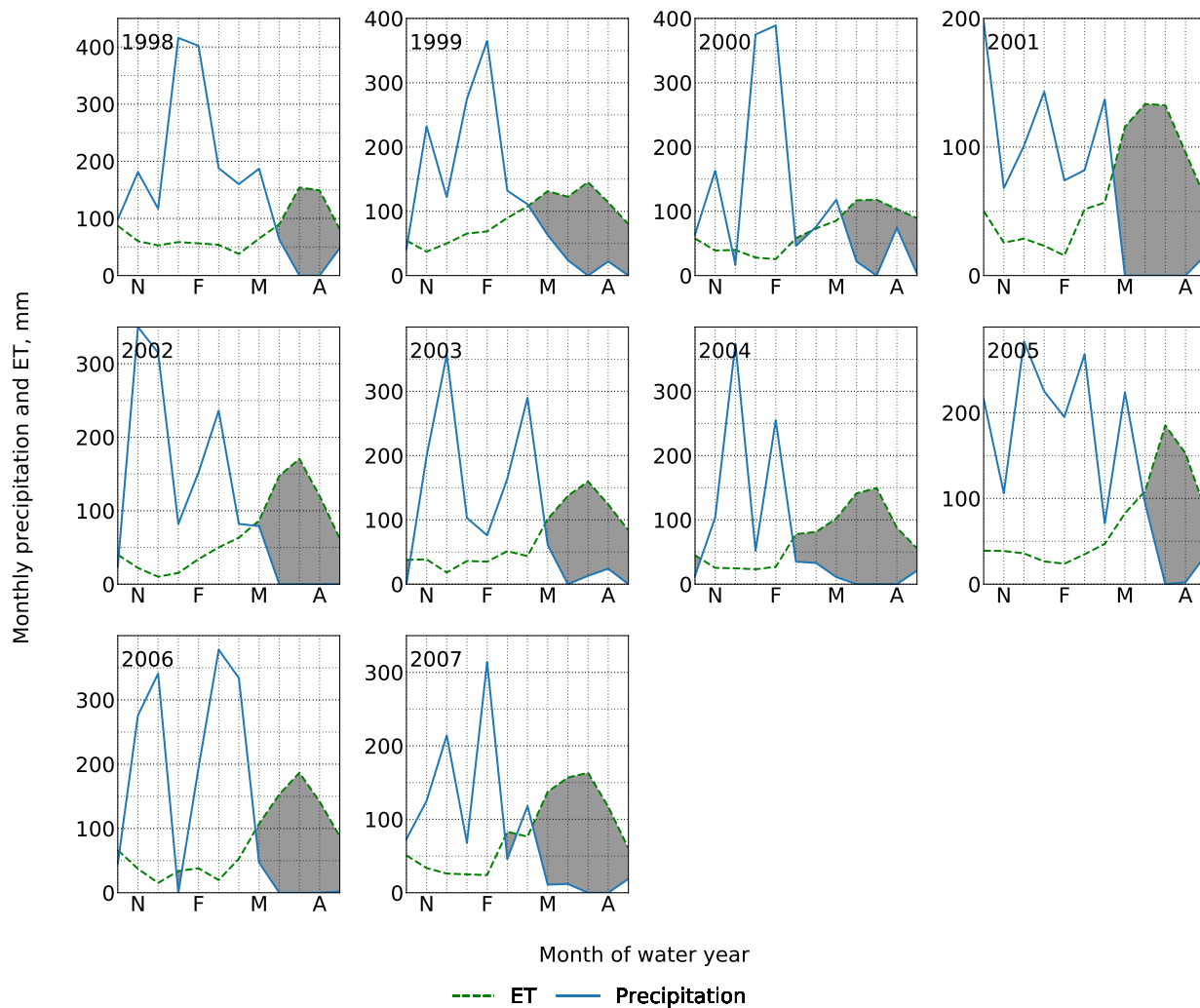


Figure A.1.1: US-Blo monthly evapotranspiration (ET) and precipitation for each water year

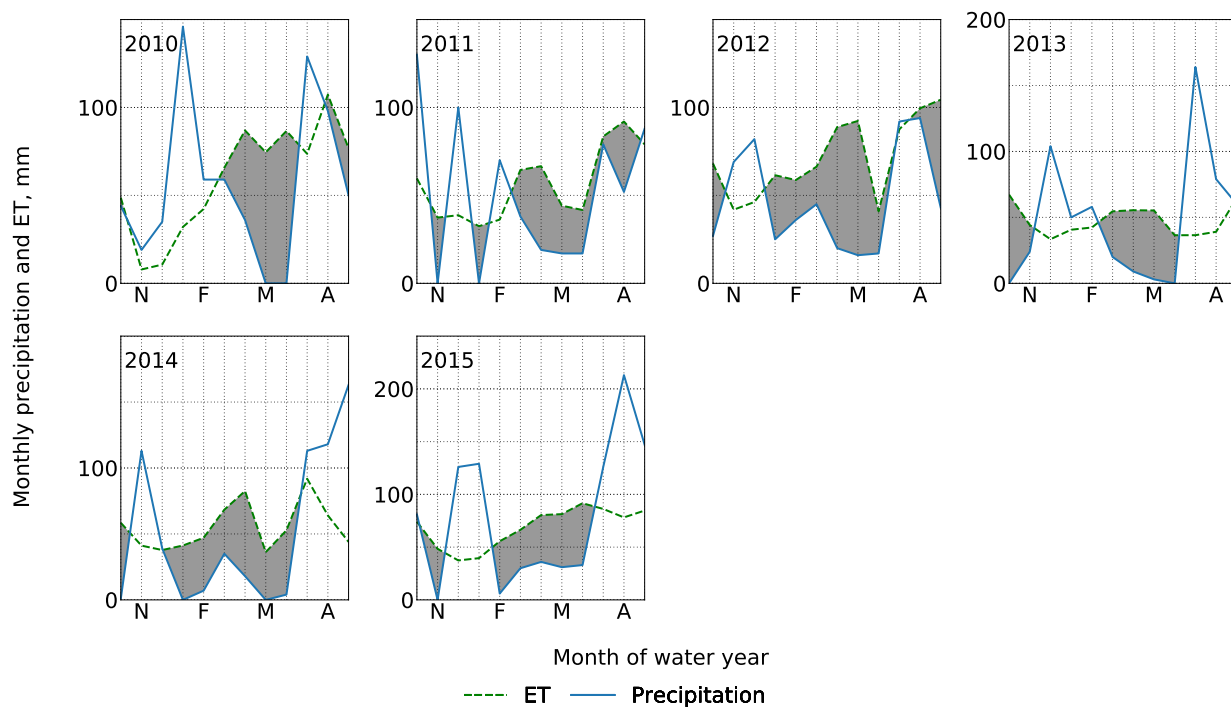


Figure A.1.2: MB monthly evapotranspiration (ET) and precipitation for each water year

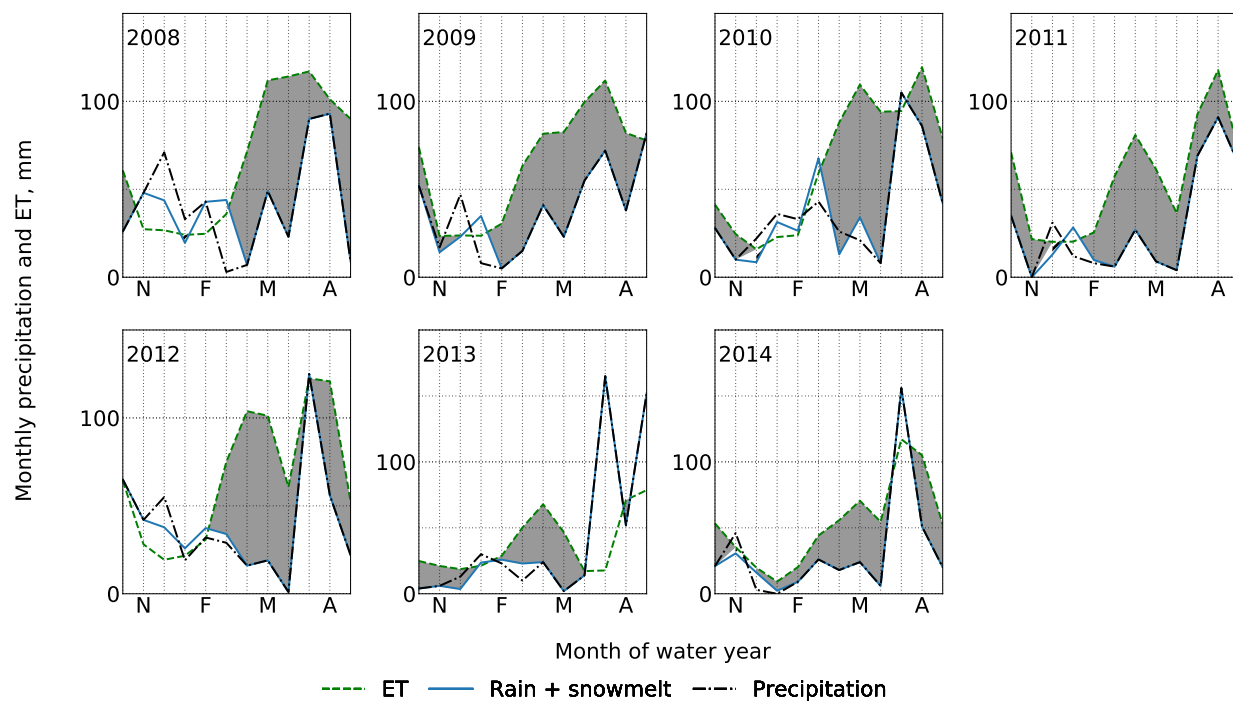


Figure A.1.3: US-Vcp monthly evapotranspiration (ET) and precipitation for each water year

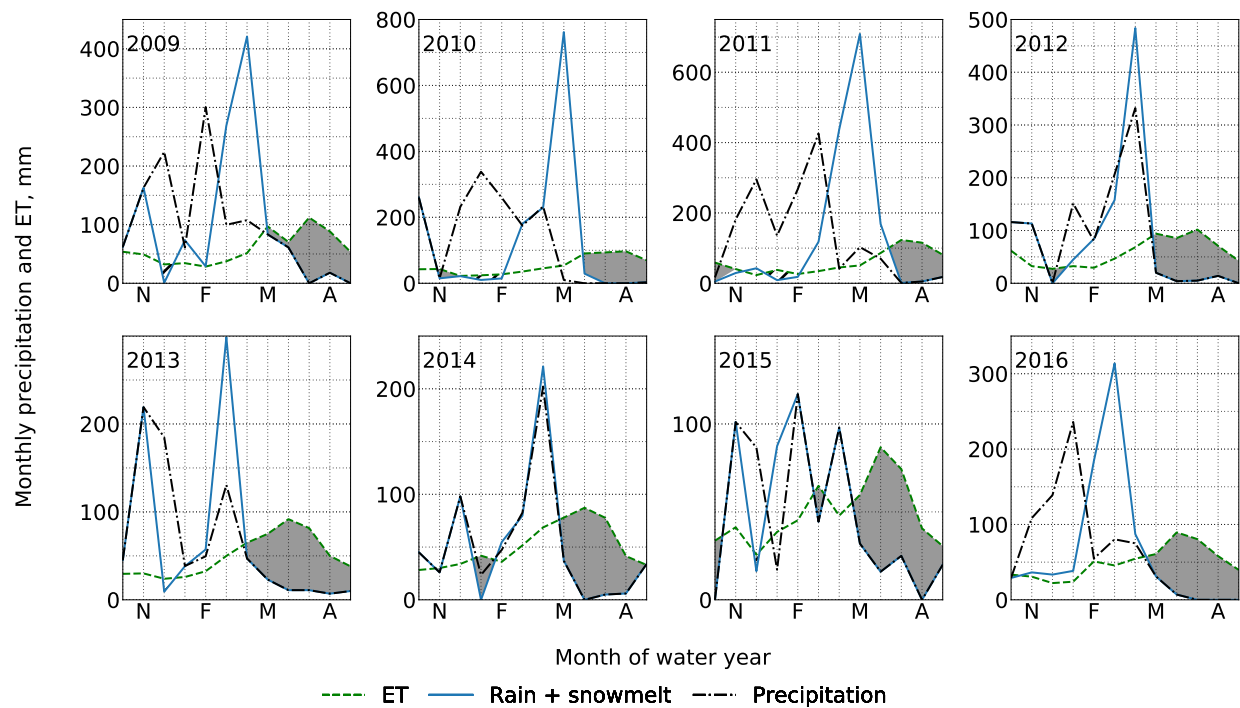


Figure A.1.4: US-CZ3 monthly evapotranspiration (ET) and precipitation for each water year

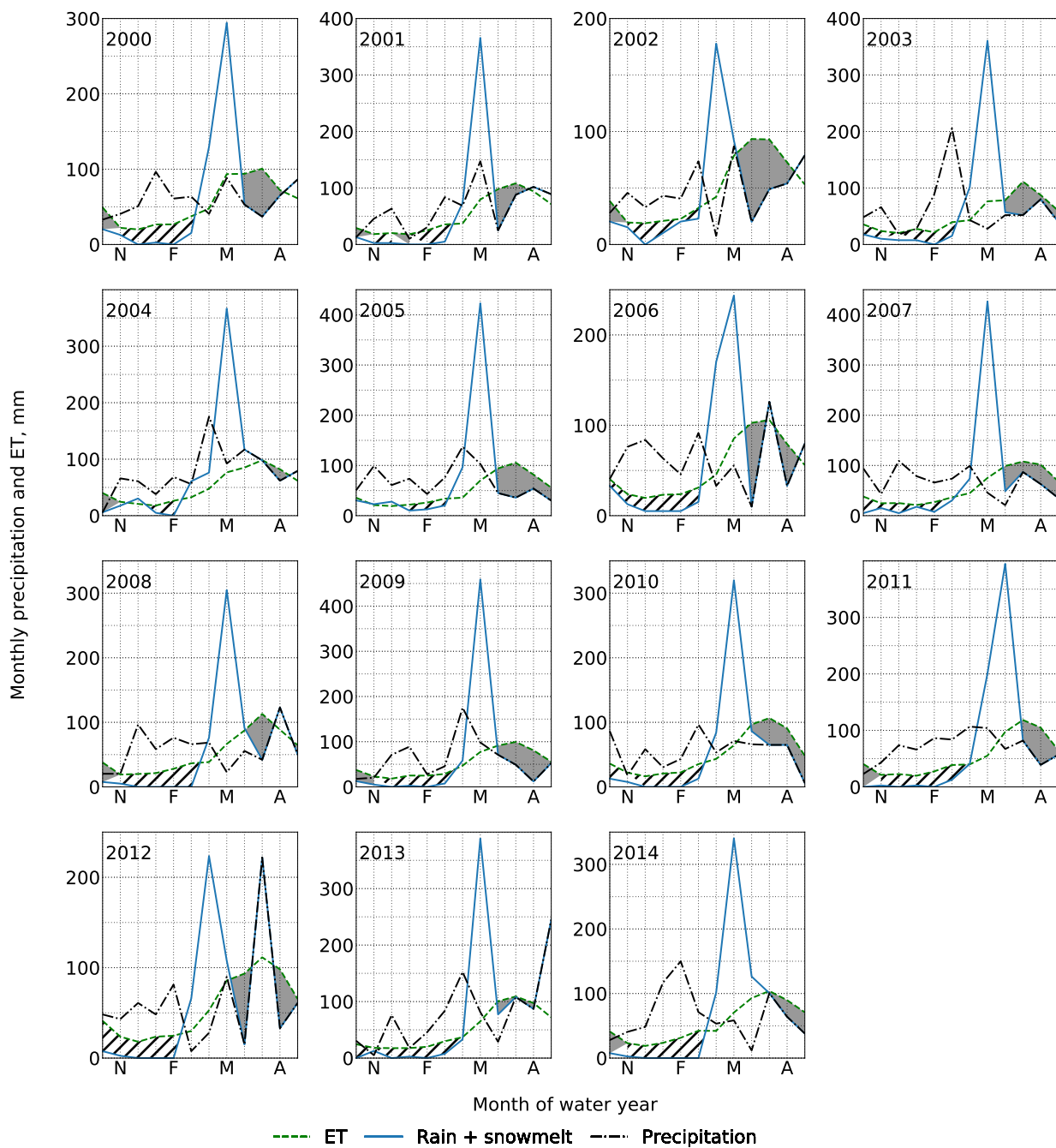


Figure A.1.5: US-NR1 monthly evapotranspiration (ET) and precipitation for each water year

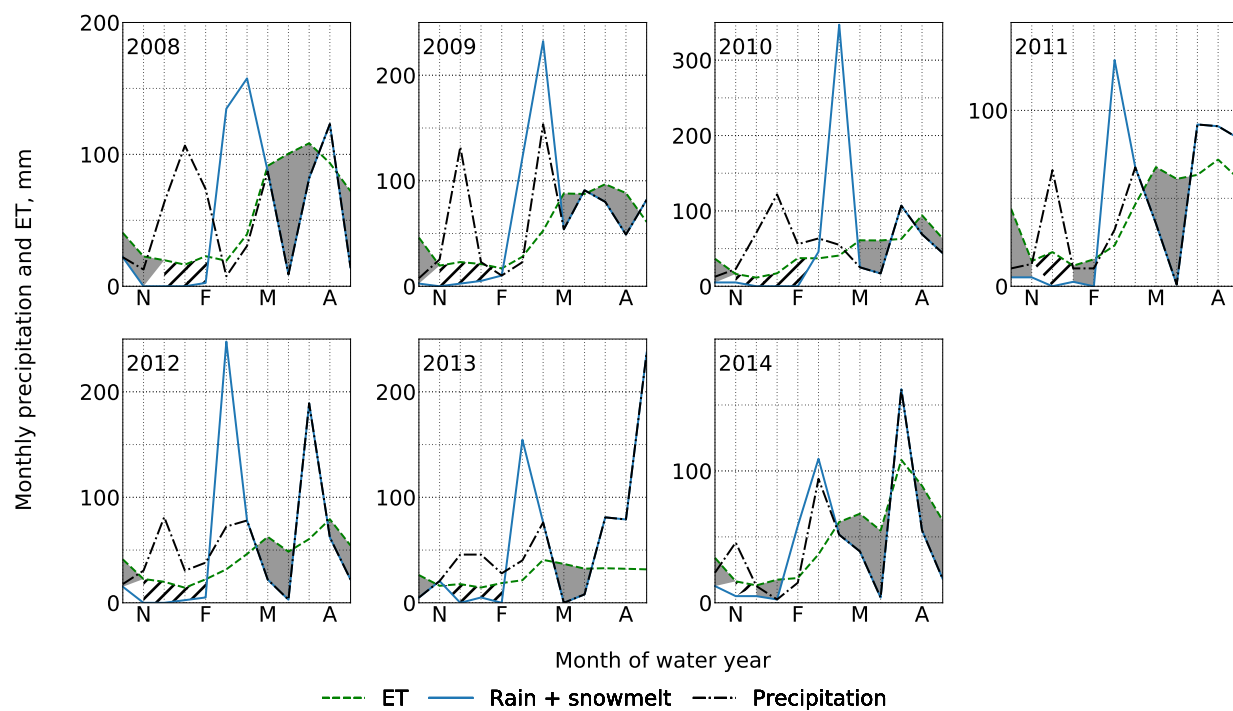


Figure A.1.6: US-Vcm monthly evapotranspiration (ET) and precipitation for each water year

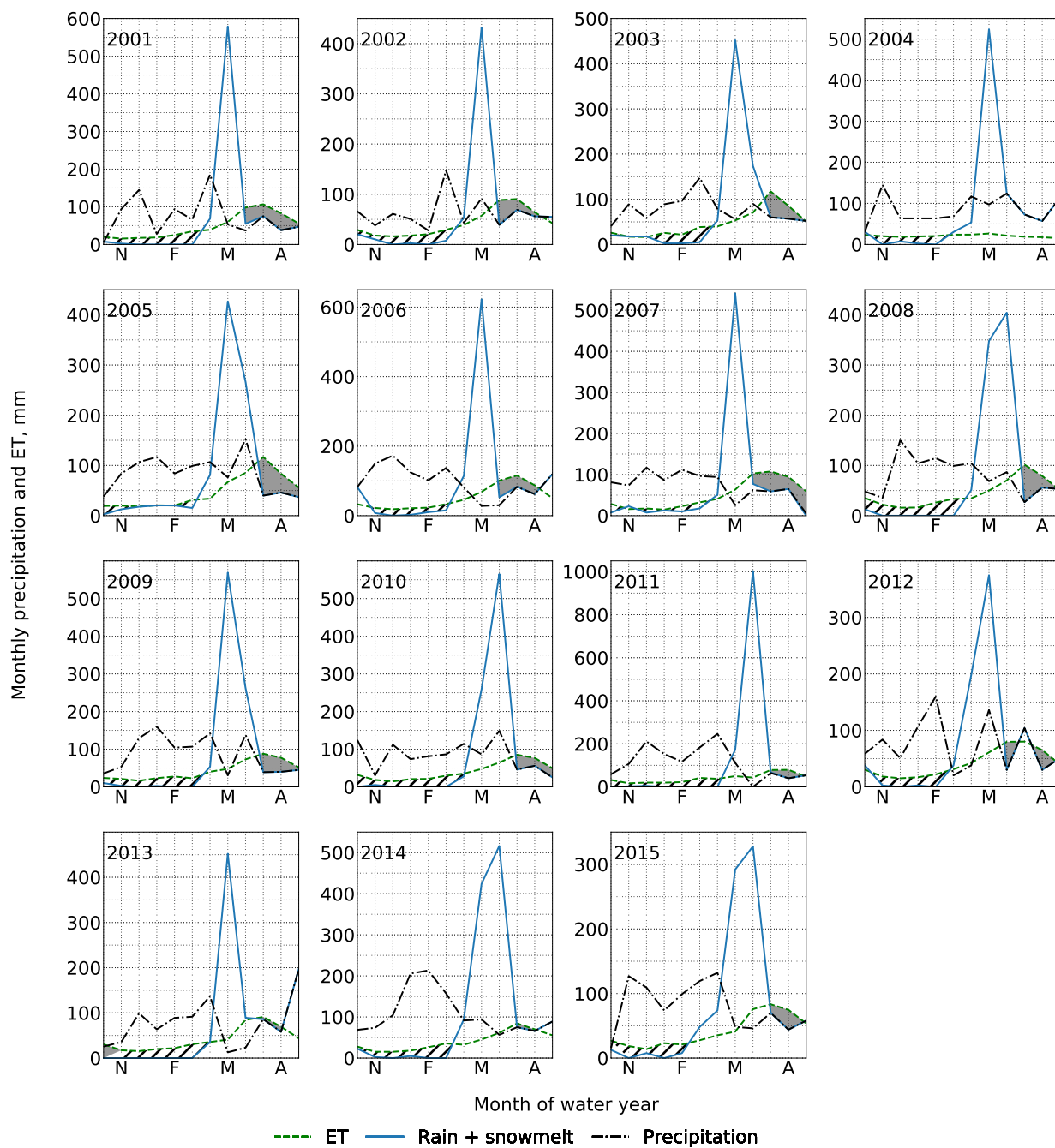


Figure A.1.7: US-GLE monthly evapotranspiration (ET) and precipitation for each water year

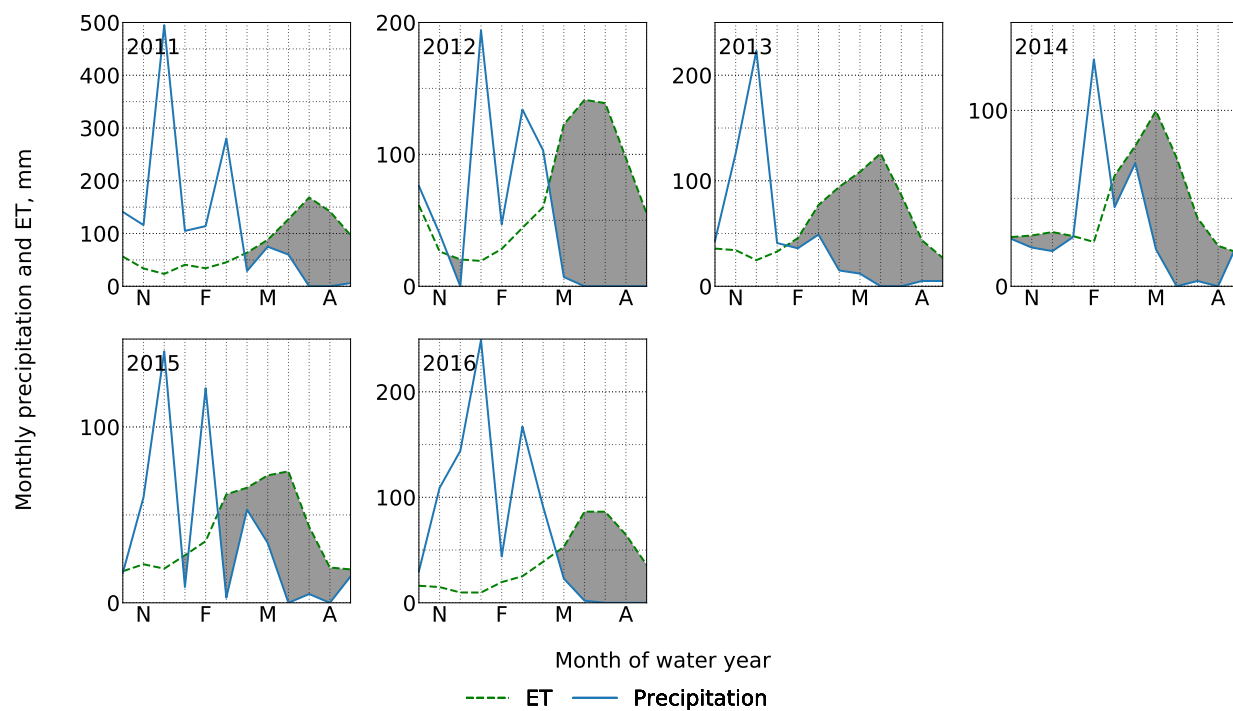


Figure A.1.8: US-CZ2 monthly evapotranspiration (ET) and precipitation for each water year

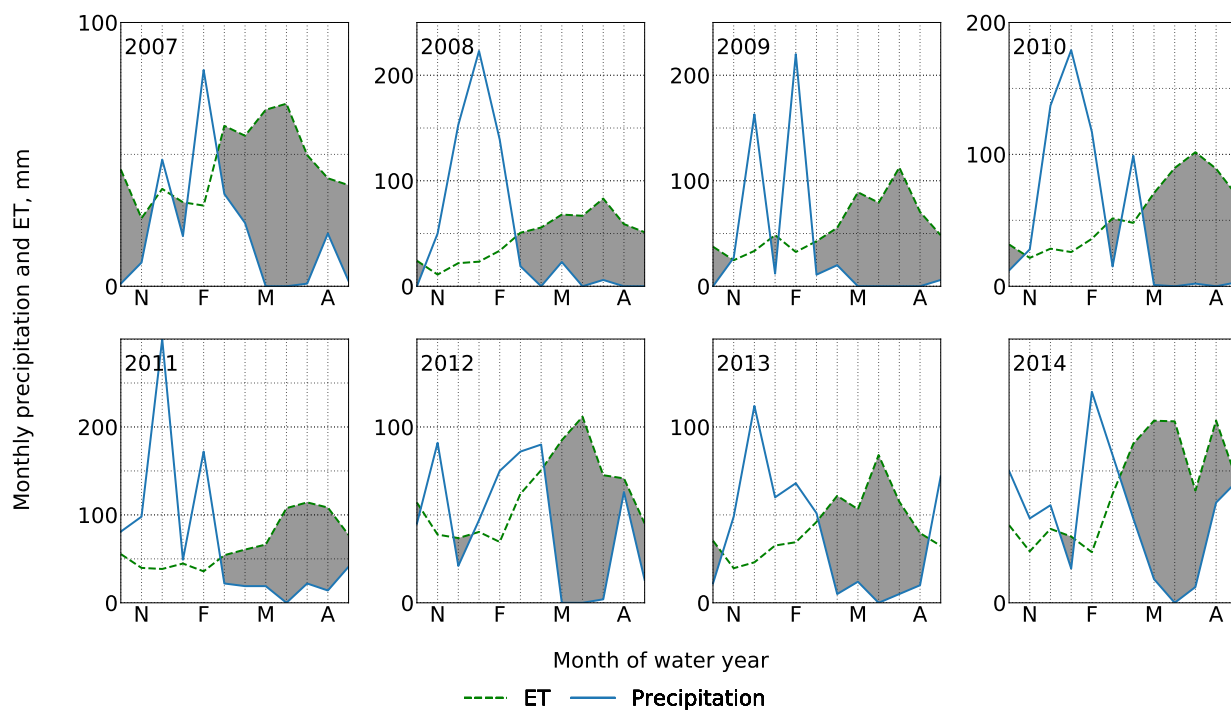


Figure A.1.9: US-SCf monthly evapotranspiration (ET) and precipitation for each water year

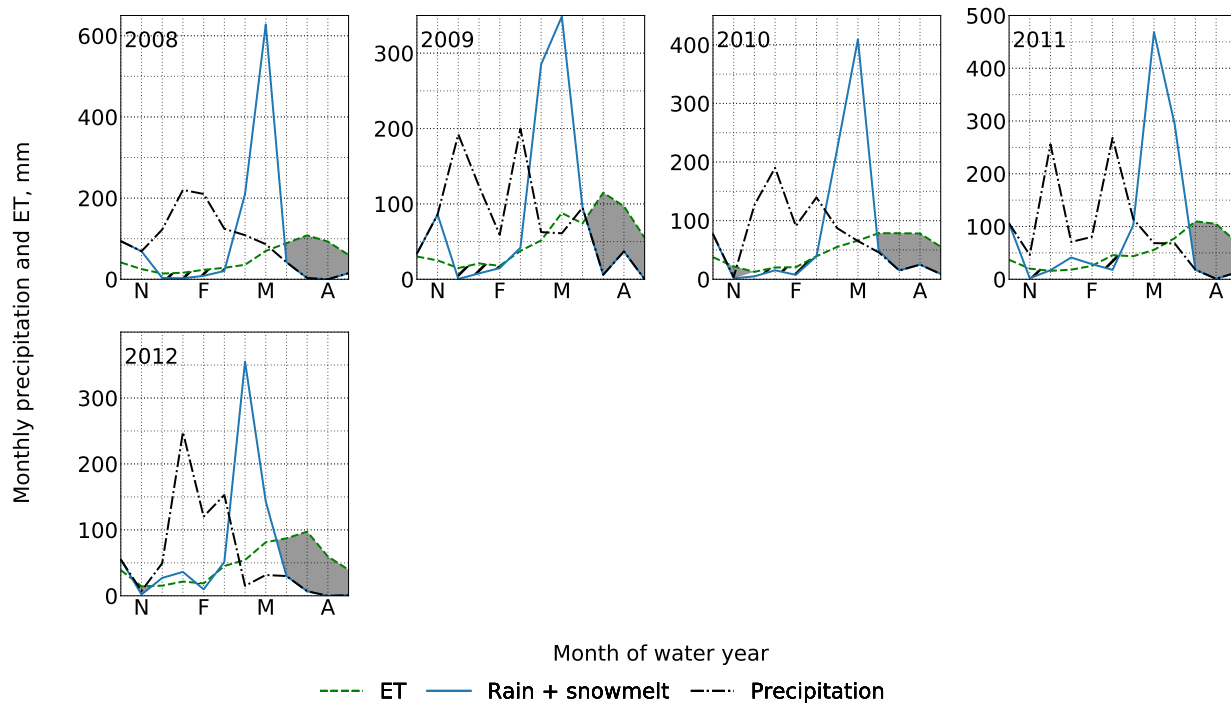


Figure A.1.10: RMEA monthly evapotranspiration (ET) and precipitation for each water year

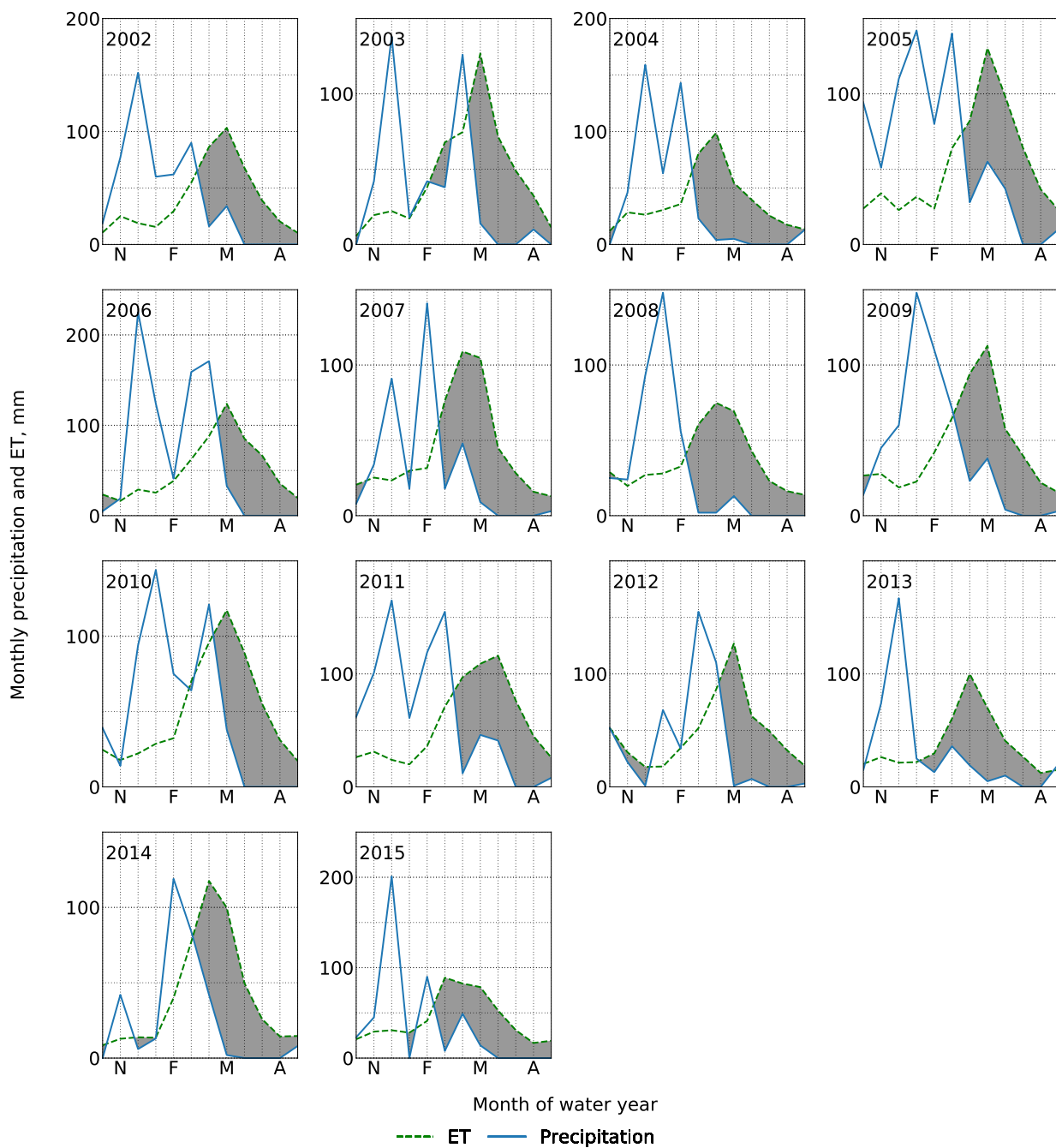


Figure A.1.11: US-Ton monthly evapotranspiration (ET) and precipitation for each water year

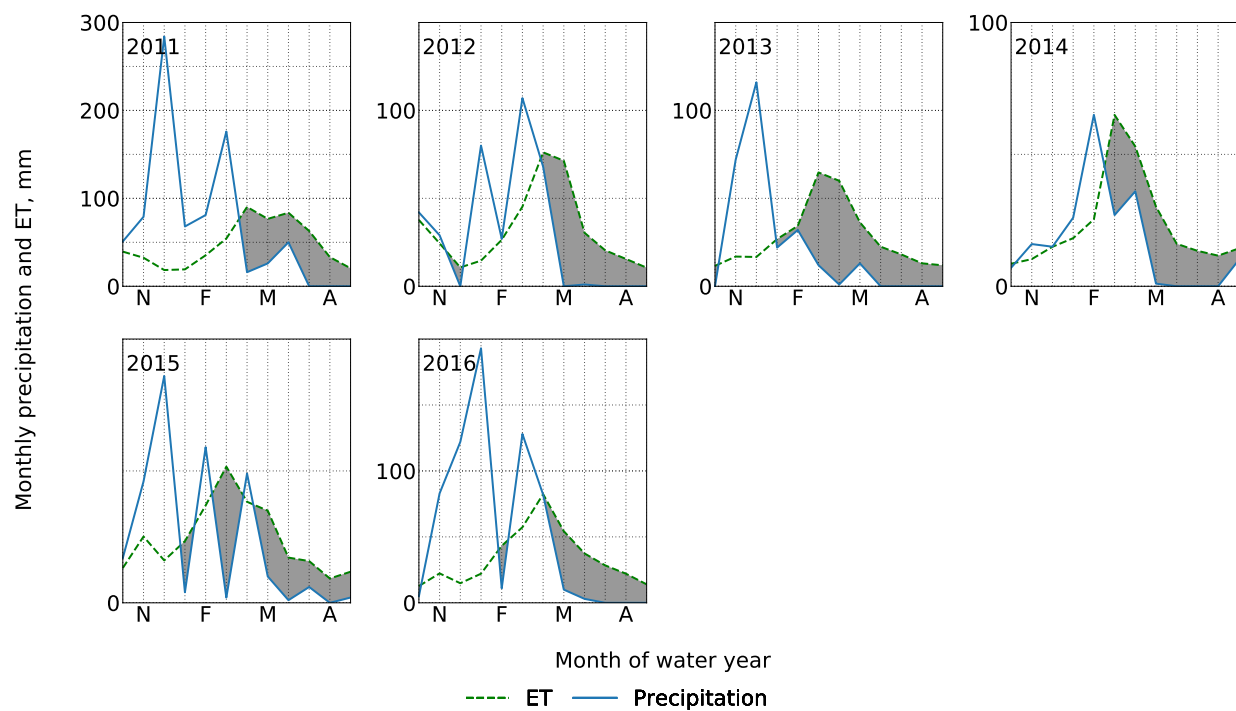


Figure A.1.12: US-CZ1 monthly evapotranspiration (ET) and precipitation for each water year

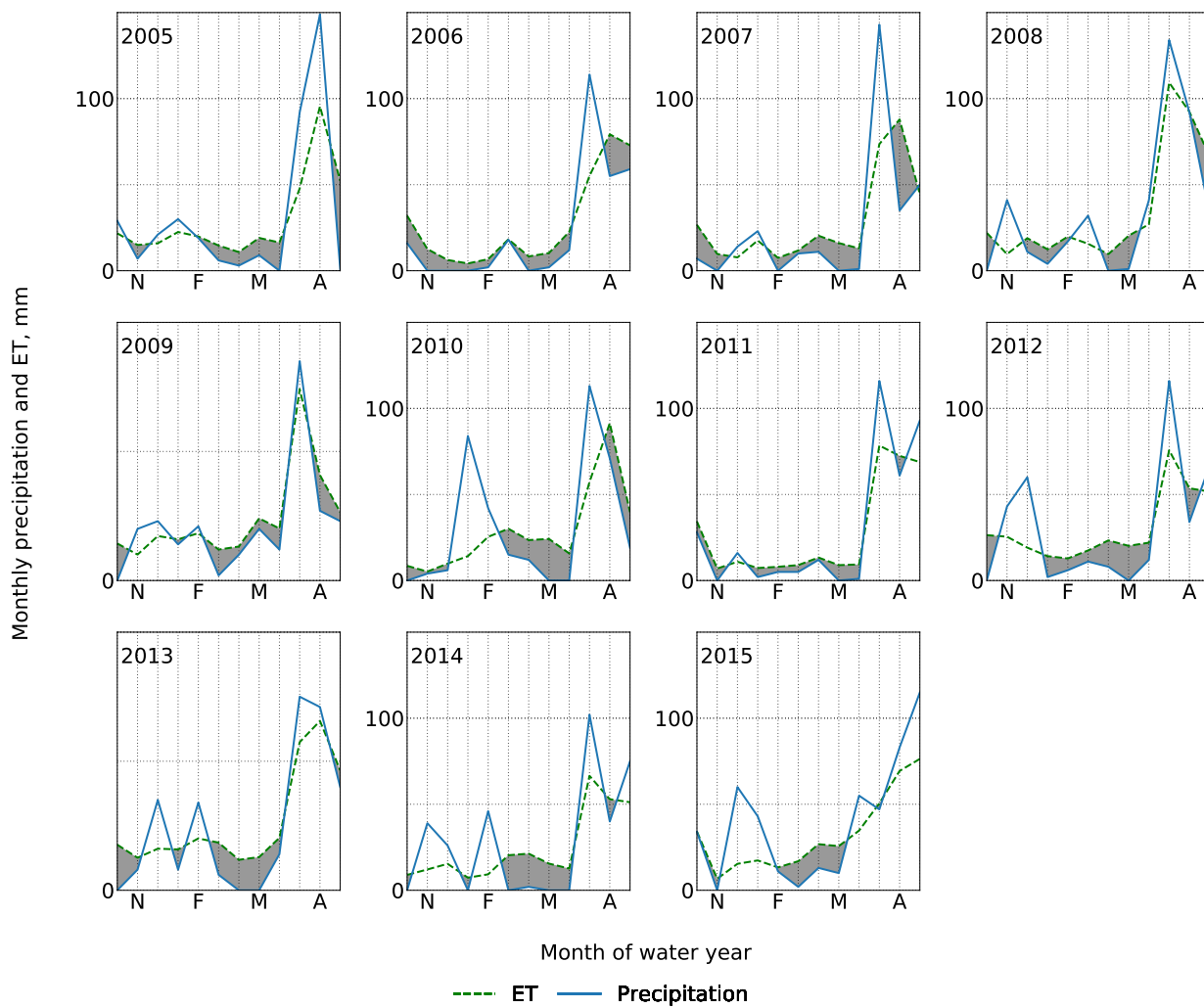


Figure A.1.13: US-SRM monthly evapotranspiration (ET) and precipitation for each water year

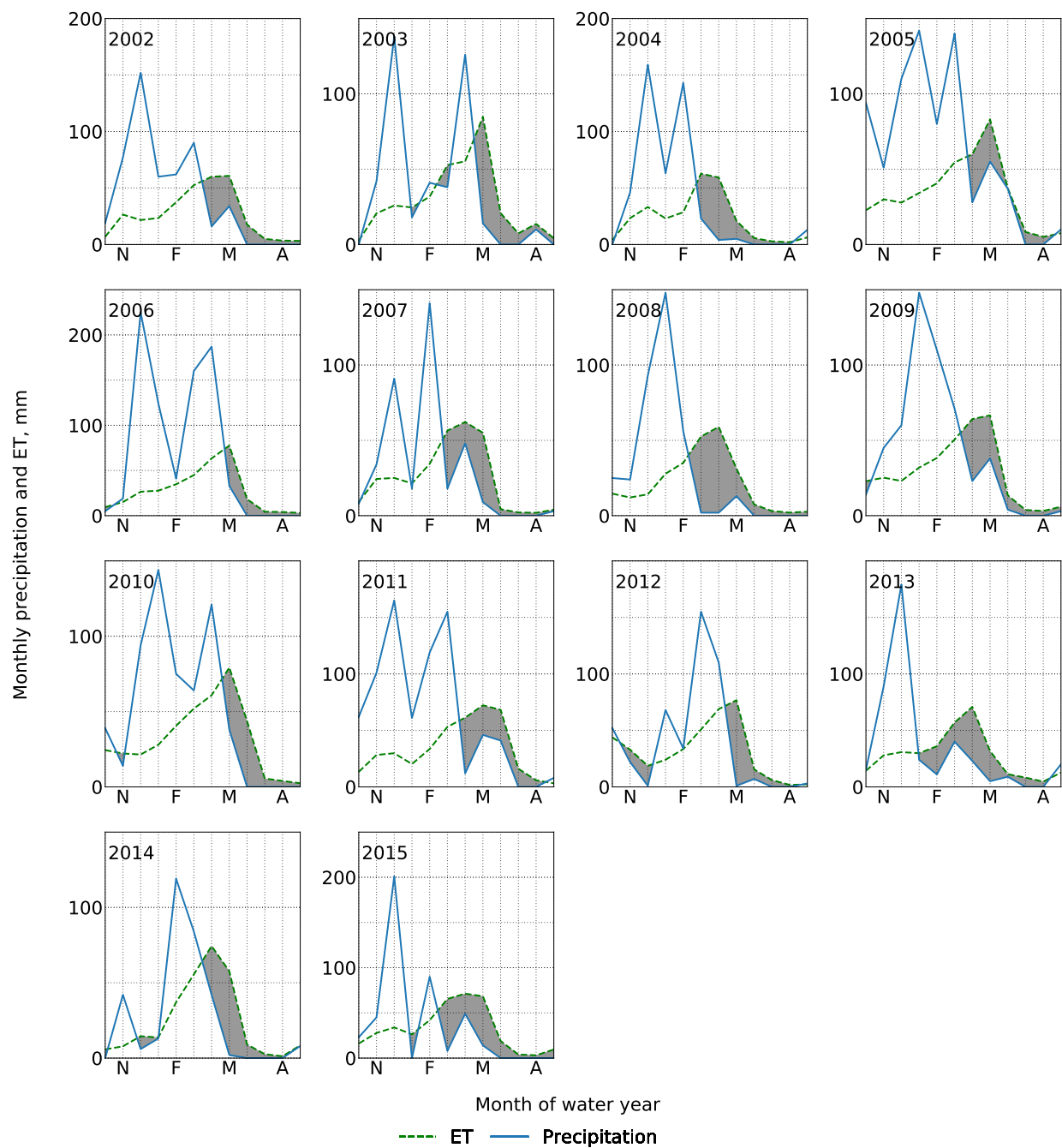


Figure A.1.14: US-Var monthly evapotranspiration (ET) and precipitation for each water year

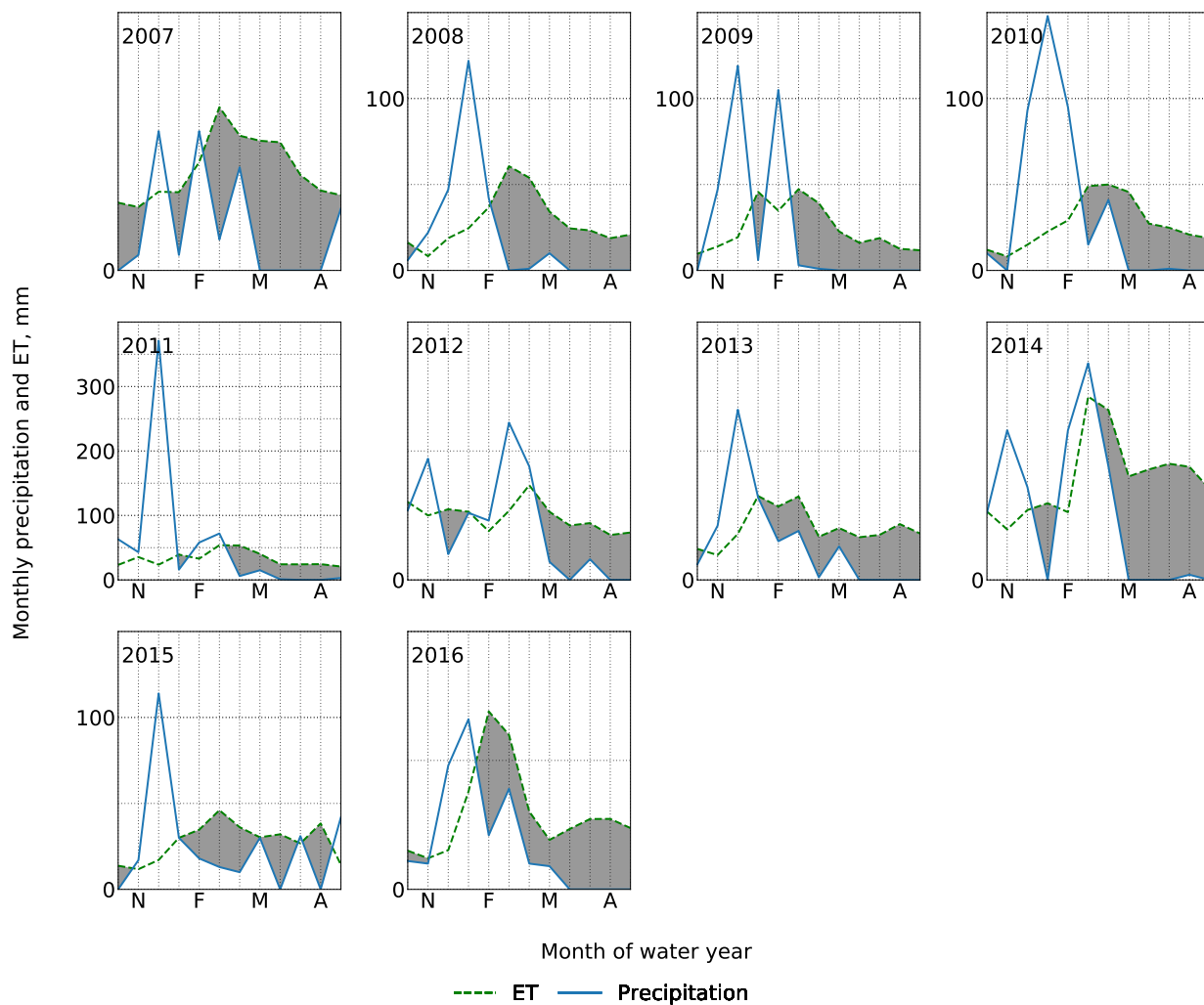


Figure A.1.15: US-SCg monthly evapotranspiration (ET) and precipitation for each water year

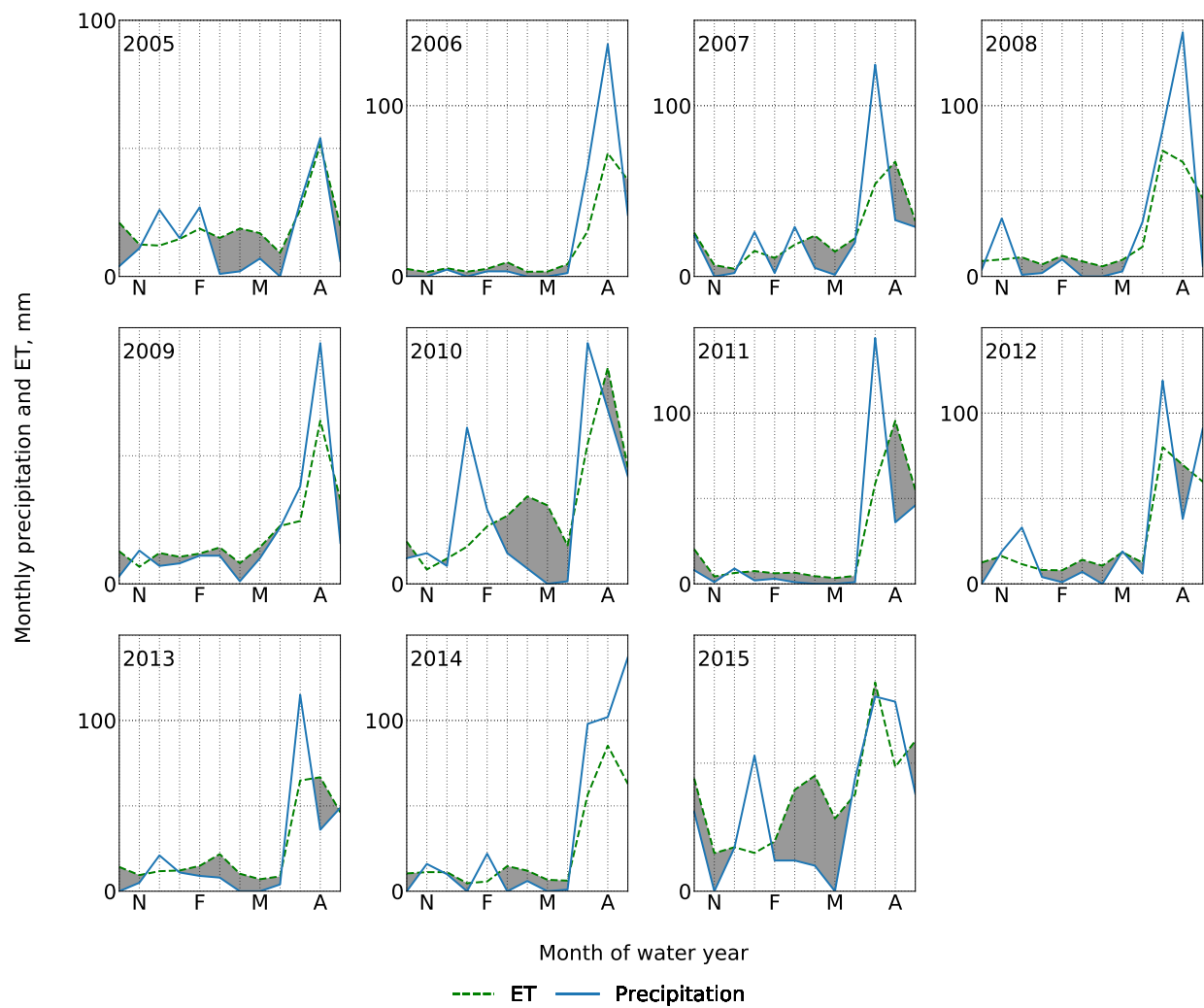


Figure A.1.16: US-Wkg monthly evapotranspiration (ET) and precipitation for each water year

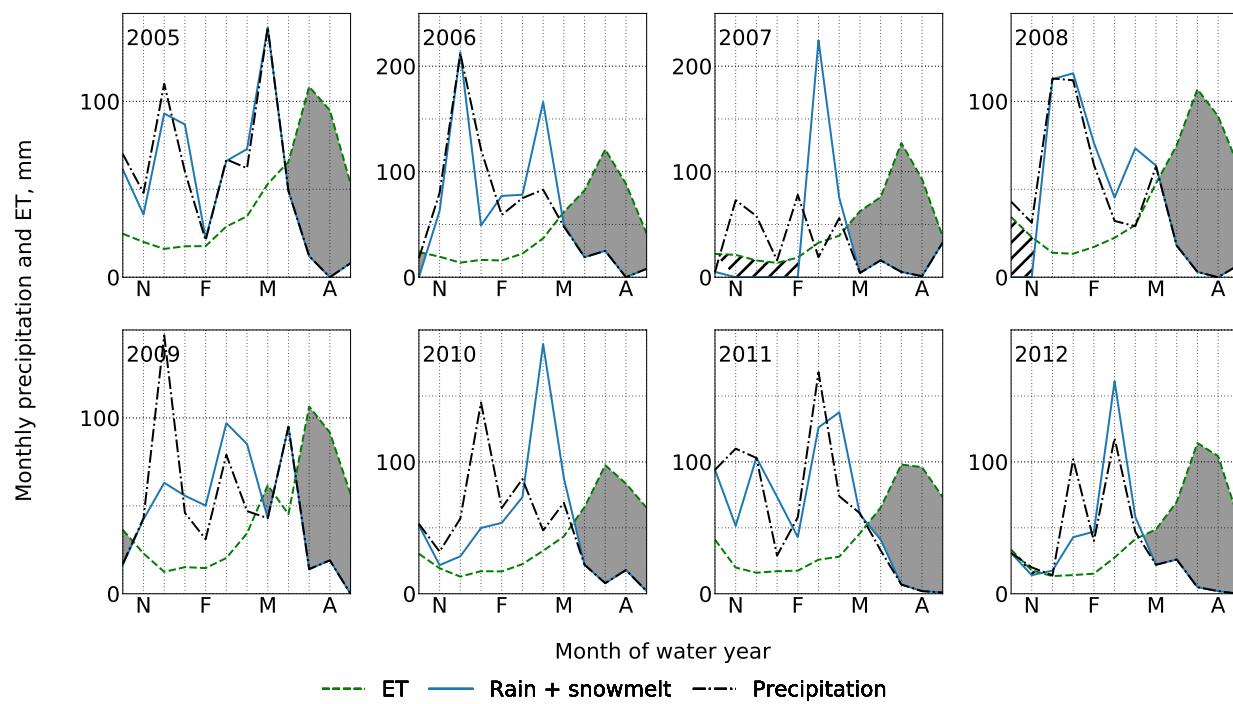


Figure A.1.17: USA monthly evapotranspiration (ET) and precipitation for each water year

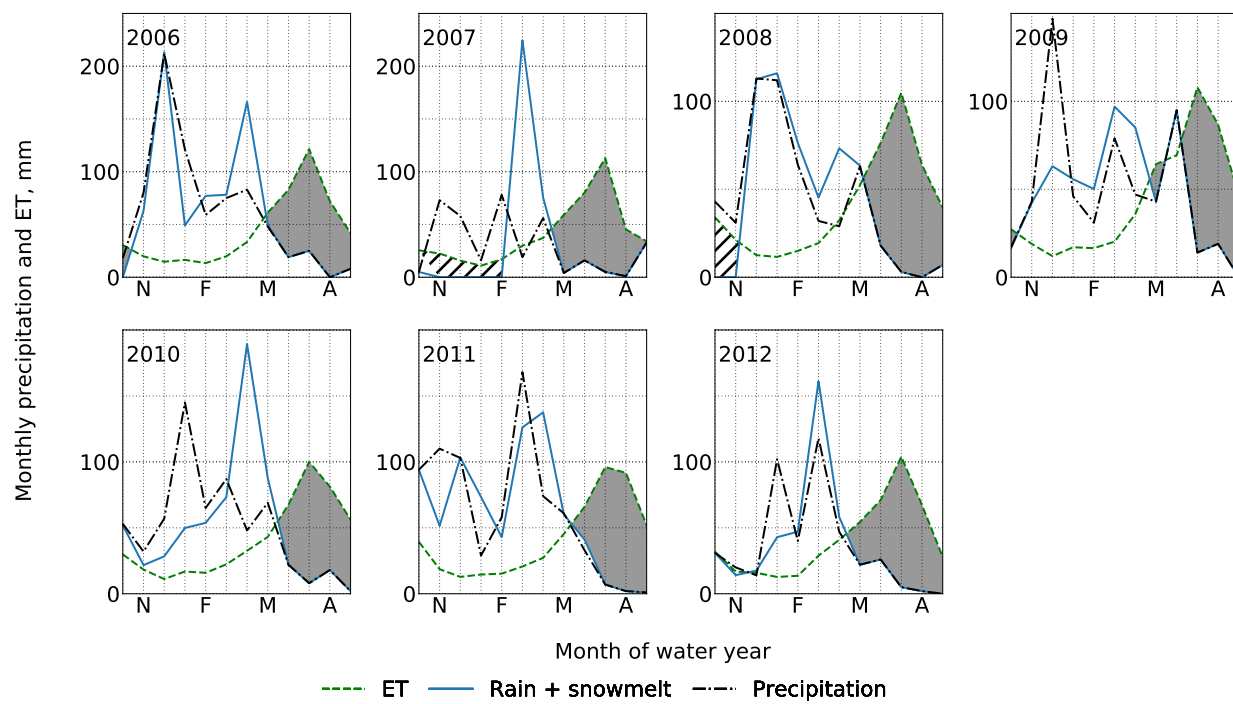


Figure A.1.18: USS monthly evapotranspiration (ET) and precipitation for each water year

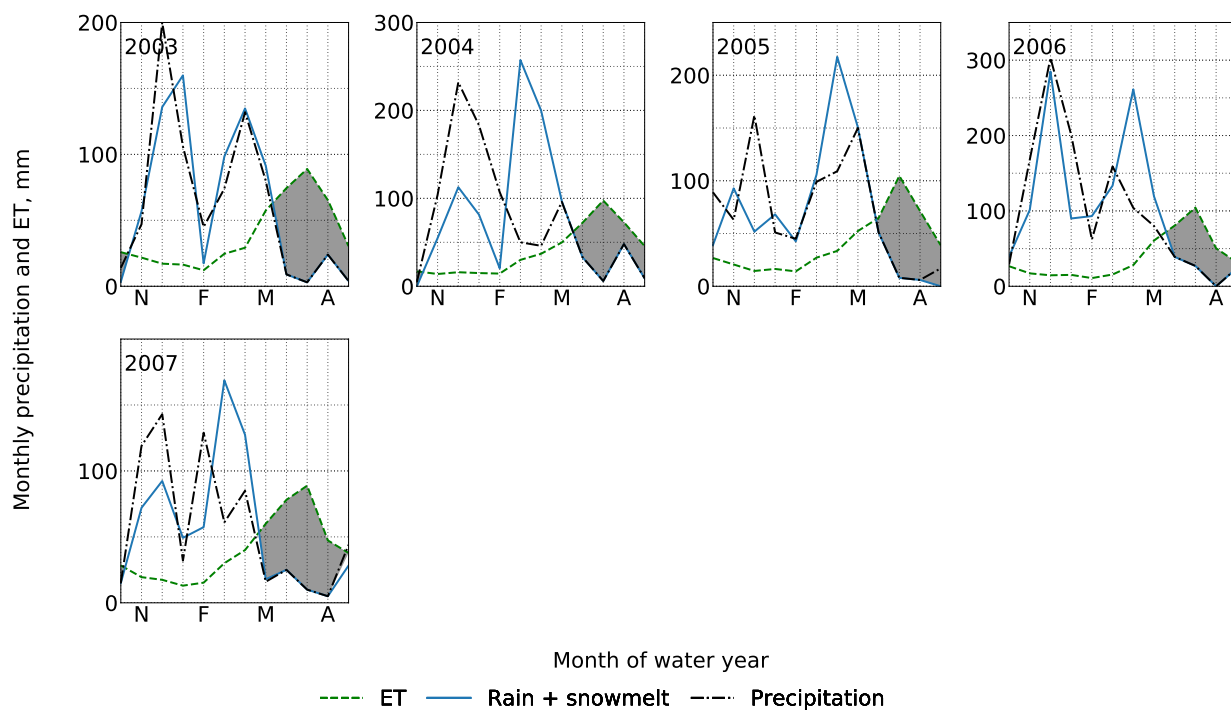


Figure A.1.19: RMES monthly evapotranspiration (ET) and precipitation for each water year

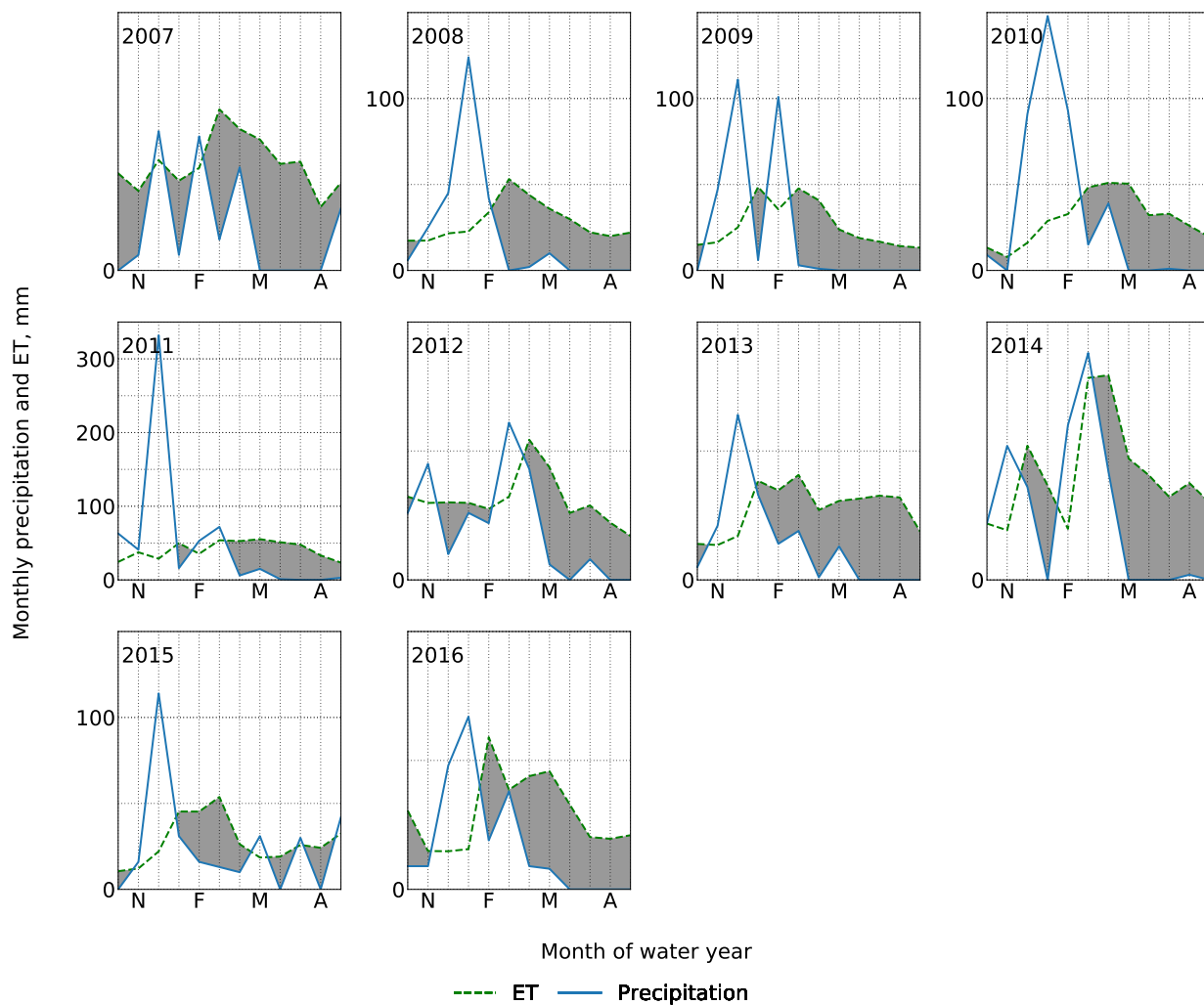


Figure A.1.20: US-SCs monthly evapotranspiration (ET) and precipitation for each water year

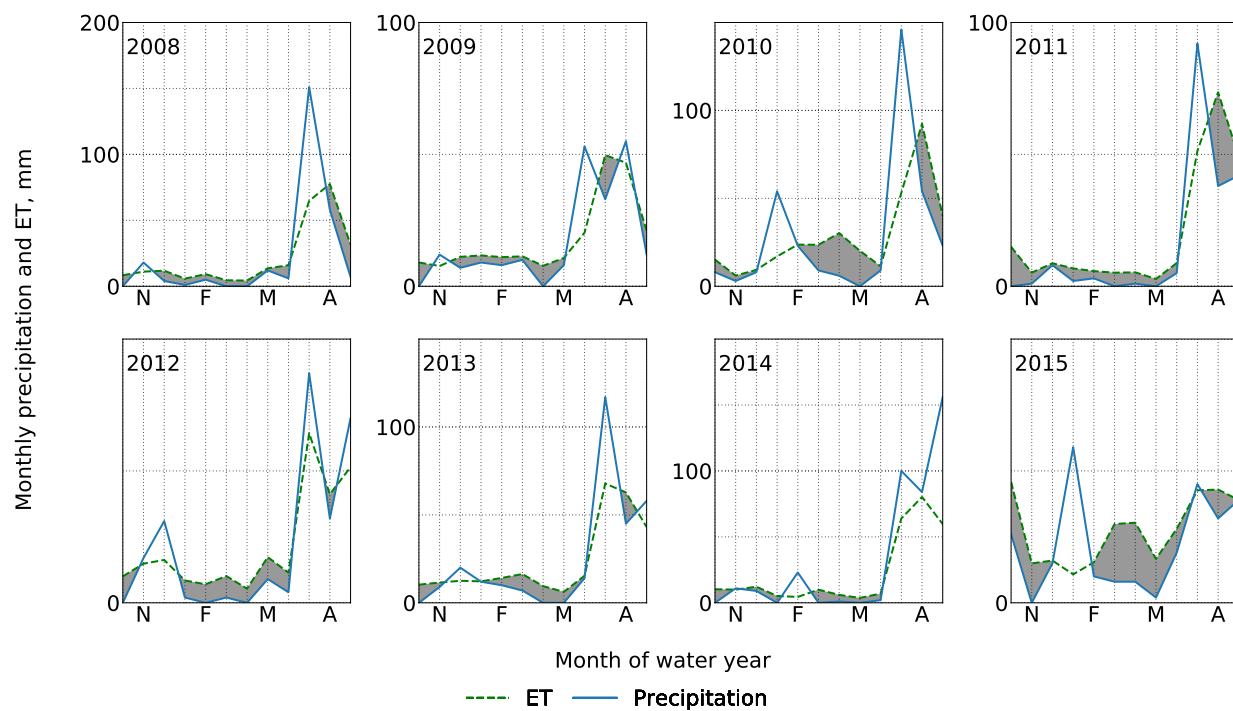


Figure A.1.21: US-Whs monthly evapotranspiration (ET) and precipitation for each water year

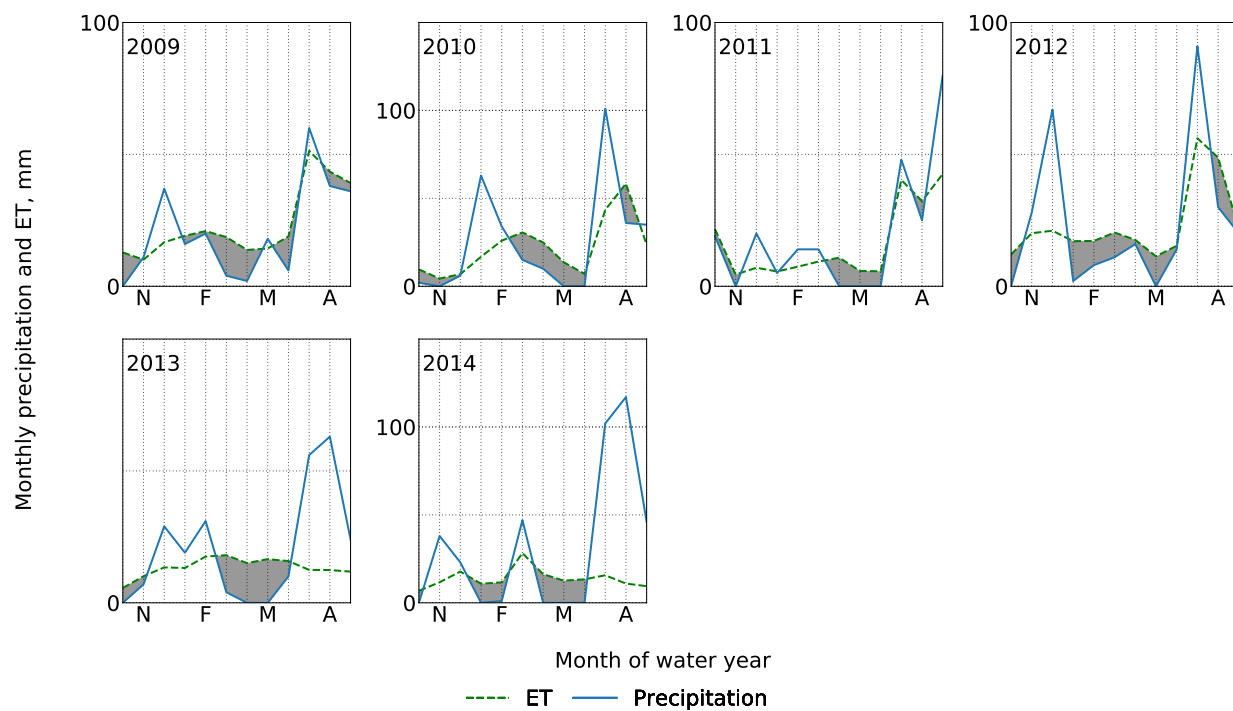


Figure A.1.22: US-SRC monthly evapotranspiration (ET) and precipitation for each water year

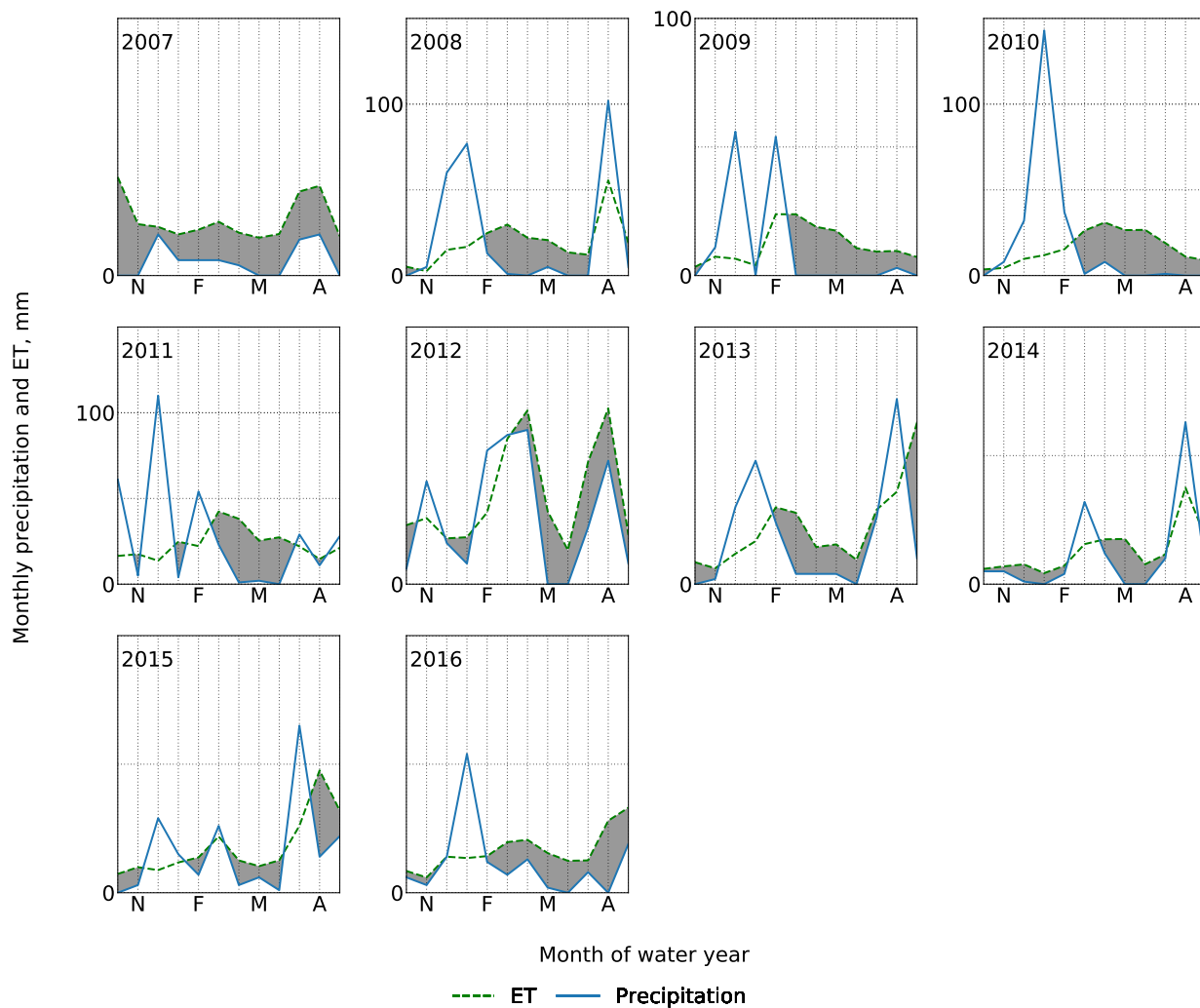


Figure A.1.23: US-SCw monthly evapotranspiration (ET) and precipitation for each water year

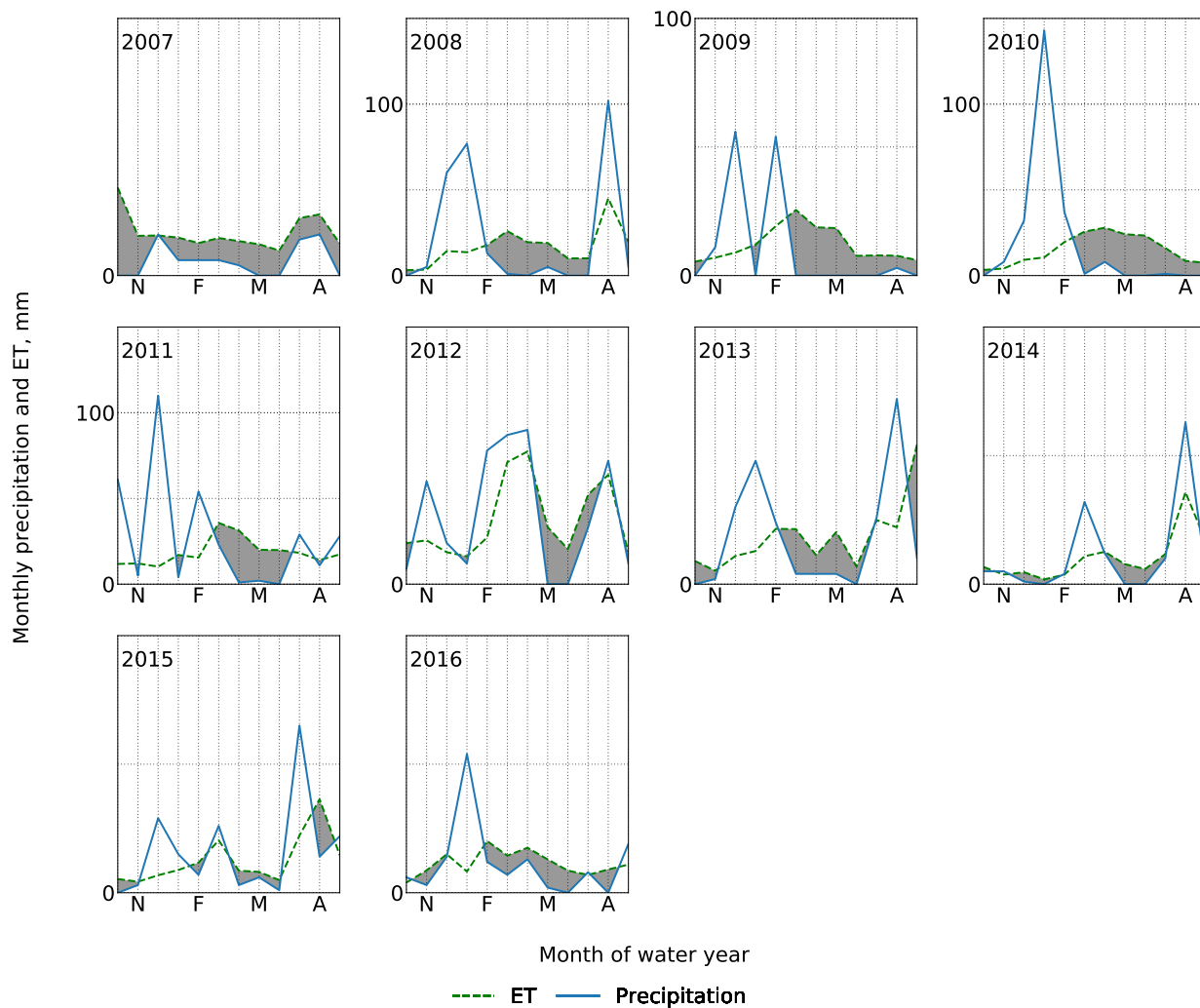


Figure A.1.24: US-SCc monthly evapotranspiration (ET) and precipitation for each water year

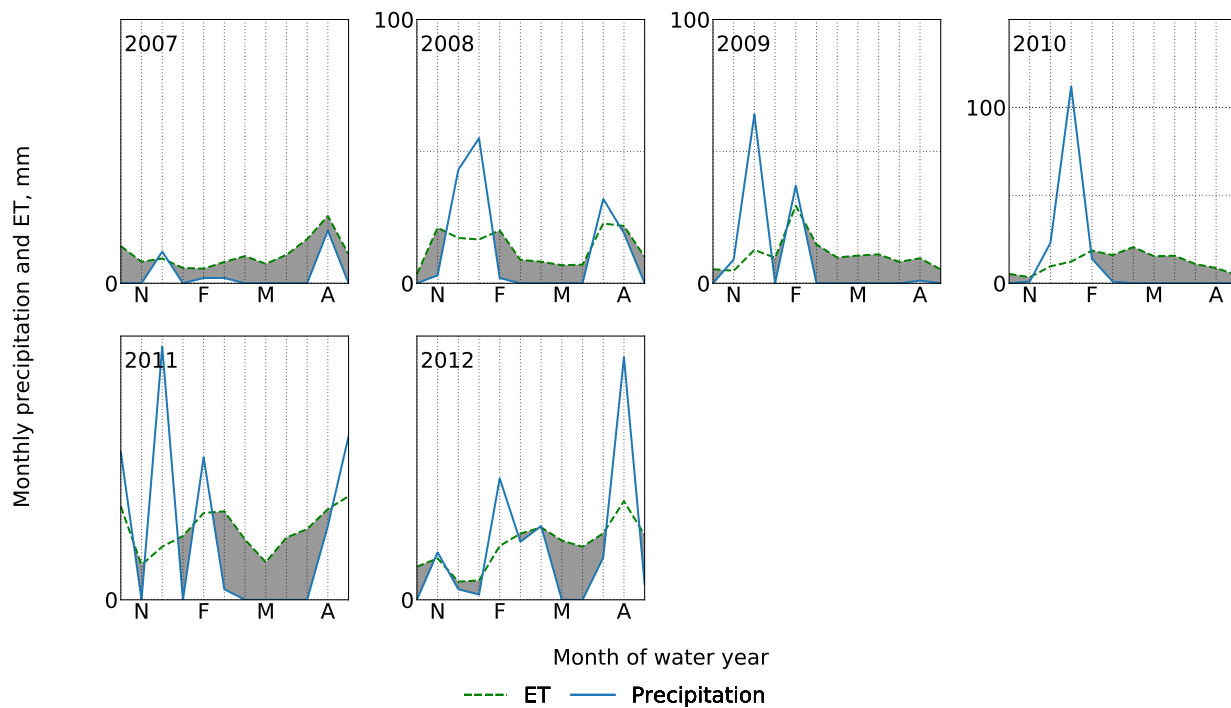


Figure A.1.25: US-SCd monthly evapotranspiration (ET) and precipitation for each water year

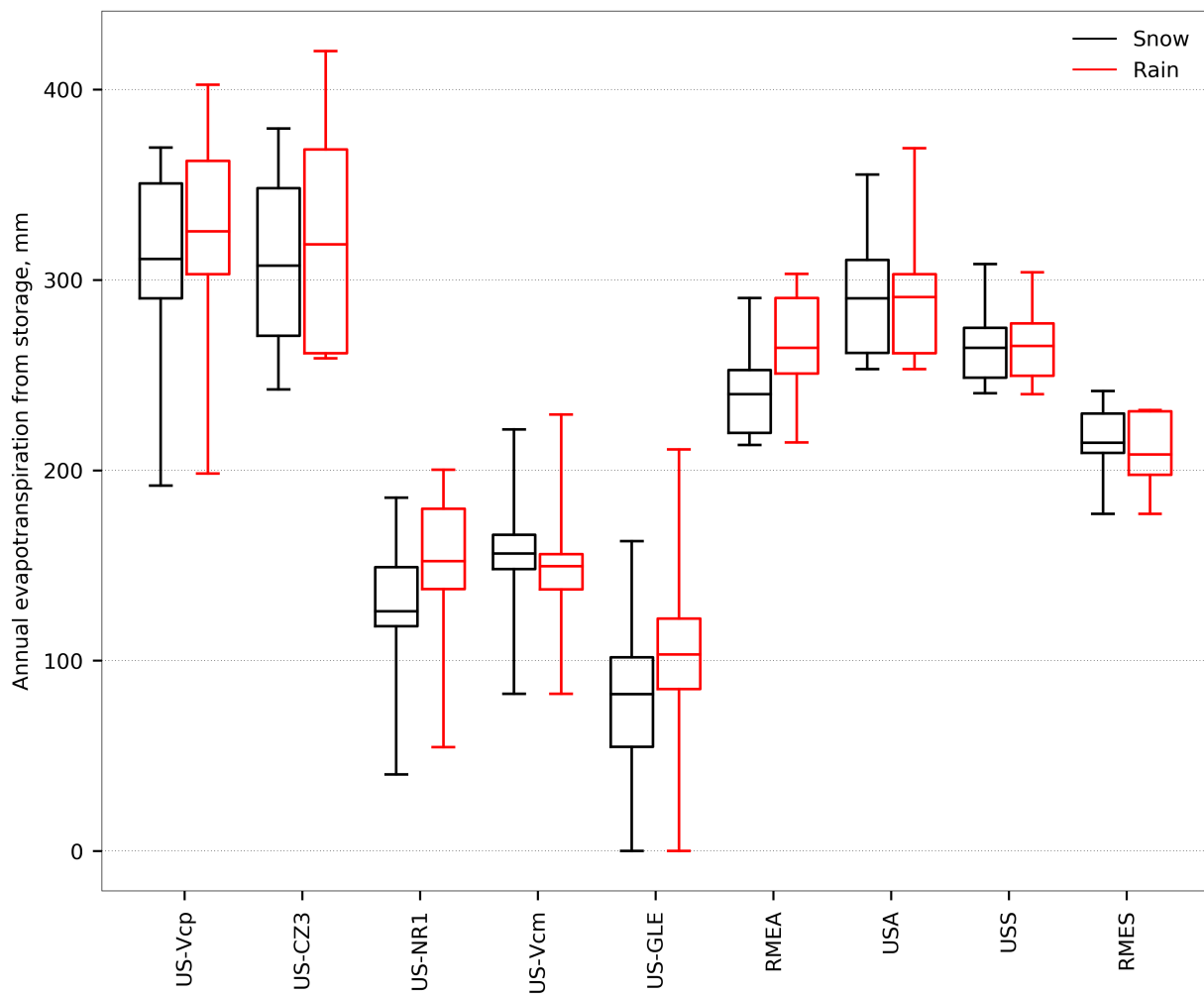


Figure A.2.1: Boxplots of annual evapotranspiration supported by storage when accounting for snow (black) and when considering all snow as rain (red) for all snow-influenced sites.

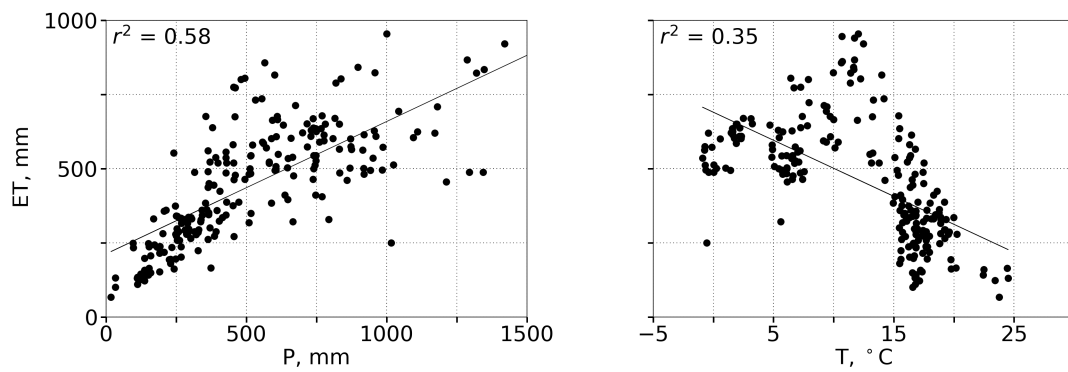


Figure A.3.1: Regressions of site-year evapotranspiration (ET) with precipitation (P) and temperature (T).

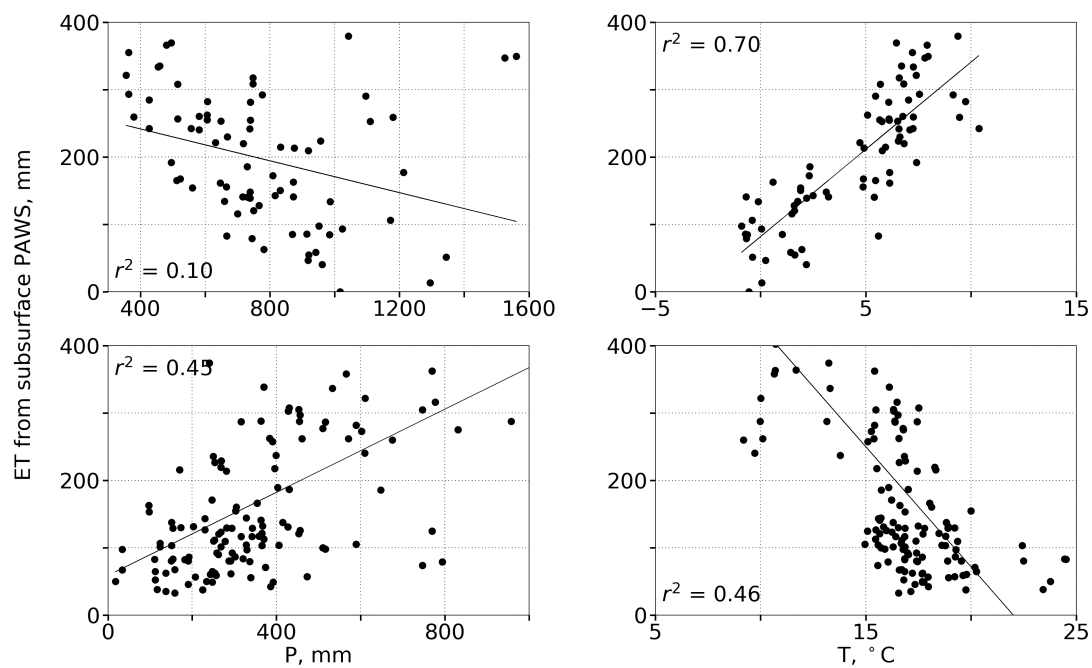


Figure A.4.1: Regressions of site-year evapotranspiration (ET) from subsurface plant-accessible water storage (PAWS) with precipitation (P) and temperature (T).

Appendix B

Appendices for Chapter 3

Table B.1: Model parameters for all models for Equation 1.

Variable	LS800m All	LS800m NoT	LS800m NoVT	LS4km All	LS4km NoT	LS4km NoVT
$w_N DVI$	0.49	0.49	0.61	0.49	0.50	0.61
$a_N DVI$	2119.20	2119.20	2119.20	2119.20	2119.20	2119.20
$b_N DVI$	1.50	1.50	1.50	1.50	1.50	1.50
w_P	0.57	0.49	0.60	0.58	0.49	0.60
a_P	8.57	8.57	8.57	5.83	5.83	5.83
b_P	0.63	0.63	0.63	0.63	0.63	0.63
w_T	-0.25	N/A	N/A	-0.26	N/A	N/A
a_T	-38.48	N/A	N/A	-37.43	N/A	N/A
b_T	1034.94	N/A	N/A	1017.35	N/A	N/A
$w_E NF$	0.00	0.00	N/A	0.00	0.00	N/A
$w_M F$	0.00	0.00	N/A	0.00	0.00	N/A
$w_W SA$	0.00	0.00	N/A	0.00	0.00	N/A
$w_G RA$	-172.45	-147.63	N/A	-172.34	-147.33	N/A
$w_O SH$	-134.49	-116.48	N/A	-130.63	-114.51	N/A
int	158.71	73.36	-90.66	160.46	69.98	-92.44

Variable	MOD800m All	MOD800m NoT	MOD800m NoVT	MOD4km All	MOD4km NoT	MOD4km NoVT
$w_N DVI$	0.58	0.66	0.65	0.58	0.67	0.65
$a_N DVI$	1449.39	1449.39	1449.39	1449.39	1449.39	1449.39
$b_N DVI$	2.08	2.08	2.08	2.08	2.08	2.08
w_P	0.51	0.44	0.60	0.51	0.44	0.60
a_P	8.47	8.47	8.47	9.00	9.00	9.00
b_P	0.64	0.64	0.64	0.63	0.63	0.63
w_T	-0.32	N/A	N/A	-0.34	N/A	N/A
a_T	-35.57	N/A	N/A	-34.40	N/A	N/A
b_T	977.75	N/A	N/A	958.42	N/A	N/A
$w_E NF$	66.68	0.00	N/A	67.52	0.00	N/A
$w_M F$	0.00	-66.16	N/A	0.00	-65.26	N/A
$w_W SA$	0.00	0.00	N/A	0.00	0.00	N/A
$w_G RA$	-160.24	-155.72	N/A	-160.11	-155.53	N/A
$w_O SH$	-102.32	-86.03	N/A	-98.91	-84.62	N/A
int	154.91	25.27	-102.27	159.26	22.76	-103.98

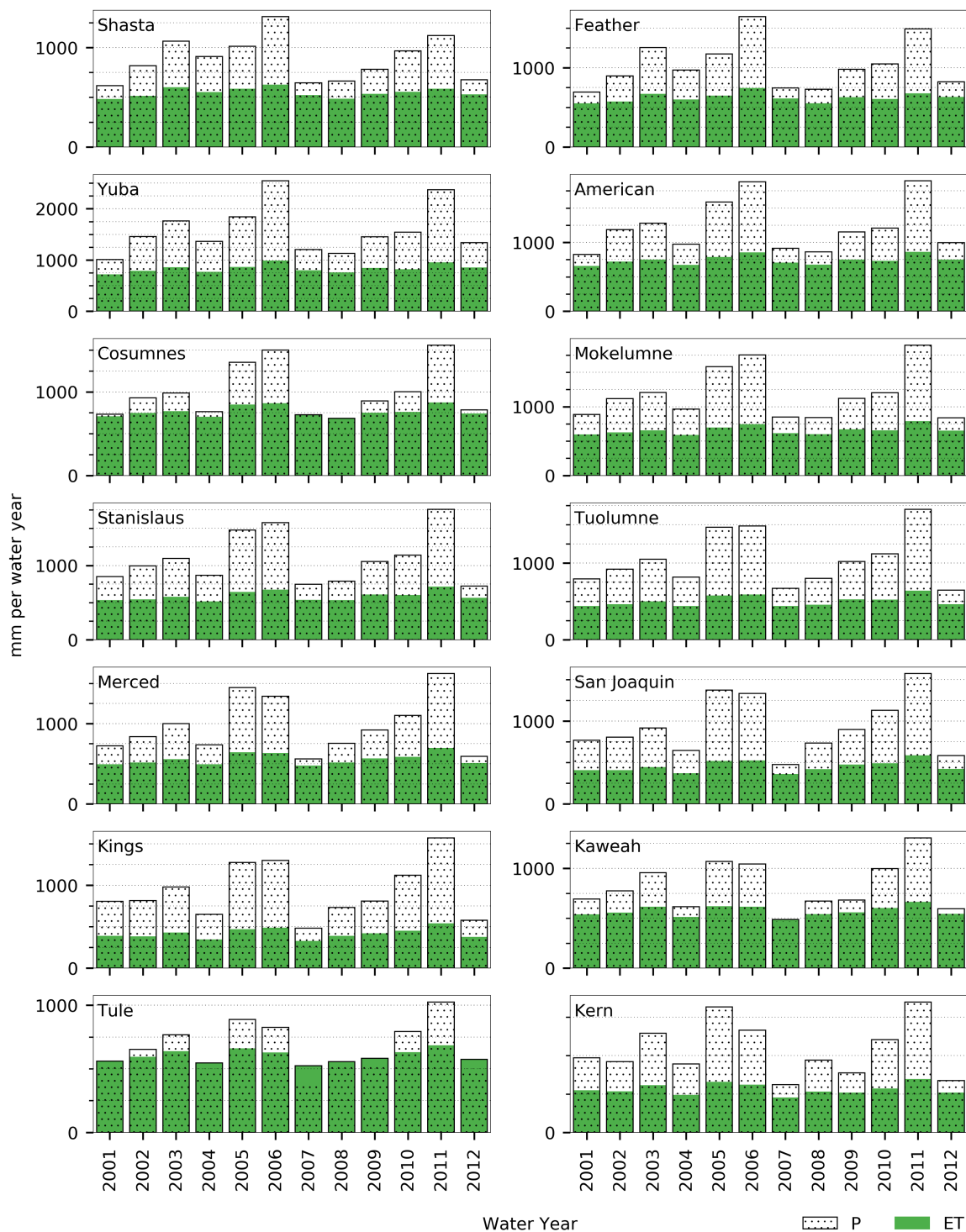


Figure B.1.1: Individual site year, by basin, of precipitation (P) and evapotranspiration (ET).

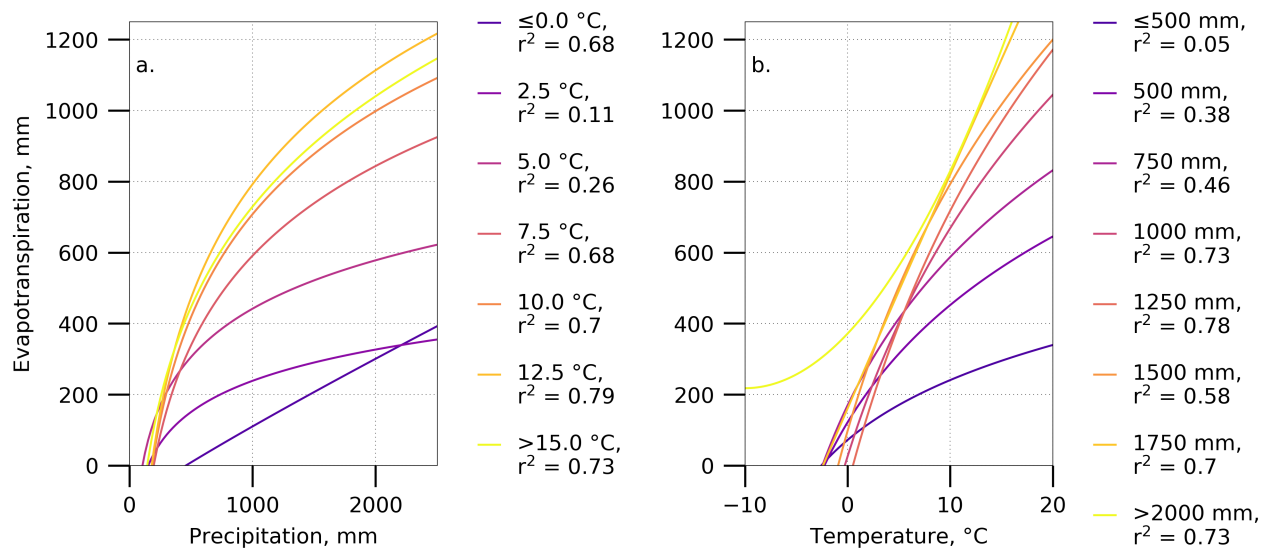


Figure B.2.1: Best fit first order power functions between evapotranspiration and precipitation binned by temperature (a.) and temperature binned by precipitation (b.).

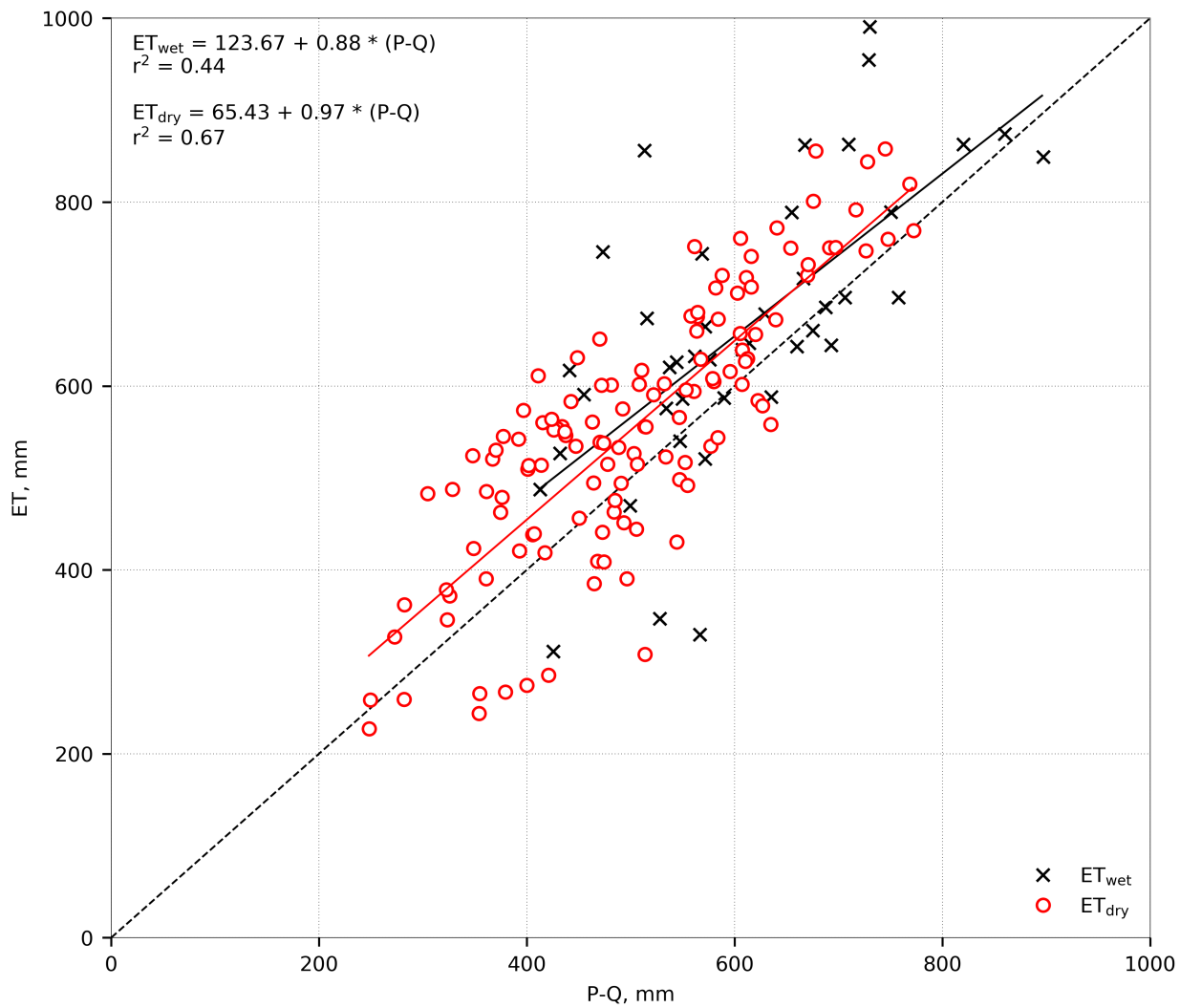


Figure B.3.1: Plot of all site years of $P - Q$ and ET . The data is binned by wet and dry years with best fit line, where wet years are years above a given basins 34-year mean and dry year are below.

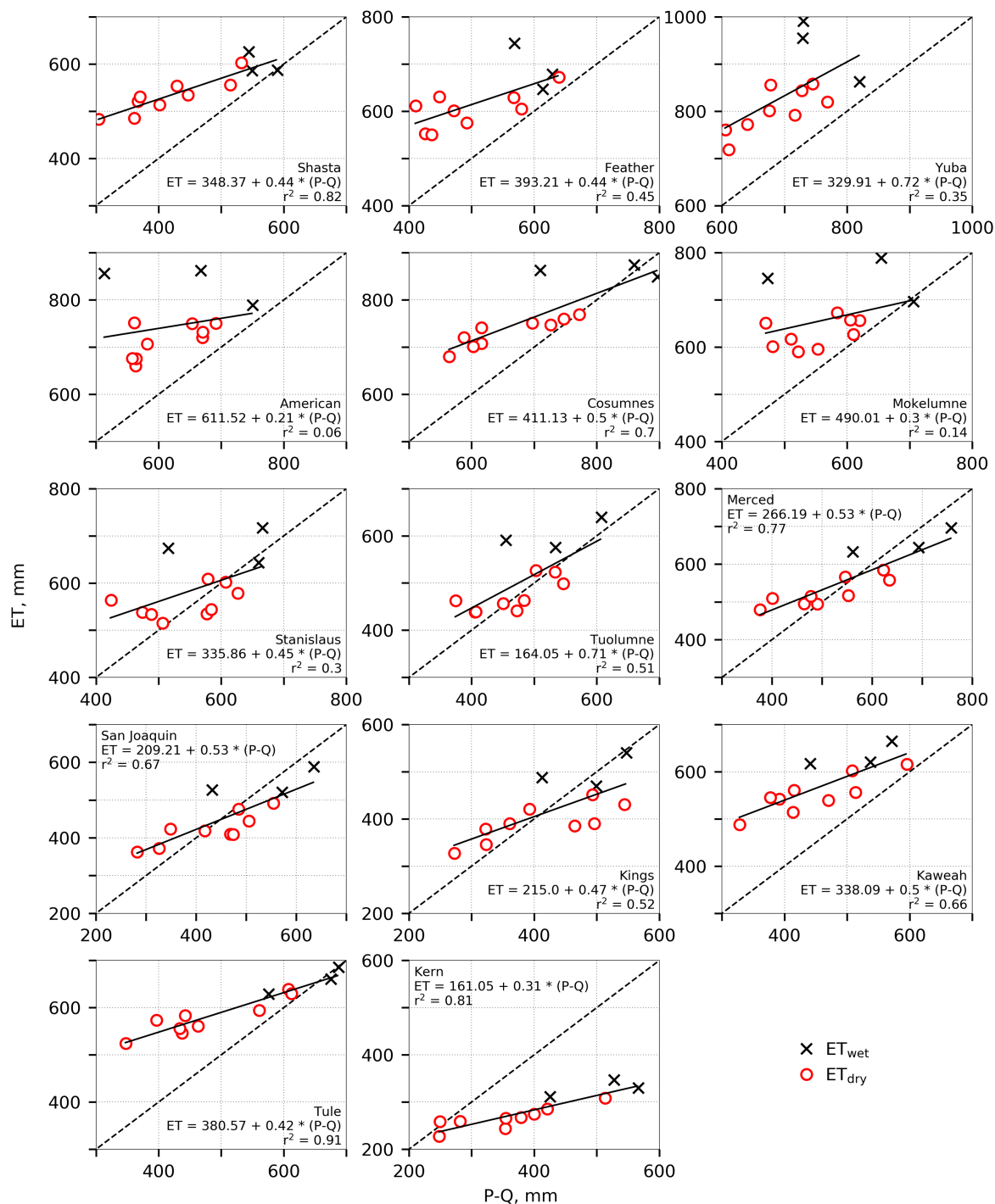


Figure B.4.1: Plots of all site years of $P - Q$ and ET by basin. The data is binned by wet and dry years with best fit line, where wet years are years above a given basin's 34-year mean and dry year are below.

Appendix C

Appendices for Chapter 4

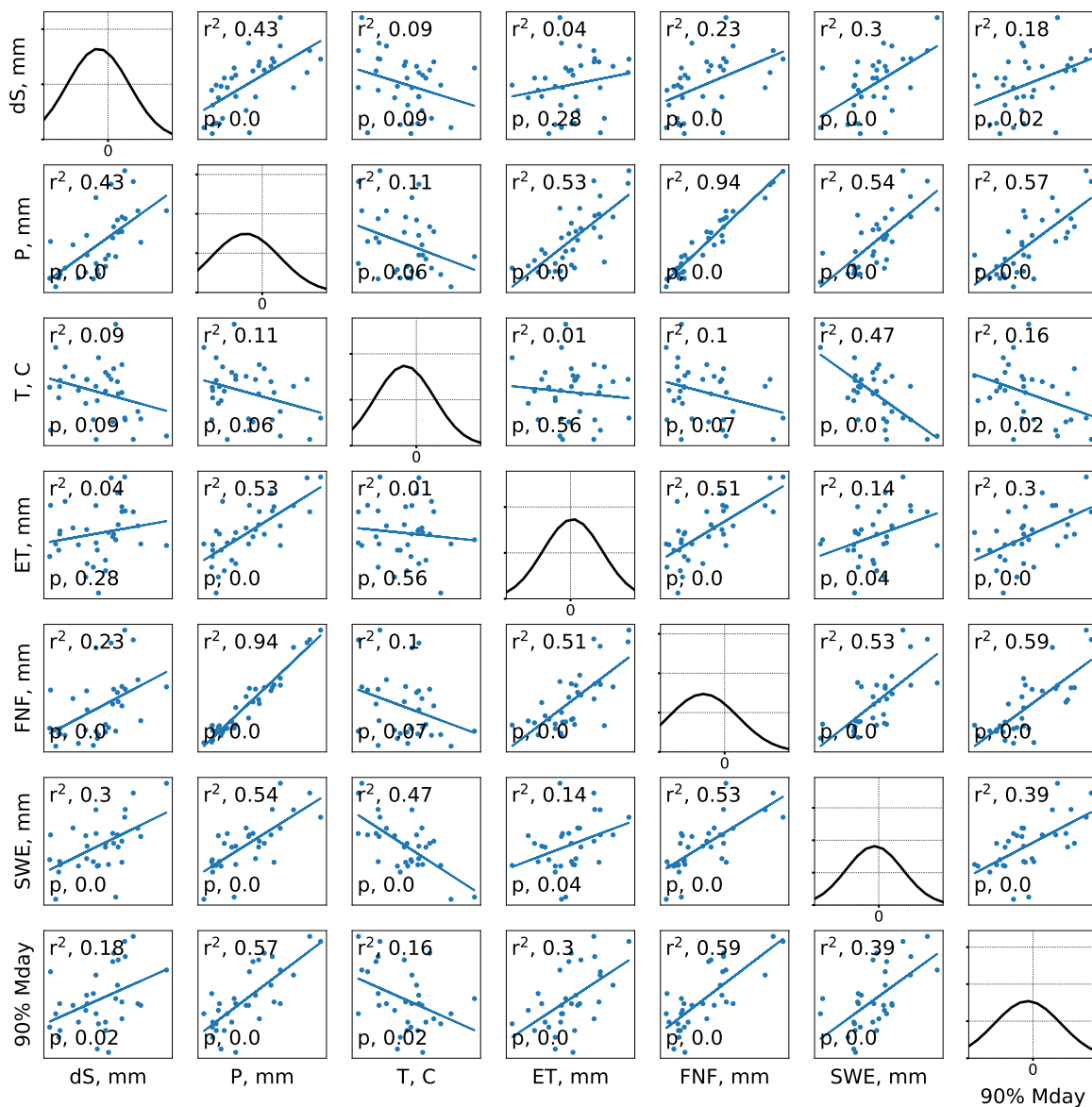


Figure C.1.1: Covariance matrix for Shasta, where dS is change in storage, P is precipitation, T is temperature, ET is evapotranspiration, FNF is unimpaired runoff, SWE is snow-water equivalent, and 90% Mday is the timing of 90% snowmelt from peak SWE.

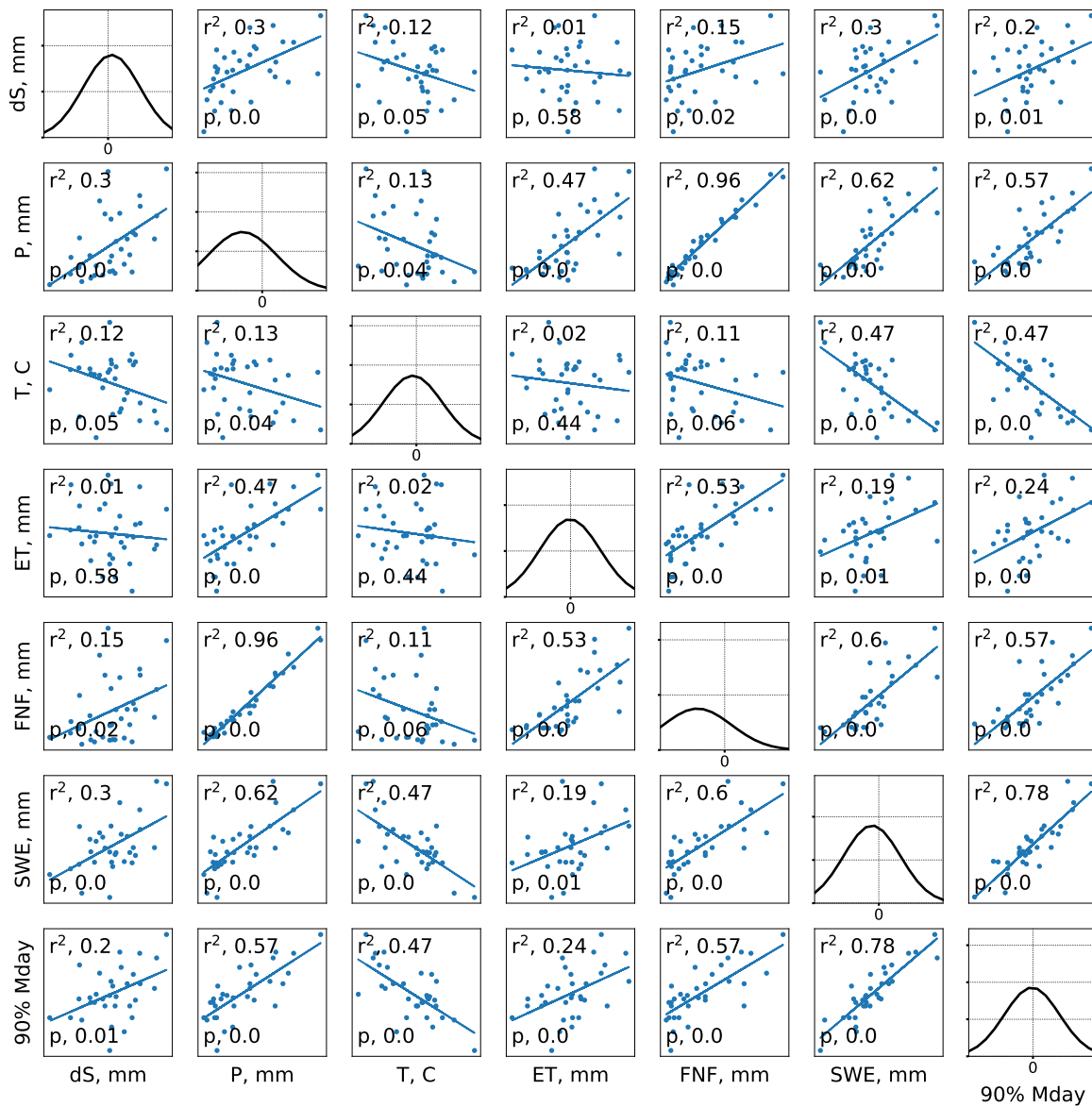


Figure C.1.2: Covariance matrix for Feather, where dS is change in storage, P is precipitation, T is temperature, ET is evapotranspiration, FNF is unimpaired runoff, SWE is snow-water equivalent, and 90% Mday is the timing of 90% snowmelt from peak SWE.

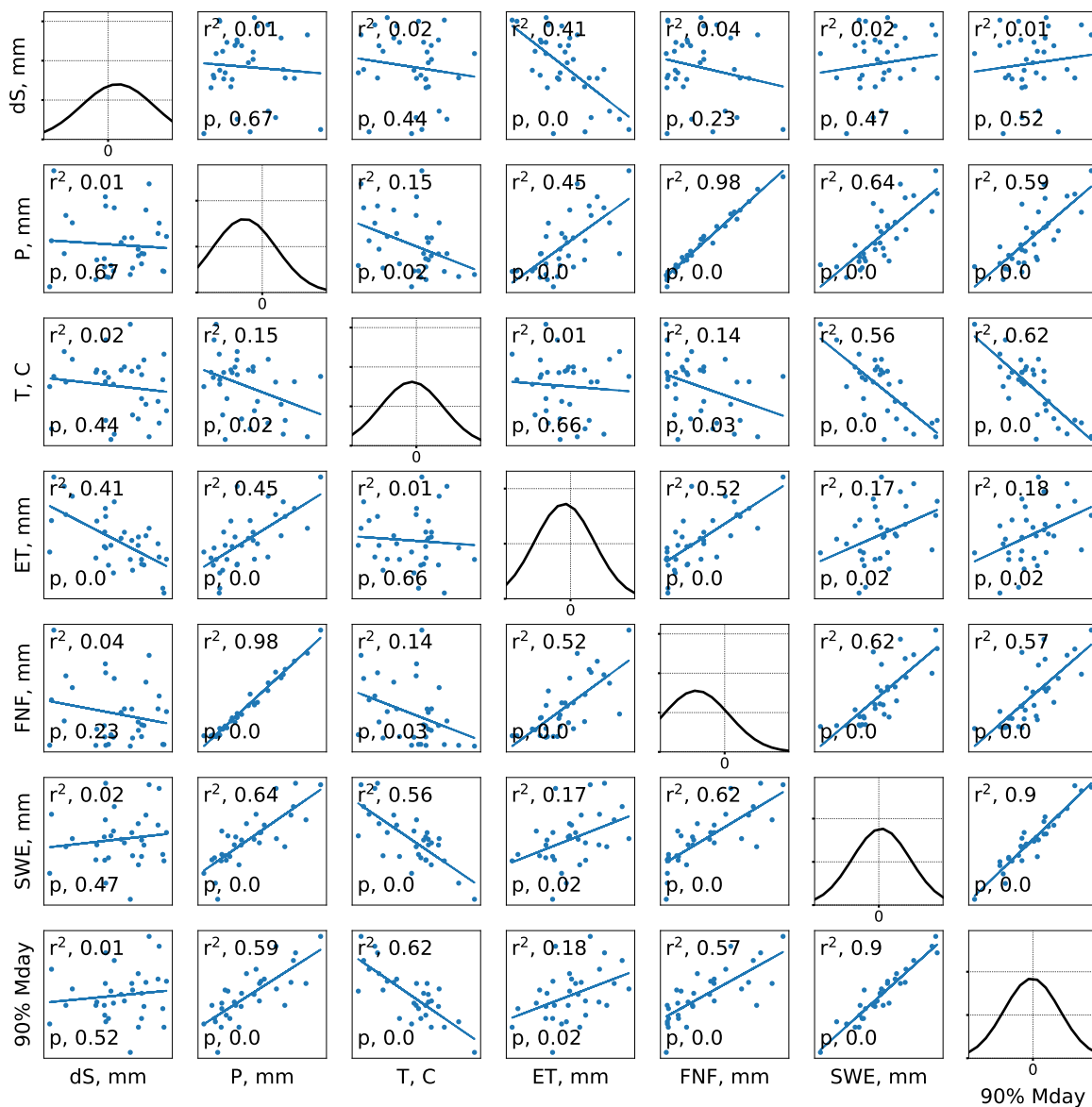


Figure C.1.3: Covariance matrix for Yuba, where dS is change in storage, P is precipitation, T is temperature, ET is evapotranspiration, FNF is unimpaired runoff, SWE is snow-water equivalent, and 90% Mday is the timing of 90% snowmelt from peak SWE.

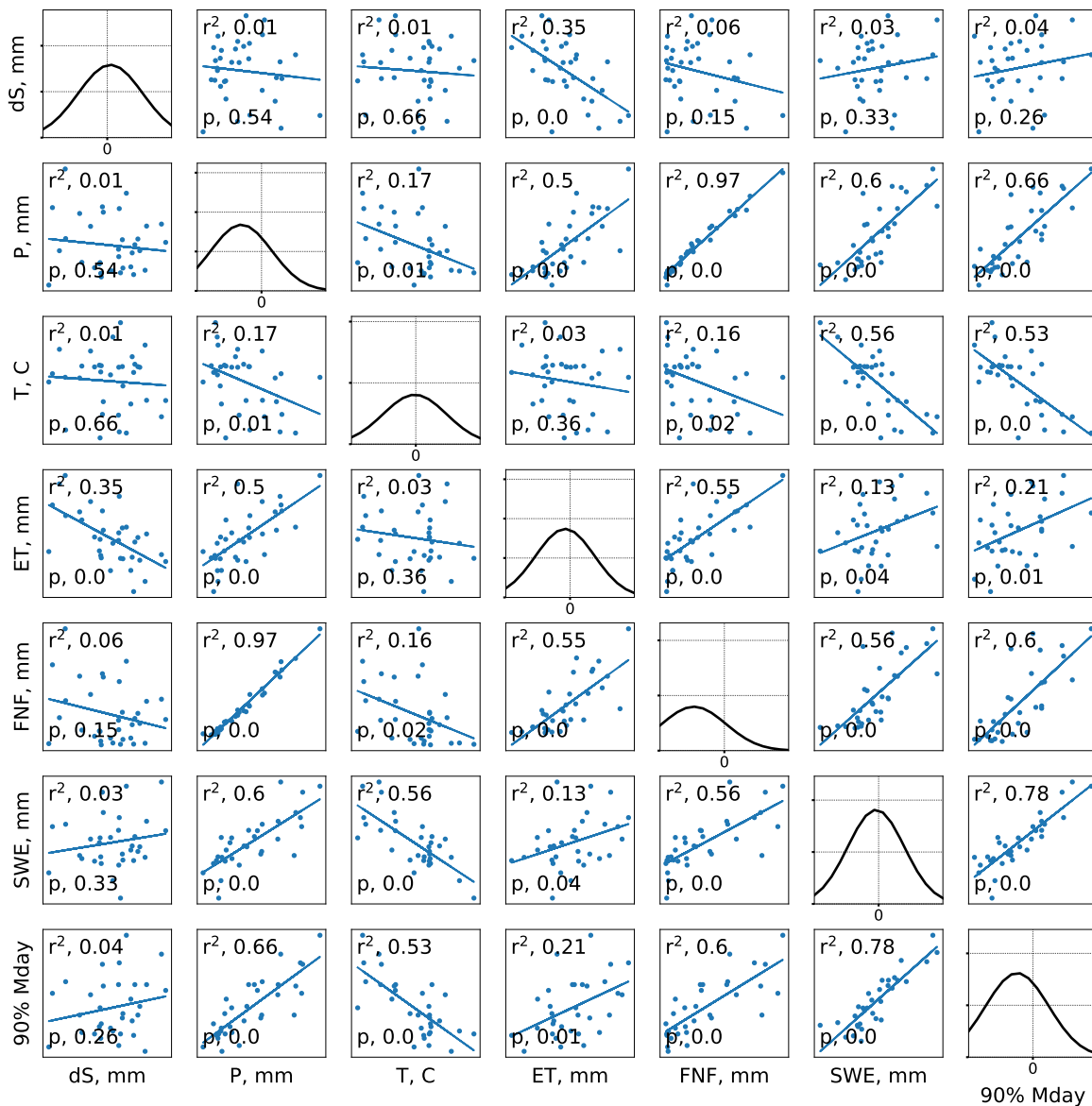


Figure C.1.4: Covariance matrix for American, where dS is change in storage, P is precipitation, T is temperature, ET is evapotranspiration, FNF is unimpaired runoff, SWE is snow-water equivalent, and 90% Mday is the timing of 90% snowmelt from peak SWE.

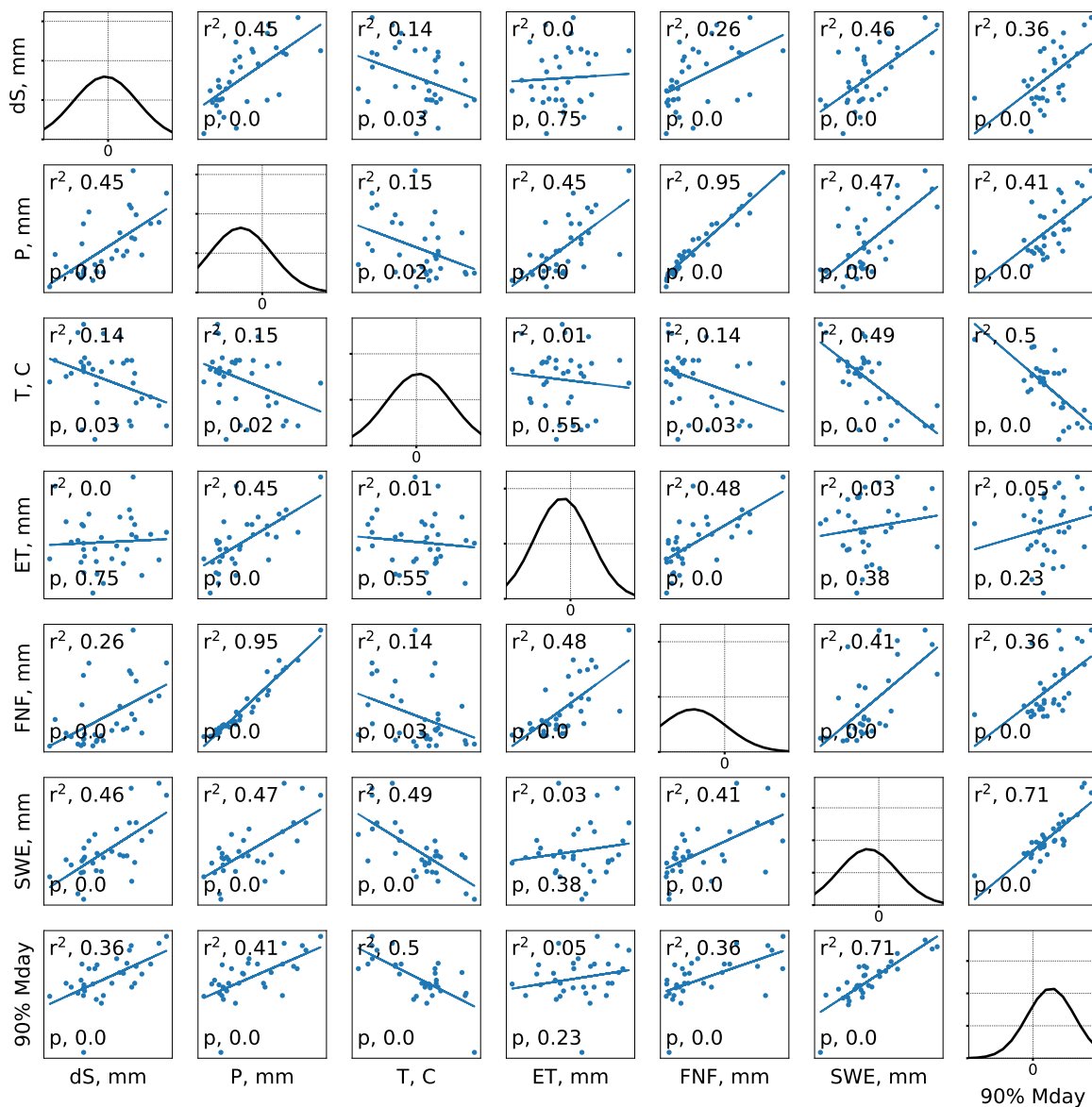


Figure C.1.5: Covariance matrix for Cosumnes, where dS is change in storage, P is precipitation, T is temperature, ET is evapotranspiration, FNF is unimpaired runoff, SWE is snow-water equivalent, and 90% Mday is the timing of 90% snowmelt from peak SWE.

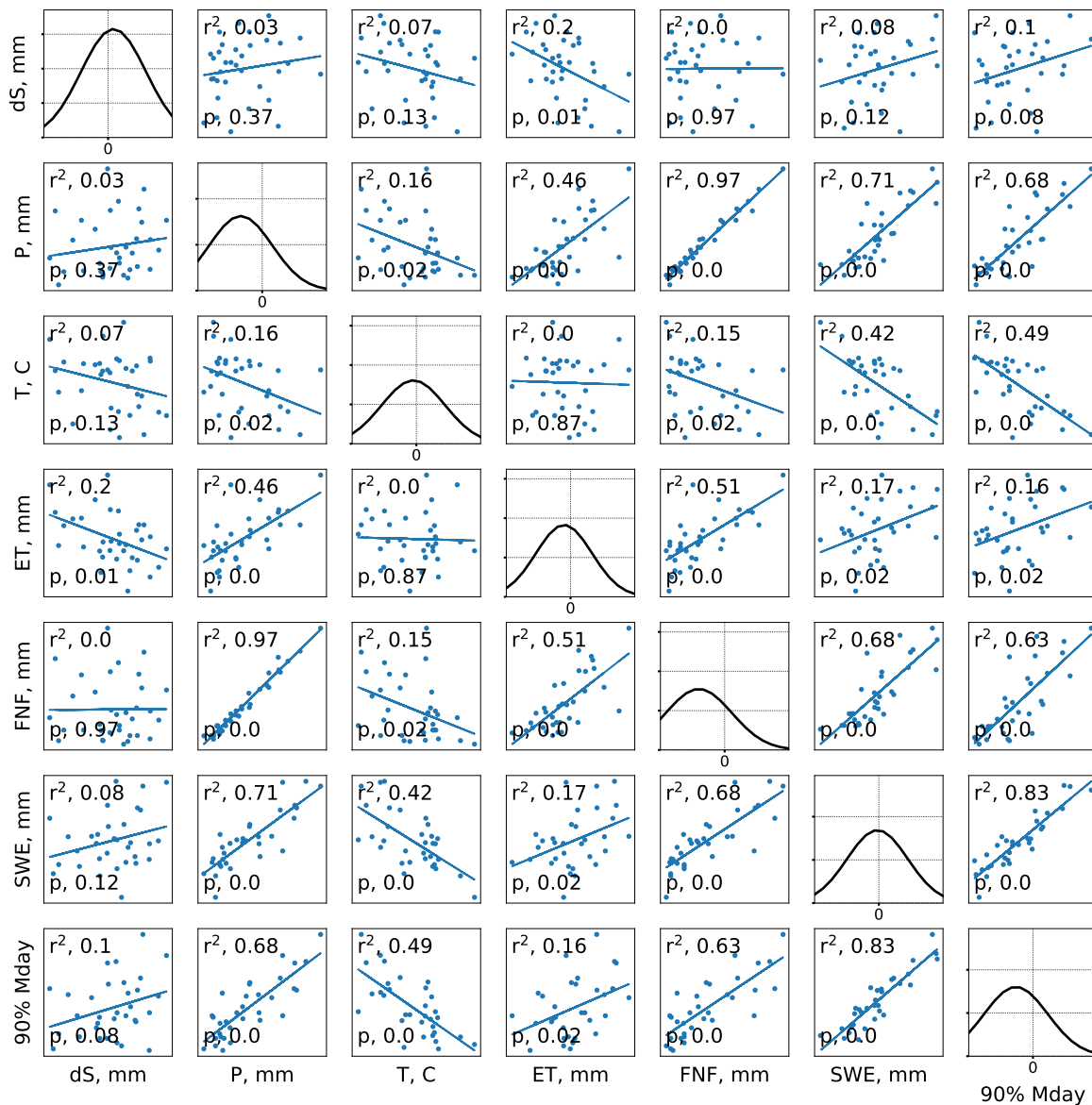


Figure C.1.6: Covariance matrix for Mokelumne, where dS is change in storage, P is precipitation, T is temperature, ET is evapotranspiration, FNF is unimpaired runoff, SWE is snow-water equivalent, and 90% Mday is the timing of 90% snowmelt from peak SWE.

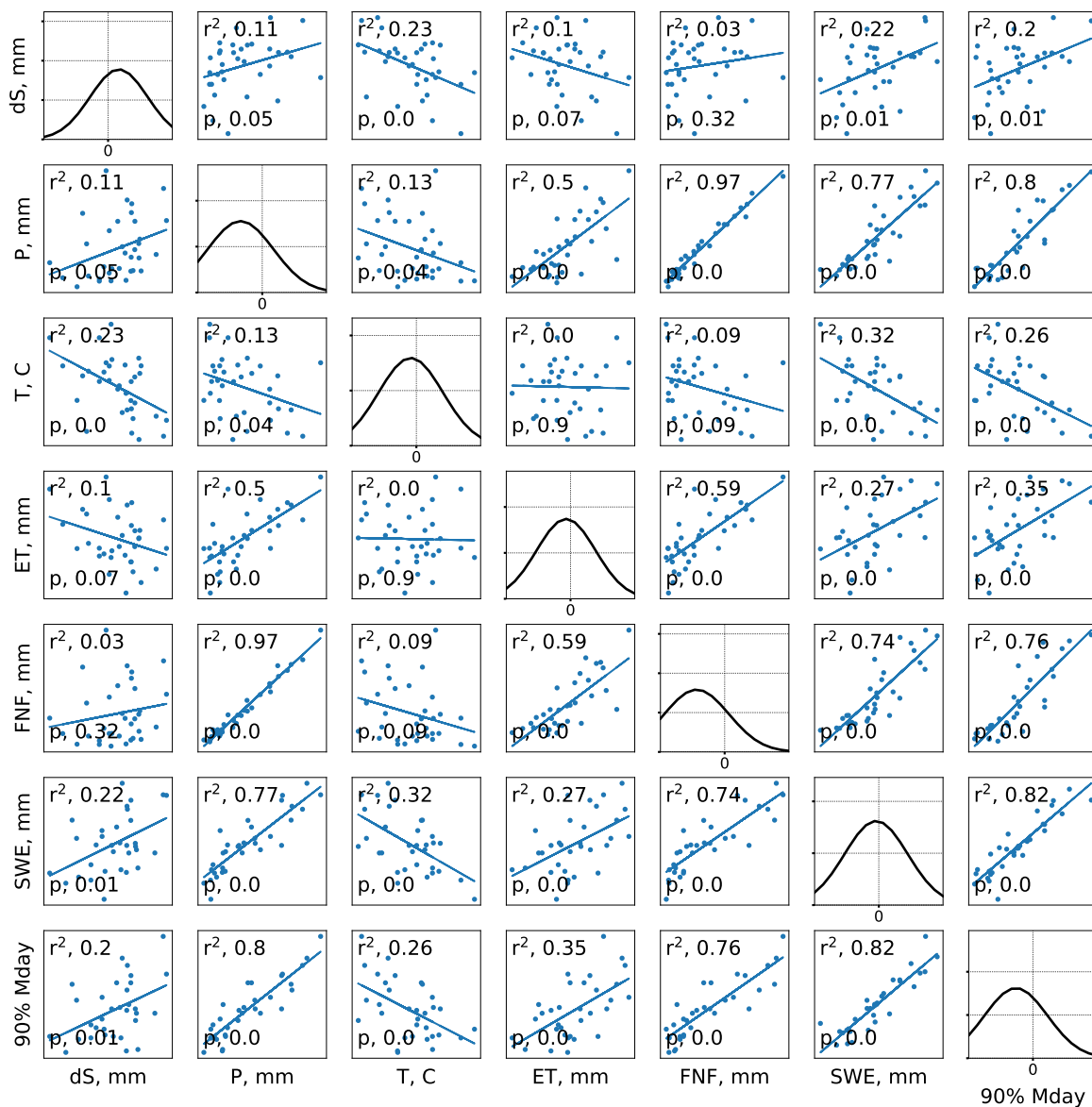


Figure C.1.7: Covariance matrix for Stanislaus, where dS is change in storage, P is precipitation, T is temperature, ET is evapotranspiration, FNF is unimpaired runoff, SWE is snow-water equivalent, and 90% Mday is the timing of 90% snowmelt from peak SWE.

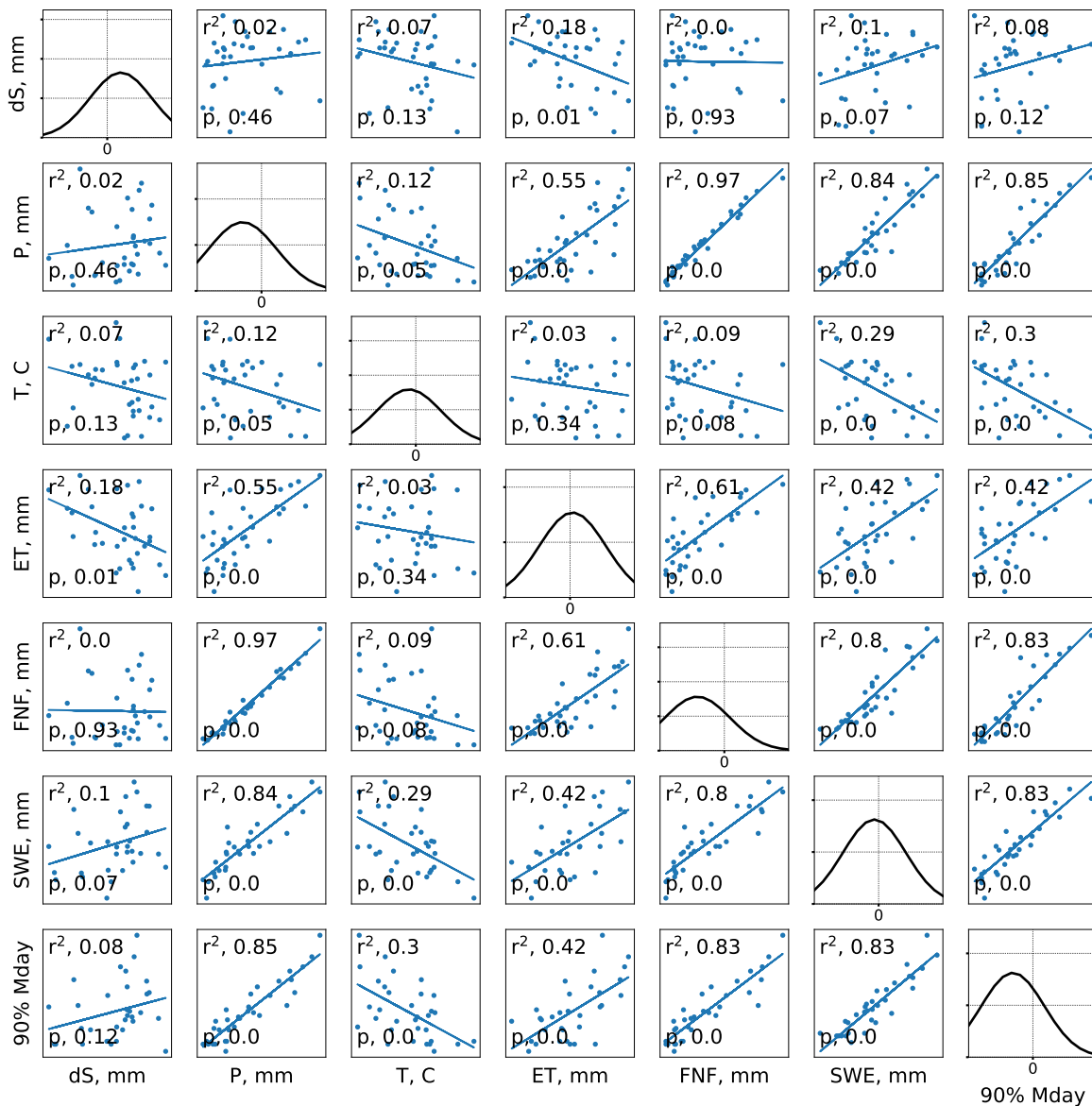


Figure C.1.8: Covariance matrix for Tuolumne, where dS is change in storage, P is precipitation, T is temperature, ET is evapotranspiration, FNF is unimpaired runoff, SWE is snow-water equivalent, and 90% Mday is the timing of 90% snowmelt from peak SWE.

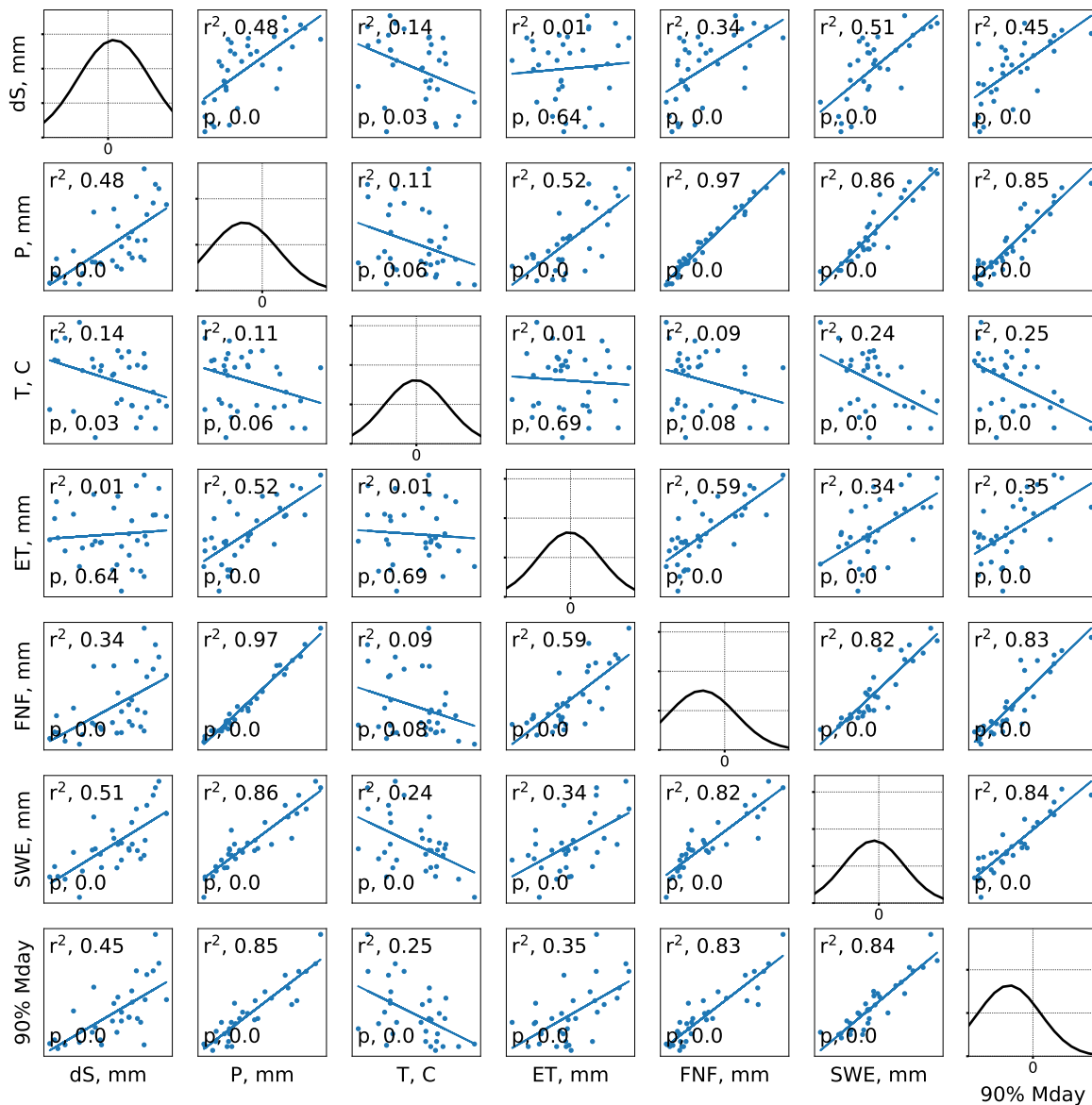


Figure C.1.9: Covariance matrix for Merced, where dS is change in storage, P is precipitation, T is temperature, ET is evapotranspiration, FNF is unimpaired runoff, SWE is snow-water equivalent, and 90% Mday is the timing of 90% snowmelt from peak SWE.

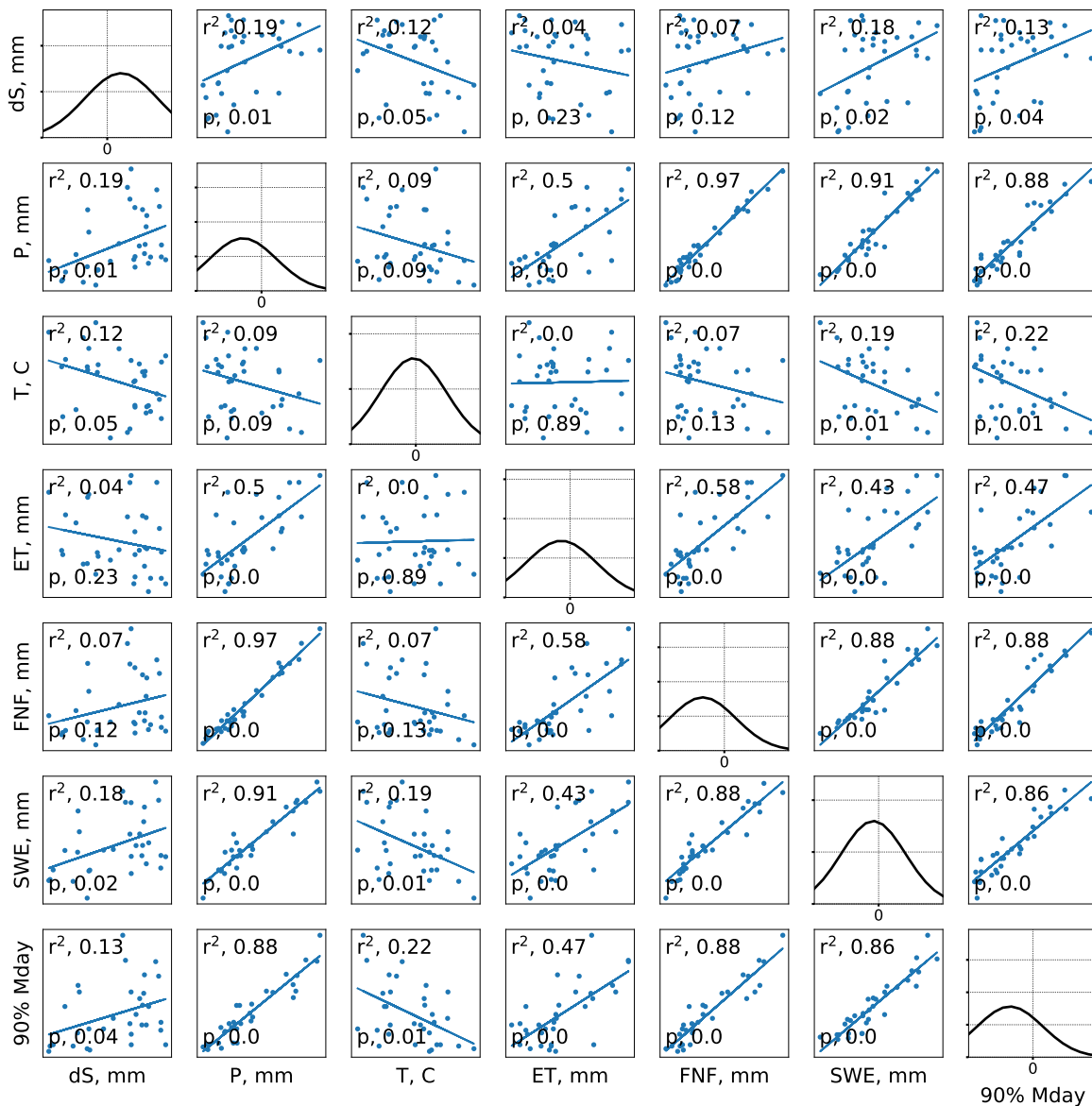


Figure C.1.10: Covariance matrix for San Joaquin, where dS is change in storage, P is precipitation, T is temperature, ET is evapotranspiration, FNF is unimpaired runoff, SWE is snow-water equivalent, and 90% Mday is the timing of 90% snowmelt from peak SWE.

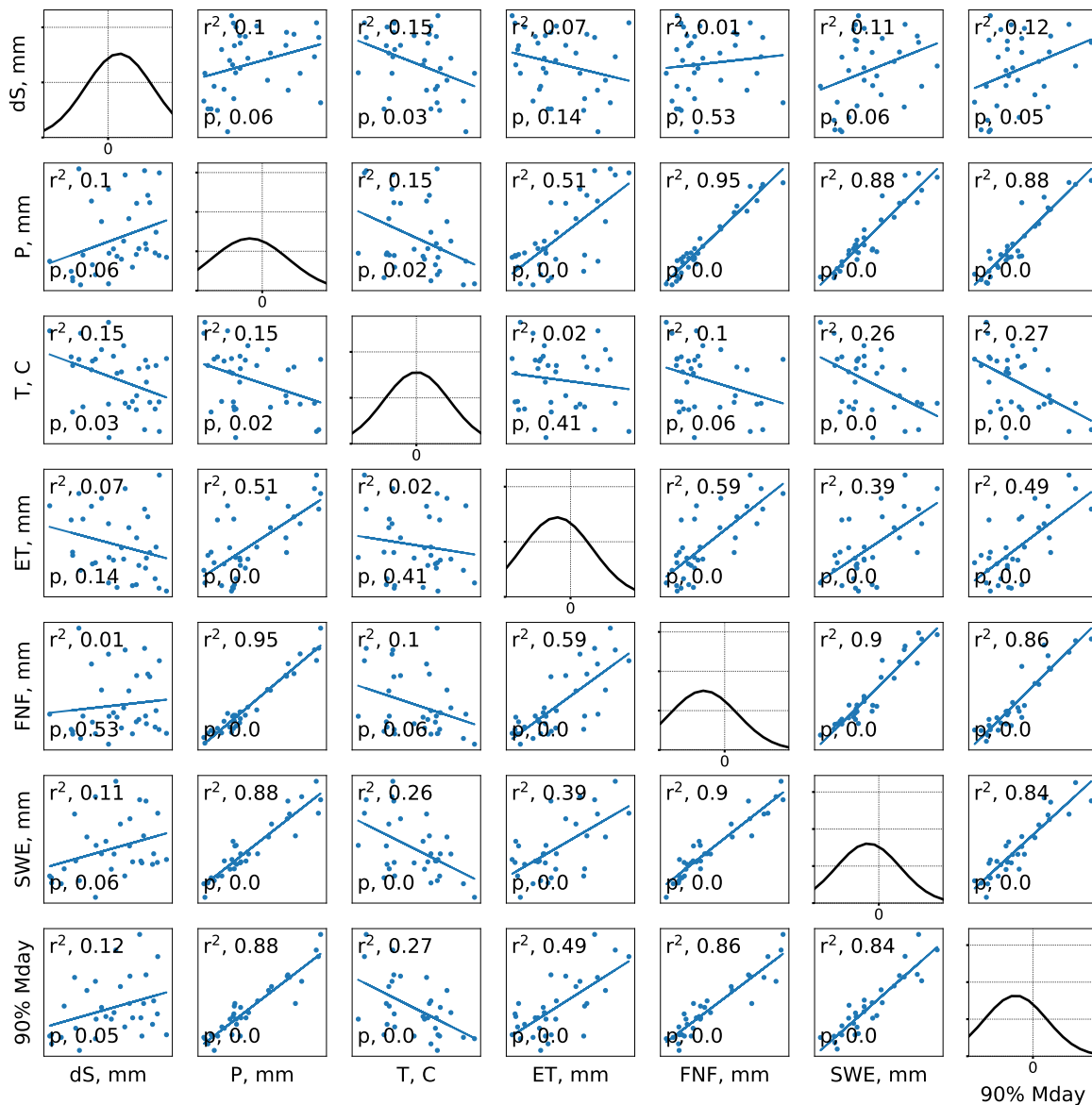


Figure C.1.11: Covariance matrix for Kings, where dS is change in storage, P is precipitation, T is temperature, ET is evapotranspiration, FNF is unimpaired runoff, SWE is snow-water equivalent, and 90% Mday is the timing of 90% snowmelt from peak SWE.

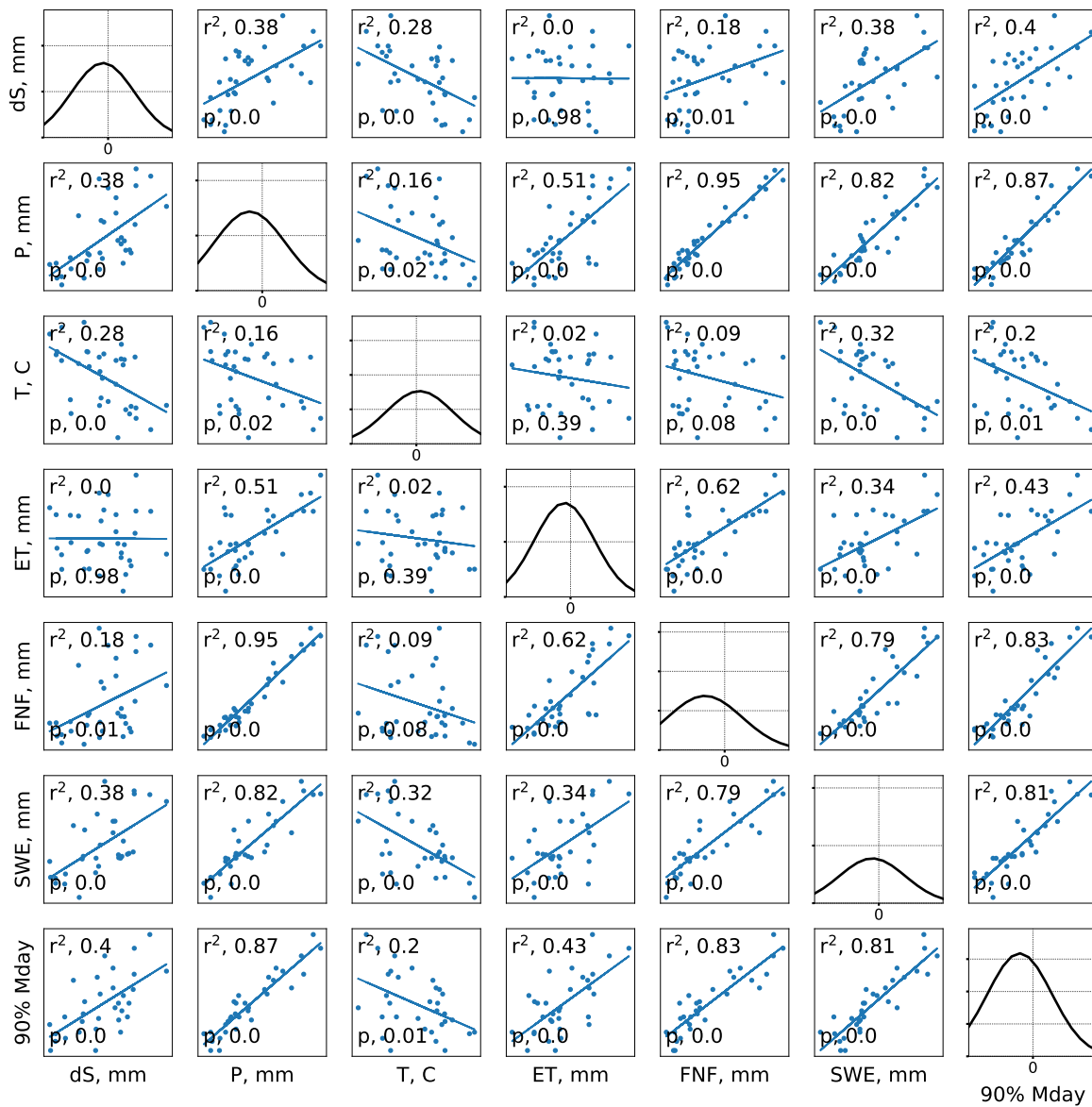


Figure C.1.12: Covariance matrix for Kaweah, where dS is change in storage, P is precipitation, T is temperature, ET is evapotranspiration, FNF is unimpaired runoff, SWE is snow-water equivalent, and 90% Mday is the timing of 90% snowmelt from peak SWE.

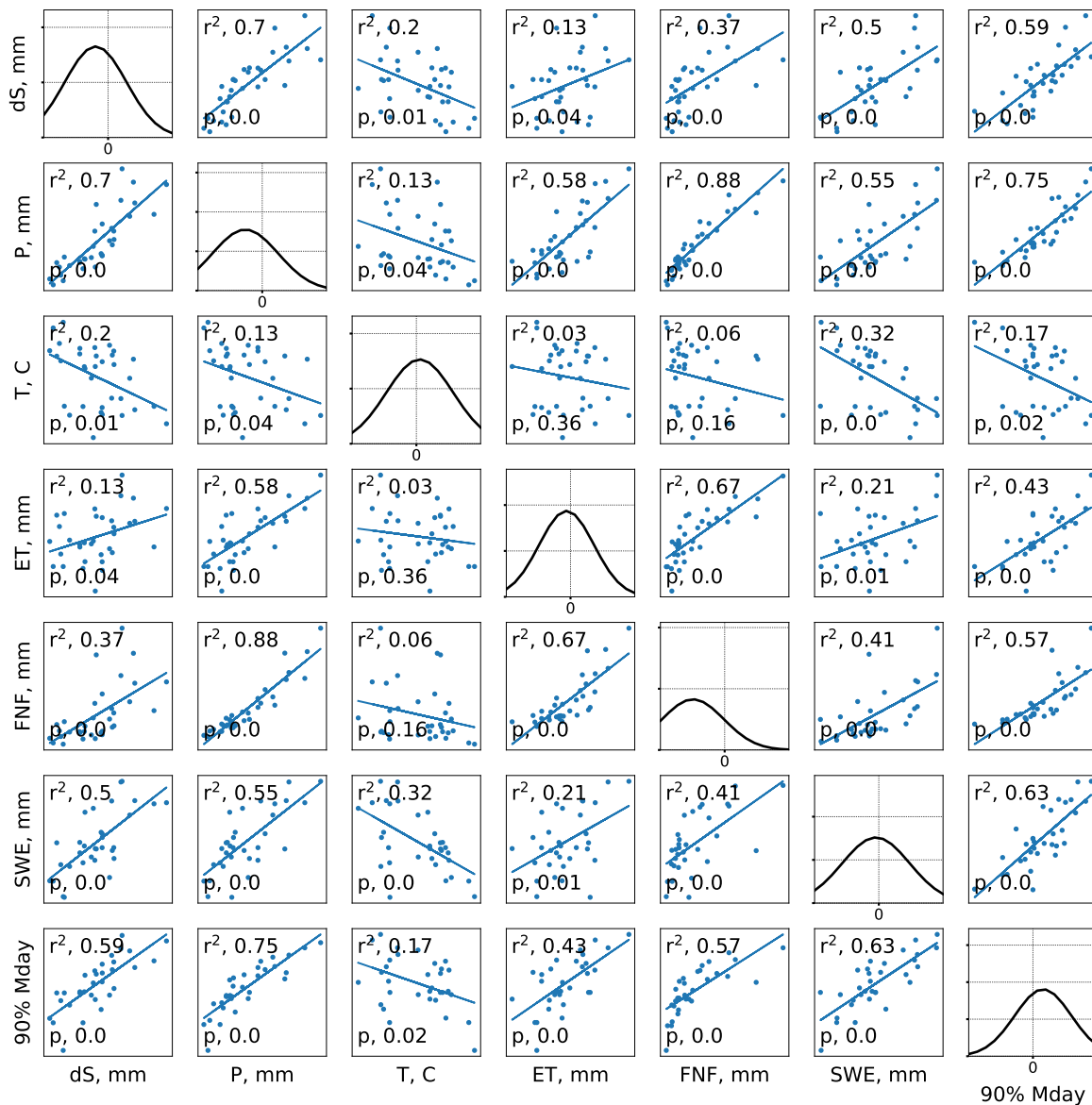


Figure C.1.13: Covariance matrix for Tule, where dS is change in storage, P is precipitation, T is temperature, ET is evapotranspiration, FNF is unimpaired runoff, SWE is snow-water equivalent, and 90% Mday is the timing of 90% snowmelt from peak SWE.

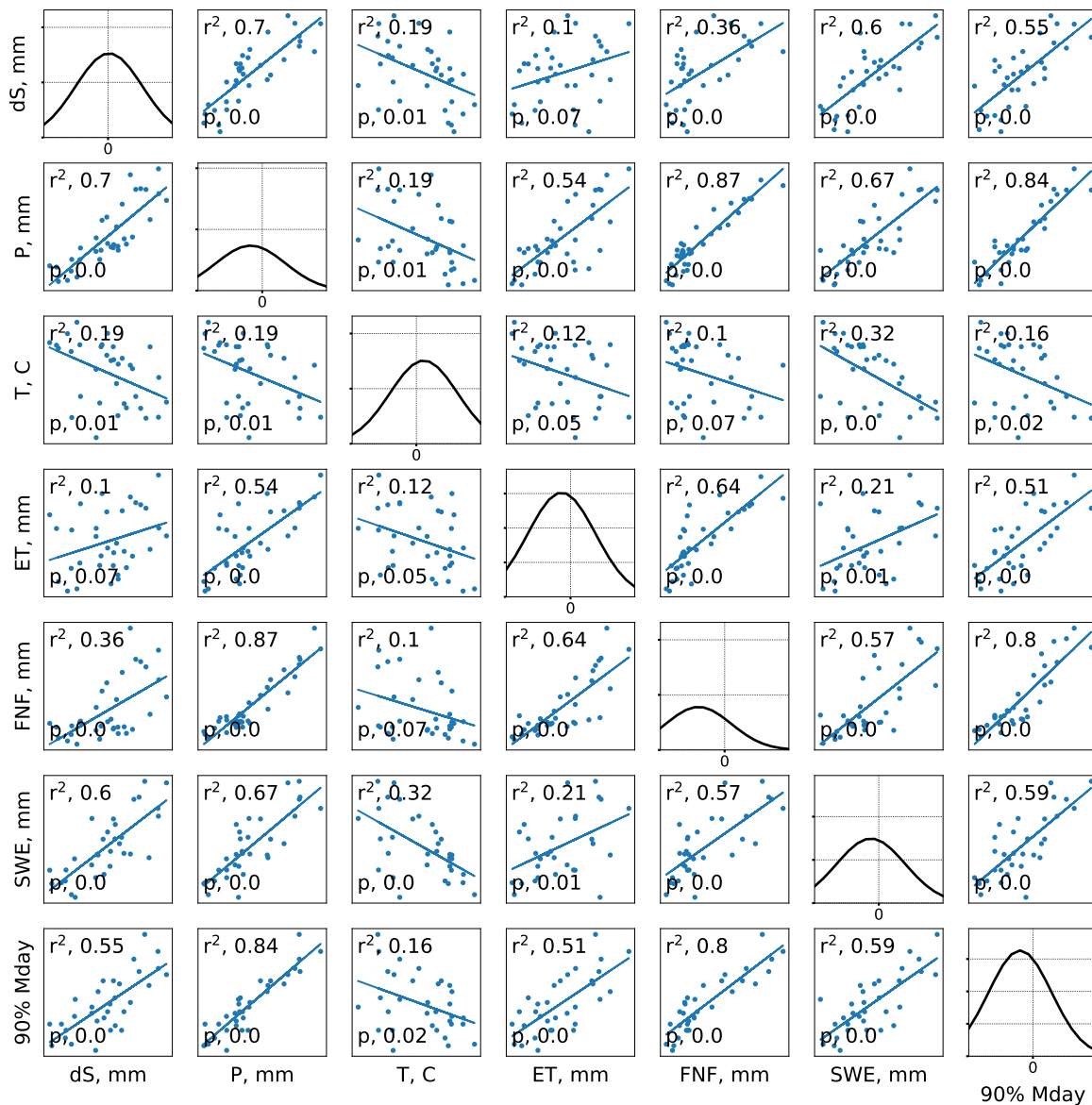


Figure C.1.14: Covariance matrix for Kern, where dS is change in storage, P is precipitation, T is temperature, ET is evapotranspiration, FNF is unimpaired runoff, SWE is snow-water equivalent, and 90% Mday is the timing of 90% snowmelt from peak SWE.

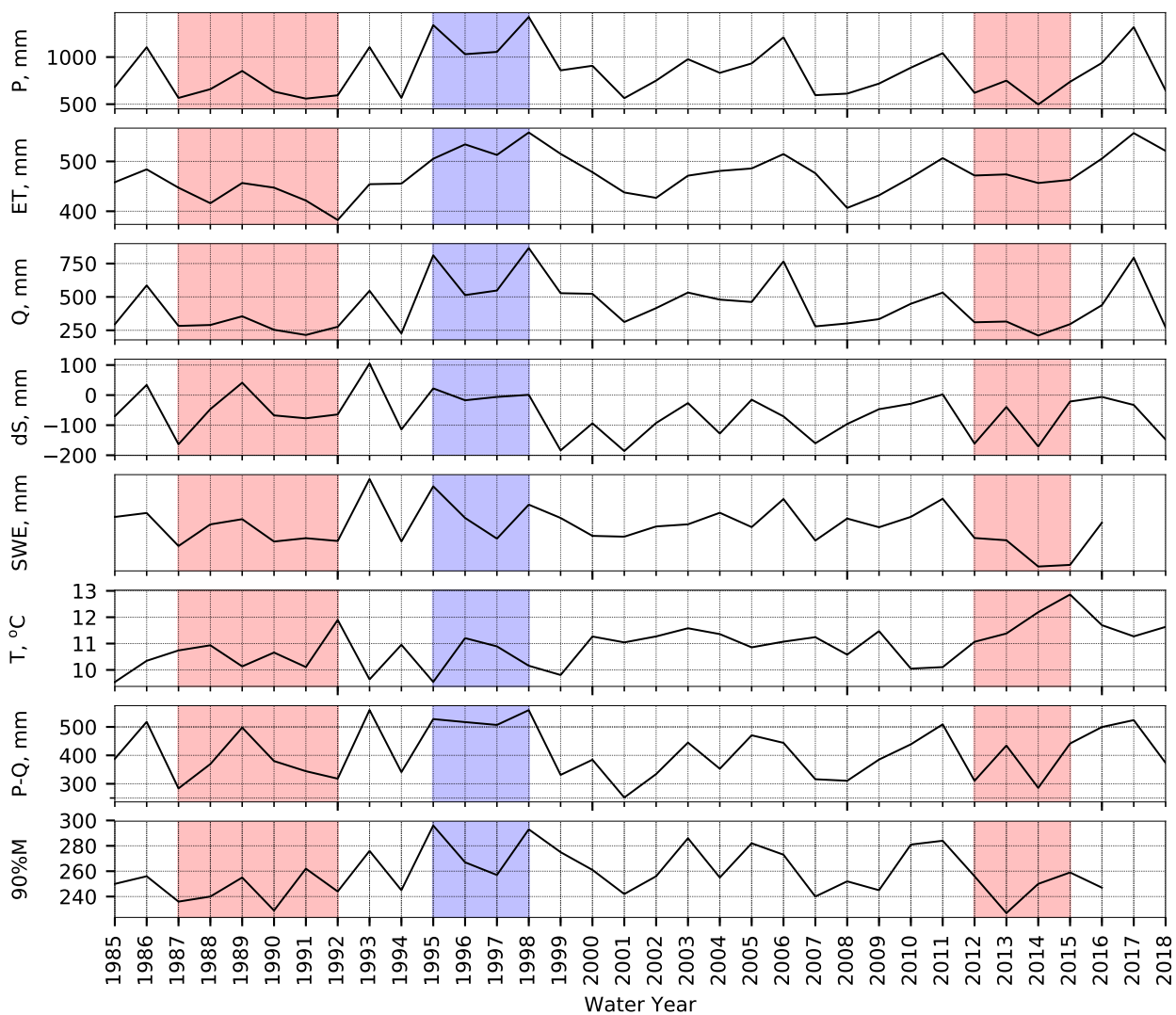


Figure C.2.1: Time series of major variables for Shasta. The red and blue vertical shading represents multiyear dry and wet periods, respectively.

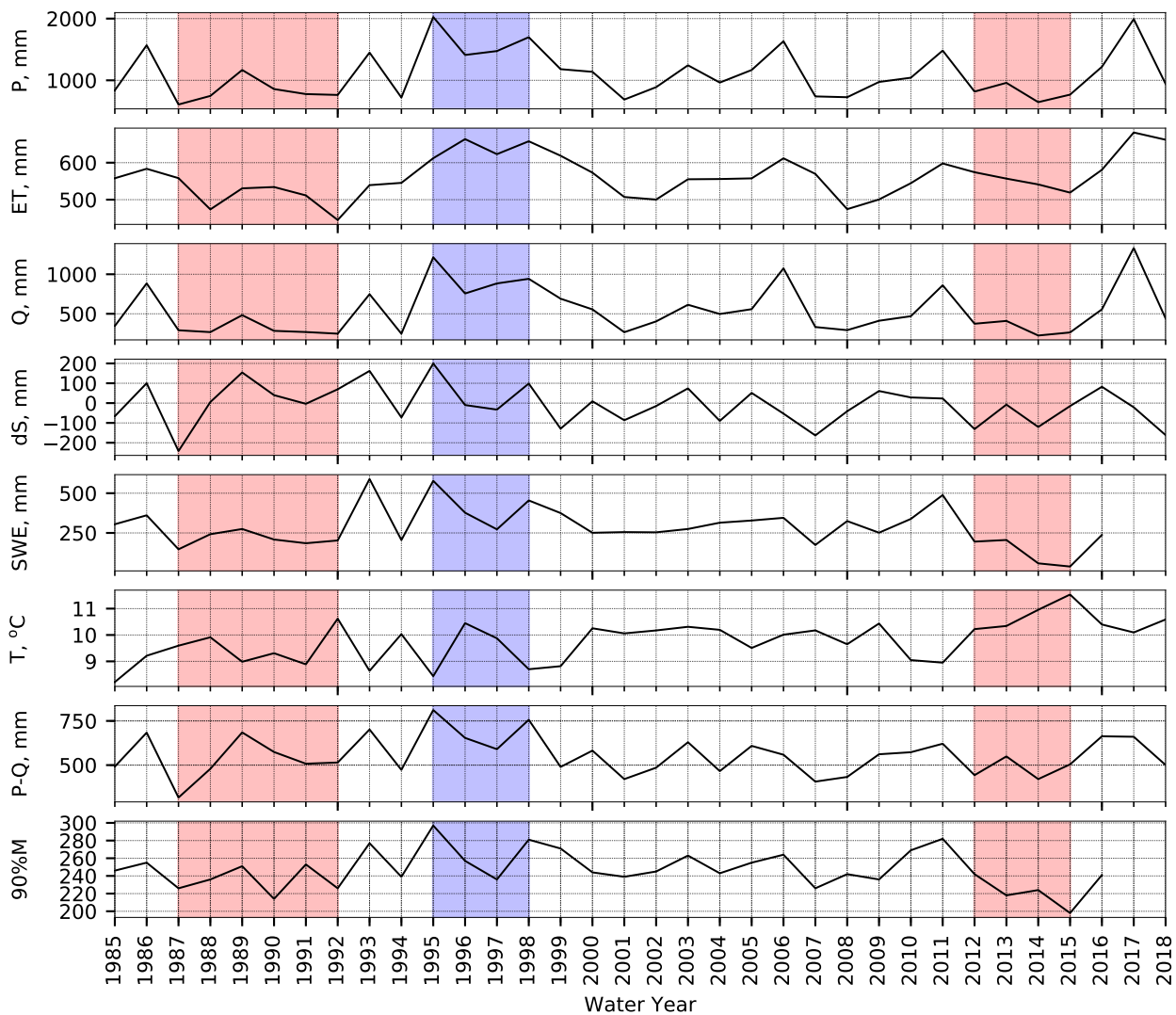


Figure C.2.2: Time series of major variables for Feather. The red and blue vertical shading represents multiyear dry and wet periods, respectively.

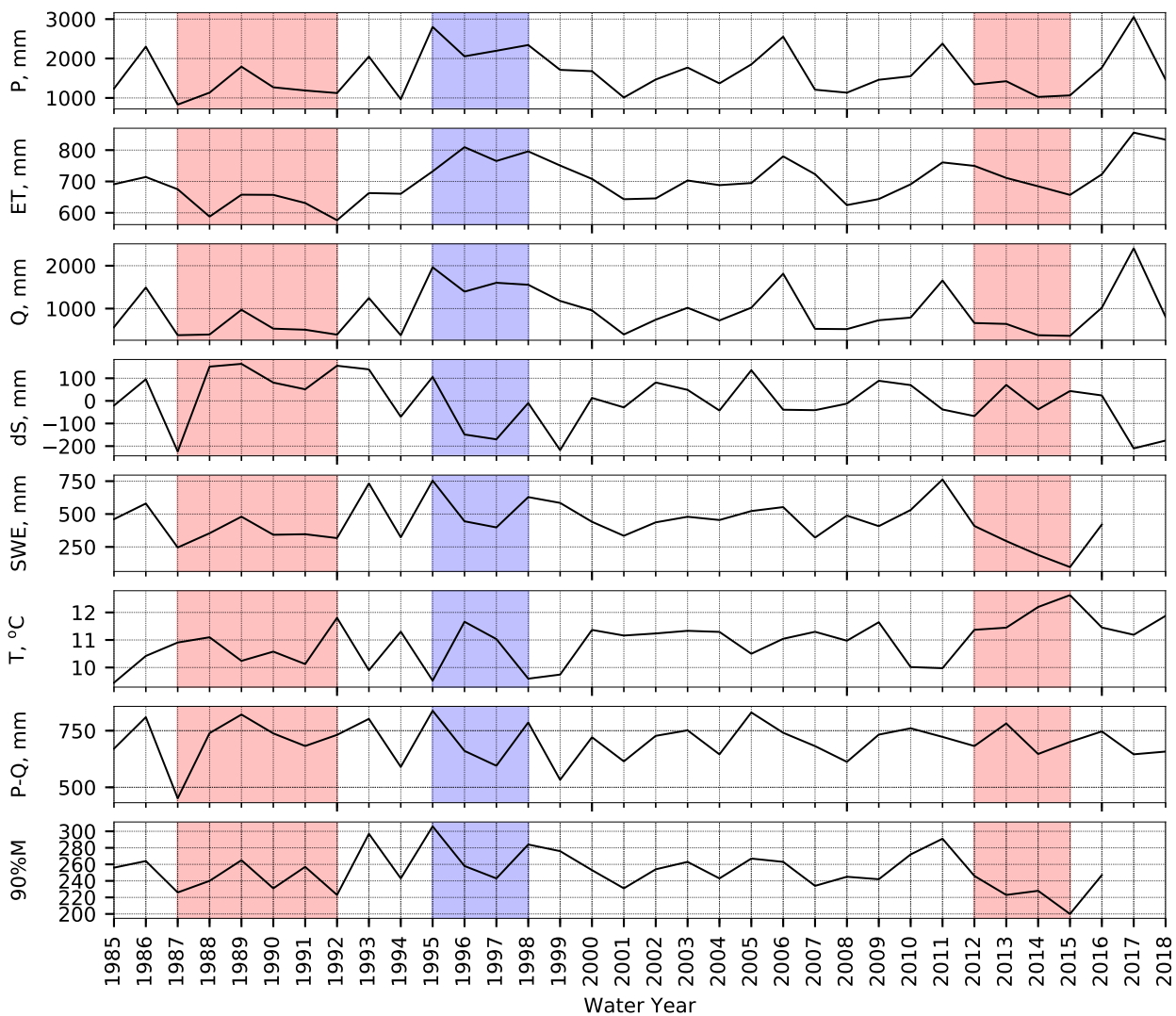


Figure C.2.3: Time series of major variables for Yuba. The red and blue vertical shading represents multiyear dry and wet periods, respectively.

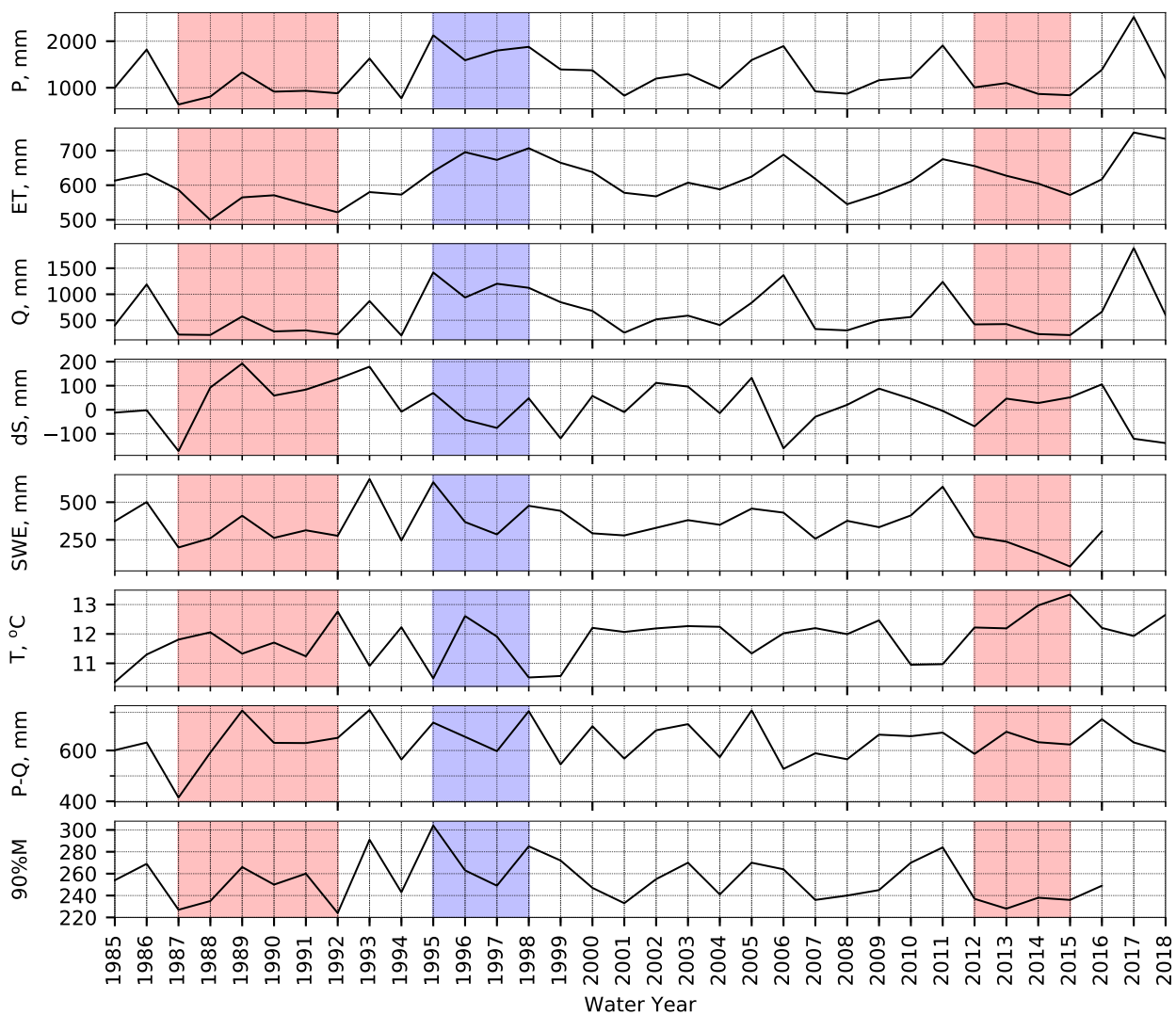


Figure C.2.4: Time series of major variables for American. The red and blue vertical shading represents multiyear dry and wet periods, respectively.

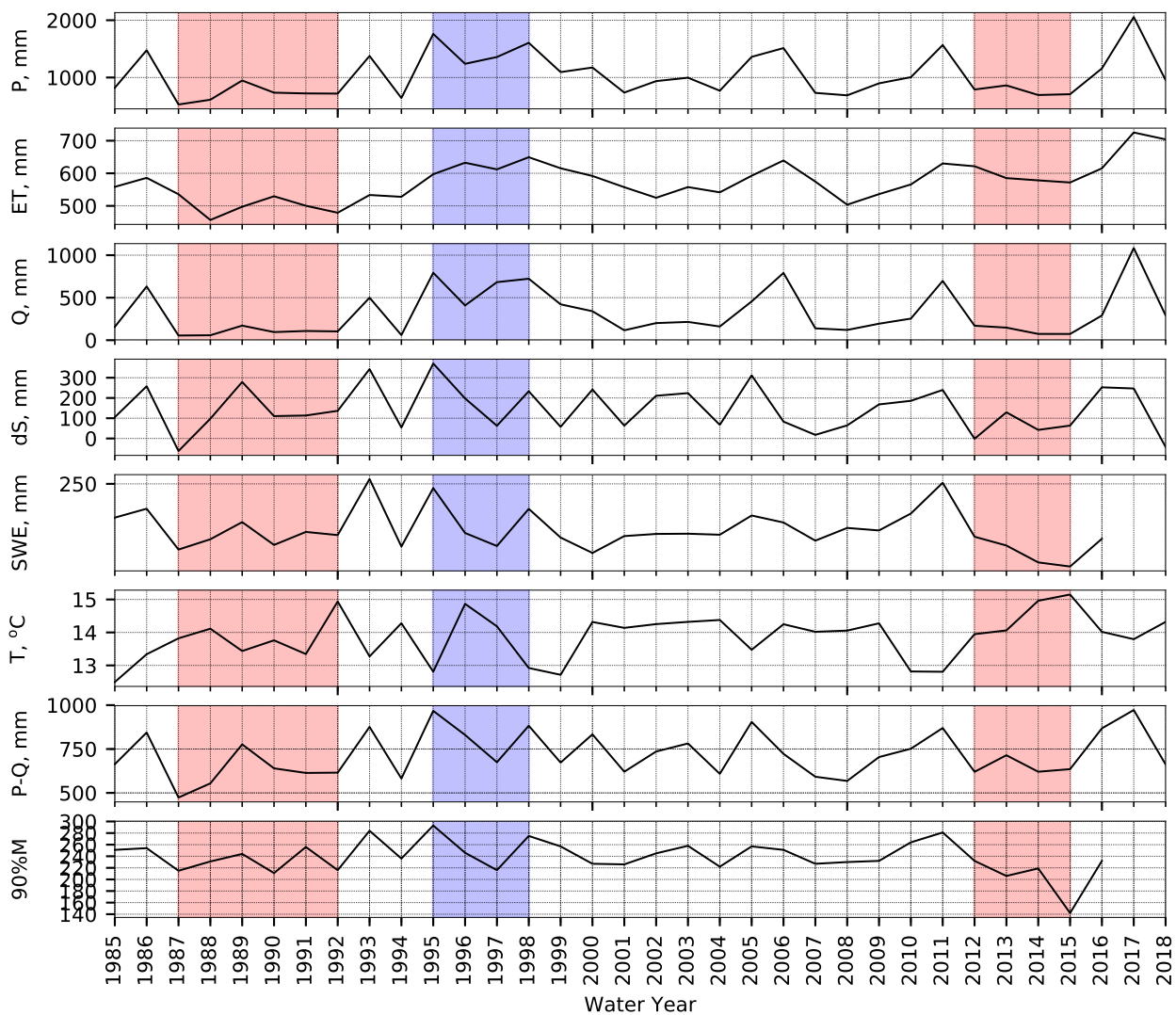


Figure C.2.5: Time series of major variables for Cosumnes. The red and blue vertical shading represents multiyear dry and wet periods, respectively.

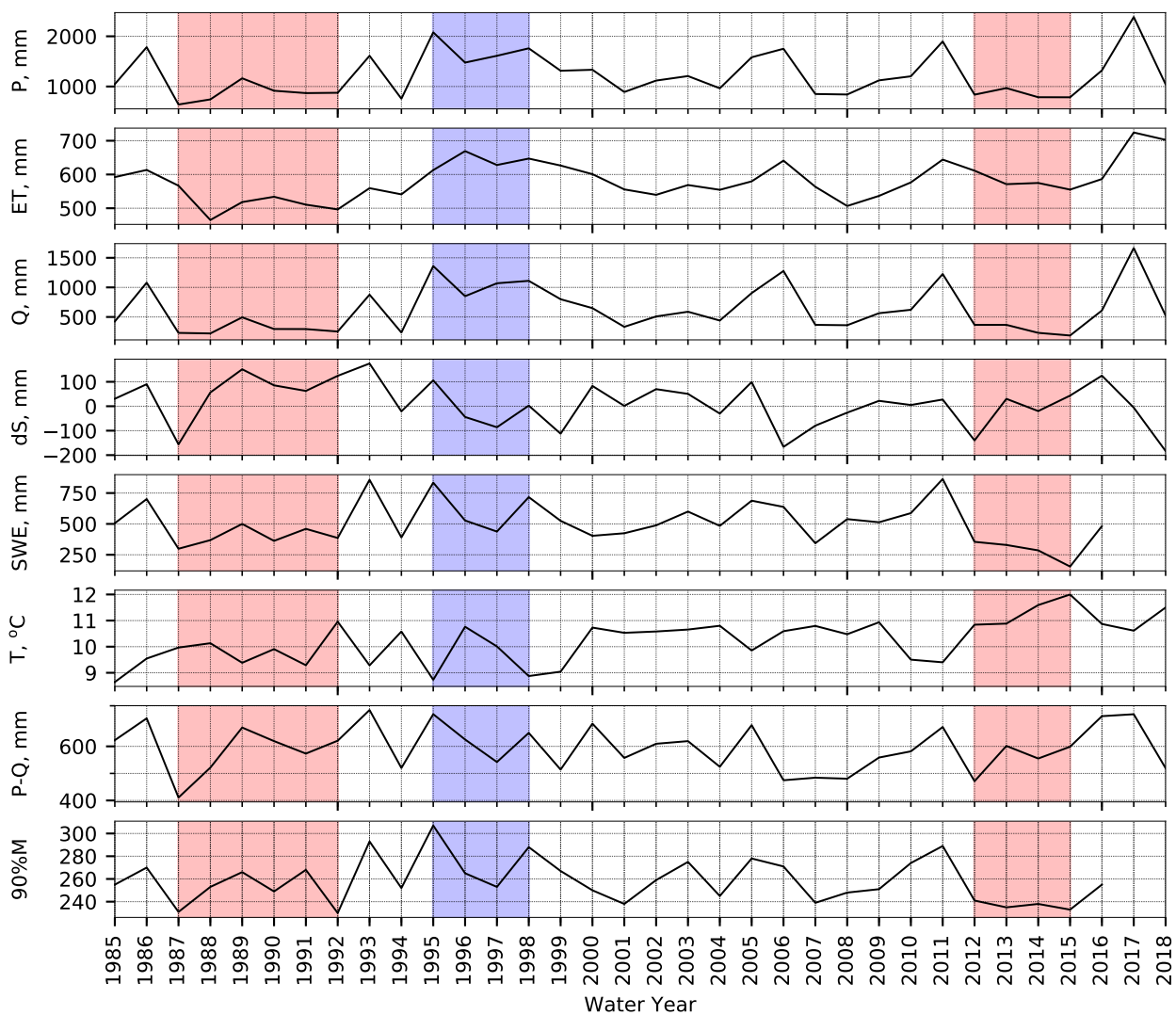


Figure C.2.6: Time series of major variables for Mokelumne. The red and blue vertical shading represents multiyear dry and wet periods, respectively.

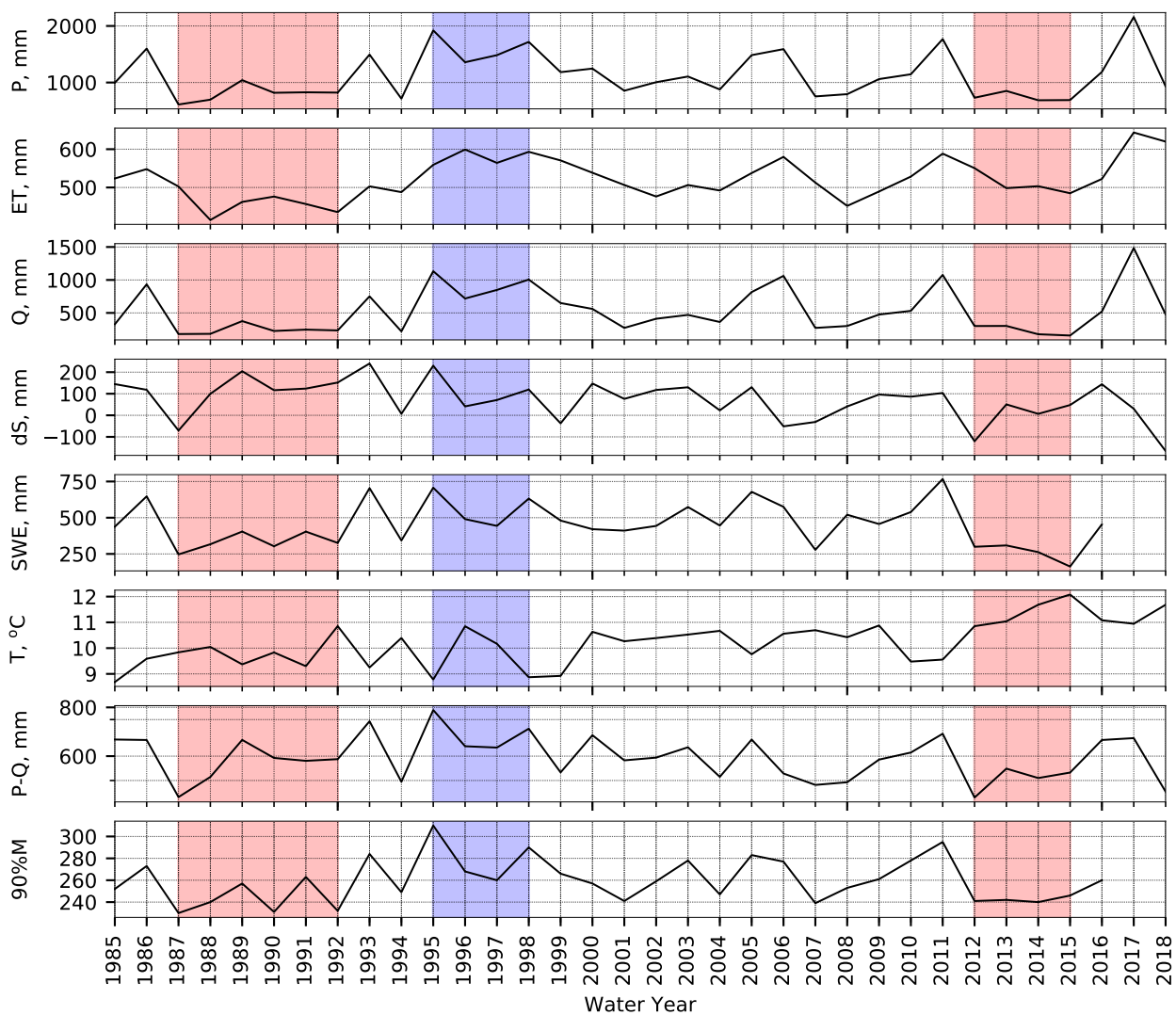


Figure C.2.7: Time series of major variables for Stanislaus. The red and blue vertical shading represents multiyear dry and wet periods, respectively.

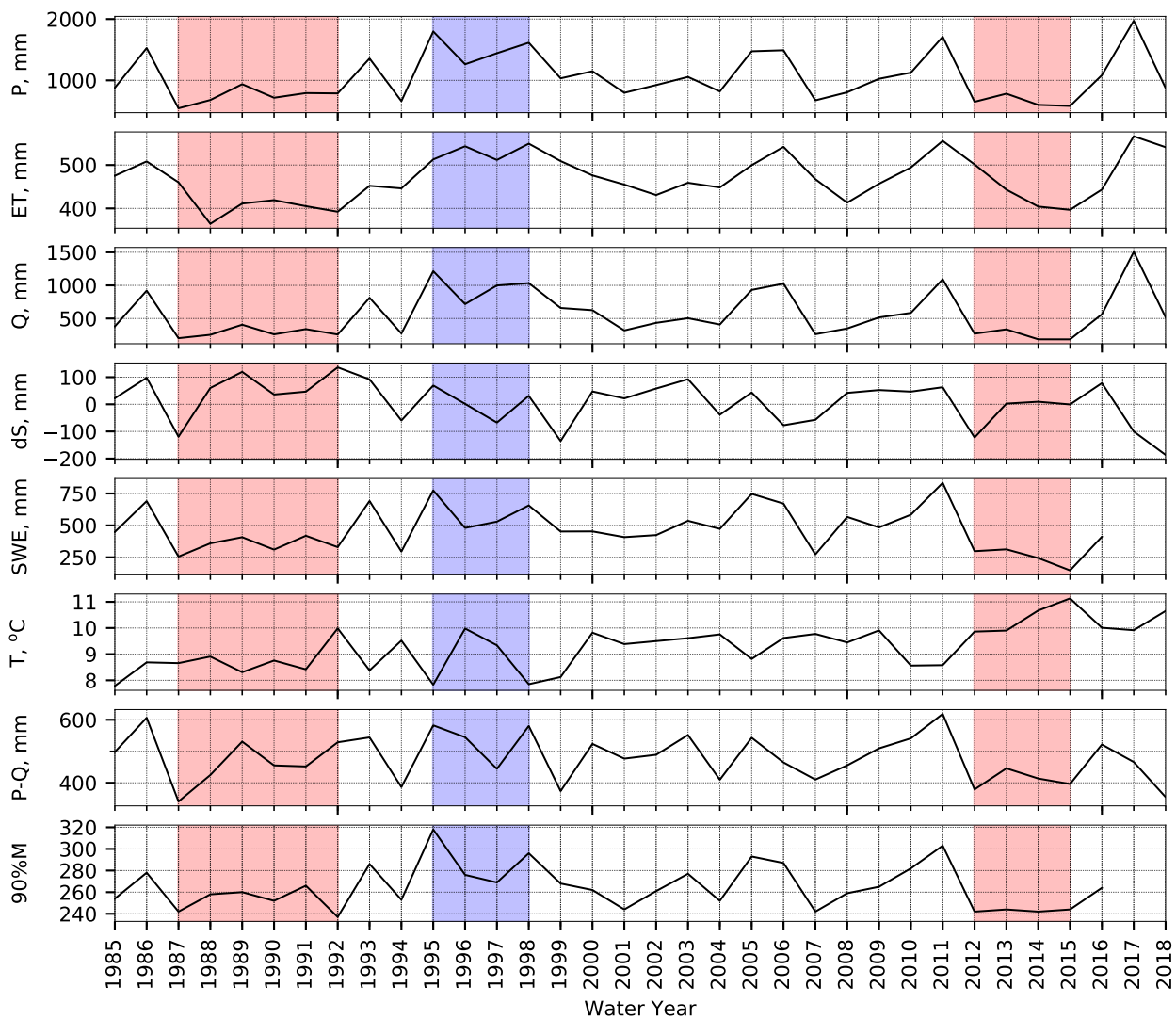


Figure C.2.8: Time series of major variables for Tuolumne. The red and blue vertical shading represents multiyear dry and wet periods, respectively.

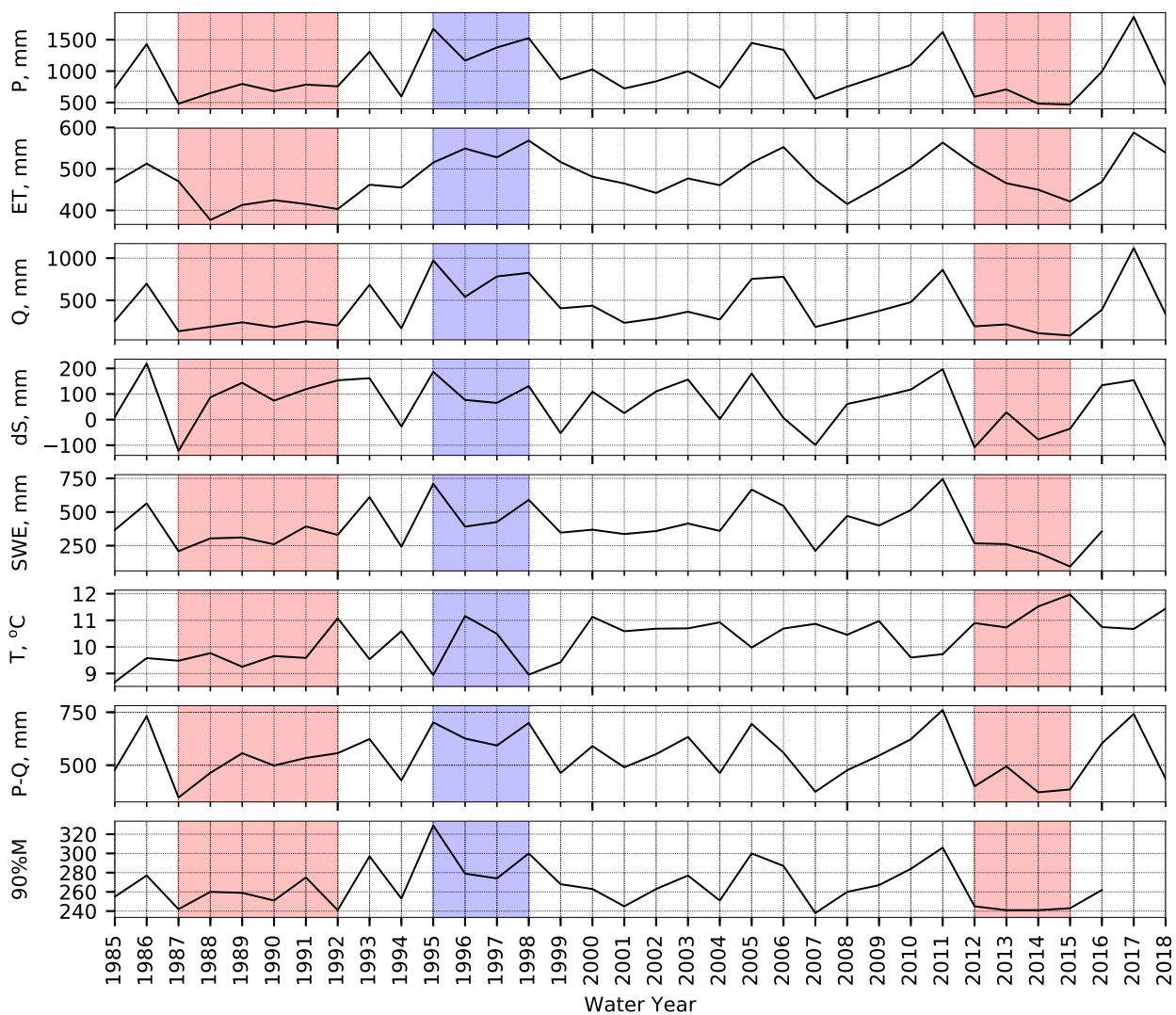


Figure C.2.9: Time series of major variables for Merced. The red and blue vertical shading represents multiyear dry and wet periods, respectively.

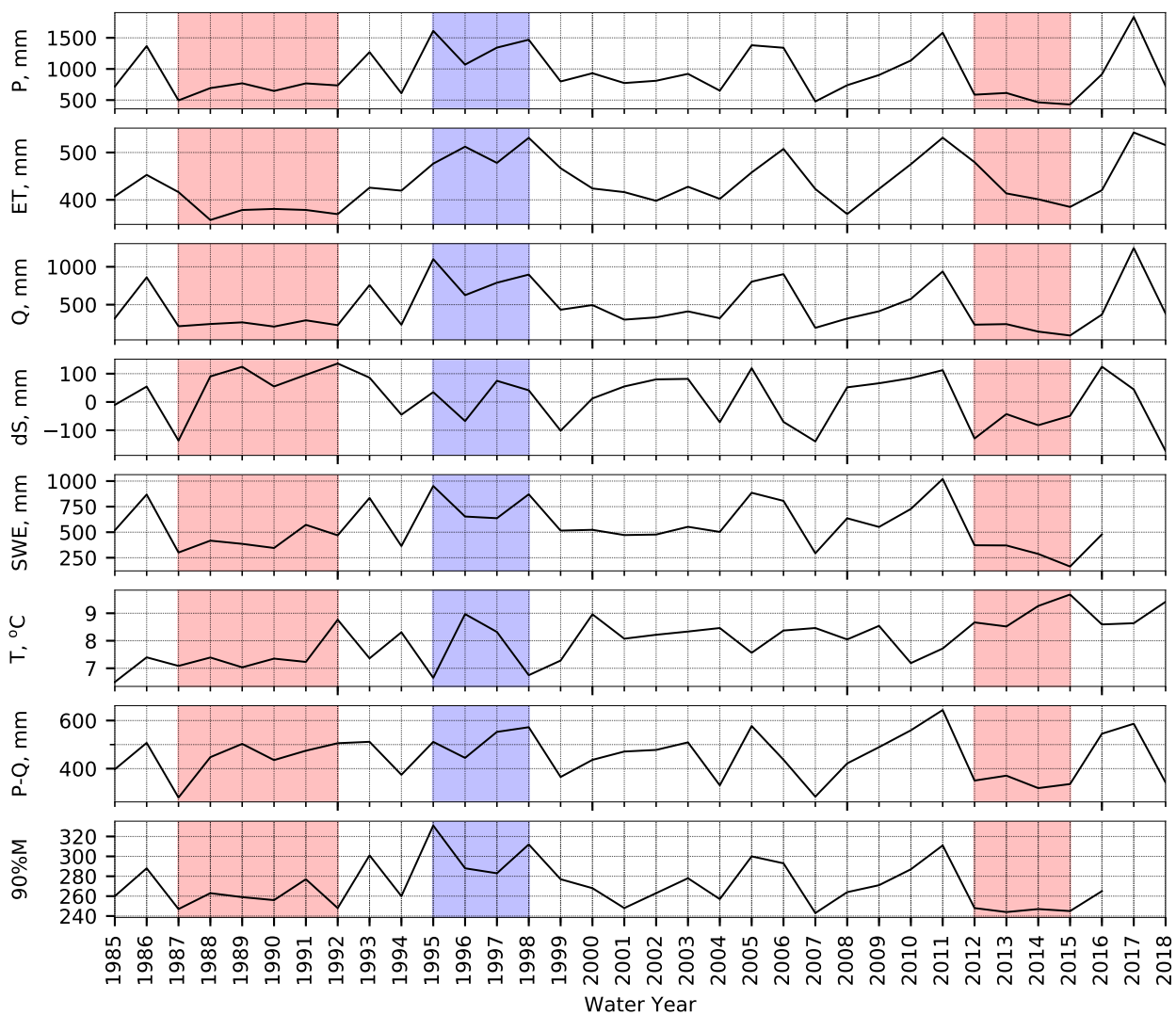


Figure C.2.10: Time series of major variables for San Joaquin. The red and blue vertical shading represents multiyear dry and wet periods, respectively.

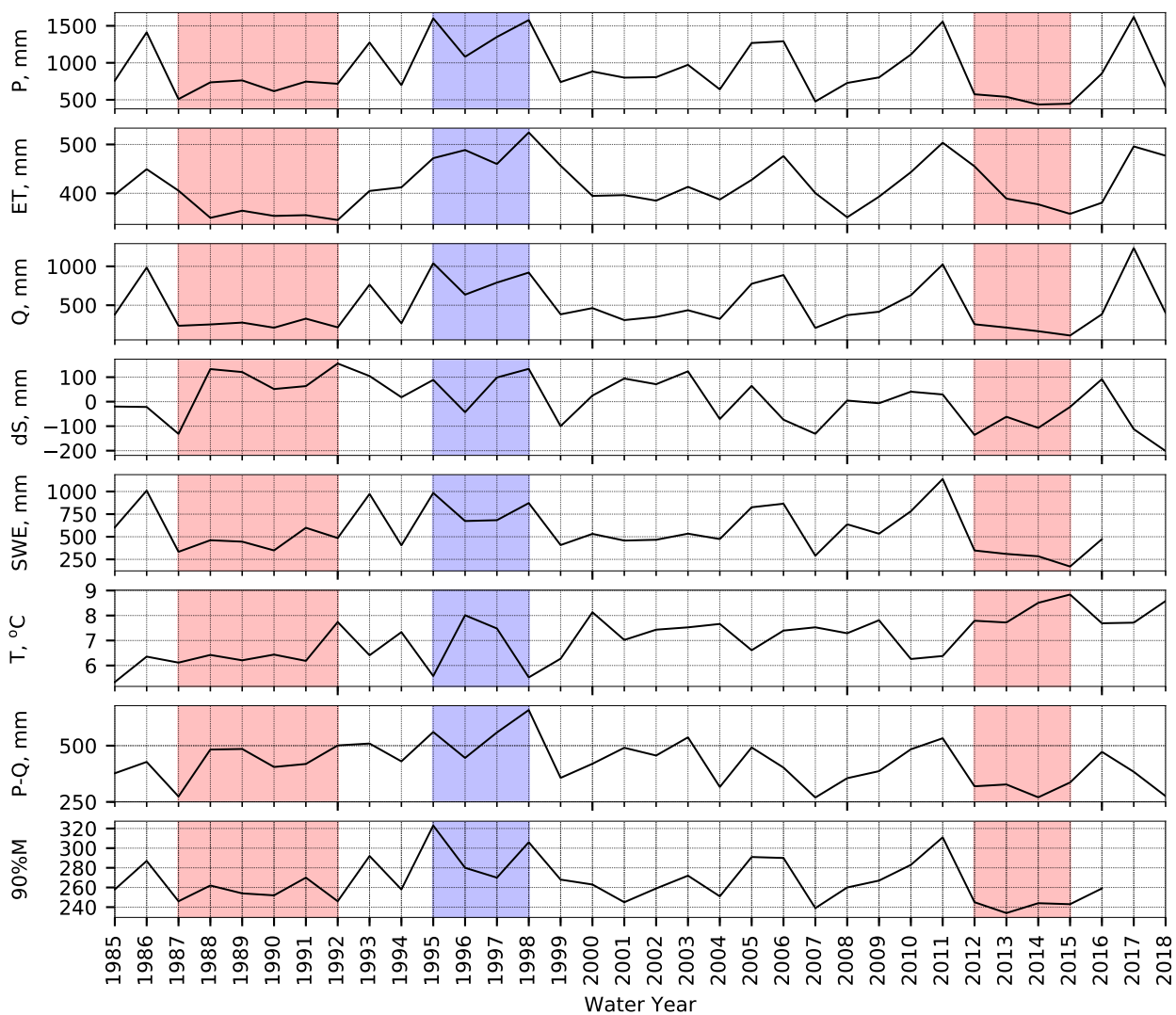


Figure C.2.11: Time series of major variables for Kings. The red and blue vertical shading represents multiyear dry and wet periods, respectively.

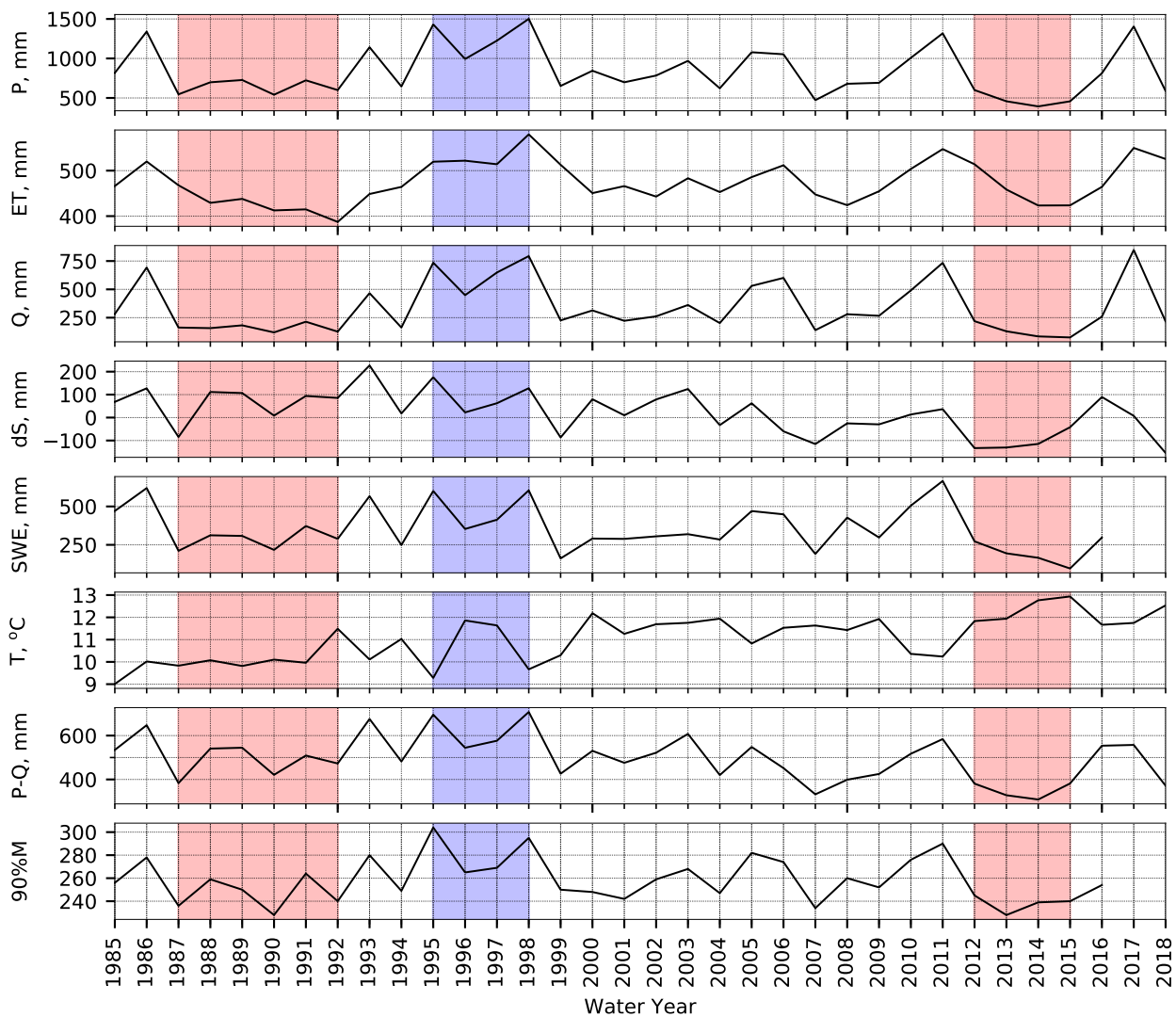


Figure C.2.12: Time series of major variables for Kaweah. The red and blue vertical shading represents multiyear dry and wet periods, respectively.

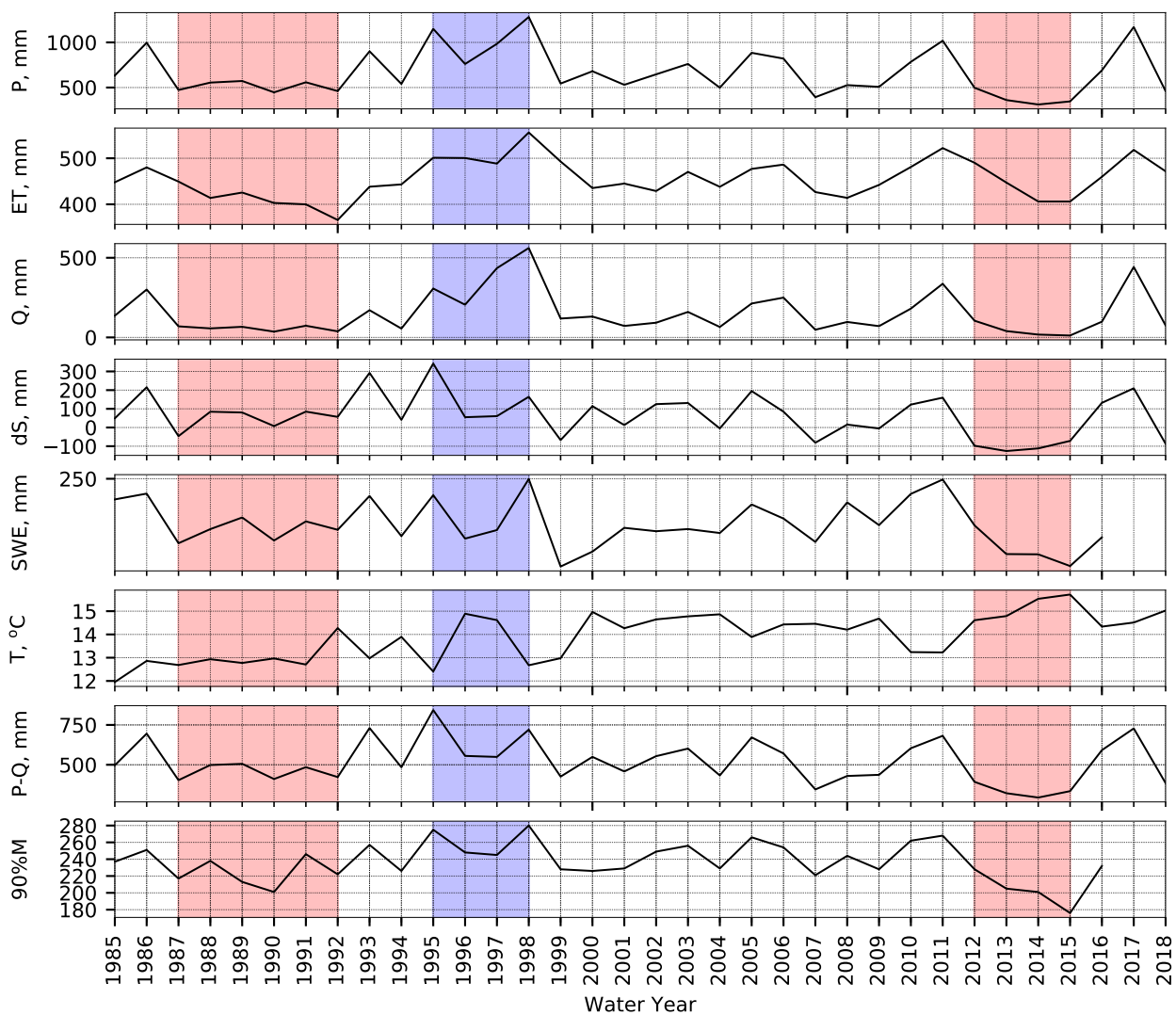


Figure C.2.13: Time series of major variables for Tule. The red and blue vertical shading represents multiyear dry and wet periods, respectively.

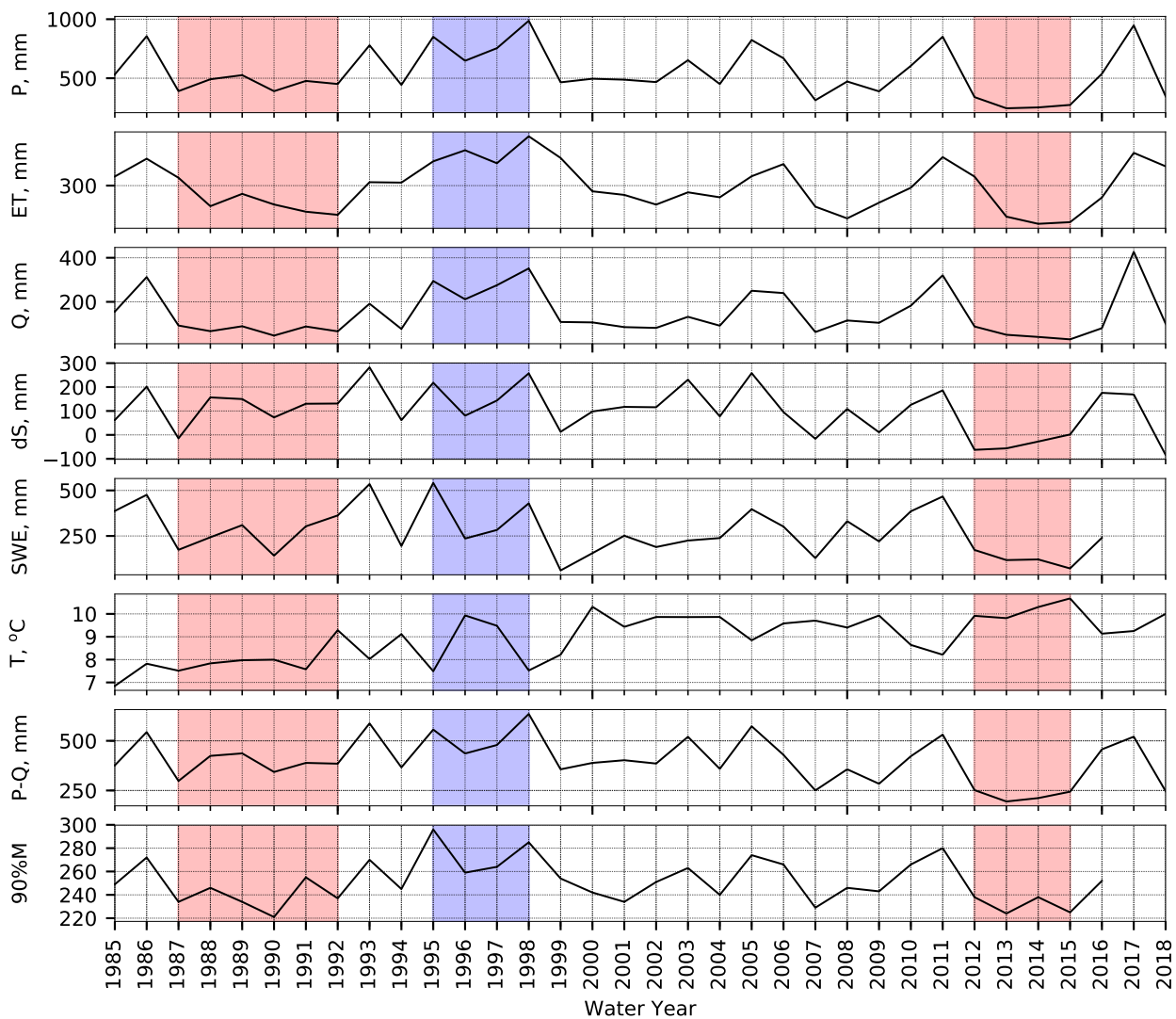


Figure C.2.14: Time series of major variables for Kern. The red and blue vertical shading represents multiyear dry and wet periods, respectively.

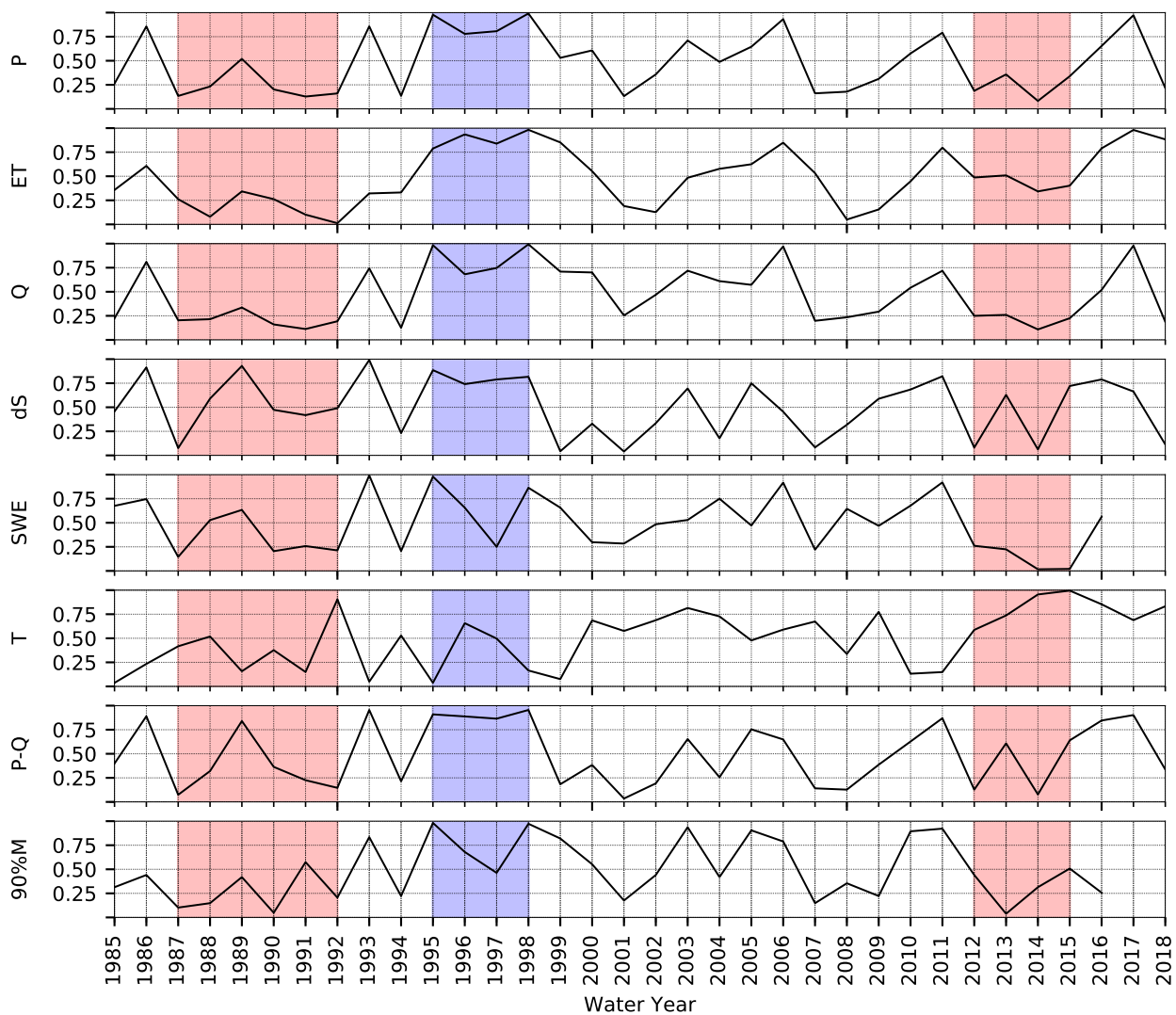


Figure C.3.1: Time series of normalized major variables for Shasta. The red and blue vertical shading represents multiyear dry and wet periods, respectively.

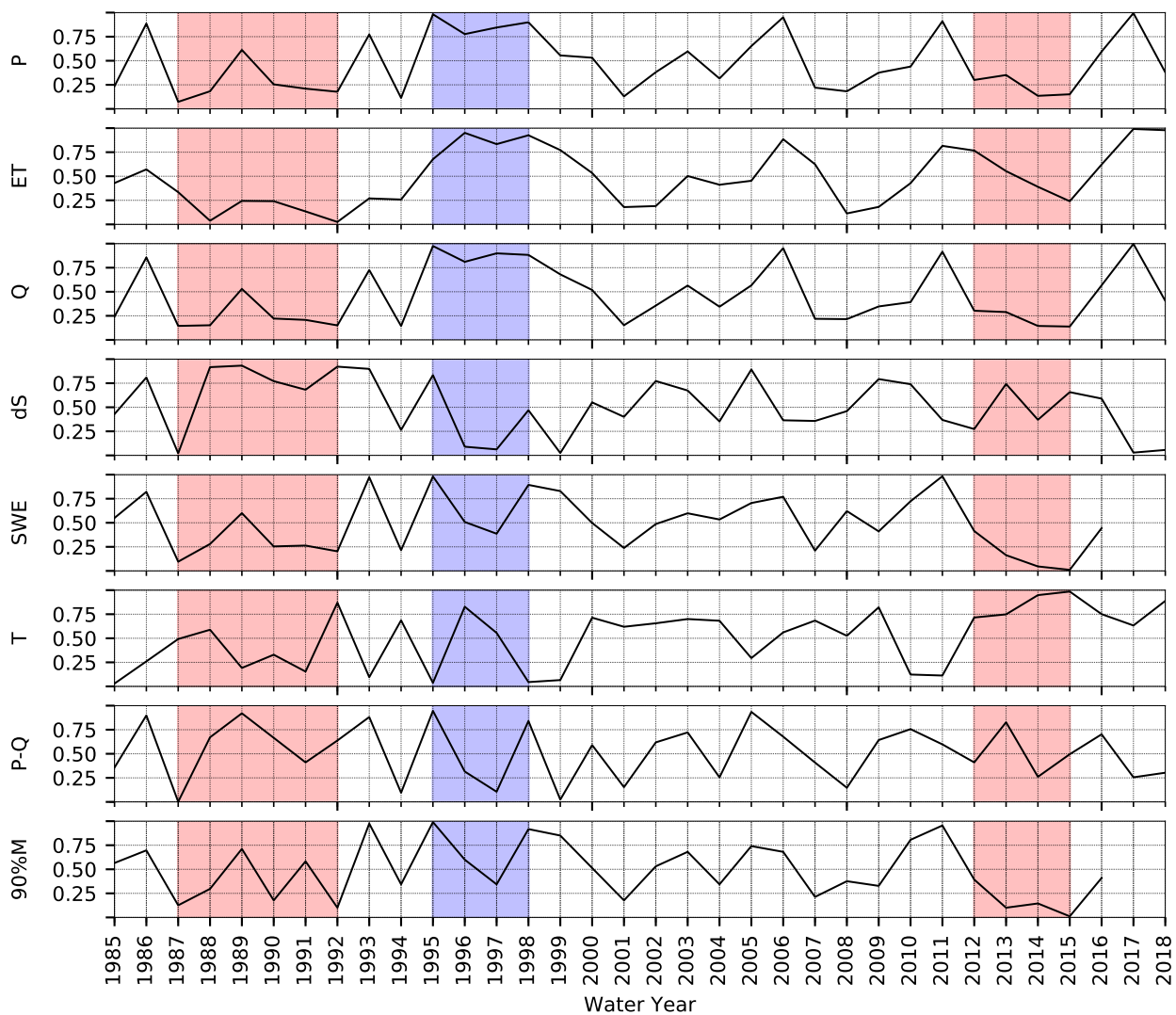


Figure C.3.2: Time series of normalized major variables for Yuba. The red and blue vertical shading represents multiyear dry and wet periods, respectively.

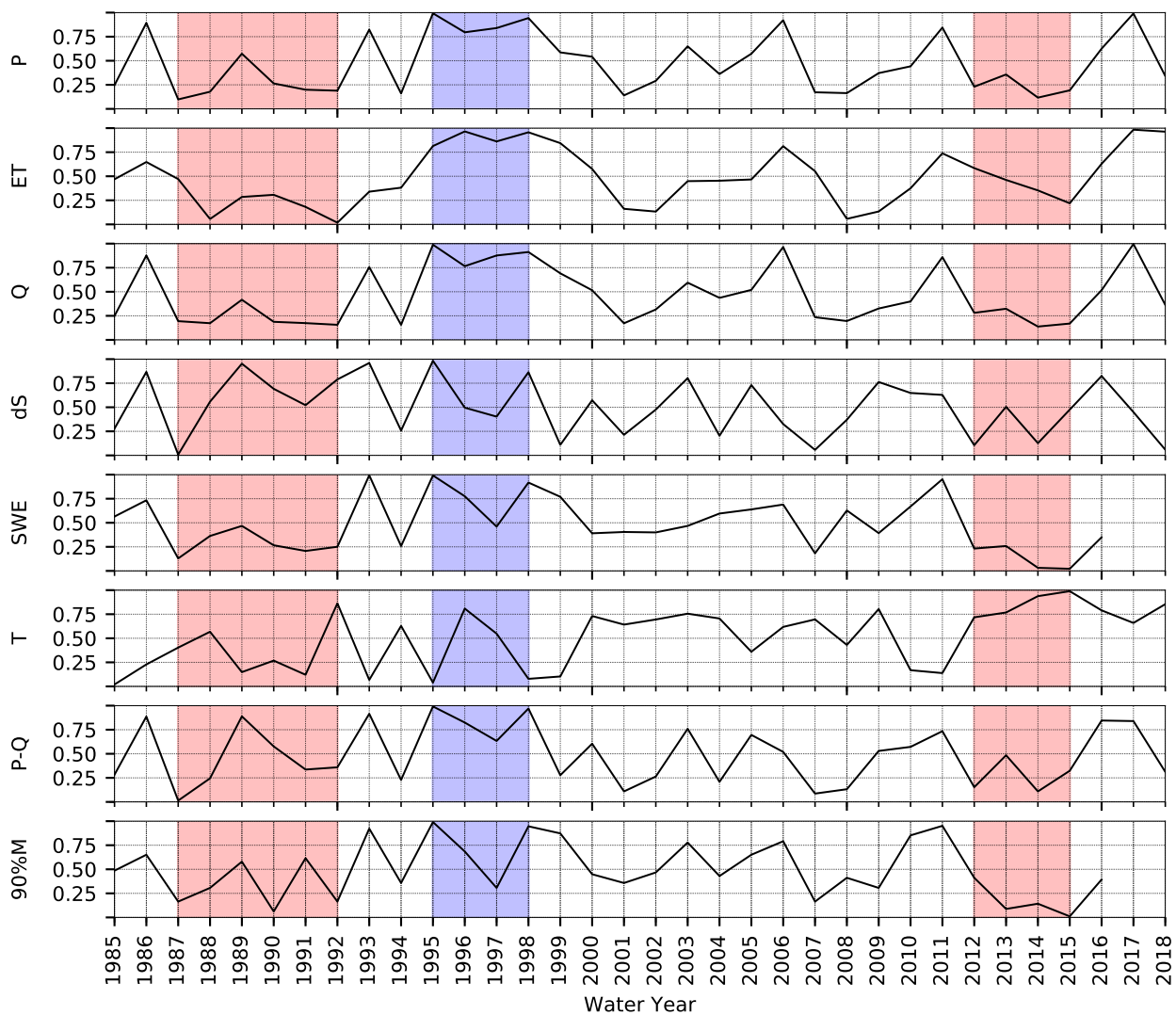


Figure C.3.3: Time series of normalized major variables for Feather. The red and blue vertical shading represents multiyear dry and wet periods, respectively.

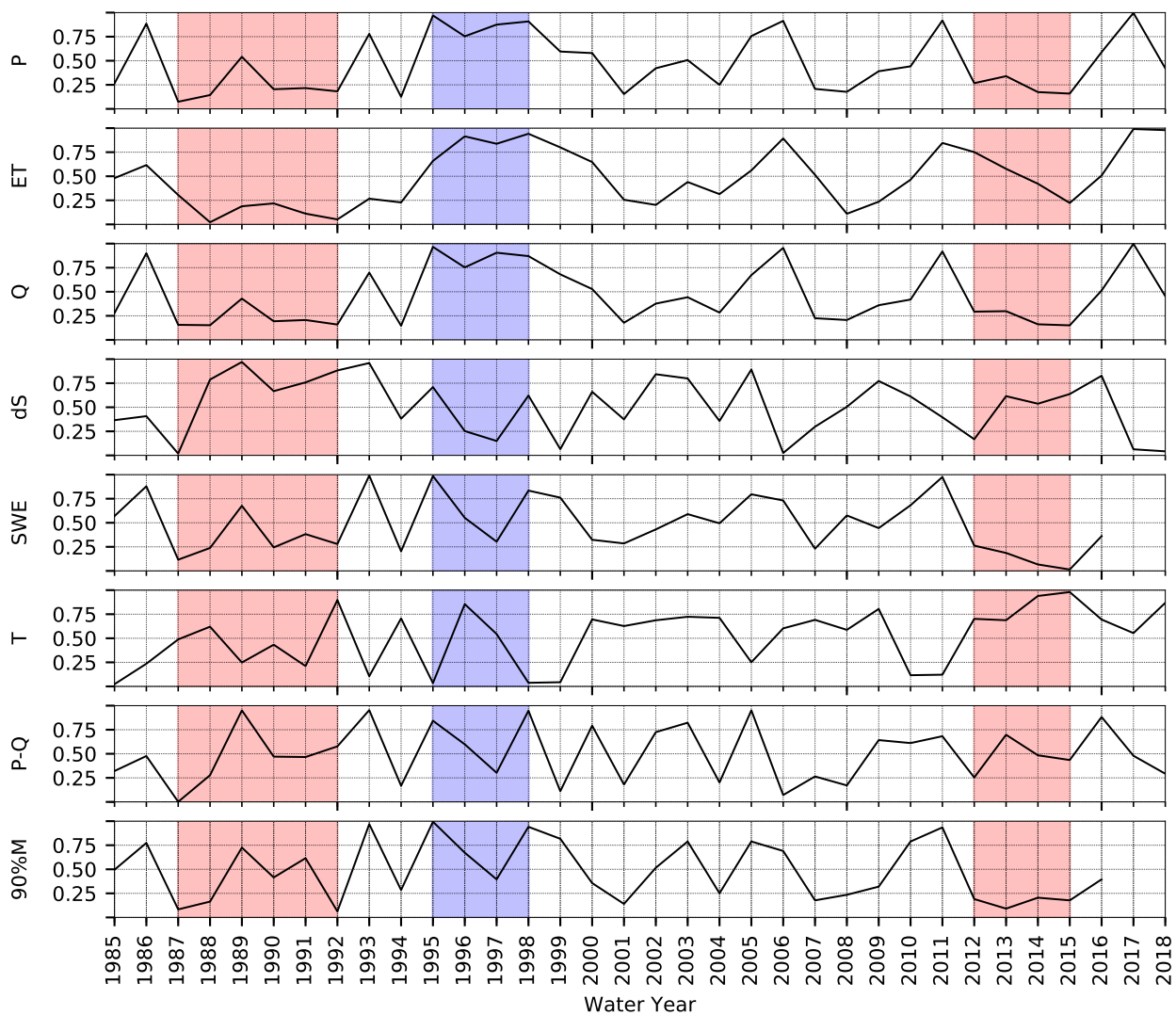


Figure C.3.4: Time series of normalized major variables for American. The red and blue vertical shading represents multiyear dry and wet periods, respectively.

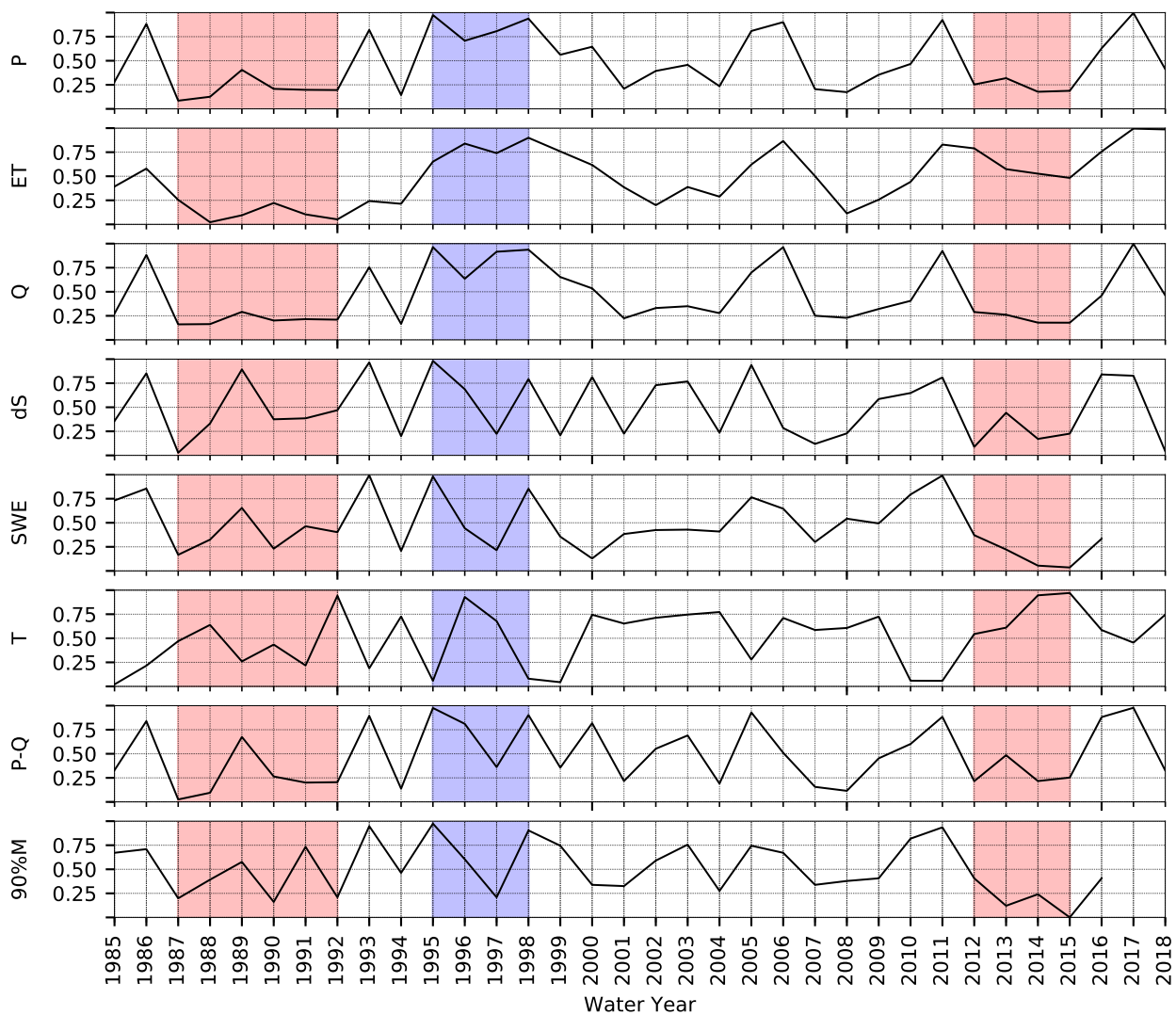


Figure C.3.5: Time series of normalized major variables for Cosumnes. The red and blue vertical shading represents multiyear dry and wet periods, respectively.

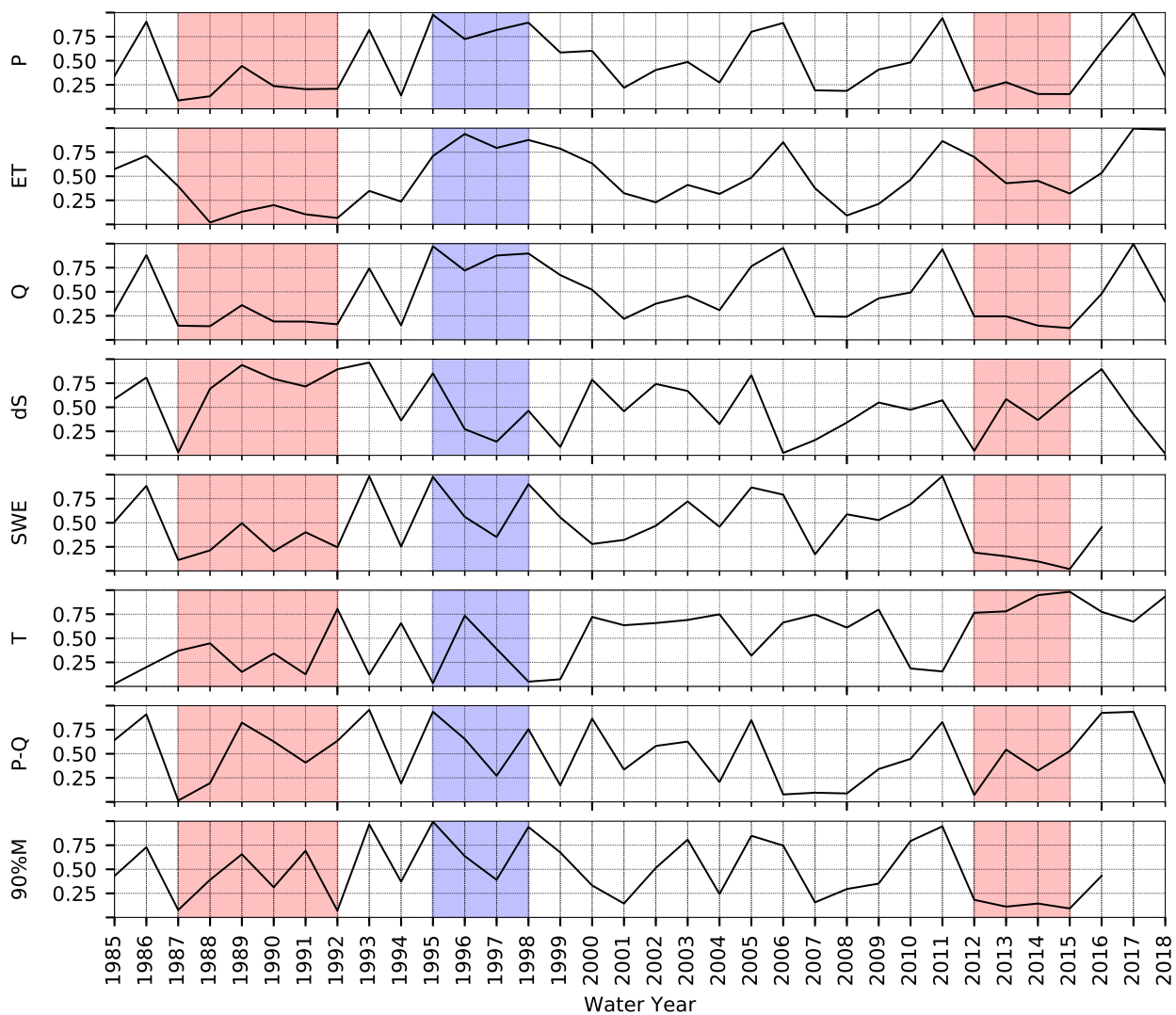


Figure C.3.6: Time series of normalized major variables for Mokelumne. The red and blue vertical shading represents multiyear dry and wet periods, respectively.

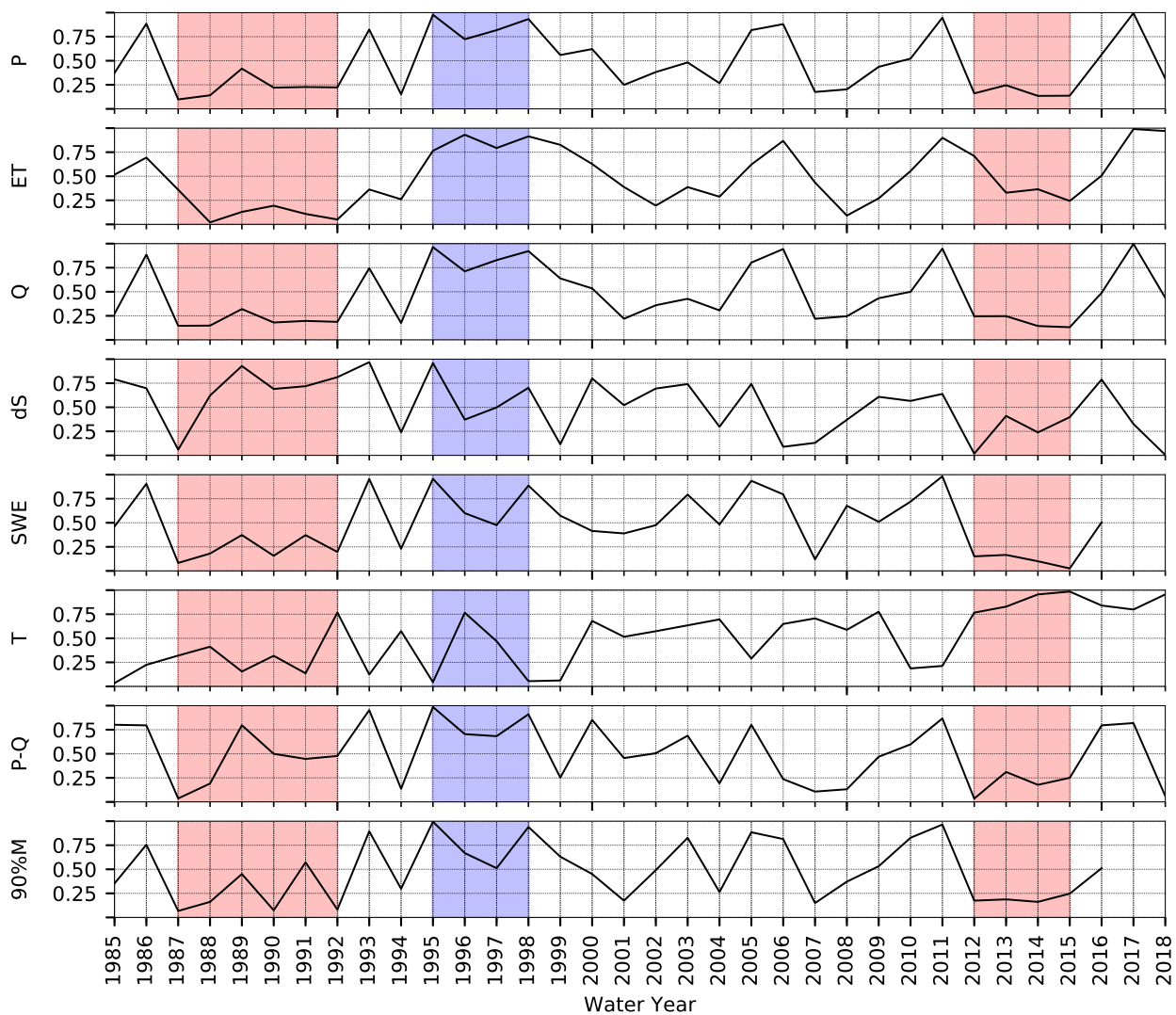


Figure C.3.7: Time series of normalized major variables for Stanislaus. The red and blue vertical shading represents multiyear dry and wet periods, respectively.

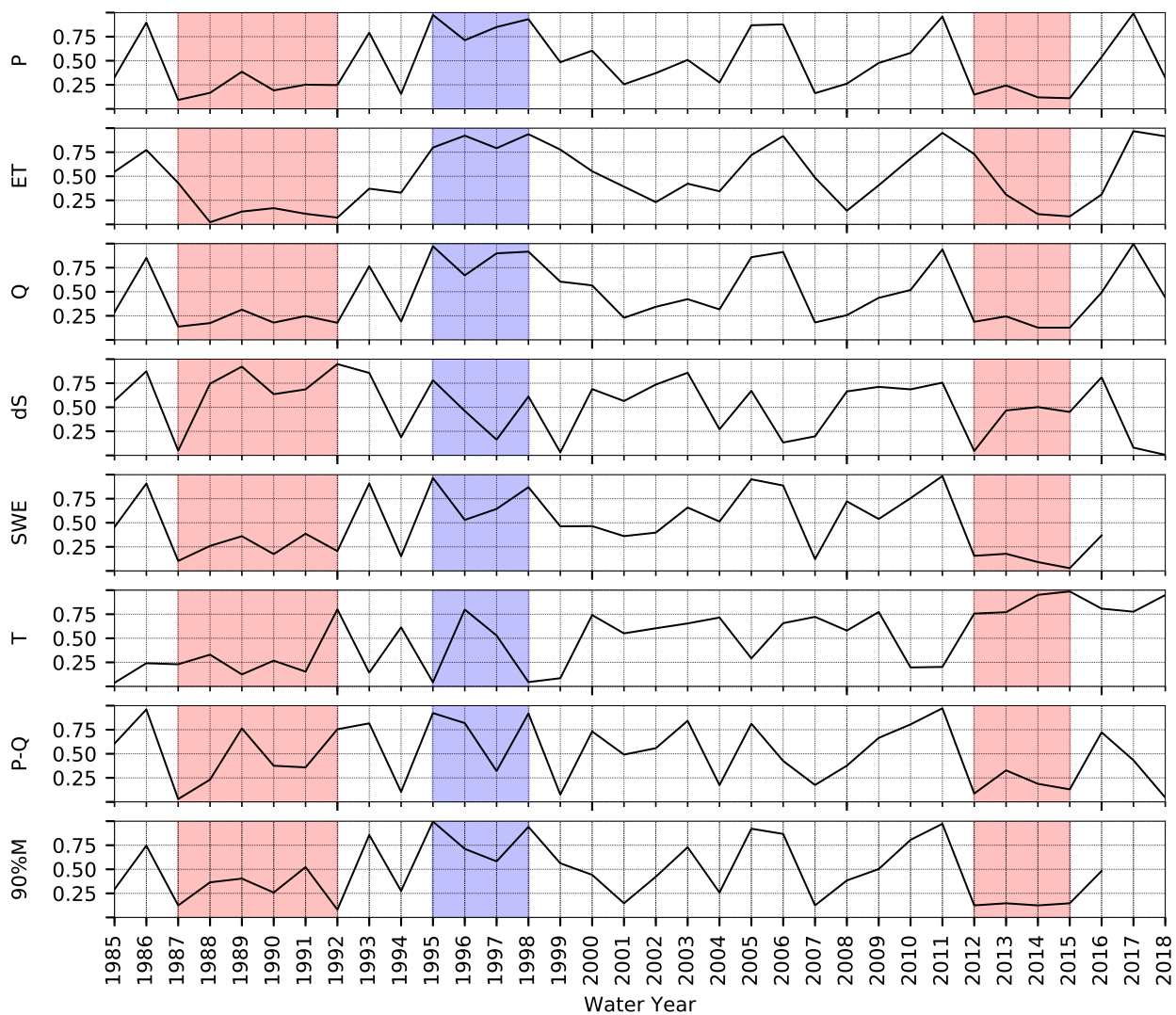


Figure C.3.8: Time series of normalized major variables for Tuolumne. The red and blue vertical shading represents multiyear dry and wet periods, respectively.

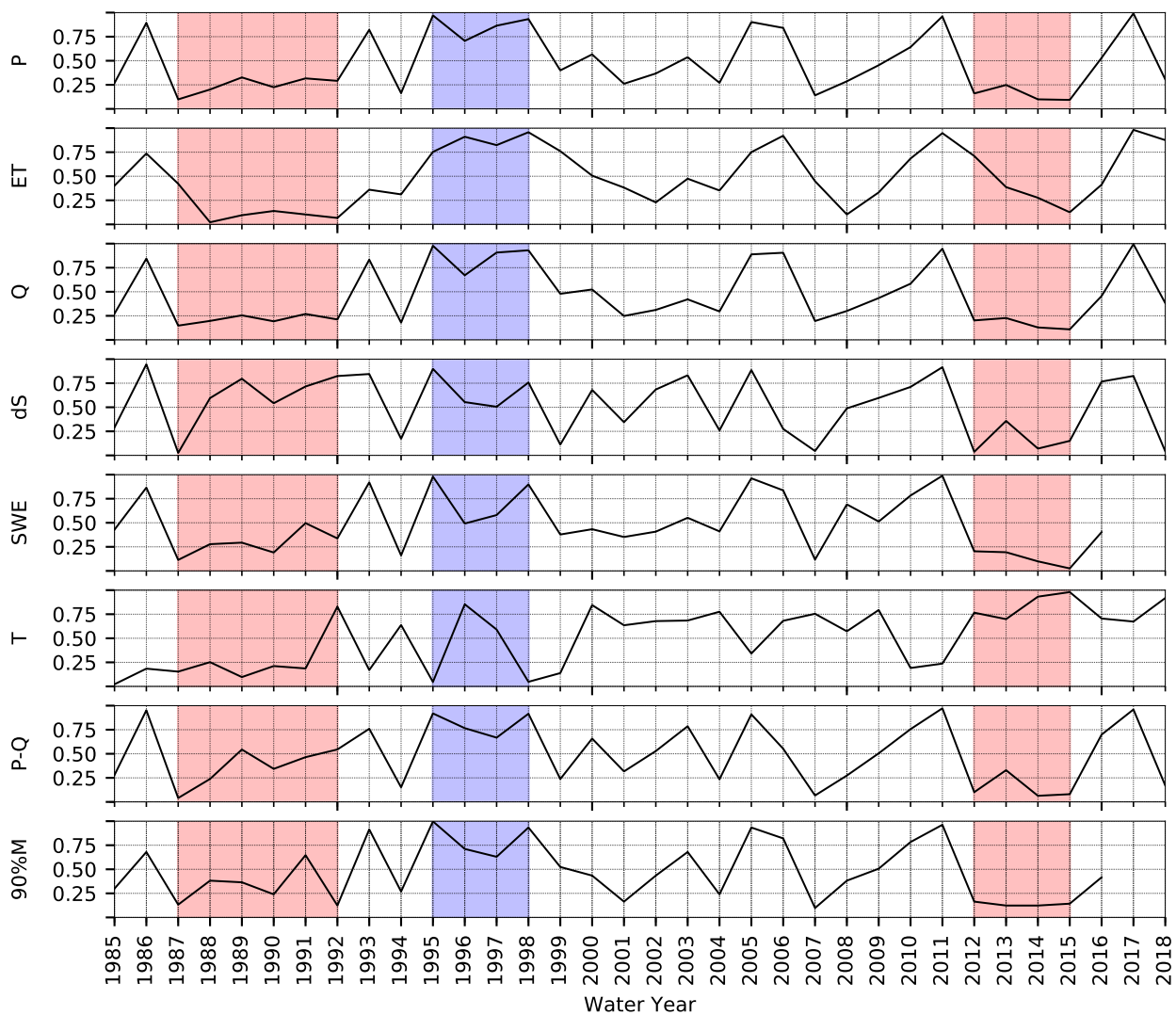


Figure C.3.9: Time series of normalized major variables for Merced. The red and blue vertical shading represents multiyear dry and wet periods, respectively.

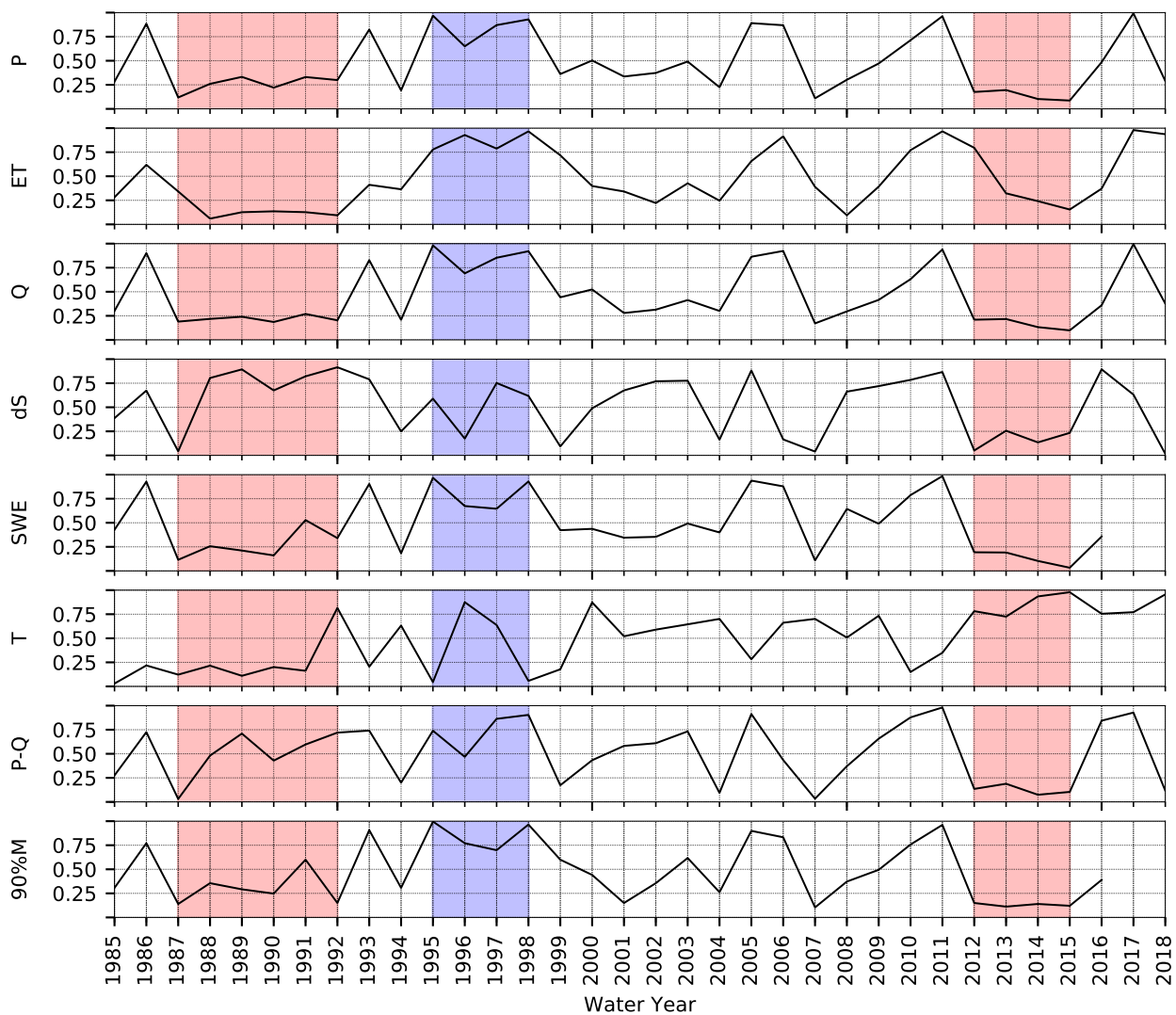


Figure C.3.10: Time series of normalized major variables for San Joaquin. The red and blue vertical shading represents multiyear dry and wet periods, respectively.

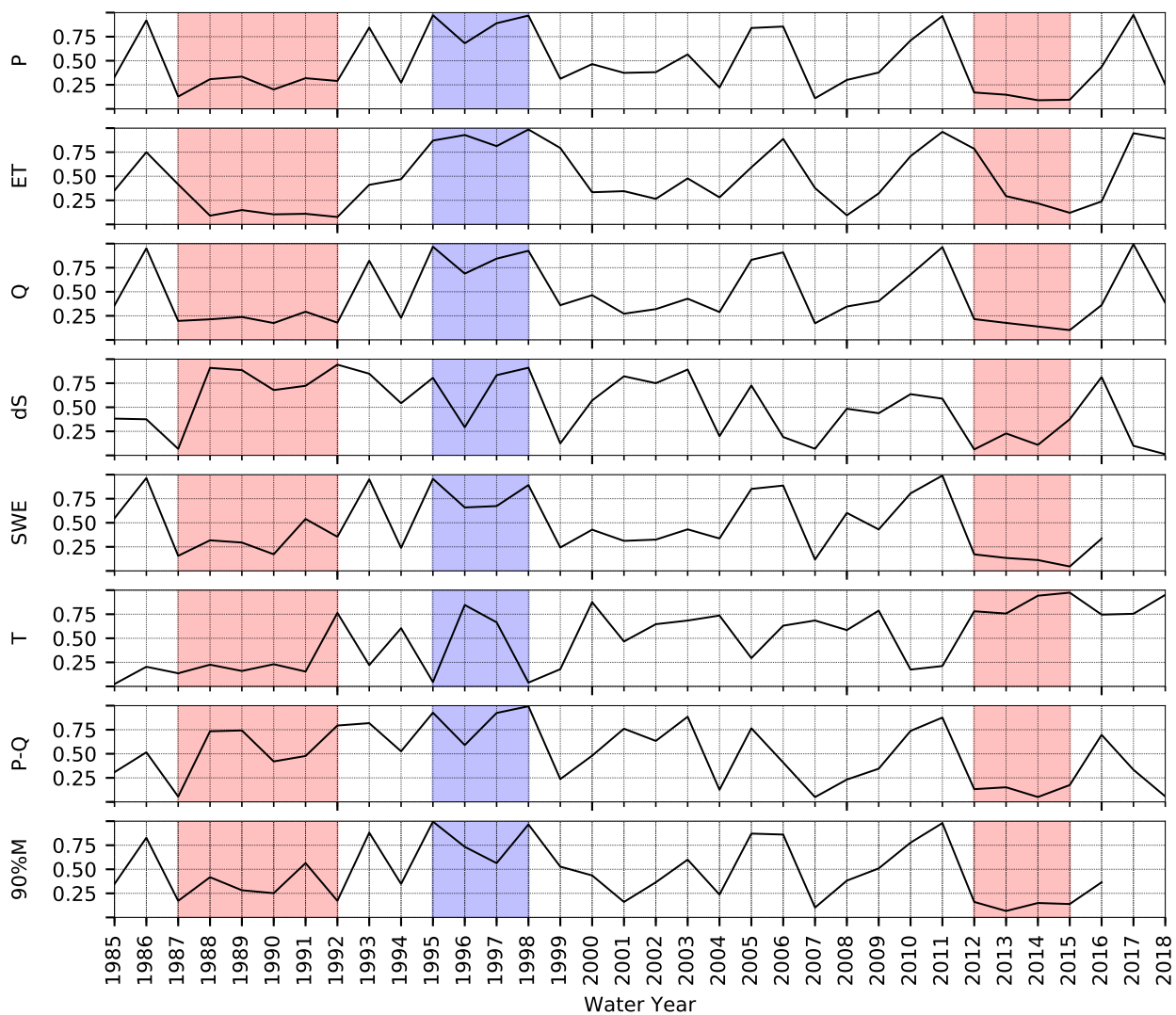


Figure C.3.11: Time series of normalized major variables for Kings. The red and blue vertical shading represents multiyear dry and wet periods, respectively.

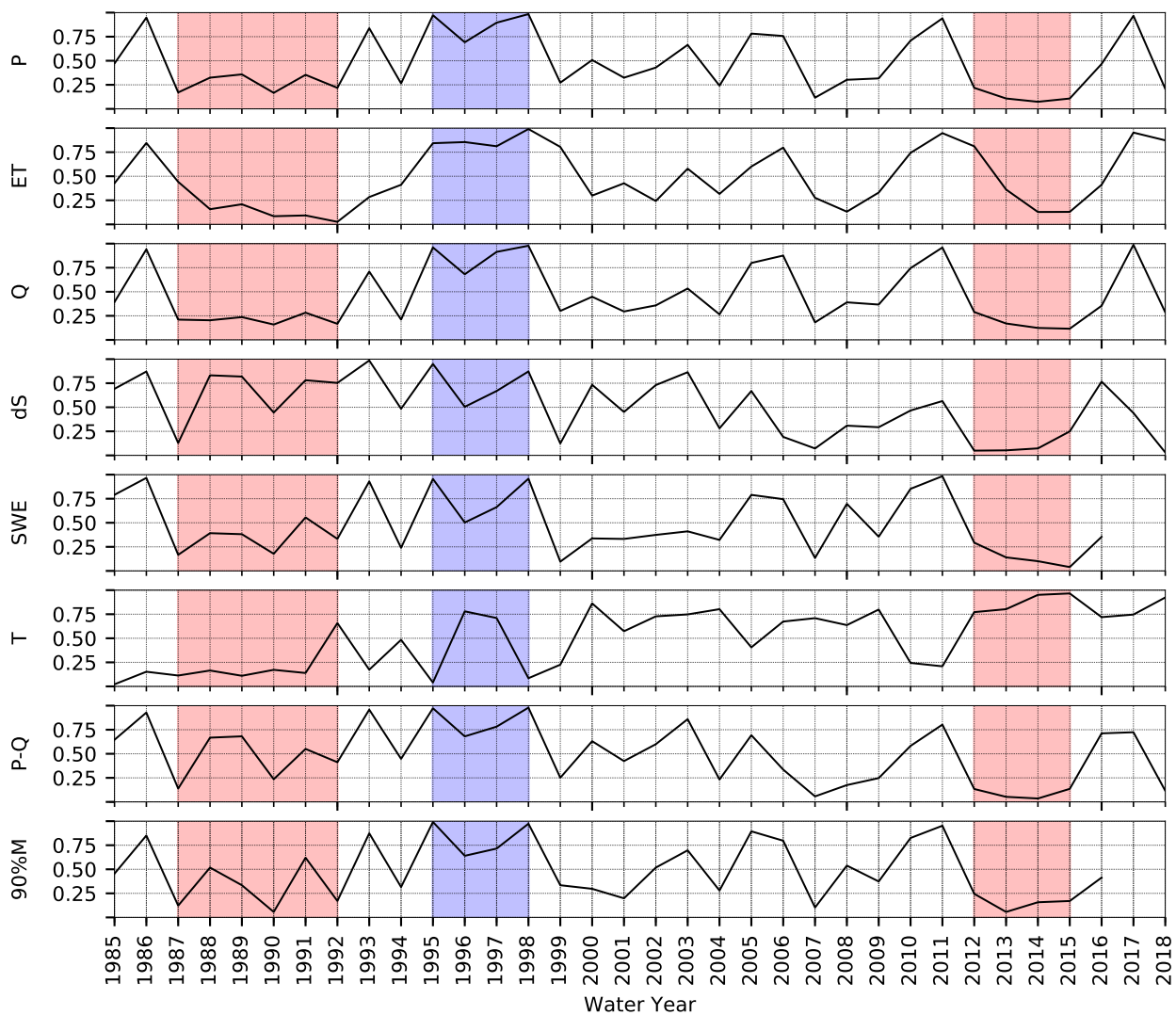


Figure C.3.12: Time series of normalized major variables for Kaweah. The red and blue vertical shading represents multiyear dry and wet periods, respectively.

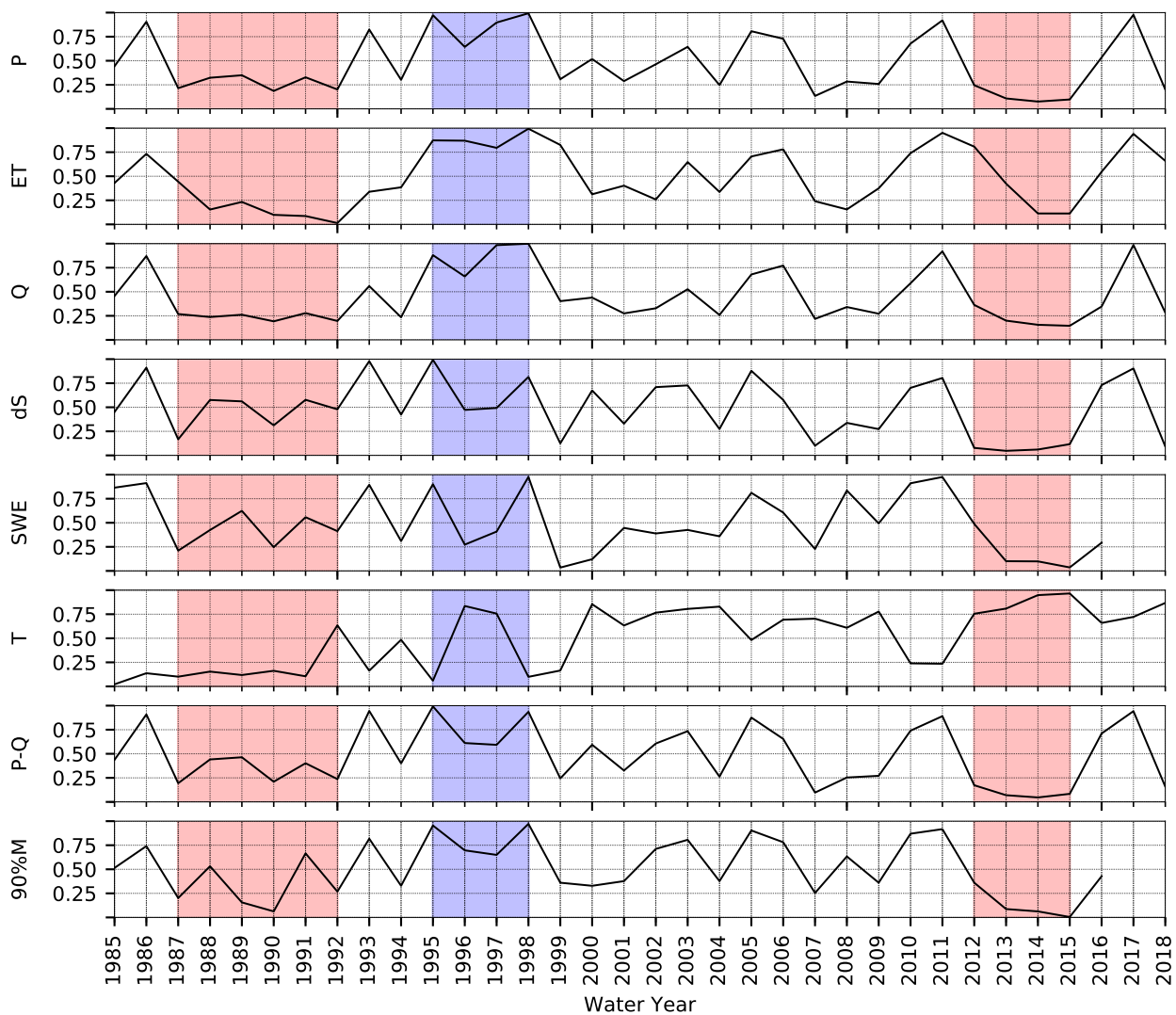


Figure C.3.13: Time series of normalized major variables for Tule. The red and blue vertical shading represents multiyear dry and wet periods, respectively.

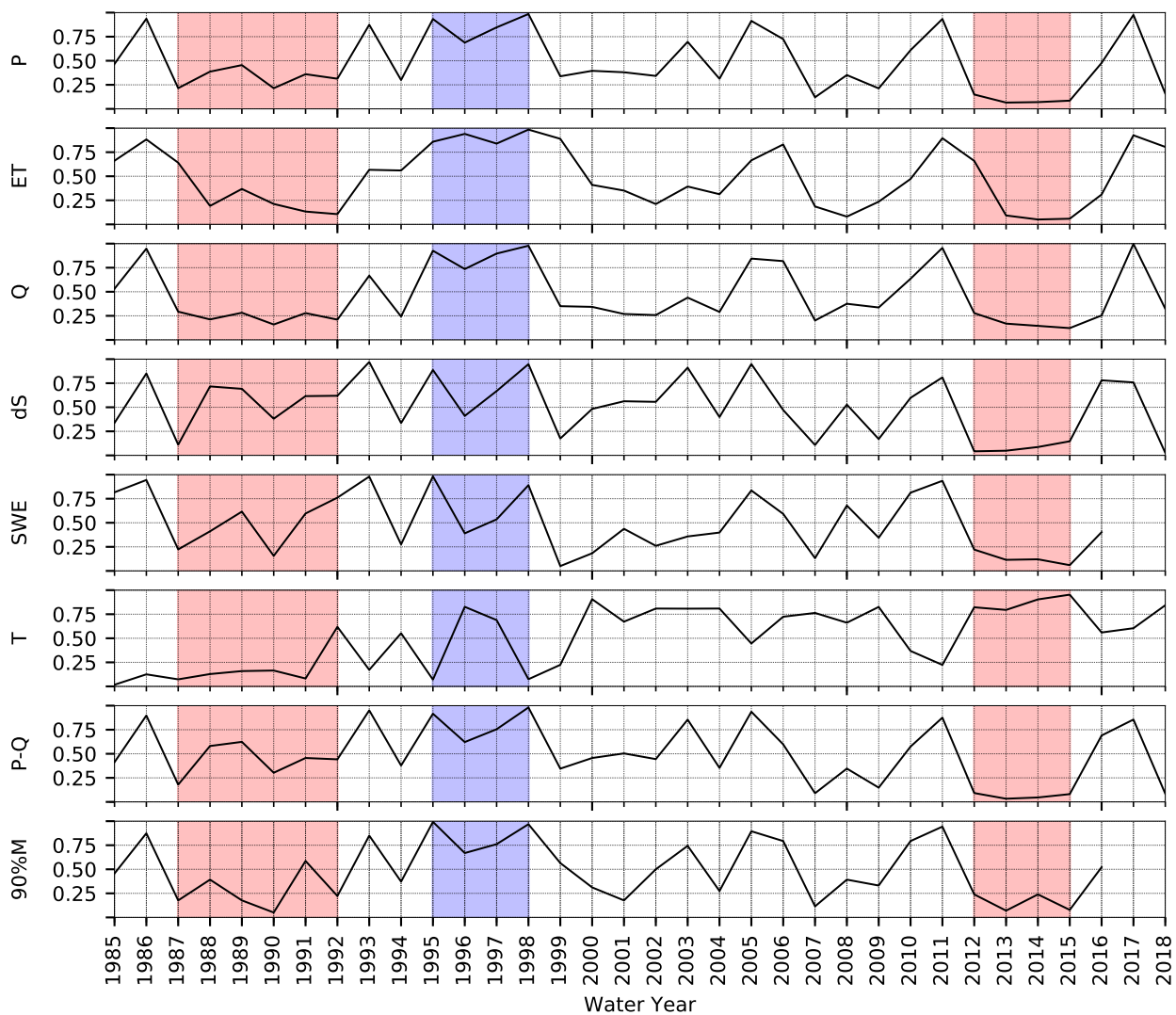


Figure C.3.14: Time series of normalized major variables for Kern. The red and blue vertical shading represents multiyear dry and wet periods, respectively.

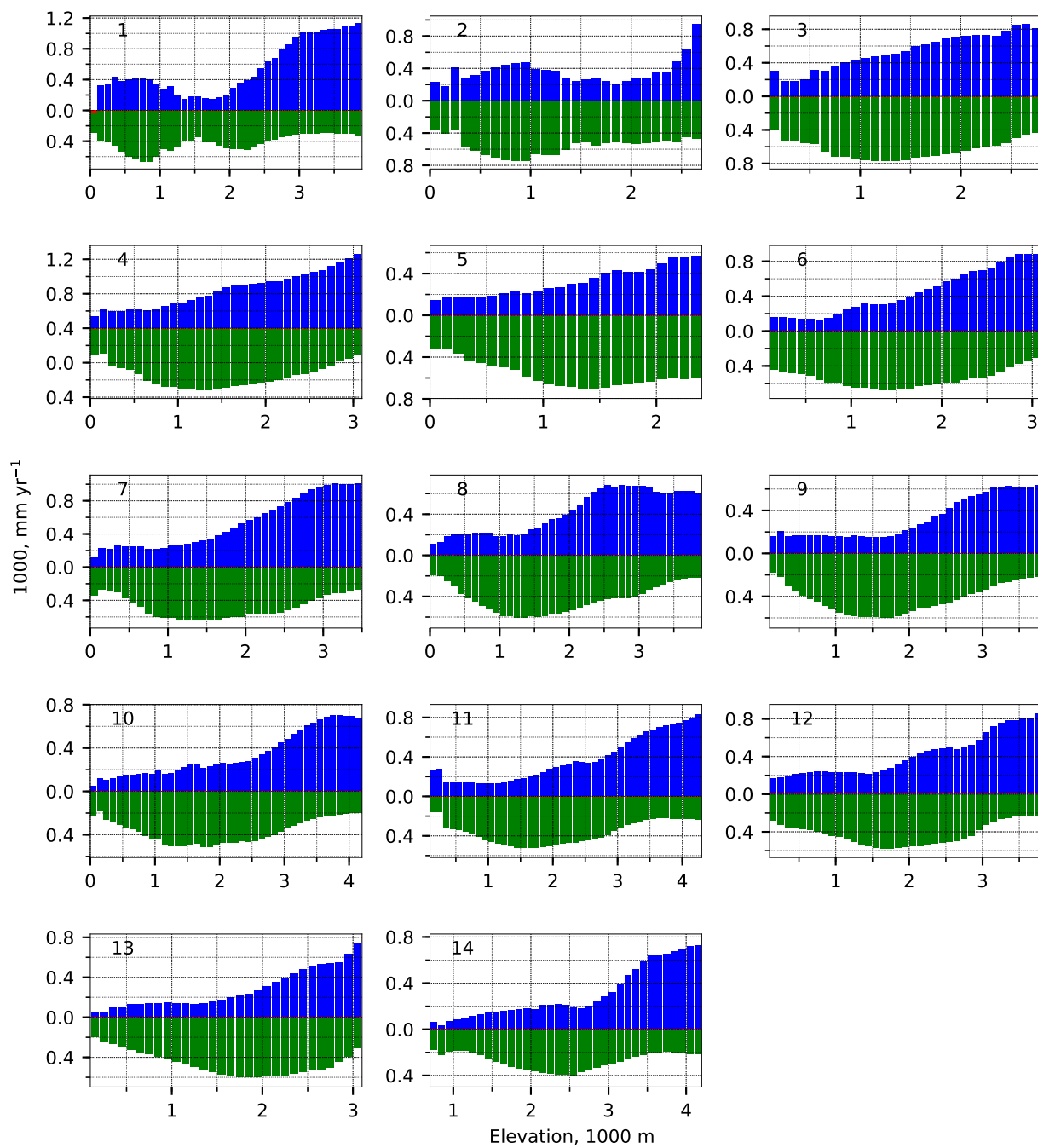


Figure C.4.1: Runoff (blue), evapotranspiration (green), precipitation (dotted hatch), and change in storage (red) binned by basins and elevation for water year 1985. Number corresponds with Basin numbers in Figure 1.

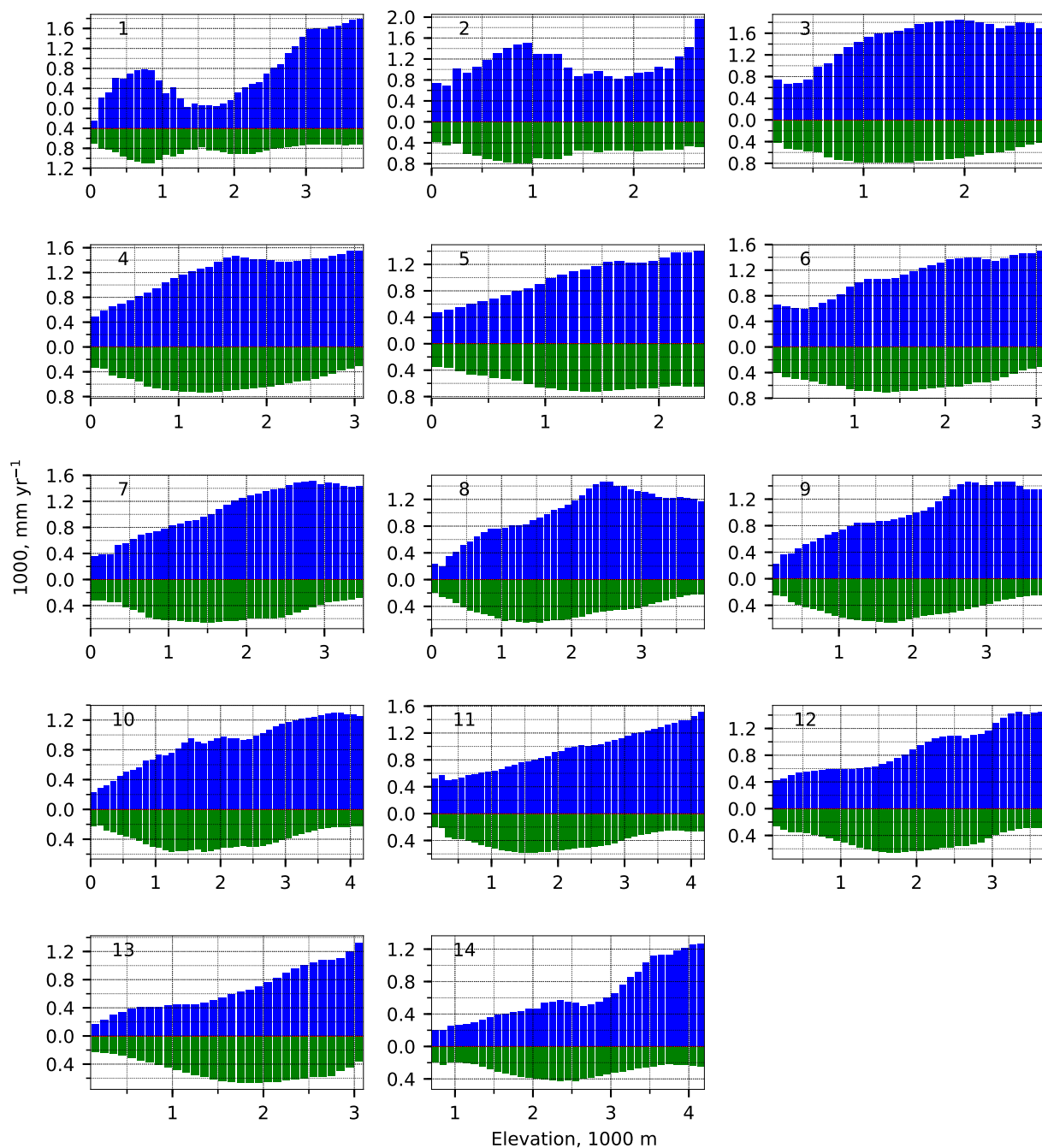


Figure C.4.2: Runoff (blue), evapotranspiration (green), precipitation (dotted hatch), and change in storage (red) binned by basins and elevation for water year 1986. Number corresponds with Basin numbers in Figure 1.

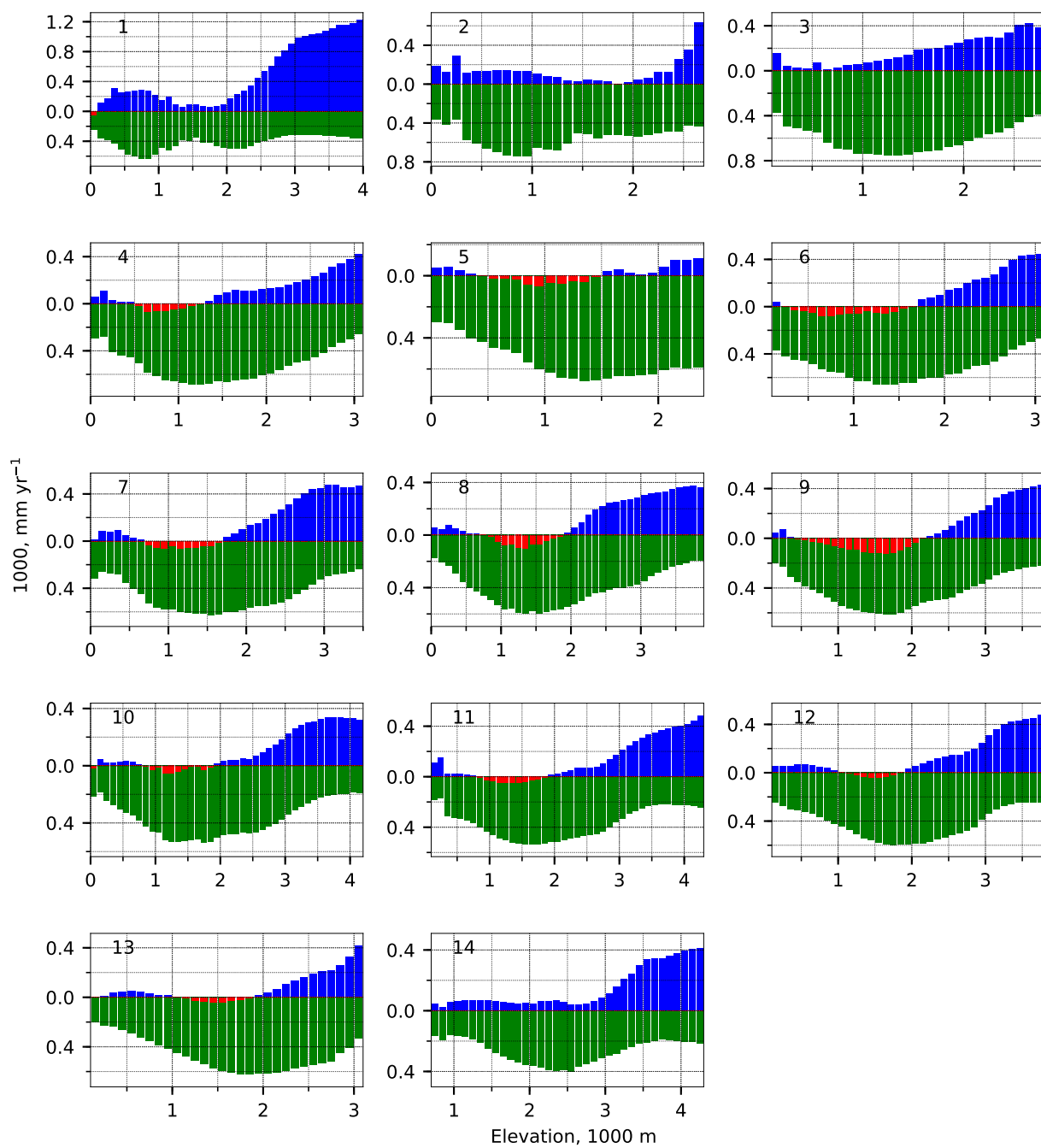


Figure C.4.3: Runoff (blue), evapotranspiration (green), precipitation (dotted hatch), and change in storage (red) binned by basins and elevation for water year 1987. Number corresponds with Basin numbers in Figure 1.

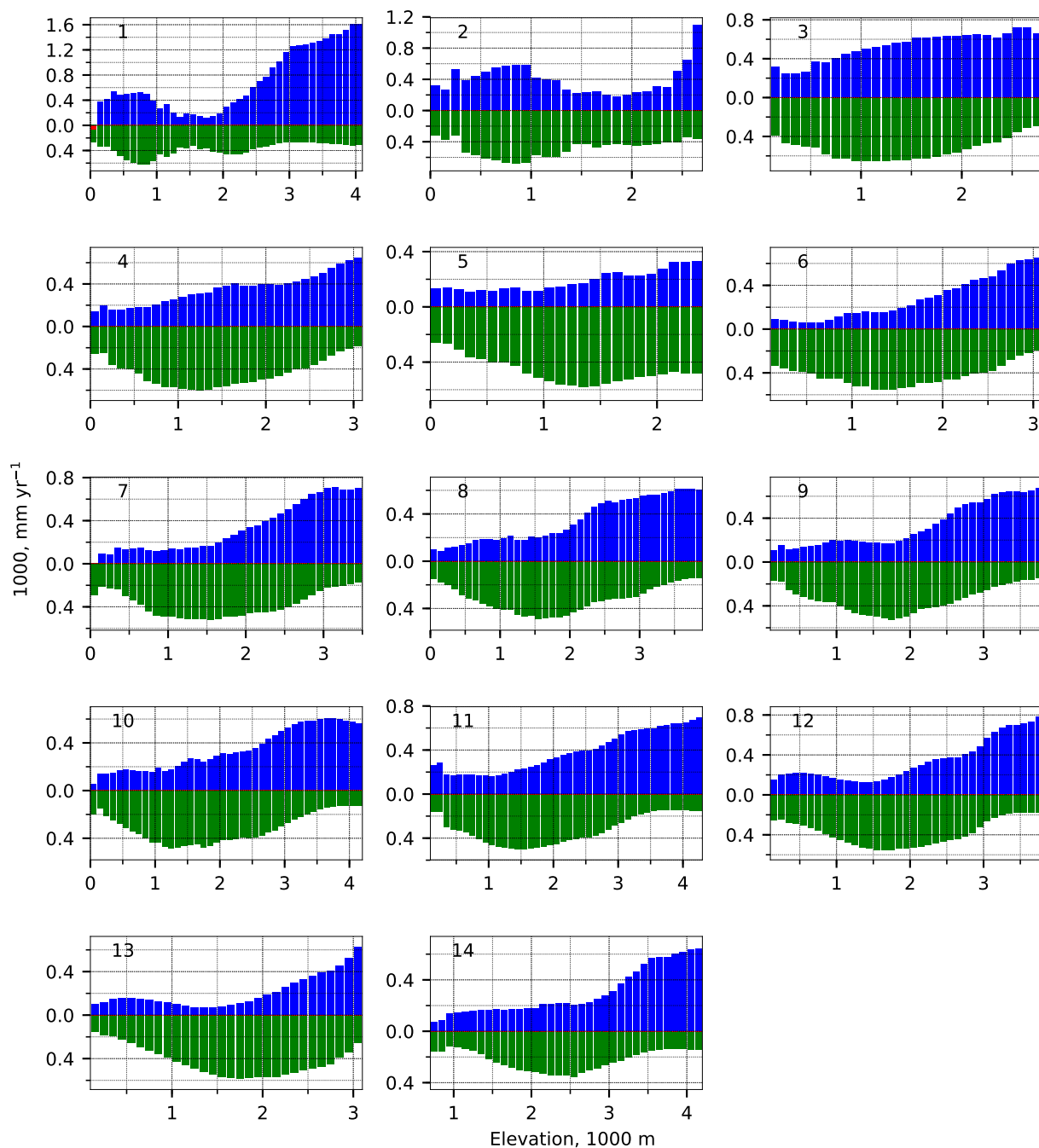


Figure C.4.4: Runoff (blue), evapotranspiration (green), precipitation (dotted hatch), and change in storage (red) binned by basins and elevation for water year 1988. Number corresponds with Basin numbers in Figure 1.

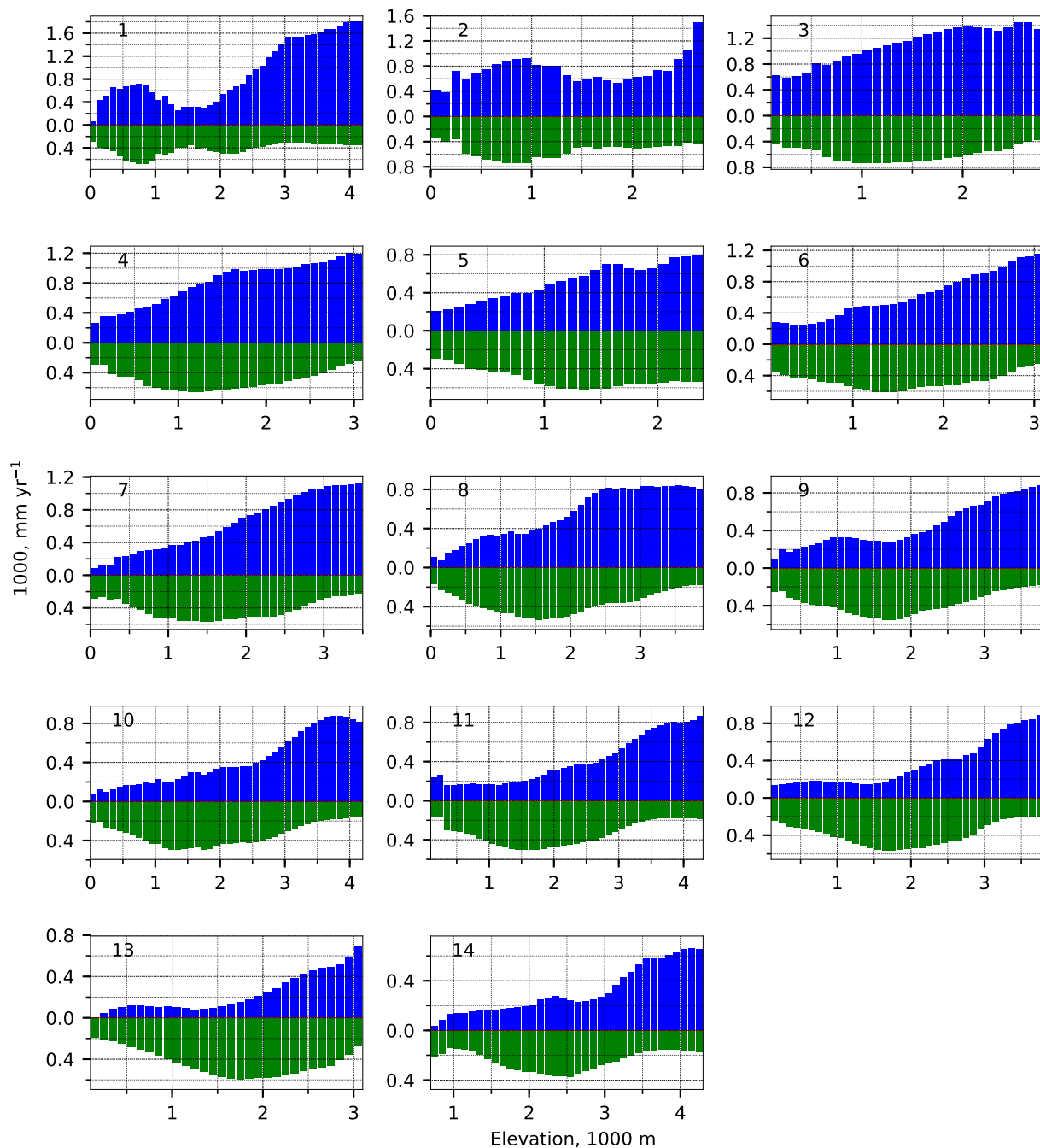


Figure C.4.5: Runoff (blue), evapotranspiration (green), precipitation (dotted hatch), and change in storage (red) binned by basins and elevation for water year 1989. Number corresponds with Basin numbers in Figure 1.

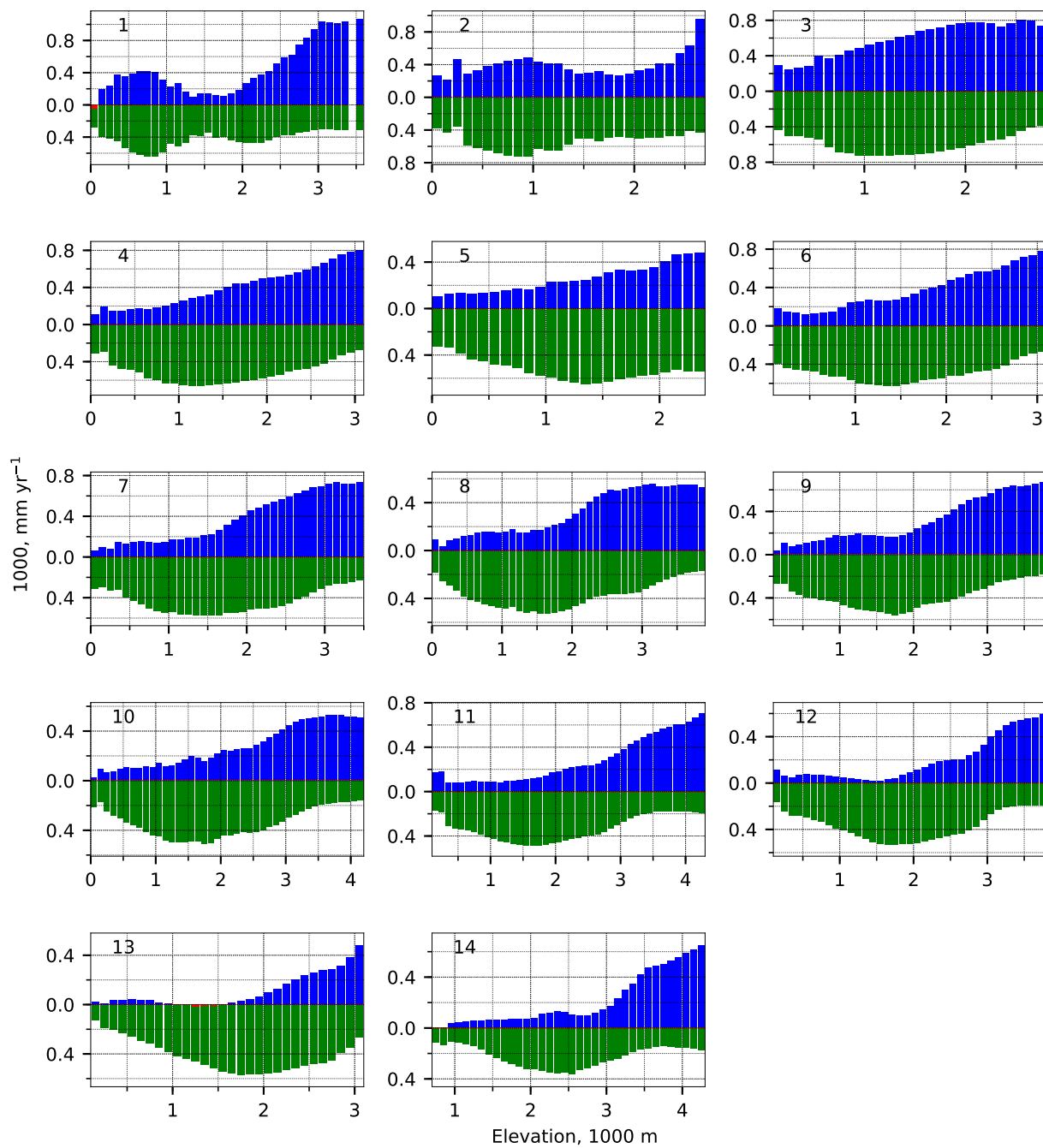


Figure C.4.6: Runoff (blue), evapotranspiration (green), precipitation (dotted hatch), and change in storage (red) binned by basins and elevation for water year 1990. Number corresponds with Basin numbers in Figure 1.

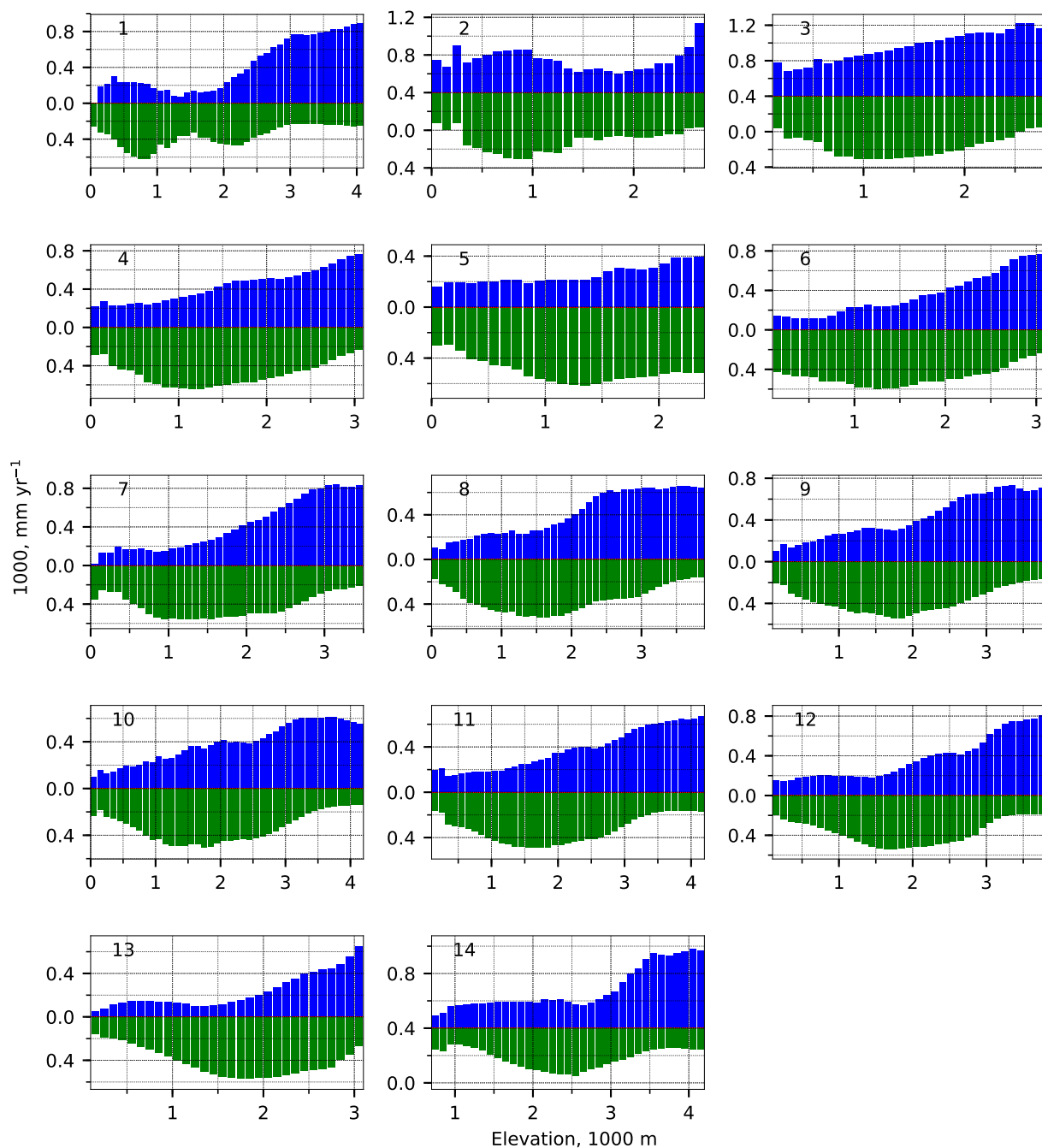


Figure C.4.7: Runoff (blue), evapotranspiration (green), precipitation (dotted hatch), and change in storage (red) binned by basins and elevation for water year 1991. Number corresponds with Basin numbers in Figure 1.

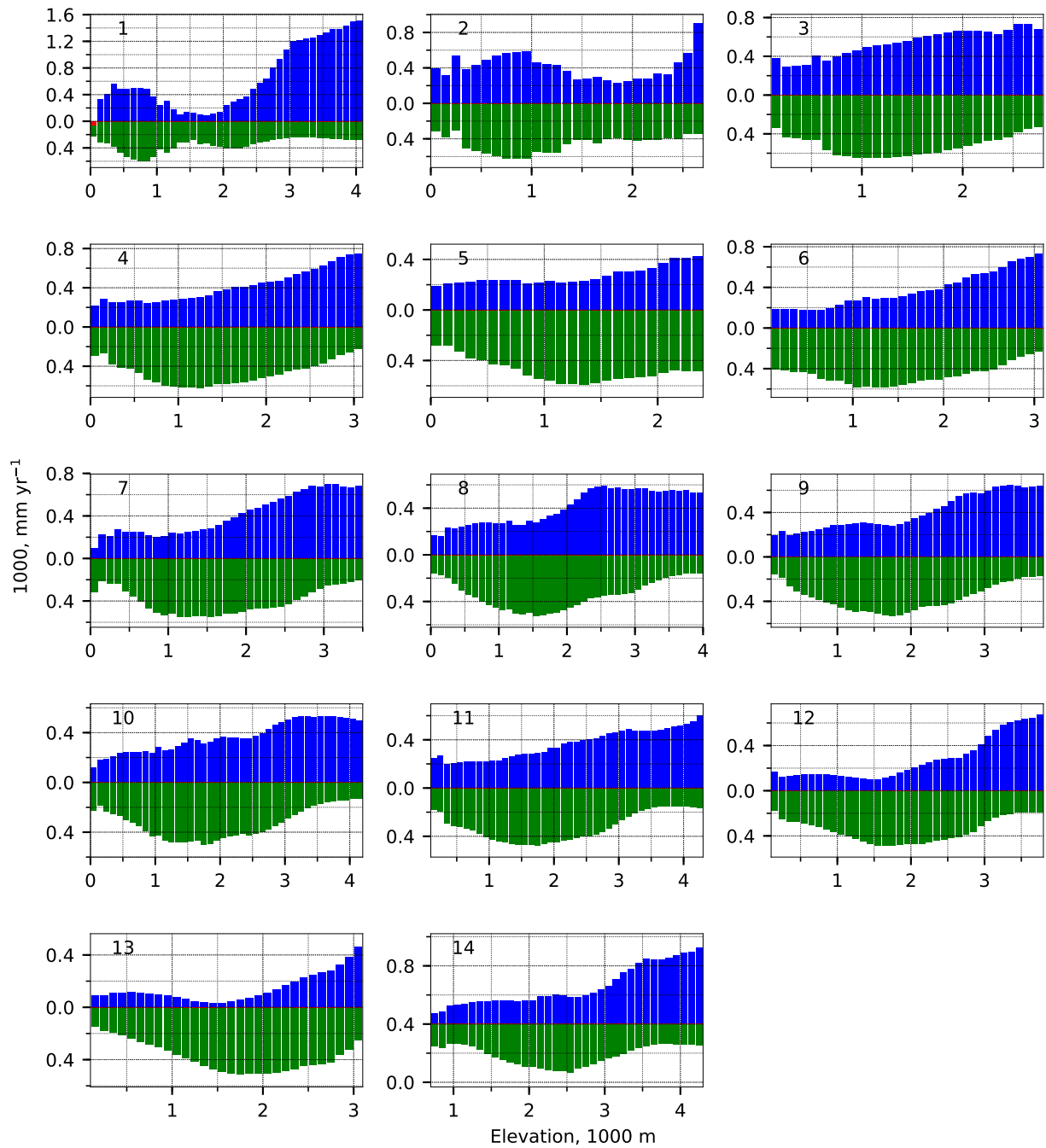


Figure C.4.8: Runoff (blue), evapotranspiration (green), precipitation (dotted hatch), and change in storage (red) binned by basins and elevation for water year 1992. Number corresponds with Basin numbers in Figure 1.

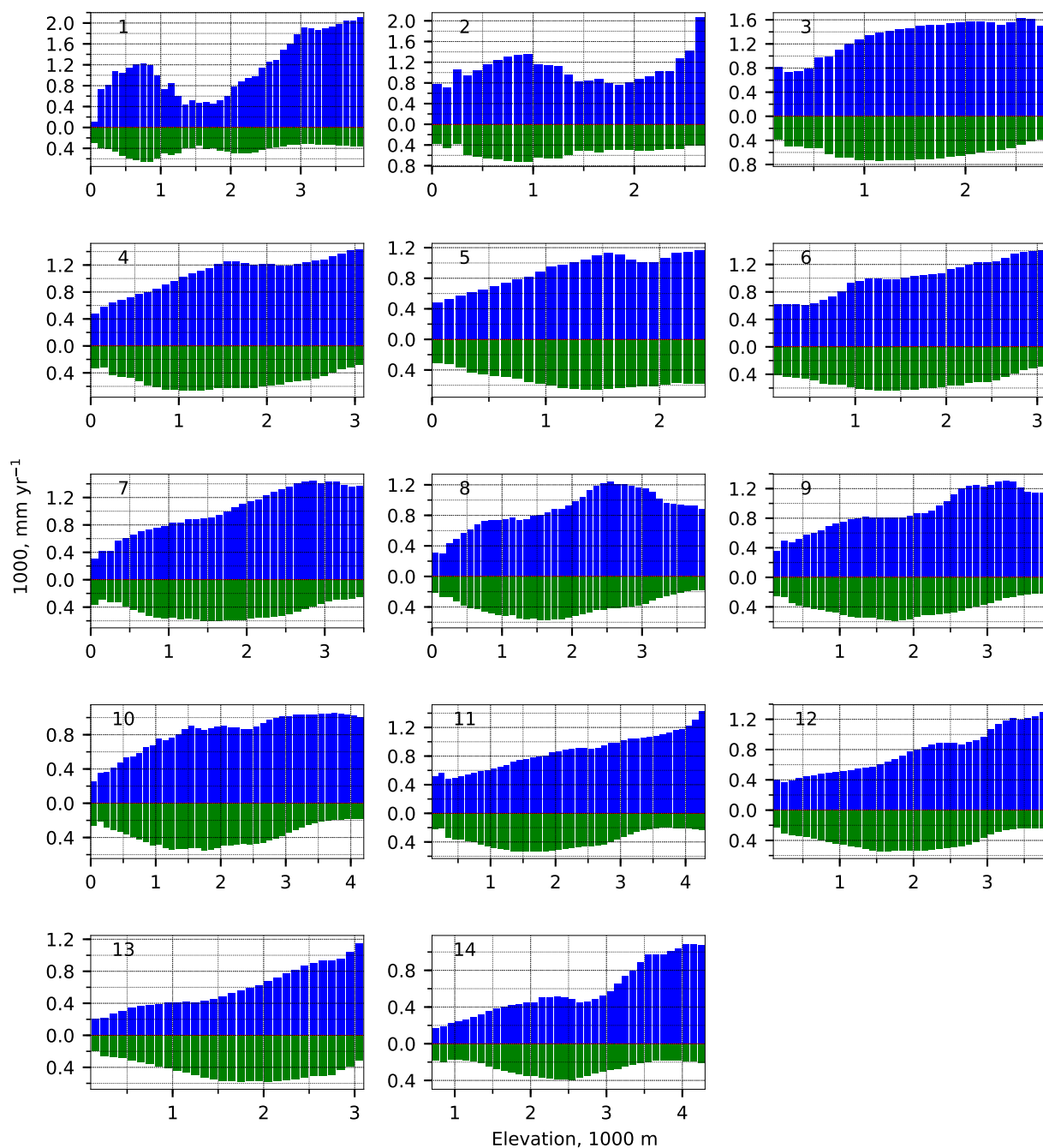


Figure C.4.9: Runoff (blue), evapotranspiration (green), precipitation (dotted hatch), and change in storage (red) binned by basins and elevation for water year 1993. Number corresponds with Basin numbers in Figure 1.

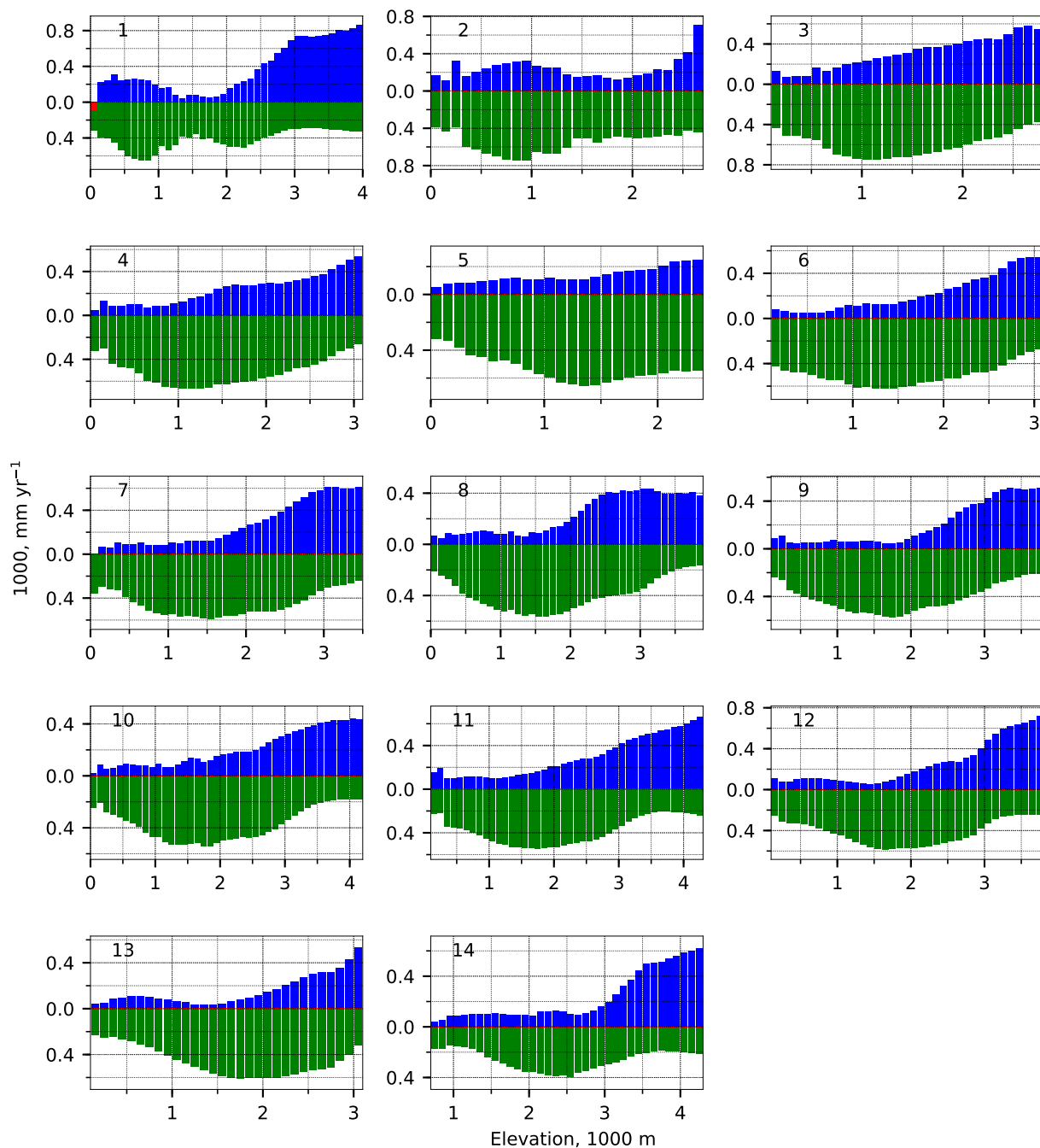


Figure C.4.10: Runoff (blue), evapotranspiration (green), precipitation (dotted hatch), and change in storage (red) binned by basins and elevation for water year 1994. Number corresponds with Basin numbers in Figure 1.

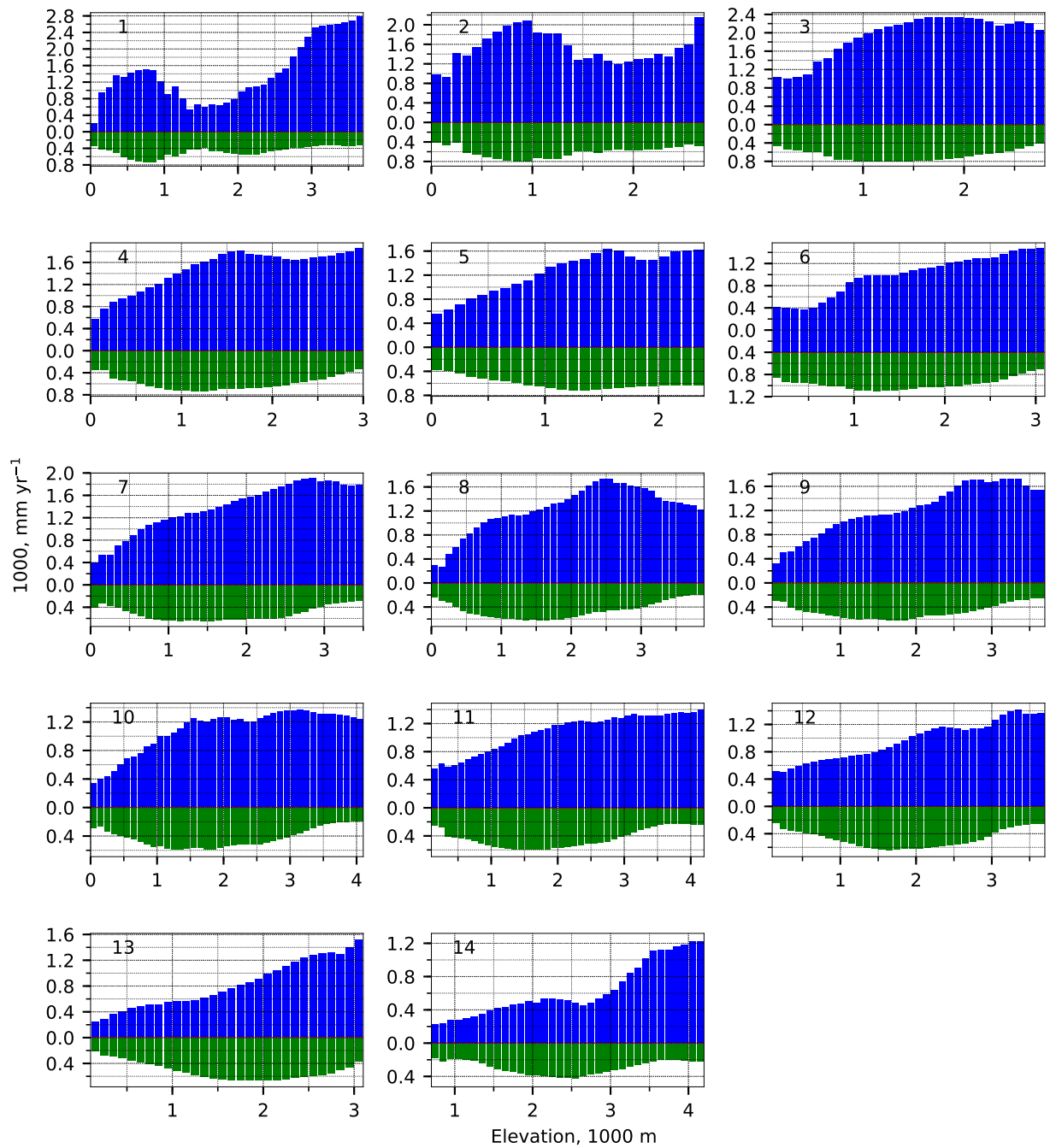


Figure C.4.11: Runoff (blue), evapotranspiration (green), precipitation (dotted hatch), and change in storage (red) binned by basins and elevation for water year 1995. Number corresponds with Basin numbers in Figure 1.

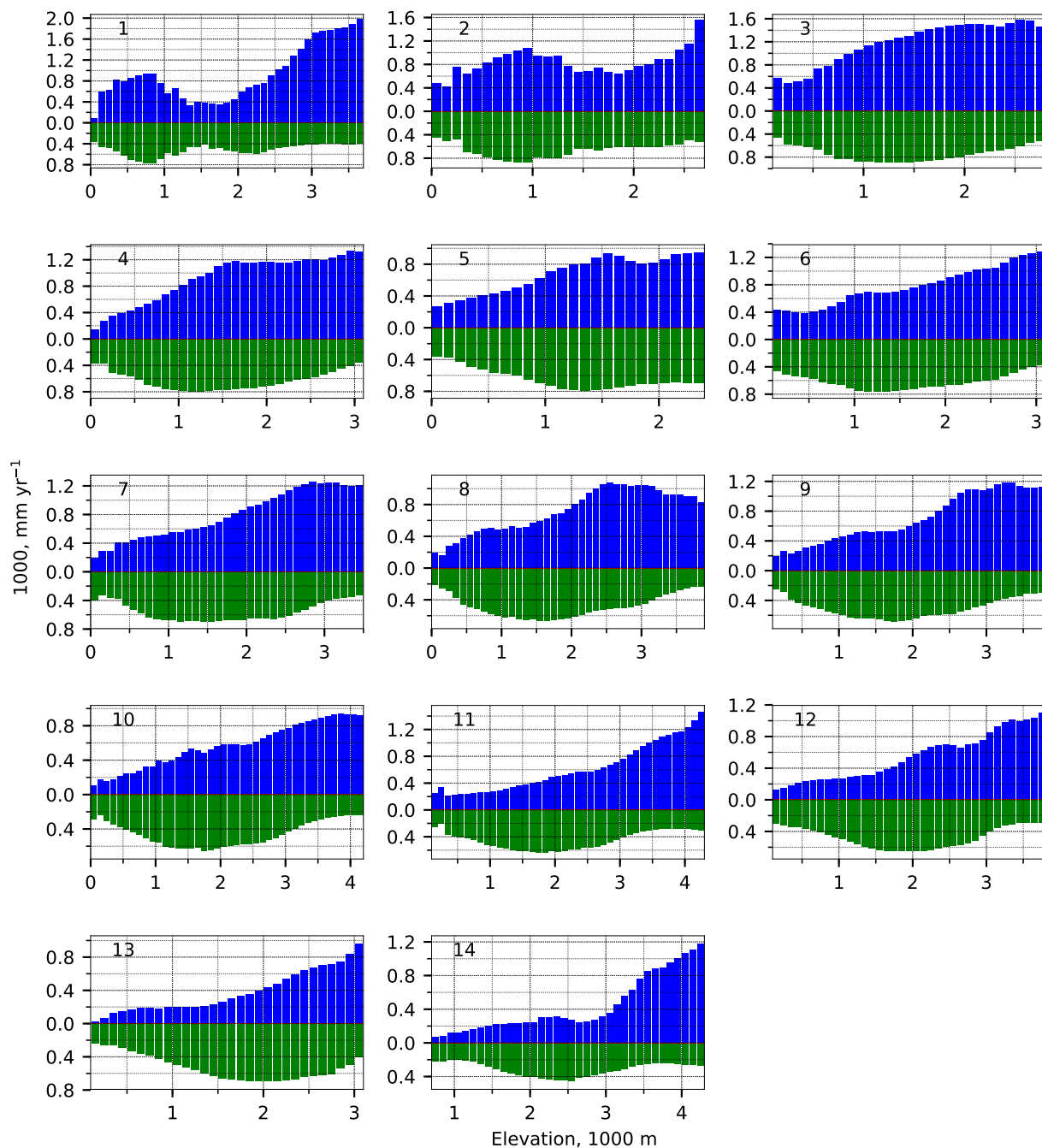


Figure C.4.12: Runoff (blue), evapotranspiration (green), precipitation (dotted hatch), and change in storage (red) binned by basins and elevation for water year 1996. Number corresponds with Basin numbers in Figure 1.

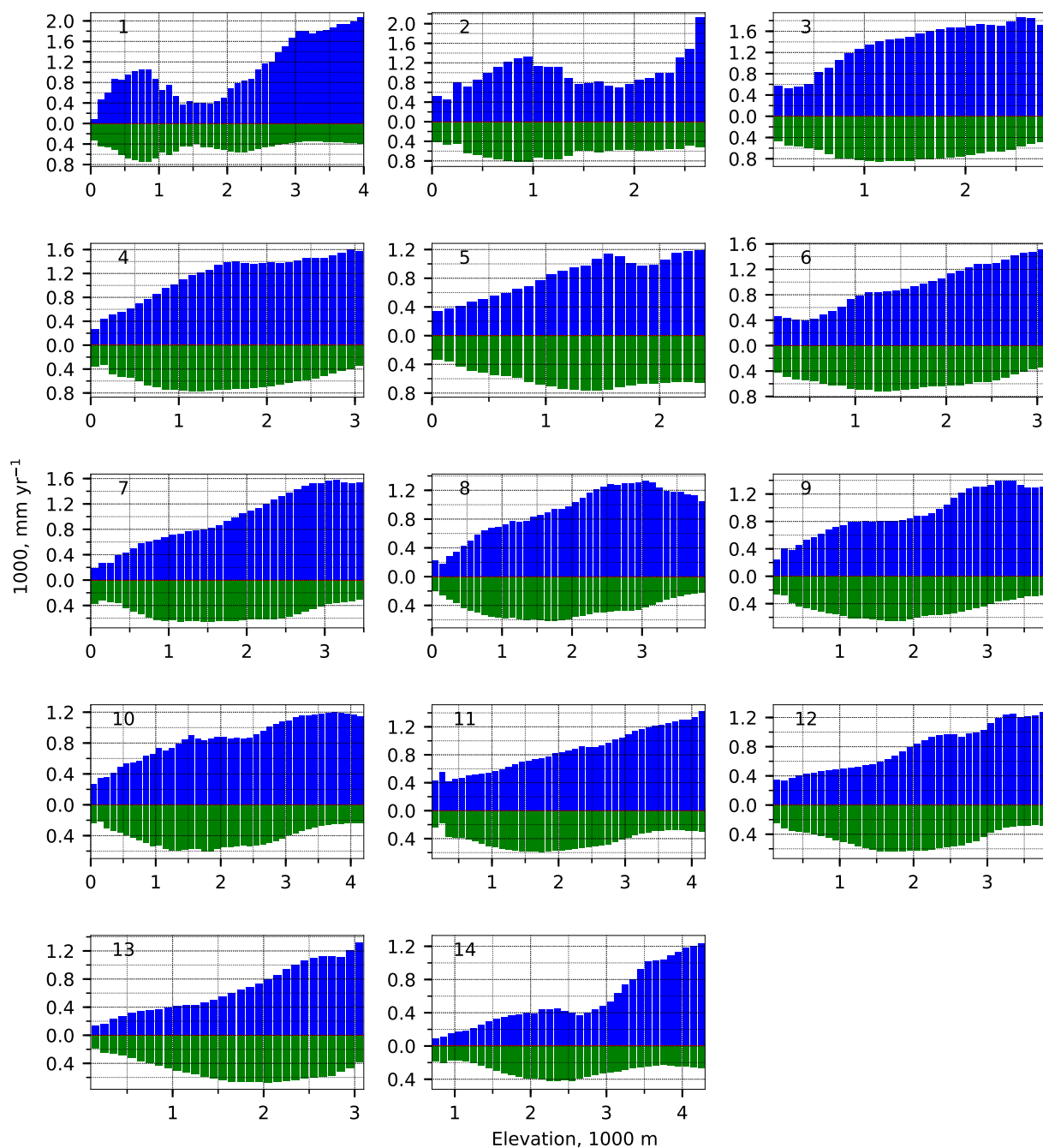


Figure C.4.13: Runoff (blue), evapotranspiration (green), precipitation (dotted hatch), and change in storage (red) binned by basins and elevation for water year 1997. Number corresponds with Basin numbers in Figure 1.

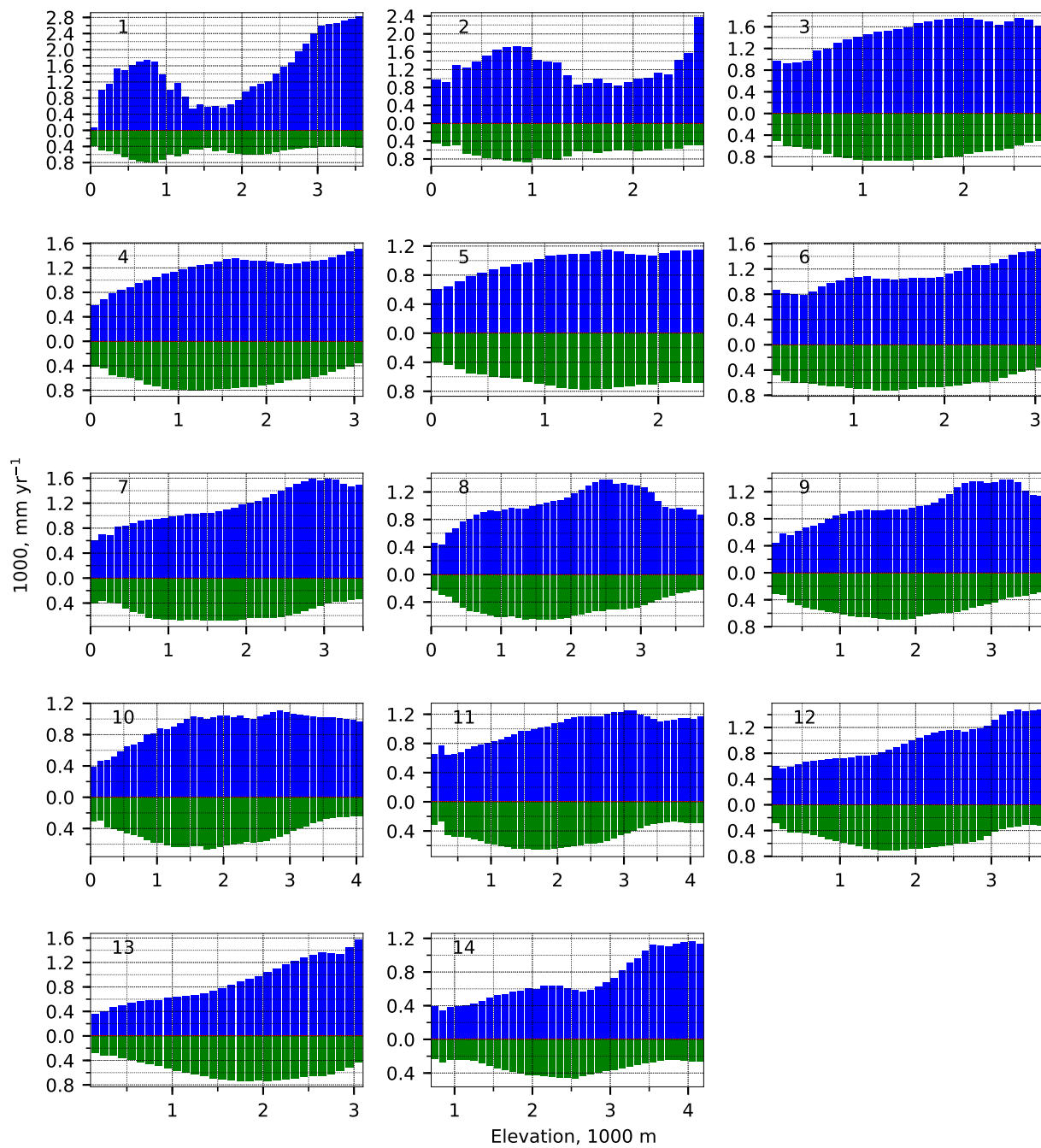


Figure C.4.14: Runoff (blue), evapotranspiration (green), precipitation (dotted hatch), and change in storage (red) binned by basins and elevation for water year 1998. Number corresponds with Basin numbers in Figure 1.

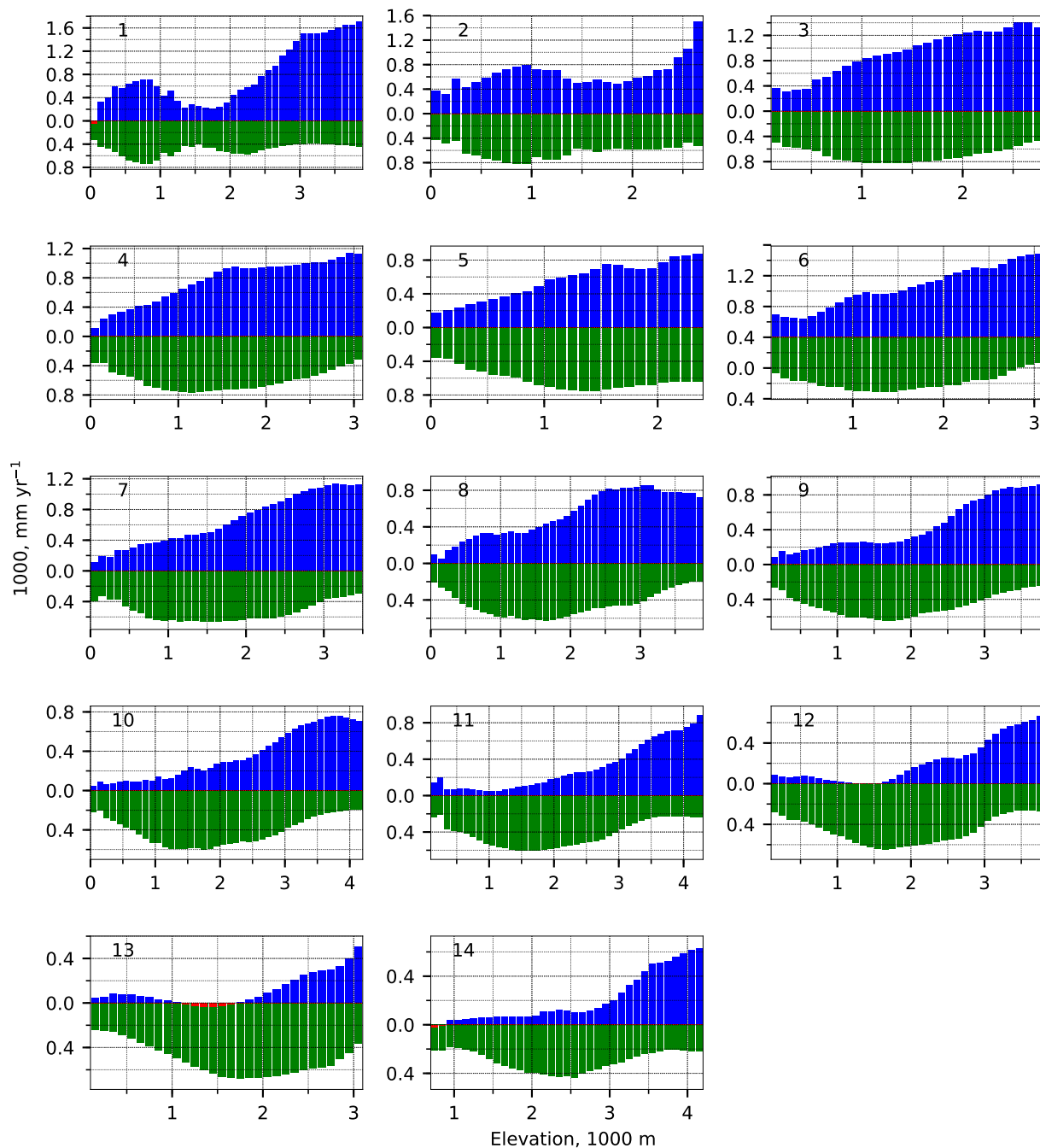


Figure C.4.15: Runoff (blue), evapotranspiration (green), precipitation (dotted hatch), and change in storage (red) binned by basins and elevation for water year 1999. Number corresponds with Basin numbers in Figure 1.

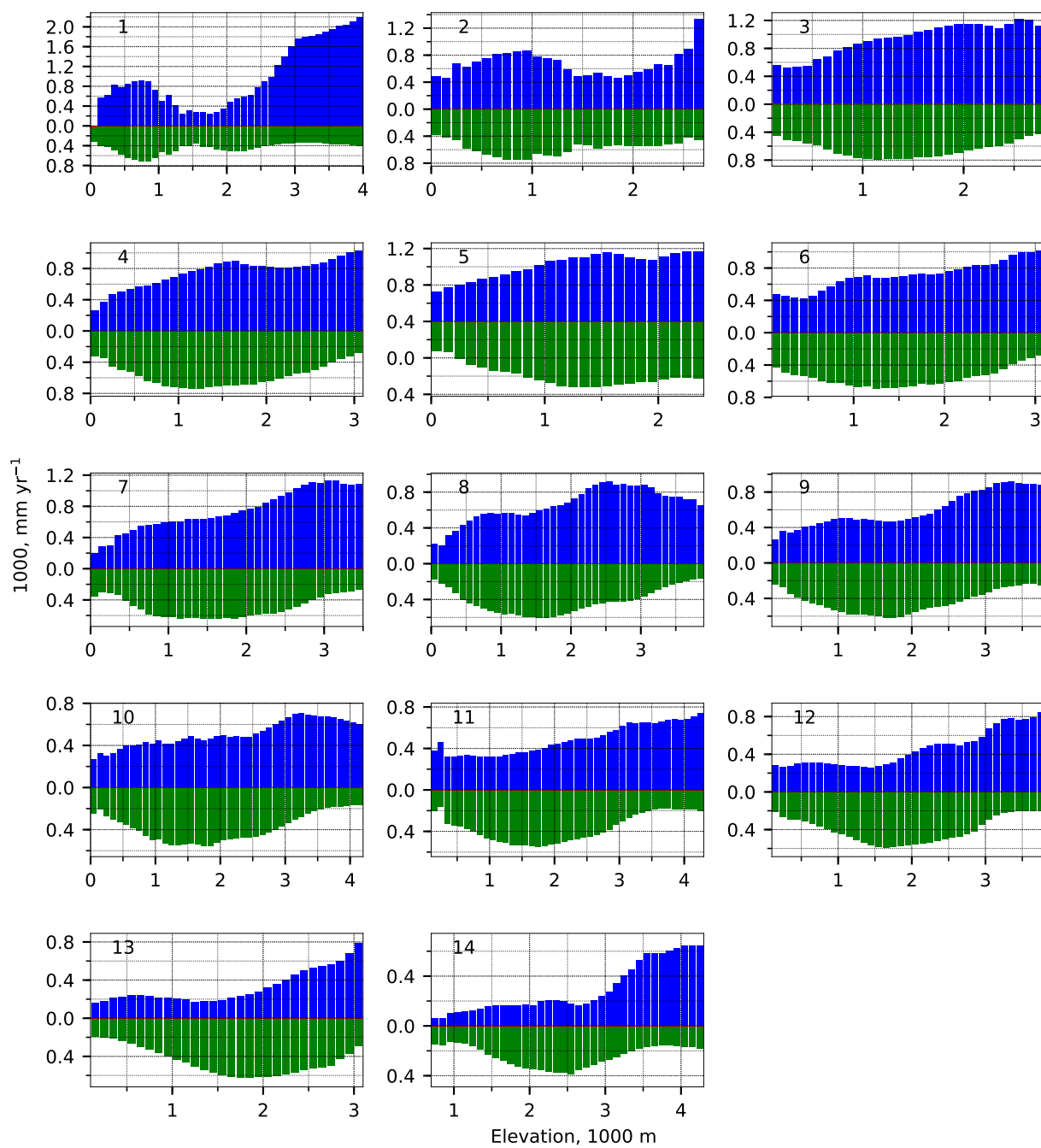


Figure C.4.16: Runoff (blue), evapotranspiration (green), precipitation (dotted hatch), and change in storage (red) binned by basins and elevation for water year 2000. Number corresponds with Basin numbers in Figure 1.

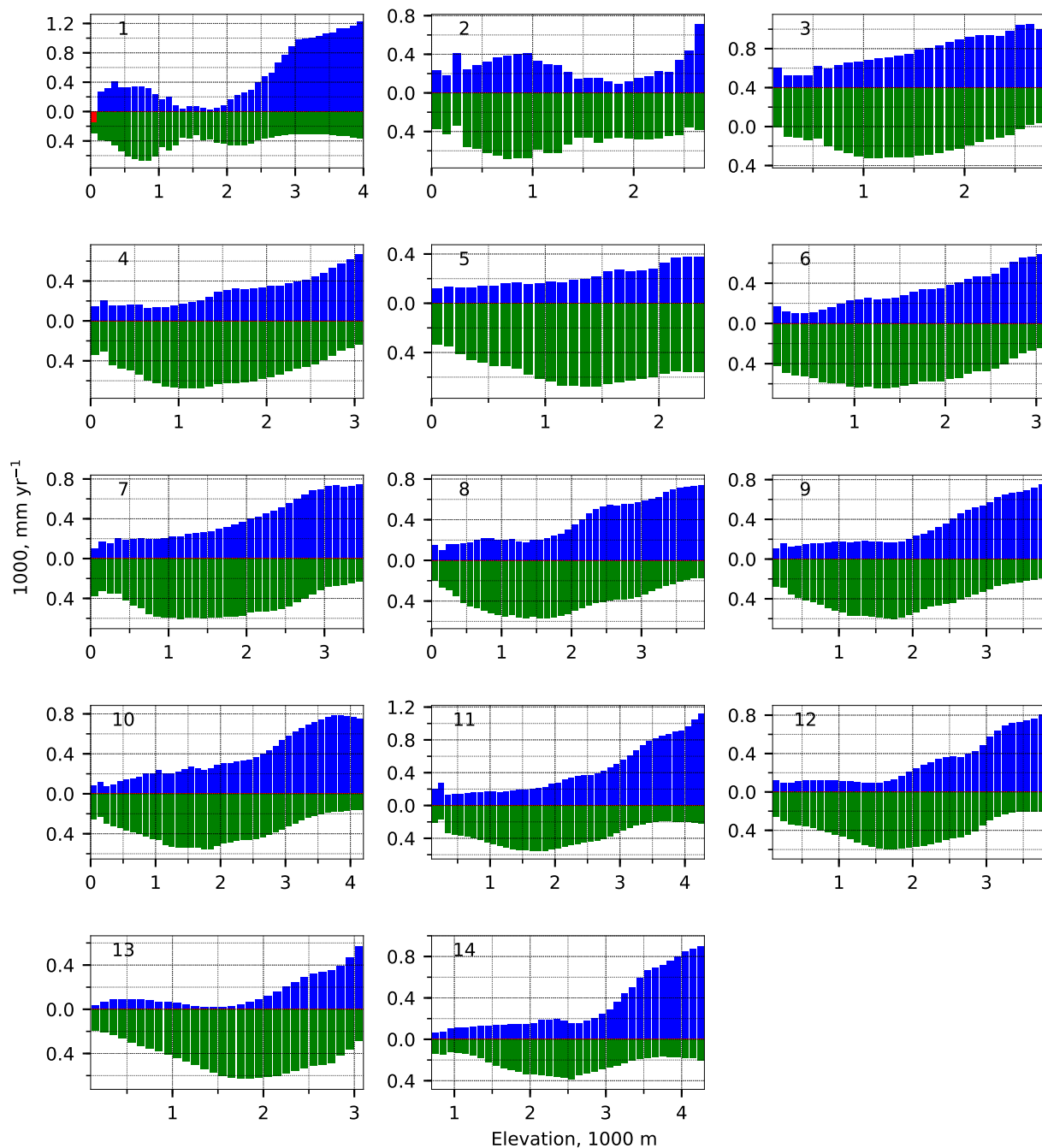


Figure C.4.17: Runoff (blue), evapotranspiration (green), precipitation (dotted hatch), and change in storage (red) binned by basins and elevation for water year 2001. Number corresponds with Basin numbers in Figure 1.

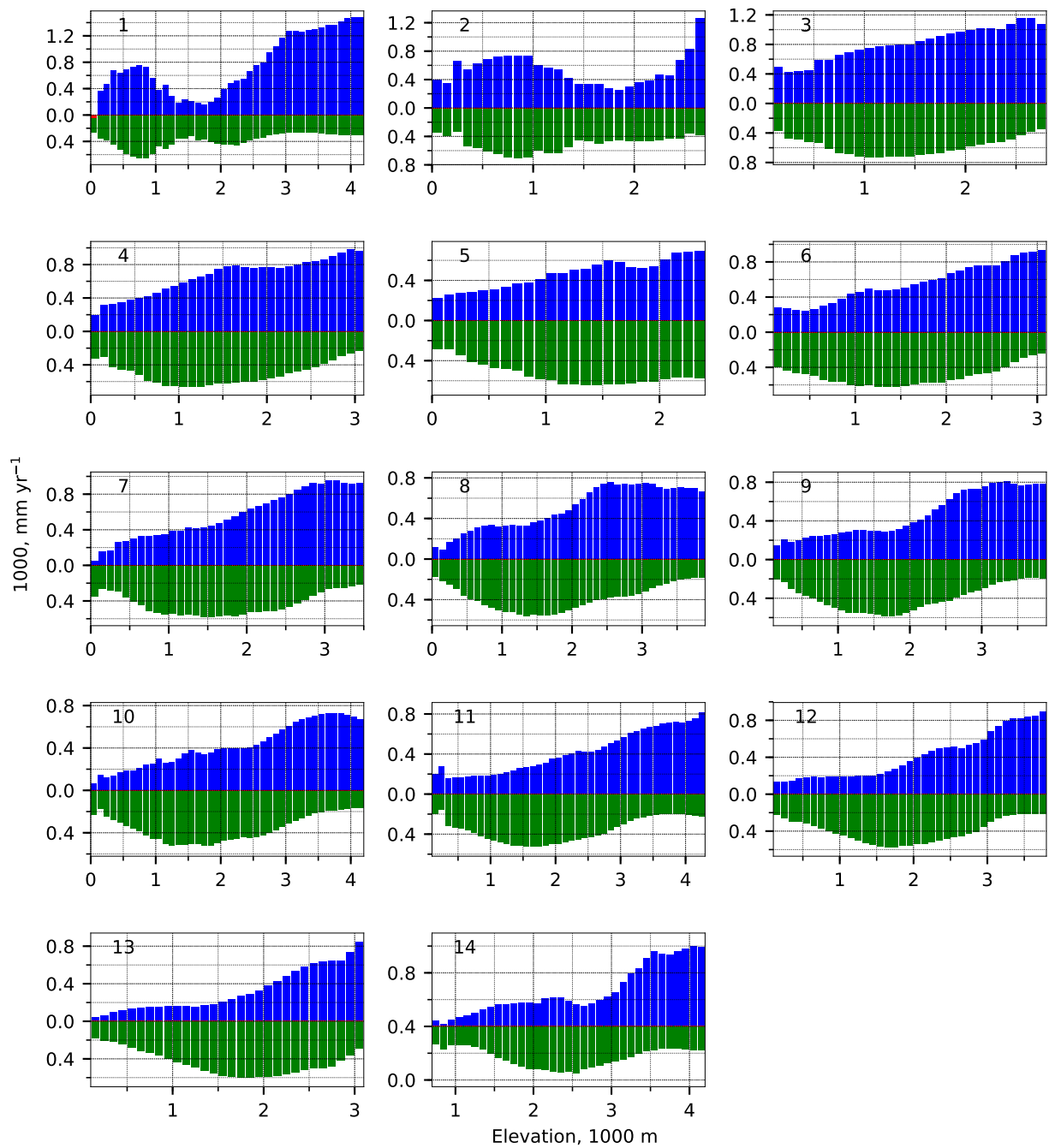


Figure C.4.18: Runoff (blue), evapotranspiration (green), precipitation (dotted hatch), and change in storage (red) binned by basins and elevation for water year 2002. Number corresponds with Basin numbers in Figure 1.

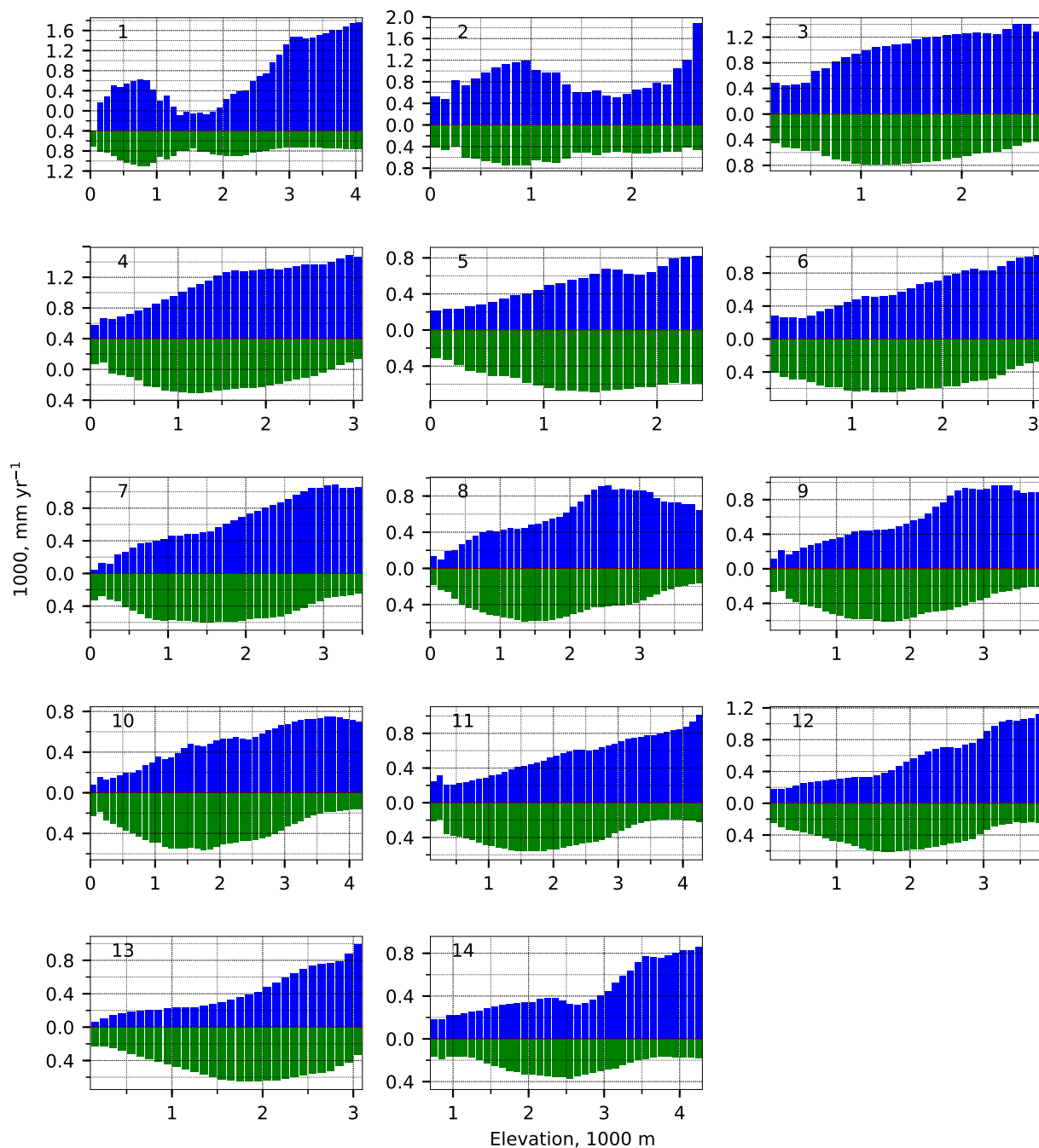


Figure C.4.19: Runoff (blue), evapotranspiration (green), precipitation (dotted hatch), and change in storage (red) binned by basins and elevation for water year 2003. Number corresponds with Basin numbers in Figure 1.

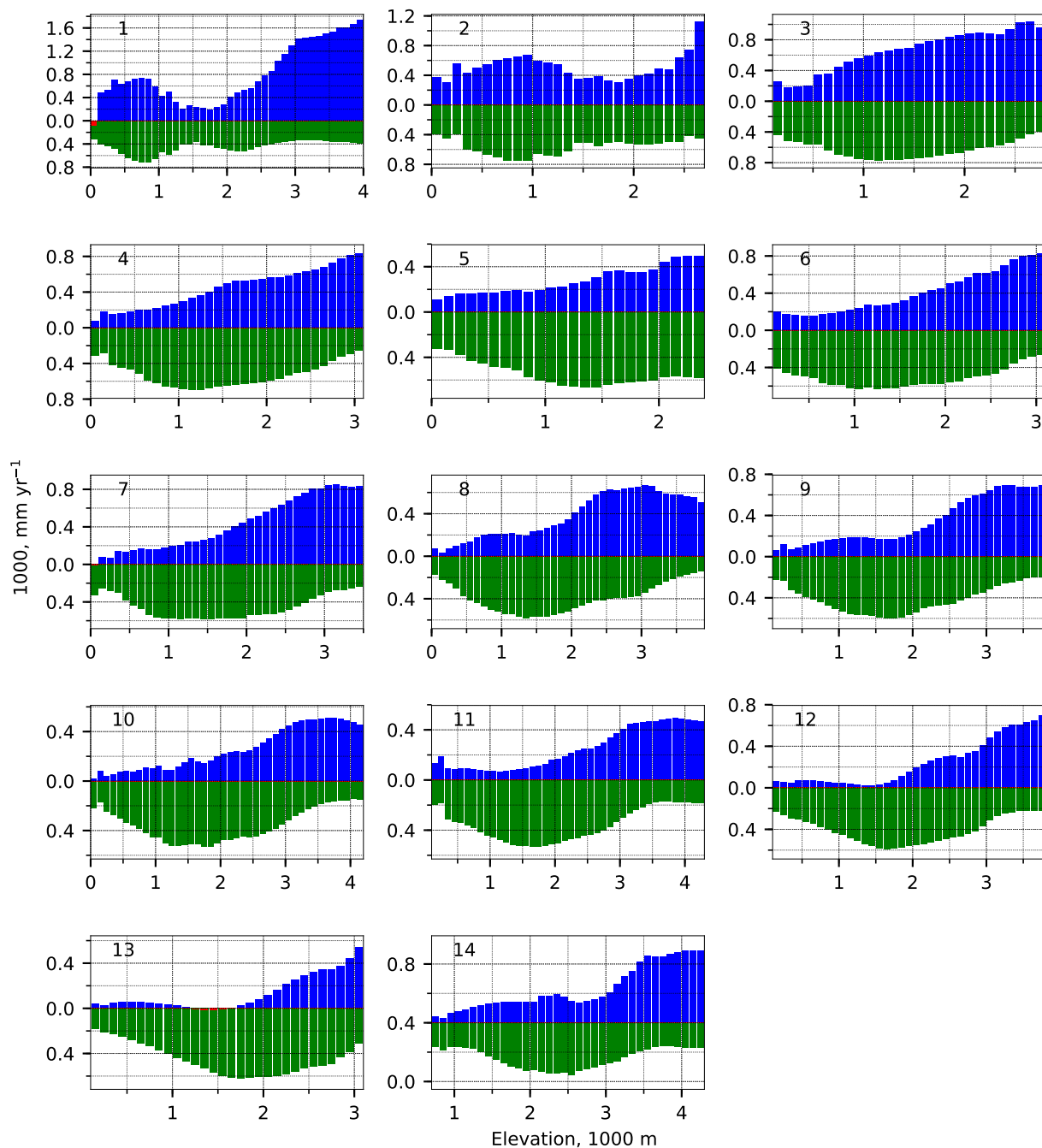


Figure C.4.20: Runoff (blue), evapotranspiration (green), precipitation (dotted hatch), and change in storage (red) binned by basins and elevation for water year 2004. Number corresponds with Basin numbers in Figure 1.

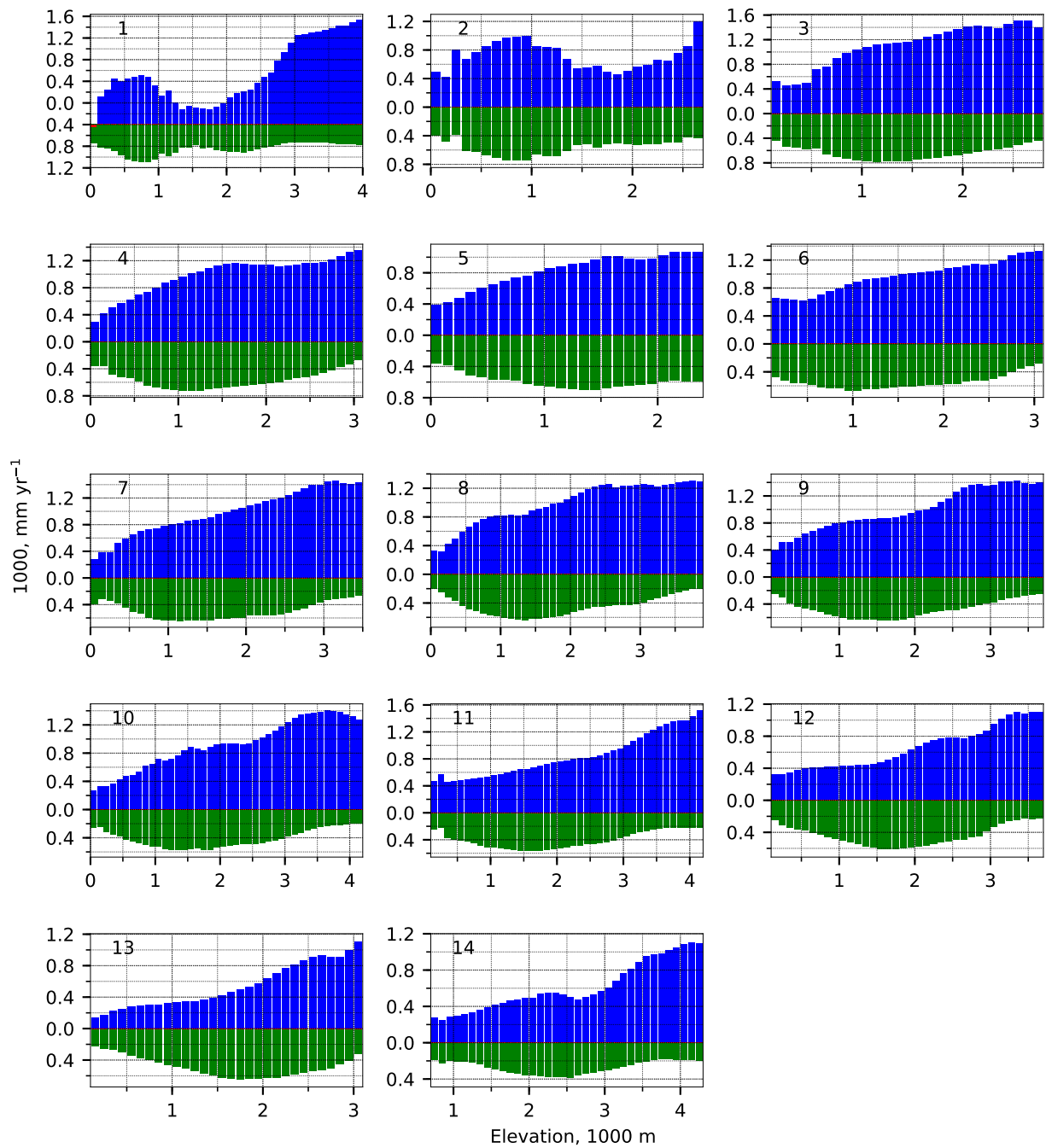


Figure C.4.21: Runoff (blue), evapotranspiration (green), precipitation (dotted hatch), and change in storage (red) binned by basins and elevation for water year 2005. Number corresponds with Basin numbers in Figure 1.

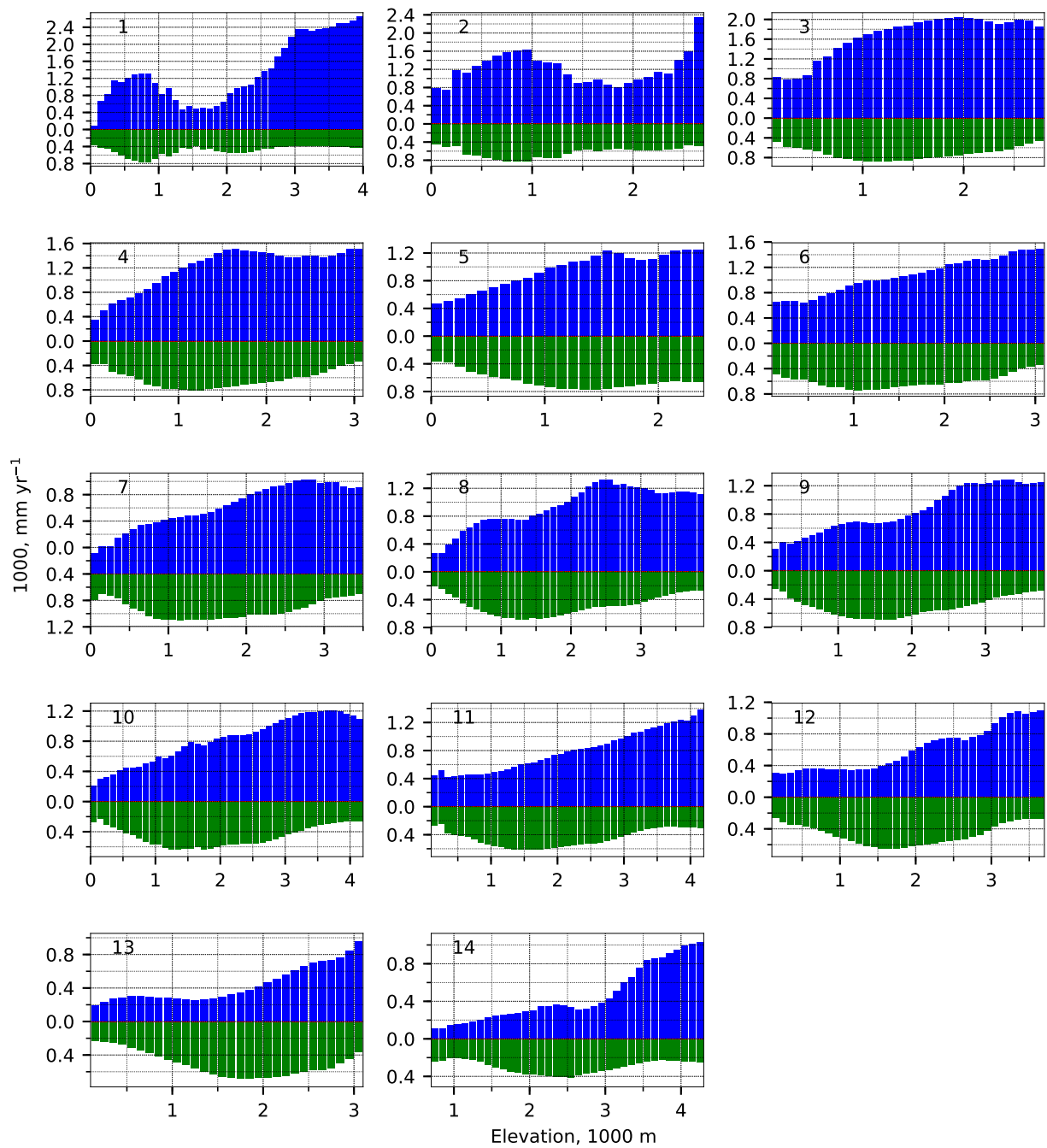


Figure C.4.22: Runoff (blue), evapotranspiration (green), precipitation (dotted hatch), and change in storage (red) binned by basins and elevation for water year 2006. Number corresponds with Basin numbers in Figure 1.

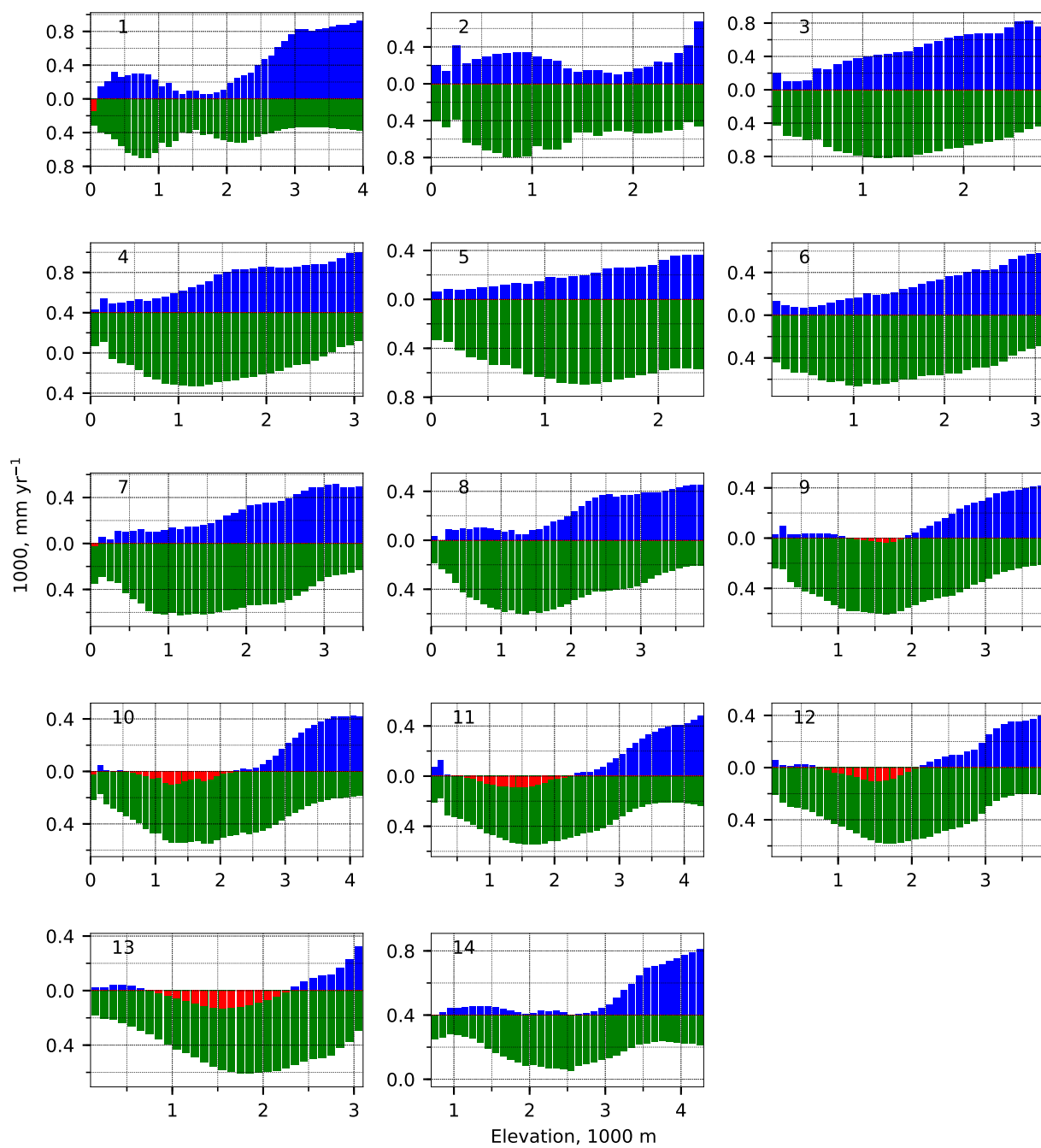


Figure C.4.23: Runoff (blue), evapotranspiration (green), precipitation (dotted hatch), and change in storage (red) binned by basins and elevation for water year 2007. Number corresponds with Basin numbers in Figure 1.

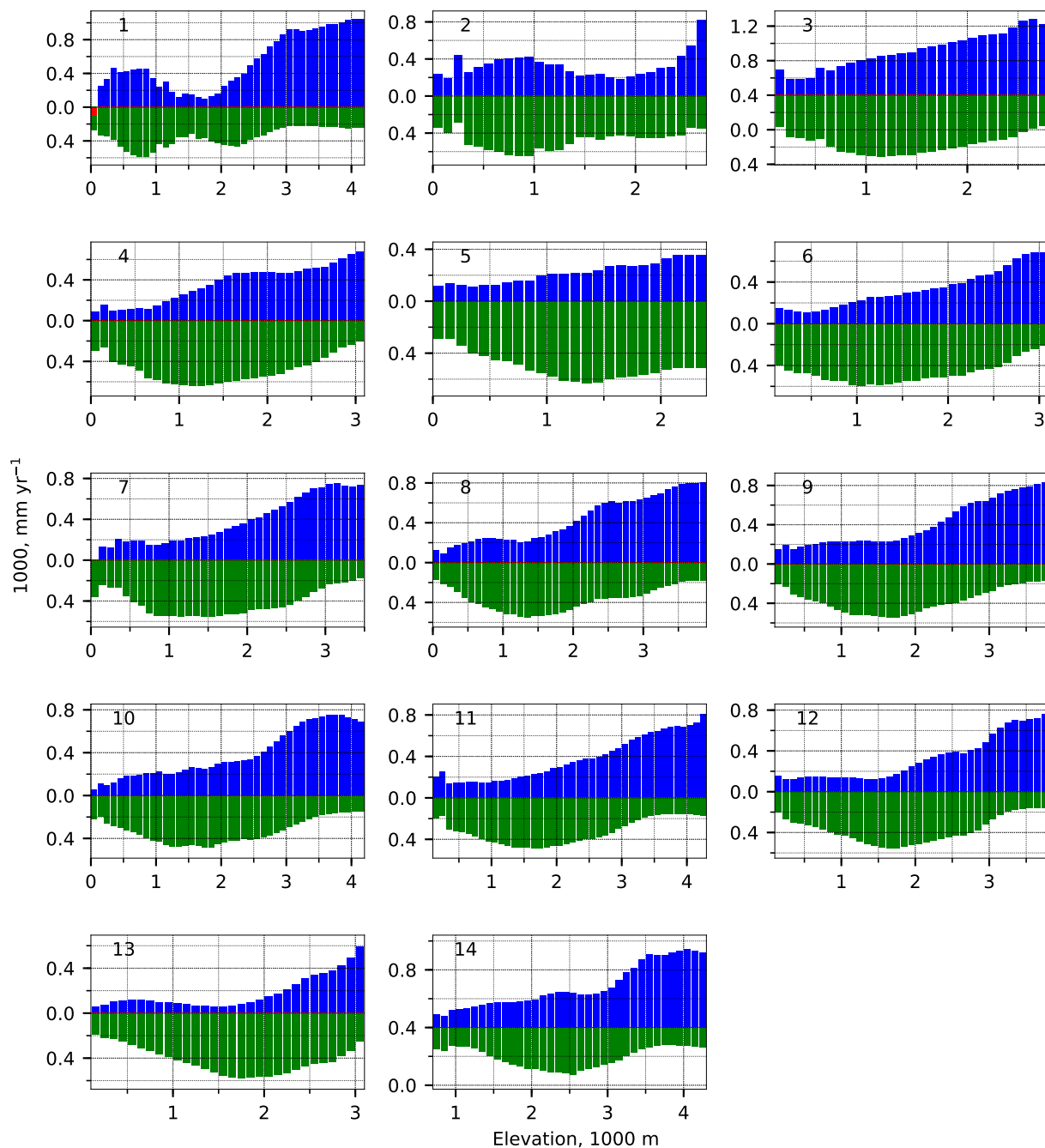


Figure C.4.24: Runoff (blue), evapotranspiration (green), precipitation (dotted hatch), and change in storage (red) binned by basins and elevation for water year 2008. Number corresponds with Basin numbers in Figure 1.

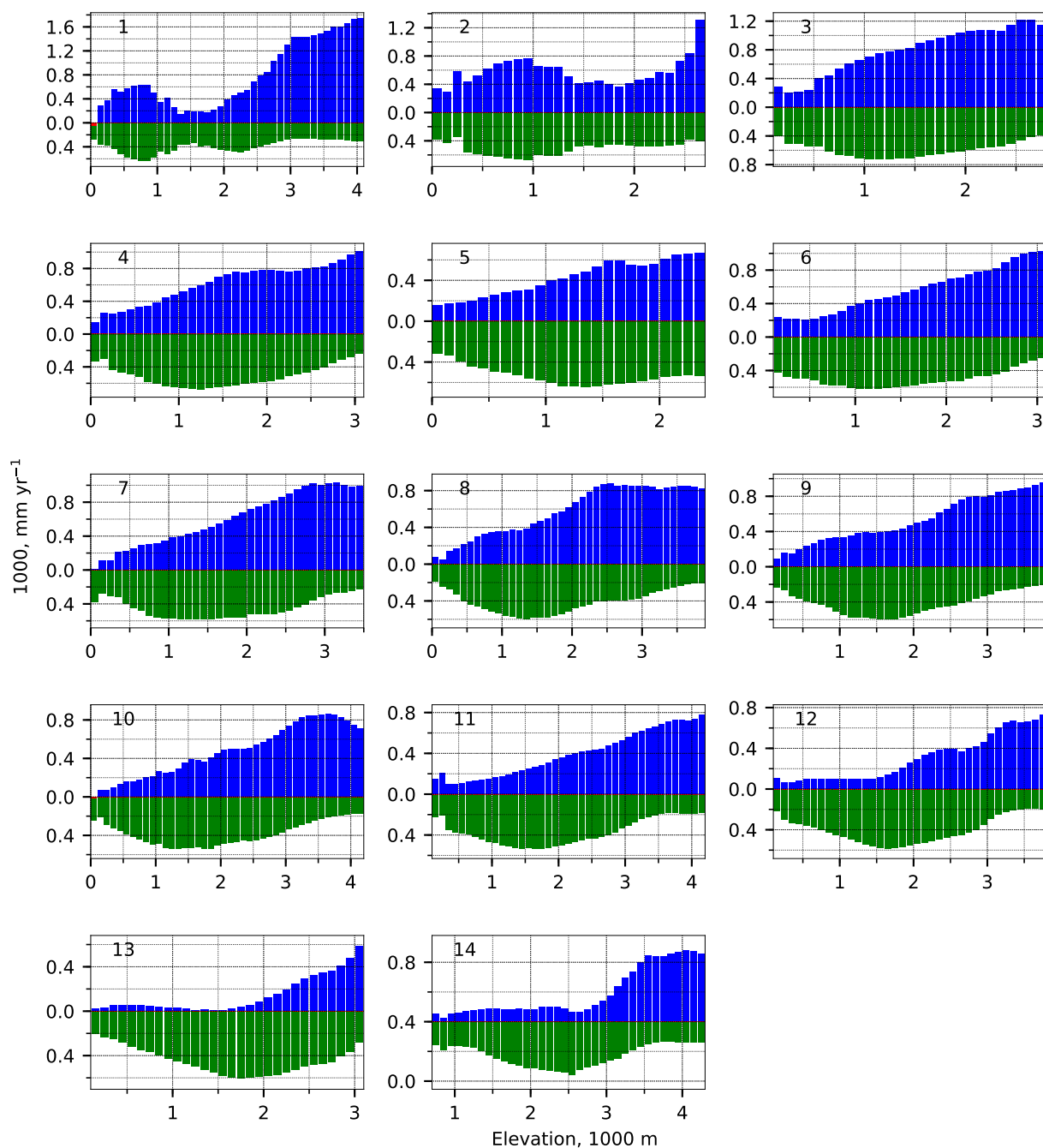


Figure C.4.25: Runoff (blue), evapotranspiration (green), precipitation (dotted hatch), and change in storage (red) binned by basins and elevation for water year 2009. Number corresponds with Basin numbers in Figure 1.

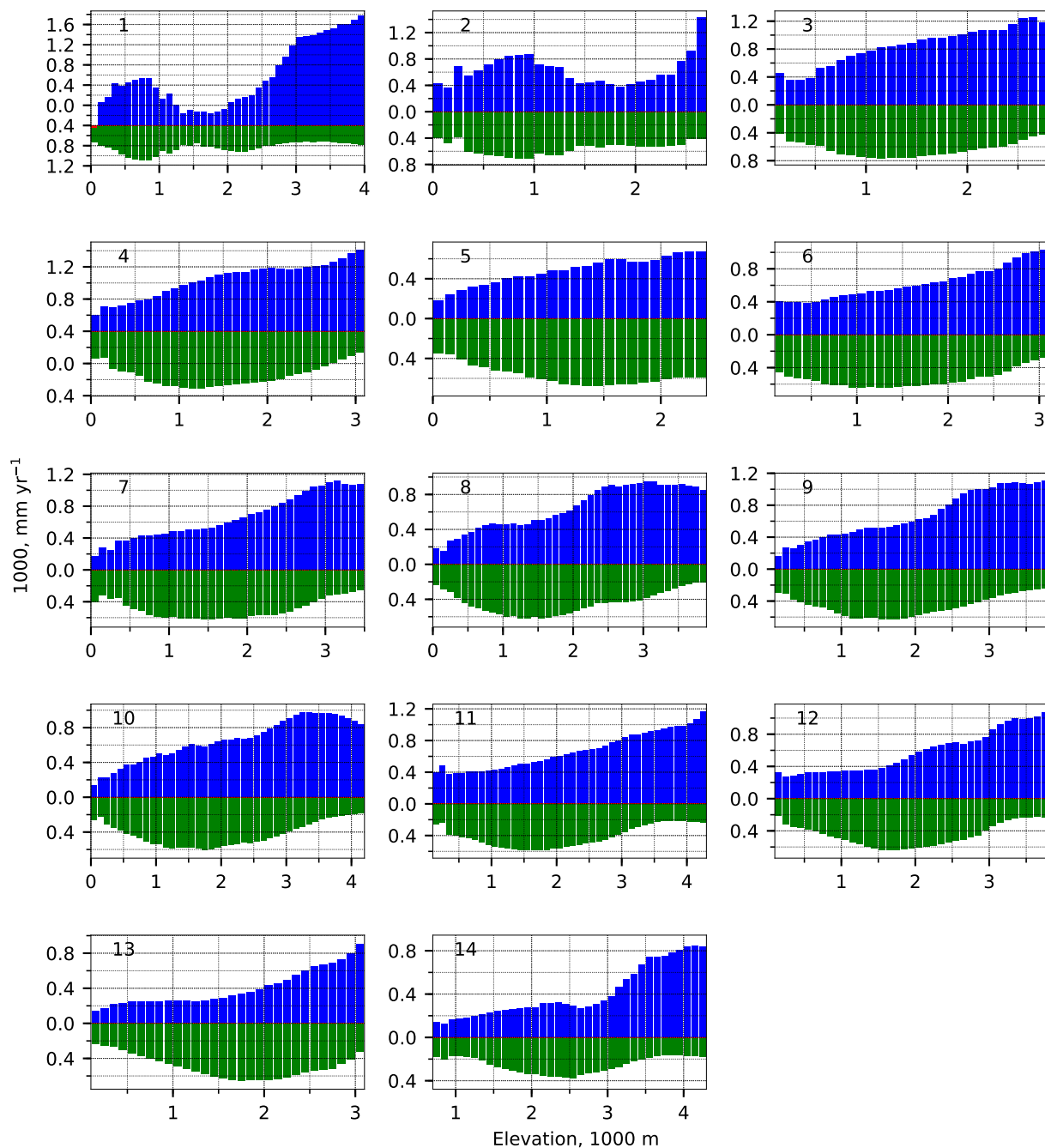


Figure C.4.26: Runoff (blue), evapotranspiration (green), precipitation (dotted hatch), and change in storage (red) binned by basins and elevation for water year 2010. Number corresponds with Basin numbers in Figure 1.

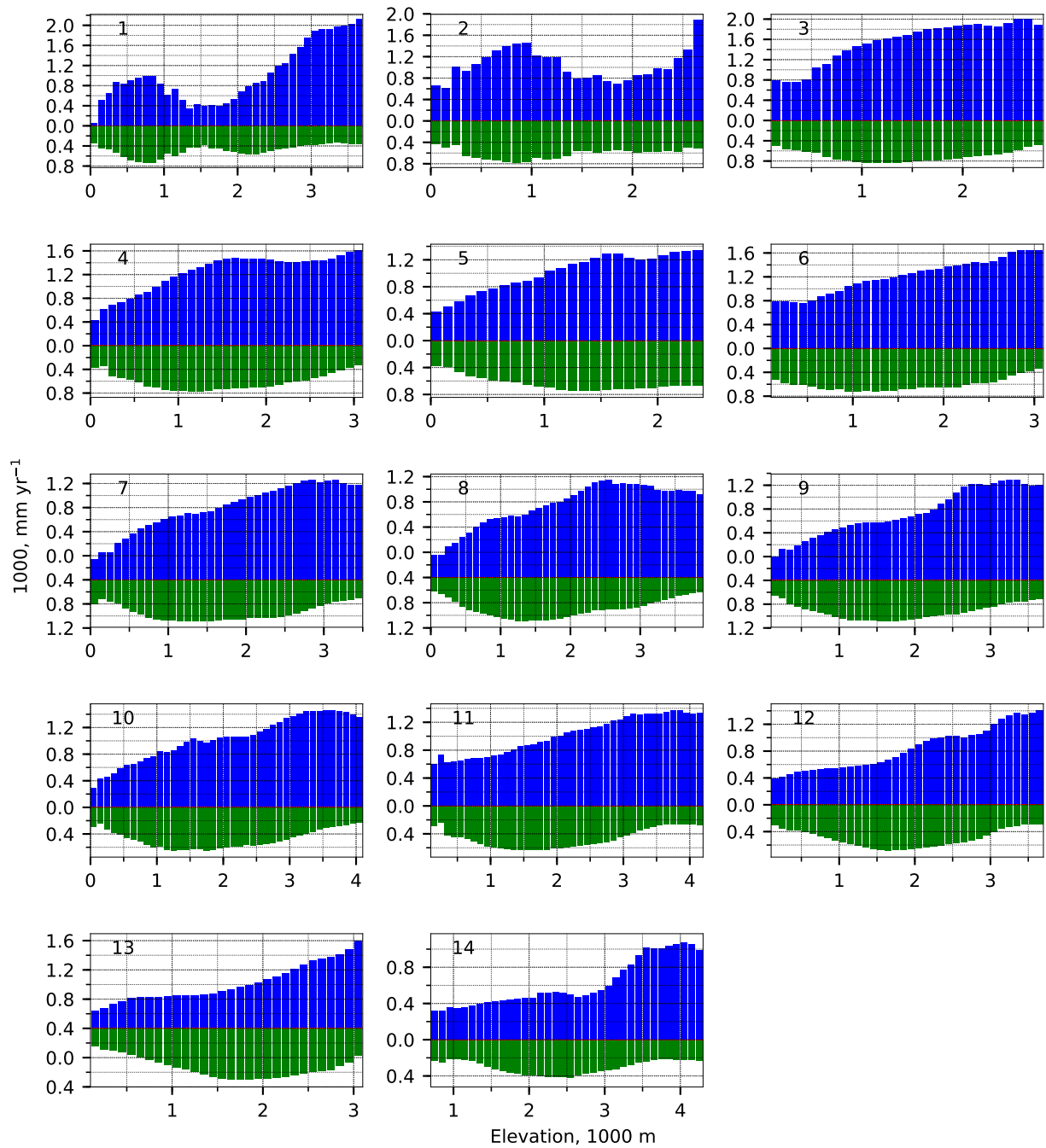


Figure C.4.27: Runoff (blue), evapotranspiration (green), precipitation (dotted hatch), and change in storage (red) binned by basins and elevation for water year 2011. Number corresponds with Basin numbers in Figure 1.

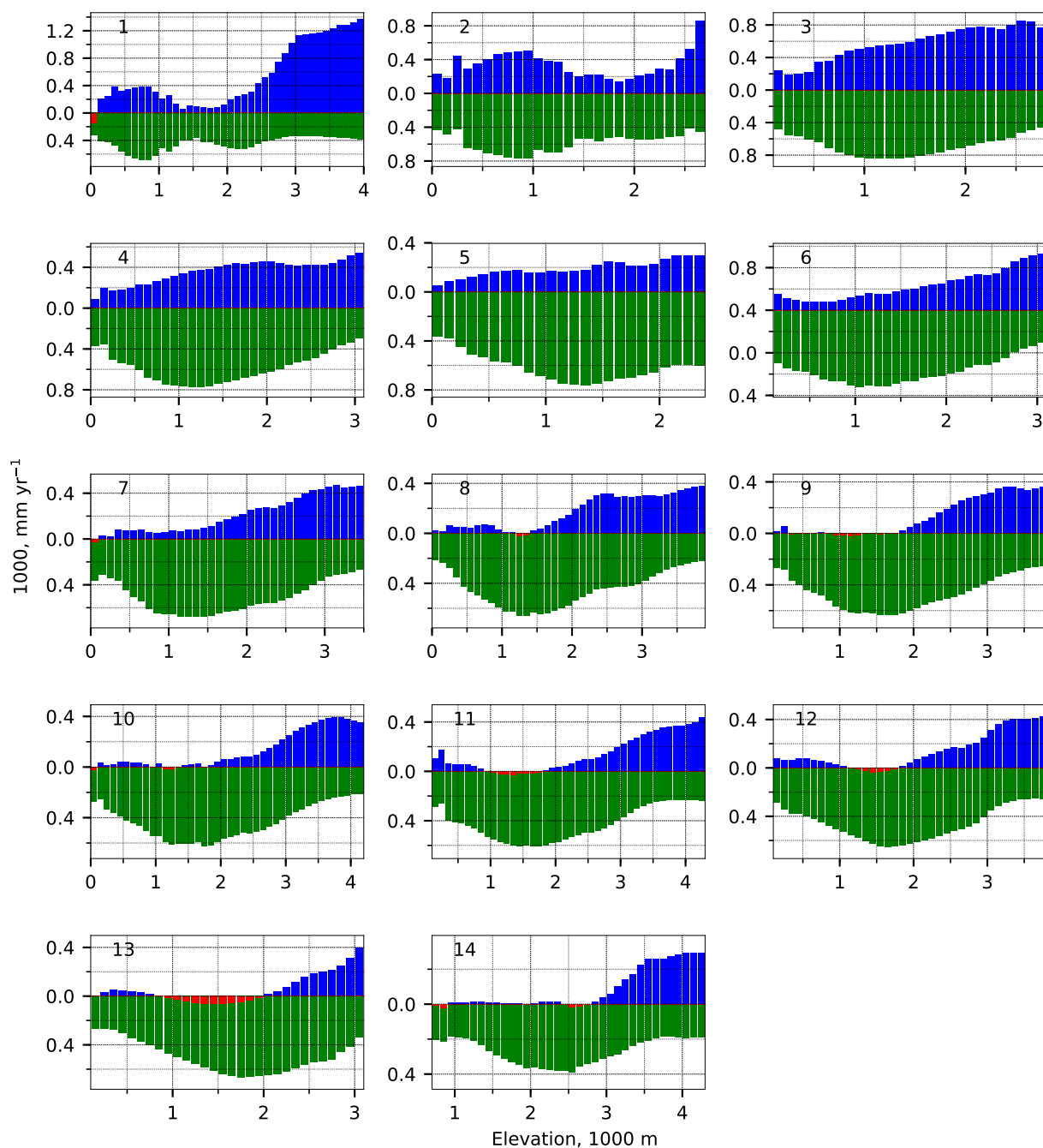


Figure C.4.28: Runoff (blue), evapotranspiration (green), precipitation (dotted hatch), and change in storage (red) binned by basins and elevation for water year 2012. Number corresponds with Basin numbers in Figure 1.

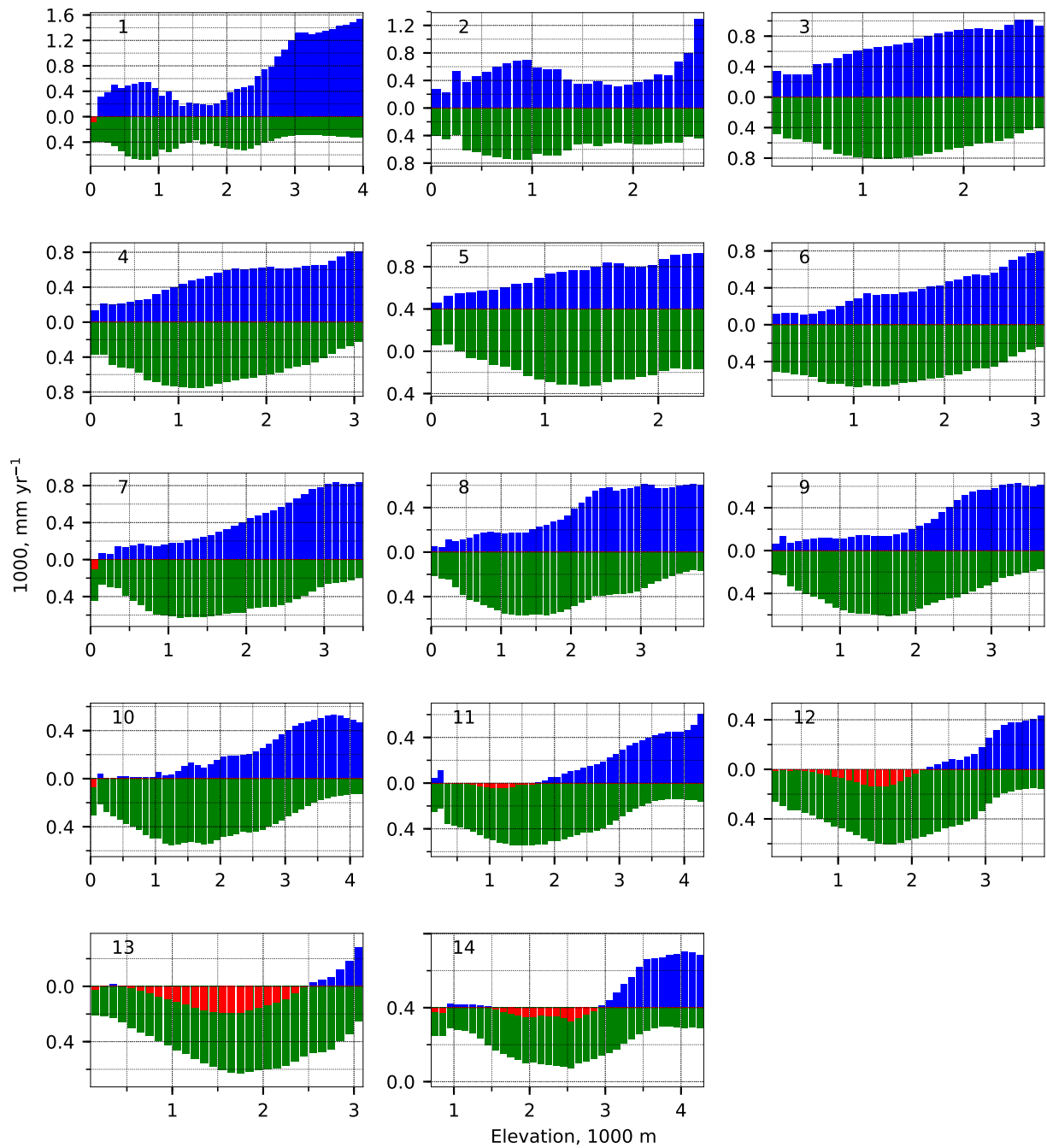


Figure C.4.29: Runoff (blue), evapotranspiration (green), precipitation (dotted hatch), and change in storage (red) binned by basins and elevation for water year 2013. Number corresponds with Basin numbers in Figure 1.

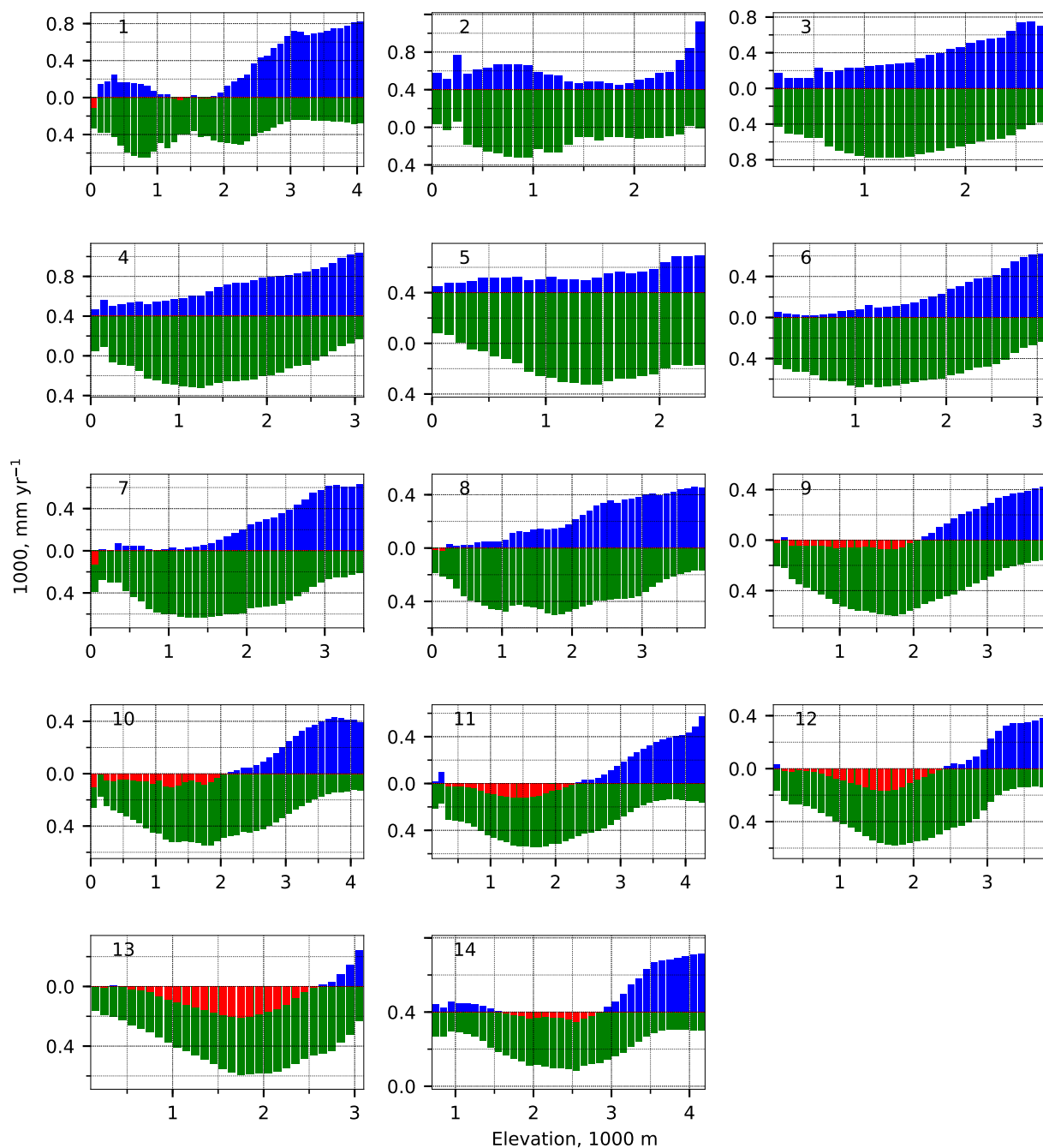


Figure C.4.30: Runoff (blue), evapotranspiration (green), precipitation (dotted hatch), and change in storage (red) binned by basins and elevation for water year 2014. Number corresponds with Basin numbers in Figure 1.

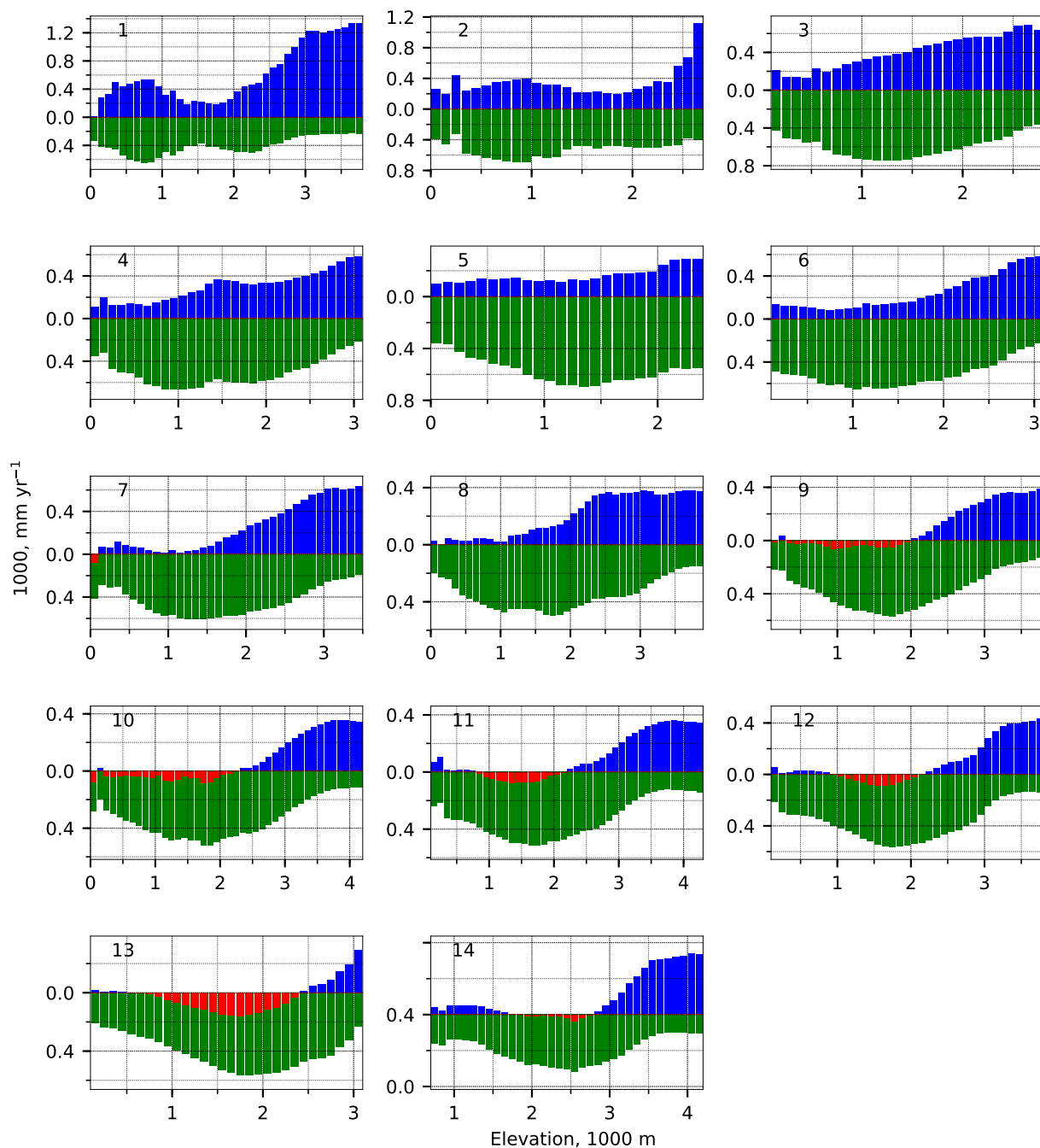


Figure C.4.31: Runoff (blue), evapotranspiration (green), precipitation (dotted hatch), and change in storage (red) binned by basins and elevation for water year 2015. Number corresponds with Basin numbers in Figure 1.

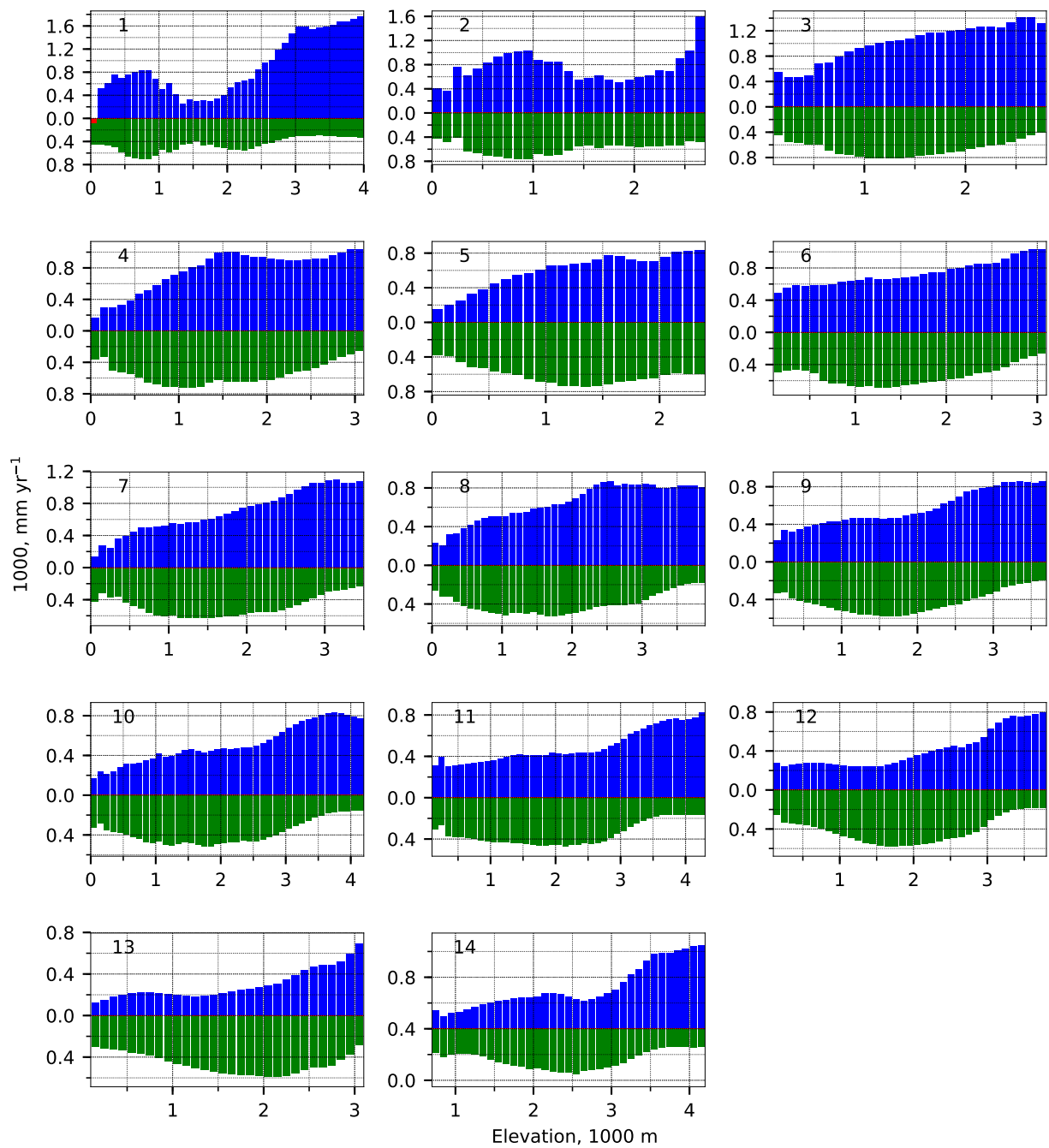


Figure C.4.32: Runoff (blue), evapotranspiration (green), precipitation (dotted hatch), and change in storage (red) binned by basins and elevation for water year 2016. Number corresponds with Basin numbers in Figure 1.

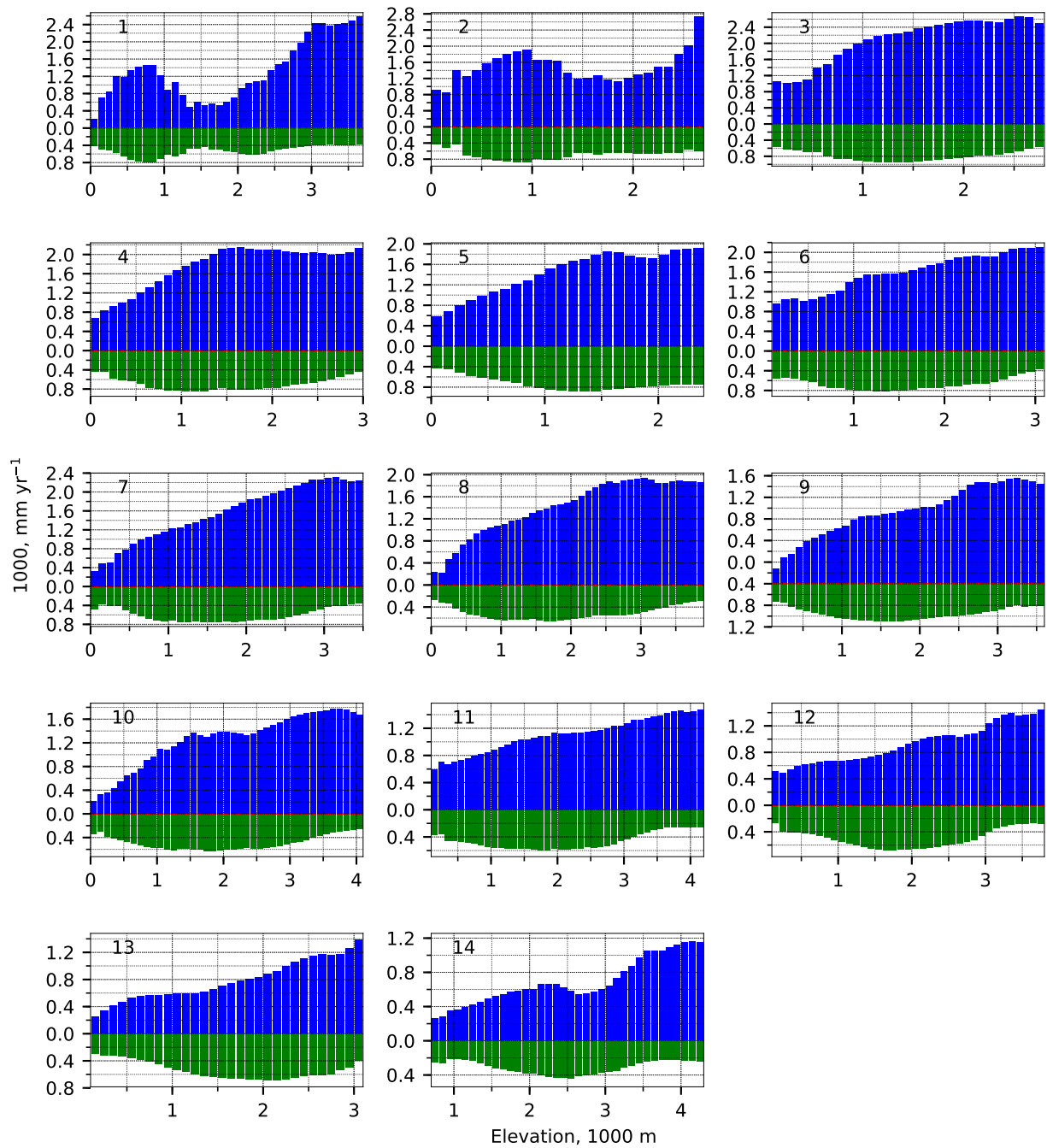


Figure C.4.33: Runoff (blue), evapotranspiration (green), precipitation (dotted hatch), and change in storage (red) binned by basins and elevation for water year 2017. Number corresponds with Basin numbers in Figure 1.

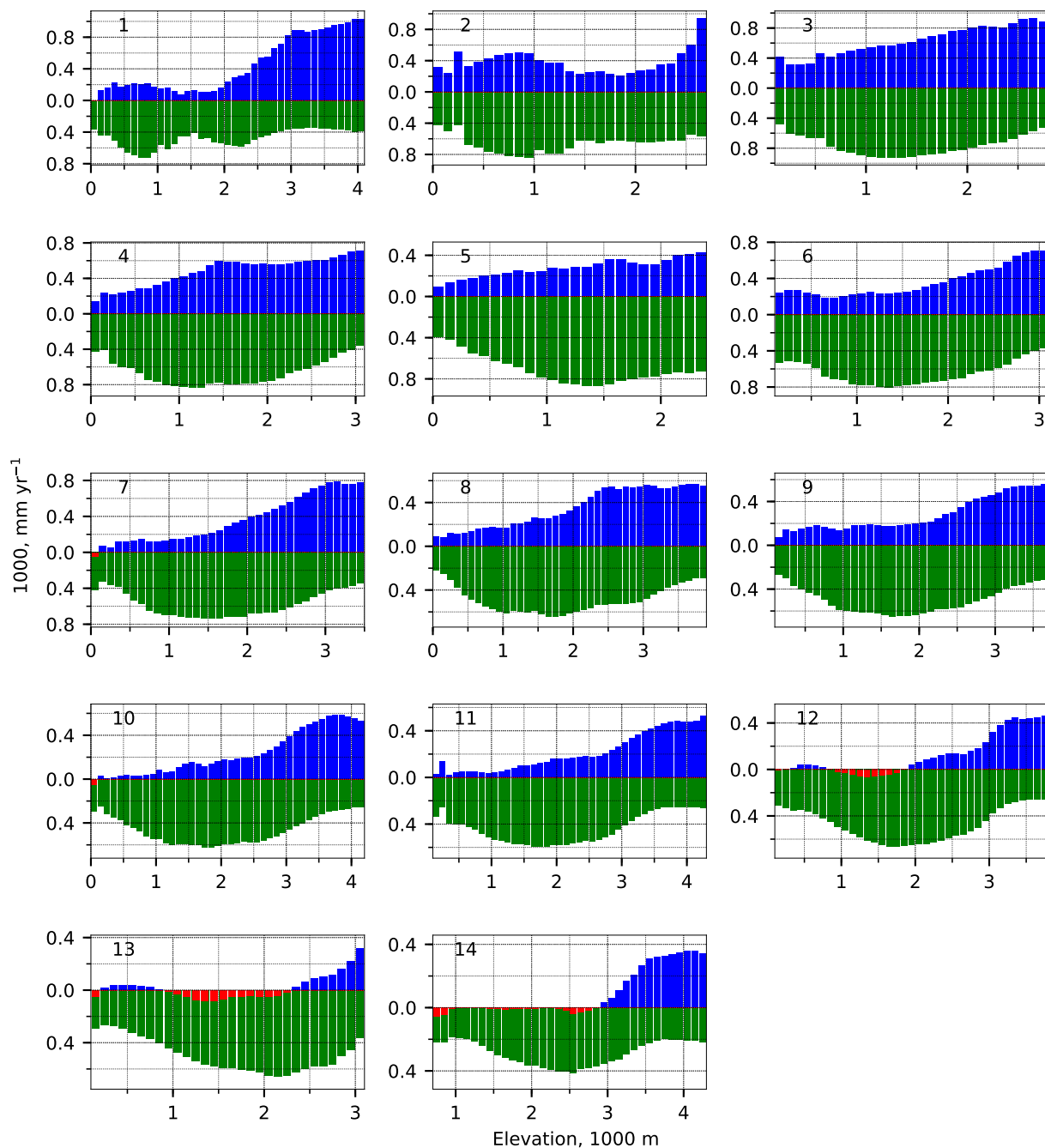


Figure C.4.34: Runoff (blue), evapotranspiration (green), precipitation (dotted hatch), and change in storage (red) binned by basins and elevation for water year 2018. Number corresponds with Basin numbers in Figure 1.